BULGARIAN CHEMICAL COMMUNICATIONS

Preface

Dear Reader,

The VI-th National Crystallographic Symposium (NCS2016), held in the Grand Hall of the Bulgarian Academy of Sciences, on 05–07 October 2016 is the successive initiative of a project started in the beginning of 2009 by a group of Bulgarian crystallographers – enthusiasts and it is nowadays conducted under the auspices of the Bulgarian Crystallographic Society (BCS). During the years one of the main goals of the Symposium has been the promotion of the various crystallographic techniques, methods, programs, software to a larger audience from different scientific fields: theoretical crystallography, crystal growth, mineralogy, materials science, solid state physics, structural biology, chemical crystallography and other areas, as well. This was a memorable opportunity to review current developments in crystallography, addressing materials science challenges imposed by new materials. The progress in this direction is determined mostly by the level of experimental techniques – new possibilities emerging from new, intense, tunable and precisely focused X-ray beams, as well as from high resolution, sensitive, energy dispersive detectors – that were presented by our kind sponsors: TA instruments, Jeol, Bruker, Panalytical, Zeiss, ELTA'90, Aquachim, Labexpert, InfoLab.

Following the path, established during the previous Symposia, the organizers in conjunction with the BCS have dedicated a special honorary sign to Prof. Kostadin Petrov from the Institute of General and Inorganic Chemistry of Bulgarian Academy of Sciences (see photo). He was the first amongst the enthusiasts to start not only thinking but really to act for the establishment of an independent Crystallographic Society in Bulgaria. The National Crystallographic Committee, which was chaired by Professor Kostadin Petrov laid down the foundations for the appearance of the Bulgarian Crystallographic Society in 2009.

The lecturers of the NCS2016 were leading researchers in their respective fields: Svetlana Mintova, ENSICAEN, France, Professor Katharina Fromm, University of Fribourg, Department of Chemistry, Professor Krzysztof Wozniak, University of Warsaw, Poland, Professor Atul Khanna, Department of Physics, Guru Nanak Dev University, India, Professor Srebri Petrov, University of Toronto, Canada, Professor Boriana Mihailova, University of Hamburg, Germany, Evdokiya Salamanova, Karolinska Institute, Department of Biosciences and Nutrition, Sweden, Professor Bogdan Ranguelov, IC–BAS, Professor Pavleta Shestakova, IOCCP – BAS, Professor Radostina Stoyanova IGIC – BAS, Professor Yuri Kalvachev, IMC-BAS, Ivanina Sergeeva, IG-BAS, Professor Alexander Karamanov, IPC-BAS, Liliya Vladislavova, Otto-Schott-Institut für Materialforschung, Friedrich-Schiller-Universität Jena, Germany, Professor Tzonko Kolev, IMB-BAS, Professor Galina Gencheva, Sofia University. Their participation made the Symposium attractive and useful for a wide range of participants and showed the audience the current directions and

Professor Kostadin Petrov (on the left) receiving the honorary sign from Professor Ognyan Petrov (there is no relation between the two professors, the "Petrov" family is widespread in Bulgaria)

5

trends in the application and development of modern science. The audience featured more than 130 scientists (110 registered) from seven Bulgarian universities, 16 institutes of the Bulgarian Academy of Sciences and scientists from universities and institutes from Poland, Switzerland, Germany, France, Sweden, Italy, Slovakia, Spain, Estonia, Turkey, the Republic of Macedonia, Czech republic, Canada, USA and India. A total of 22 oral and 65 poster presentations involved more than 250 authors to present their investigations during the three days of the Symposium.

It is worth noting that over 50% of the participants were students, PhD students and young scientists who actively participated in the poster sessions (with very few exceptions all posters were presented by young scientists). The practice of the organizers of the National Crystallographic Symposia is to encourage and support the scientific progress of young researchers and for the second time the organizers were helped by the Ministry of Science and Education and the Bulgarian National Science Fund through a grant (ДПМНФ 01/13 – 27.09.2016 г.) especially targeting the young scientists. We would like to thank the members of the international jury who had the difficult task to select the best young scientist poster presentation namely Maria Kalapsazova for presenting "Diffraction methods for analysis of layered $Na_xNi_{0.5}Mn_{0.5}O_2$ as cathode materials".

The Symposium attracted the attention of several different Bulgarian Official Institutions: the Deputy-chairman of the Bulgarian Parliament Ivan Ivanov, members of the Parliament's Commissions: for "Education and science", "Children, Youths and Sports", "Environment and Water", Parliament's Deputy Chairpersons Borislav Velikov and Vili Lilkov, The Minister of Education and Science

Maria Kalapsazova receiving the award for best young scientist poster presentation from Professor Katharina Fromm

Meglena Kuneva, the Rector of the University of Chemical Technology and Metallurgy, Professor Mitko Georgiev and the President of Bulgarian Academy of Sciences, represented by the Vice-President Corresponding member Professor Nikolay Miloshev.

We would like to announce that in 2017 two events will be organized under the auspices of the Bulgarian Crystallographic Society:

A workshop on powder diffraction basics (scheduled for June 2017)

International Autumn School on Fundamental and Electron Crystallography, 8–13 October 2017, Sofia, Bulgaria

It is our sincere hope that we are going to see you at the next Bulgarian crystallographic symposium in 2018.

Daniela Karashanova and Boris Shivachev,
Co-chairs of the Organizing Committee

Crystal chemistry and structural characterization of natural Cr-spinels

I. S. Sergeeva[1]*, T. N. Kerestedjian[1], R. P. Nikolova[2],
Z. P. Cherkezova-Zheleva[3], F. Gervilla[4]

[1] *Geological Institute "StrashimirDimitrov", Bulgarian Academy of Sciences, Acad. G Bonchev str.,
bl. 24, 1113 Sofia, Bulgaria*
[2] *Institute of Mineralogy and Crystallography "Acad. Ivan Kostov", Bulgarian Academy of Sciences,
Acad. G. Bonchev str., bl.107, 1113 Sofia, Bulgaria*
[3] *Institute of Catalysis, Bulgarian Academy of Sciences, Acad. G Bonchev str., bl. 11,
1113 Sofia, Bulgaria*
[4] *Departamento de Mineralogıa y Petrologia, Universidad de Granada-CSIC,
Avda.Fuentenueva s/n, 18002 Granada, Spain*

Two natural chromian spinel samples were examined by means of electron microprobe chemical analysis (EPMA), powder X-ray diffraction, single-crystal X-ray diffraction and Mössbauer spectroscopy, in order to reveal some aspects of the relationships between composition and structural parameters. The samples originate from the East Rhodopean serpentinite massive of Golyamo Kamenyane in Bulgaria, which is part of a dismembered ophiolite complex. The two samples differ significantly in textural, chemical and structural respect. One of the samples is chromium rich and can be regarded as Cr-spinel, whereas the other one is very rich in Fe^{2+} and Fe^{3+} (as shown by EMPA and Mössbauer spectroscopy), approximating magnesioferrite end member of the spinel group. These contrasting compositional differences result in very pronounced differences in structural parameters – unit cell parameter and *u* oxygen positional parameter, which reflect different conditions of formation and/or alteration. The *u* parameter is indicative for the thermal history of the hosting ultramafic rock. It depends on cation distribution, but not very strongly, which allows rather accurate determination of *u* within reasonable limits of cation distribution uncertainty. Nevertheless, our results show, that diffraction studies alone are insufficient for geothermometric purposes and have to be combined with EPMA and Mössbauer data. Calculated system closure temperatures for both samples indicate 796–1073 °C, which are acceptable for the Cr-spinel reequilibration conditions on cooling. For outer rims of the crystals, however, as well as for the iron rich sample, formed during later metamorphic events, lower temperatures should be expected.

Keywords: Cr-spinels, X-ray diffraction, structural parameters.

INTRODUCTION

The natural Cr-spinels belong to the group of 2-3 oxide spinels with general formula AB_2O_4, where:

- tetrahedrally coordinated cations A = Mg, Fe^{2+}, Zn, Mn^{2+}, etc.
- octahedrally coordinated cations B = Cr, Al, Fe^{3+}, Ti^{4+}, V^{3+}, Co, etc.

Two fully ordered cation distributions are known in spinels: normal $A[B_2]O_4$ for ideal chromite and inverse $B[AB]O_4$ for ideal magnetite. A and B represent divalent and trivalent cations respectively, occupying the tetrahedrally (round or no brackets) and octahedrally (square brackets) coordinated sites, whereas O is anion (oxygen) site in the structure. Intermediate cation distributions, are expressed with the structural formula:

- $(A_{1-x}B_x)[A_xB_{2-x}]O_4$, where x denotes inversion parameter

In the normal spinel x is equal zero and in the inverse one – unity [1].

The inversion parameter, x, is defined as the fraction of B-type cations in the tetrahedral site (A).

Both Cr-spinel and magnetite are a common constituent of serpentinized and metamorphosed ultramafic rocks, especially in ophiolite complexes [2–4]. Distinguishing of these mineral species, based on chemical criteria alone is insufficient, since both chromium containing magnetite and high iron Cr-spinel are common in metamor-

---

* To whom all correspondence should be sent:
E-mail: sergeevai@geology.bas.bg

phosed/serpentinized peridotites. The only way to identify the species is by determination of the inversion parameter.

The differentiation of both species is crucial for geological interpretation, since Cr-spinel is a typical magmatic product, while magnetite is commonly formed during later, serpentinization alteration or even late hydrothermal events. The availability of overprinting regional metamorphic events, altering the initial, pristine Cr-spinel and pretty common in such environment, additionally complicates the interpretation of observed mineral relations.

Another important parameter is the oxygen positional parameter u which can be used for determination of system closure temperature, important for the genetic interpretation of the mineral forming processes [4–7]. The determination of this parameter value requires prompt determination of cation distribution in first order.

In this paper, the crystal chemistry of two natural Cr-spinels from Golyamo Kamenyane serpentinite was studied by multiple methods in order to explore the composition – structure relations. Both unit cell parameter a and oxygen positional parameter u depend on cation distribution in tetrahedral and octahedral sites of the spinel structure. However, complex chemistry of natural spinels hampers the correct determination of cation distribution with a single research method. This is why we employ a number of supporting methods. In addition, the reliability of structural interpretations was checked by applying two independent X-ray diffraction studies – powder and single crystal.

GEOLOGICAL SETTING

The Golyamo Kamenyane serpentinite is part of a dismembered metaophiolite, located in the Avren synform, in the Upper High-Grade Unit of the metamorphic basement of Eastern Rhodopean crystalline massif, in South Bulgaria [8–10] (Fig. 1).

Metamorphism of these rocks had reached eclogite-facies conditions (up to 13–16 kbar and 600 °C) followed by variable retrogressive P–T trajectories [11–13] down to greenschist-facies conditions. This unit also includes scattered bodies of ultramafic rocks (partly serpentinized peridotites, locally preserving garnet-bearing assemblages [14].

Although the metamorphic conditions of the Golyamo Kamenyane serpentinite are not calculated yet, according to Kozhoukharova [15], amphibolitized eclogites from the Avren synform had reached 12–17 kbar and 750–811 °C.
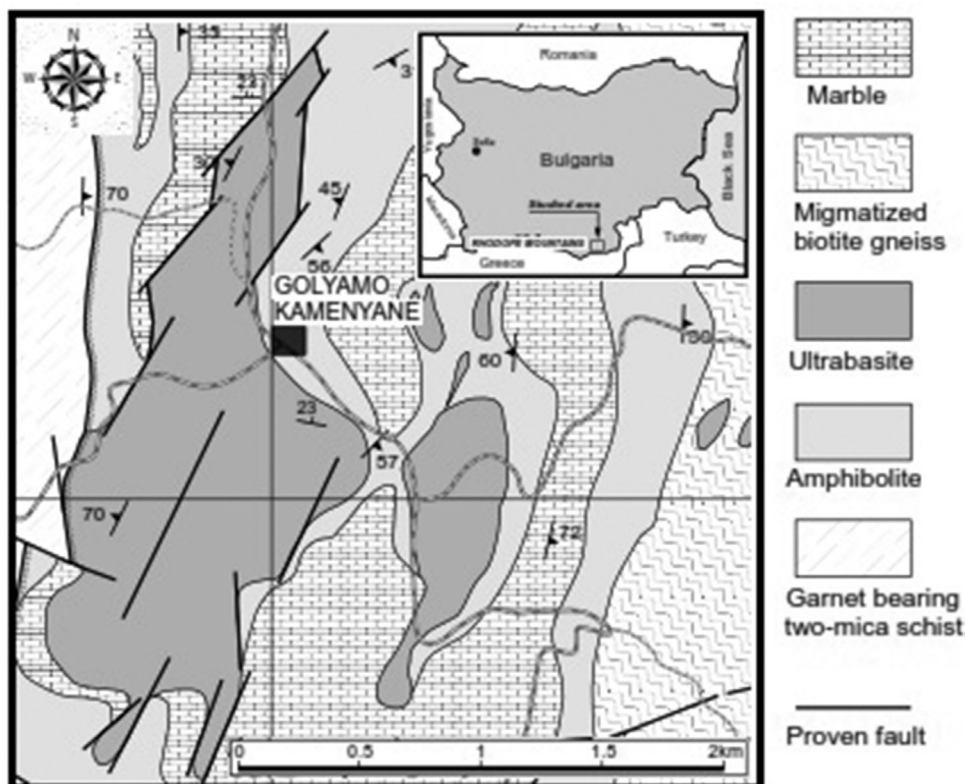

Fig. 1. Geological map of the Golyamo Kamenyane serpentinite and nearby areas (modified from Sarov et al. 2007).

MATERIALS AND METHODS

Sampe description and sample preparation

The Cr-spinels studied were extracted from chromite ore bodies (chromitites) which show massive (> 85 vol. % Cr-spinel) and semi-massive (60-85 vol. % Cr-spinel) textures. The massive chromitite is coarse grained, relatively homogeneous with minor inclusions of antigorite, whereas, the semi-massive one is associated with considerable amount of chlorite (Cr-clinochlore), filling the interstitial grain spaces and forming coatings around Cr-spinel grains.

Cr-spinel and silicate fractions were separated from all samples for XRD and Mössbauer spectroscopy analysis. The procedure involves grinding, sieving and combined magnetic and gravity separation in a vibrating micro-panner and bromoform column sedimentation.

Electron probe micro analysis

The Cr-spinel samples were studied by environmental scanning electron microscope (ESEM) in backscattered electron (BSE) mode prior to microprobe analysis (EPMA).

Spots for analysis were selected on BSE images, along core to rim cross-sections, in order to reveal the chemical composition of all alteration zones.

Chemical compositions were obtained using a CAMEBAX SX100 at the Centro de Instrumentación Científica of the University of Granada (Spain) under an excitation voltage of 20 kV and a beam current of 20 nA, with a beam of 2–3 μm in diameter. Monitored spectral lines were MgKα, FeKα, AlKα, CrKα, SiKα, TiKα, MnKα, NiKα and VKα. Standards used were MgO, Fe_2O_3, Al_2O_3, Cr_2O_3, SiO_2, TiO_2, $MnTiO_3$, NiO and $Pb_5(VO_4)_3Cl$. Structural formulae of Cr-spinel were calculated assuming stoichiometry, with correction from C-J De Hoog[17].

Mössbauer spectroscopy

Mössbauer spectra were collected at 297 K in transmission mode, using a conventional constant acceleration spectrometer (Wissenschaftliche Elektronik GMBH, Germany), and a 50 mCi ^{57}Co/Rh source. The velocity scale was calibrated according to the centroid of reference spectrum of α-Fe foil at room temperature. Mössbauer absorbers were prepared from powdered Cr-spinel samples pressed into sample holder. The experimental spectra were analyzed using least-squares program CONFIT [18], which allows evaluation of registered Mössbauer spectra with Lorenzian peak shape.

The refined parameters of hyperfine interactions were isomer shift (IS), quadrupole splitting (QS) and effective internal magnetic field (H_{eff}). Line broadening (FWHM) and relative weight of partial components (G) were also obtained. The highest convergence of experimental and theoretical spectra was accepted for the best fit.

Powder X-ray diffraction

The separated monomineralic fractions from Cr-spinel samples were grinded in agate mortar with alcohol to obtain fine suspension. The suspension was then finely deposited on thin Mylar foil, stretched onto sample holder.

X-ray powder diffraction analyses were carried out using HUBER Guinier Image Plate Camera G670 in asymmetric transmission mode, with Cu Kα₁ radiation, in the range 4–100 degrees and step size of 0.005 2θ at the Geological Institute of the Bulgarian Academy of Sciences. Diffraction data were treated with MATCH! software package for phase analysis, by CRYSTAL IMPACT, Bonn, Germany[19].

The Rietveld structure refinement was performed with FULLPROF Suite Program, by Juan Rodrigues Carvajal [20]. Structural parameters were refined within the space $Fd\bar{3}m$ group with origin at $\bar{3}m$ position and tetrahedral ions placed in 8(*a*) position; octahedral ions in 16(*d*) and oxygen ions in 32(*e*) position. The refined parameters were zero shift, scale factor, unit cell parameters, oxygen positional parameter, occupation factors for both – tetrahedral and octahedral sites and isotropic thermal displacement parameters (B) for both cationic positions and oxygen (anionic) positions. Pseudo Voigt and TCH profile functions were used for approximation of the peak shape. The background curve was modeled using linear interpolation between manually selected background points from the raw diffraction pattern. This procedure shows very good background approximation. Data from EPMA and Mössbauer spectroscopy (Fe^{2+}/Fe^{3+} distribution) were used as starting model for the Rietveld refinement. Preferred cation positions were chosen on the basis of literature data [21, 22]. Initial unit cell parameters were taken from the closest database match, proposed by MATCH! phase identification software. In order to avoid unnecessary complexity of the refinement procedure, the minor element (Ti, V, Ni, Mn) contents were fixed at values obtained from EPMA. The isotropic thermal displacement parameters in one of the samples (GK1A-7) were refined at the end of the procedure, with all previously refined parameters fixed, because very strong correlations were observed. These correlations were attributed to the high amount of peak overlapping

of different phases in this sample. For the other Cr-spinel (GK1C-1), thermal displacement parameters were refined together with the rest of general parameters.

Single crystal studies

Crystal fragments of natural Cr-spinels suitable for single crystal X-ray analyses were used. X-ray diffraction measurements were collected at room temperature by ω-scan technique on an Agilent Oxford Diffraction Super Nova Dual four-circle diffractometer equipped with Atlas CCD detector. X-ray data collection was carried out at room temperature using mirror- monochromatized MoKα radiation micro-focus source (λ=0.7107Å). The determination of unit cell parameters, data integration, scaling and absorption correction were carried out using the CrysAlisPro program package [23]. The structures were solved by direct methods (SHELXS-97) [24] and refined by full-matrix least-square procedures on F^2 (SHELXL-97) [24]. The atomic displacement parameters were refined anisotropically.

Overall six crystal fragments from both Cr-spinel samples were chosen for better statistics. Structure refinements were performed using F_o^2 in space group $Fd\bar{3}m$ (№227) constrained on full site occupancy.

Refined parameters were overall scale factor, extinction coefficient, atomic coordinates, tetrahedral and octahedral site occupancies and atomic displacement parameters U. Refined site occupancies are expressed as mean atomic number (product of atomic fraction and atomic number of chemical species entering both structural positions) in tetrahedral (Td m.a.n.) and octahedral (Oh m.a.n.) sites, respectively.

Obtained cation distribution was additionally refined according to a procedure described by Lavina et al. [21], in which both structural and chemical data (bond lengths, *a*, *u* and atomic proportions) are taken into account. In this procedure the cation distribution is obtained by minimising the differences between observed crystal-chemical parameters (*a*, *u*, Td-O, Oh-O and chemical composition, obtained from structure refinement and EPMA) and those calculated from variable site atomic fractions. The bond lengths were calculated as the linear contribution of each cation multiplied by its ideal bond length at the respective site. The ideal bond lengths for all chemical species known in spinels are well determined on the basis of analysis of more than 290 spinel structural data [21, 22]. During the minimization, the minor cations (Ni^{2+}, V^{3+}, Ti^{4+} and Mn^{2+}) were assigned according to their site preferences and fixed with atomic proportions corresponding to the EPMA data.

Finally, based on cation distributions obtained, we used the geothermometer proposed by Princivalle et al. [25] to calculate system closure temperatures.

RESULTS

SEM and EPMA studies

The Cr-spinel grains in the semi-massive sample (Fig. 2) show clear irregular zoning, with smooth
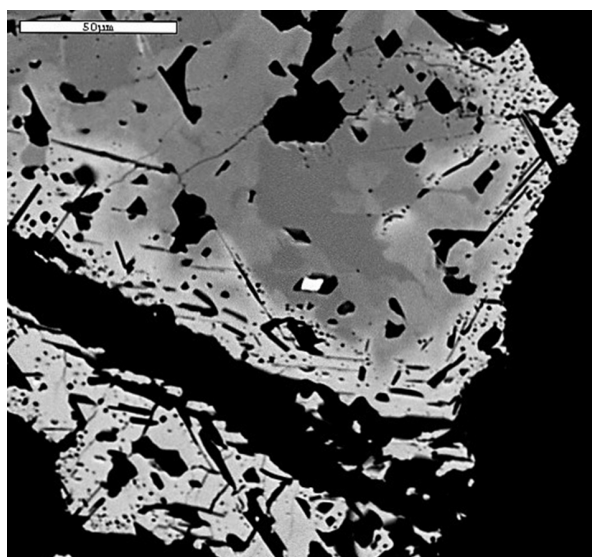

Fig. 2. BSE image of zonal Cr-spinel from the semi-massive sample. Porous rim is richer in Fe^{2+} and Cr.
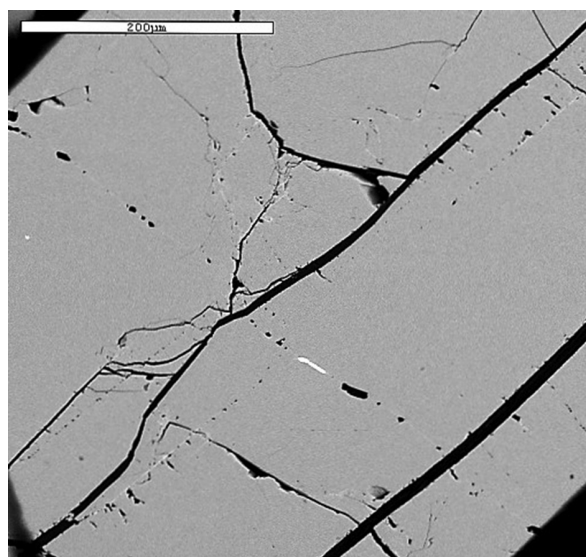

Fig. 3. BSE image of homogeneous Cr-spinel from the massive sample.

cores and pretty porous rims. This zoning is a product of reaction of Cr-spinel with surrounding silicates during retrograde metamorphic alteration [26]. For this reason hereafter we will call this Cr-spinel *zonal*. The mentioned chlorite is the respective silicate side product of the same reaction. Briefly, this alteration is characterized by Mg and Al depletion of Cr-spinel and introduction of extra Fe^{2+} from the silicates.

The Cr-spinel from the massive sample (Fig. 3) shows almost no zoning. For this reason hereafter we will call it *homogeneous*. The visible homogeneity is thought to result from secondary homogenization (magnetitization) during late metamorphic events. EPMA data show that this Cr-spinel is very rich in iron (1.88 *apfu* total Fe) with Cr, Mg, and minor Al contents, approaching magnetite – magnesioferrite joint in the compositional field of Cr-spinels.

Averaged chemical compositions of different Cr-spinel zones (columns 1–4) and bulk (column 5) for the zonal sample as well as bulk Cr-spinel composition for the homogeneous sample (column 6) are given in Table 1.

As seen in this table, zonal Cr-spinel is characterized with high Cr, Al and Mg contents. In core to rim direction a clear trend for Al and Mg depletion, compensated by Fe^{2+} and Cr enrichment are noted, while Fe^{3+}, Mn and minor elements remain fairly constant. This trend of substitution is clearly visible on Fig. 4, where the compositions of the stud-

Table 1. Microprobe data, represented as oxide wt. % and recalculated to pure element values, according to stoichiometry based on 3 cations per 4 oxygen ions. Integral compositional parameters are calculated in the bottom part of the table too

| Sample label, area and number of points	zonal					homogeneous
	GK1A-7 core 13p.	GK1A-7 rim1 13p.	GK1A-7 rim2 8p.	GK1A-7 rim3 7p.	GK1A-7 bulk 41p.	GK1C-1 21p.
Al_2O_3	21.570	17.350	13.890	11.010	16.931	0.434
MgO	14.610	13.340	12.310	11.390	13.208	4.705
FeO	12.651	13.937	14.933	15.923	14.063	23.594
Fe_2O_3	4.991	4.751	4.704	4.057	4.700	41.857
MnO	0.415	0.439	0.491	0.530	0.458	0.633
SiO_2	0.031	0.029	0.030	0.037	0.031	0.035
Cr_2O_3	45.380	49.920	53.460	57.050	50.391	27.805
TiO_2	0.071	0.067	0.070	0.066	0.069	0.260
V_2O_5	0.215	0.187	0.192	0.196	0.199	0.135
NiO	0.150	0.116	0.130	0.110	0.128	0.241
$\sum$	100.084	100.136	100.215	100.369	100.178	99.698
Al	0.776	0.641	0.524	0.422	0.624	0.019
Mg	0.666	0.623	0.587	0.552	0.618	0.258
Fe^{2+}	0.326	0.366	0.400	0.434	0.371	0.724
Fe^{3+}	0.113	0.112	0.113	0.099	0.111	1.156
Mn	0.011	0.012	0.013	0.015	0.012	0.02
Cr	1.101	1.238	1.353	1.469	1.255	0.806
Ti	0.002	0.002	0.002	0.002	0.002	0.007
V	0.004	0.003	0.003	0.003	0.003	0.002
Ni	0.004	0.003	0.003	0.003	0.003	0.007
$\sum$	3.001	3.000	2.998	2.999	2.999	2.999
$Fe^{3+}/Fe_{tot.}$ avg.	0.261	0.234	0.220	0.186	0.230	0.614
Cr/Fe_{tot}	2.51	2.59	2.64	2.76	2.60	0.43
Cr#=Cr/(Cr+Al) avg	0.585	0.659	0.721	0.777	0.668	0.977
Mg#=Mg/(Mg+Fe^{2+})	0.673	0.630	0.595	0.56	0.625	0.263
Fe#=Fe^{3+}/(Cr+Al+Fe^{3+})	0.06	0.06	0.06	0.05	0.06	0.58
$Cr^{3+}/(Cr^{3+}+Fe^{3+})$	0.906	0.917	0.923	0.937	0.920	0.411
$\sum Fe$	0.439	0.478	0.513	0.533	0.482	1.88
Fe^{3+}/Fe^{2+}	0.35	0.31	0.28	0.23	0.30	1.60
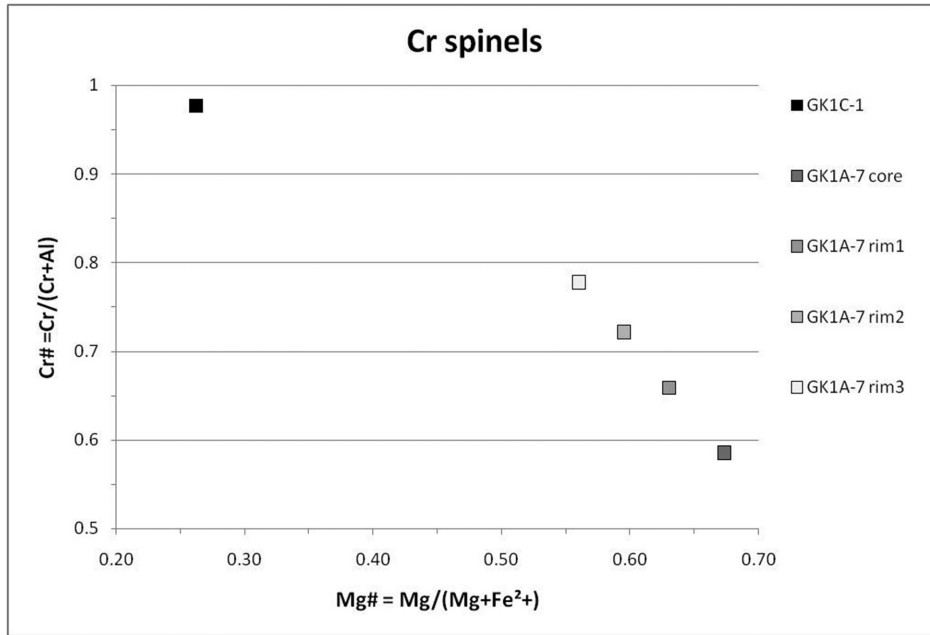
Fig. 4. Mg# vs. Cr# compositional diagram. Sample GK1A-7 (gray squares) is zonal with preserved pristine cores and GK1C-1 (black square) is homogeneous, very rich in iron Cr-spinel.

ied Cr-spinels are presented as Mg# vs. Cr# (Mg# = Mg/(Mg+Fe^{2+}), Cr# = Cr/(Cr+Al), all in at. %). The compositional variations of Al^{3+}, Cr^{3+} and Fe^{3+} are presented on the ternary diagram (Fig. 5), where zonal Cr-spinel forms four clusters (gray squares), corresponding to the 4 zones distinguished on SEM images and also marked by peak splitting in powder X-ray patterns.
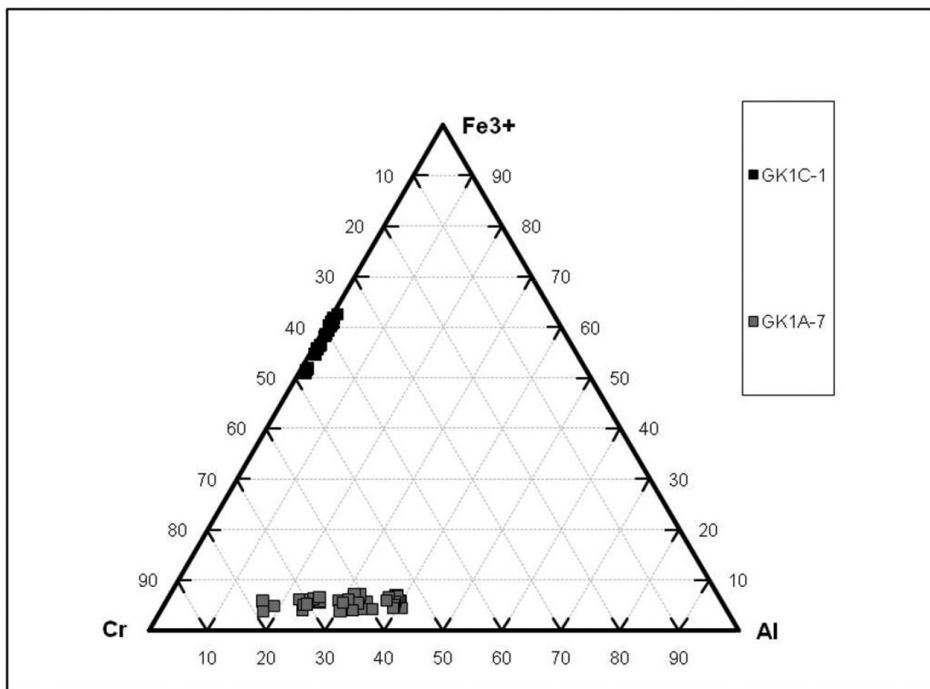
Fig. 5. Compositional variations of Al^{3+}, Cr^{3+} and Fe^{3+} in the studied Cr-spinels.

Mössbauer spectroscopy

The registered Mössbauer spectra include both sextet (Sx) and doublet (Db) components (Table 2). According to literature data the spectra of Cr-spinel samples could be interpreted both considering completely normal cation distribution and intracrystalline cation disorder. Sample GK1C-1 (homogeneous), (Fig. 6) shows three magnetically split sextets together with superposing doublets. The calculated hyperfine parameters clearly show the presence of non-stoichiometric Cr-spinel phases $Fe_{1+x}Cr_{2-x}O_4$ having sextet components typical for compositions with x<0.68. Doublet type components are characteristic for larger x value, as well as for Cr-spinel with small particle size when relaxation effects could also be observed. In the first case the extra iron substitutes Cr in octahedral sites and Fe^{3+} ions in tetrahedral position are registered. In octahedral position the presence of Fe^{3+} and Fe^{2+} ions gives rise to electron hopping [27]. Also the presence of Fe^{3+} and Cr in octahedral sites disturbs the cubic symmetry around the tetrahedrally coordinated Fe^{2+} and hence the Fe^{2+} singlet is converted into a doublet. Quadrupole splitting (QS) increases with increasing Fe^{3+} in octahedral site [28]. Sample GK1A-7 (zonal), (Fig. 7) shows doublet type spectrum, typical for Cr-spinel with high Cr content. The presence of Fe^{3+} in octahedral position and Fe^{2+} in two tetrahedral positions was registered [29].

Table 2. Mössbauer hyperfine parameters, distribution of Fe^{2+} and Fe^{3+} at different sites of Cr-spinels and $Fe^{3+}/\Sigma Fe$ ratios from the spectral areas at 298 K

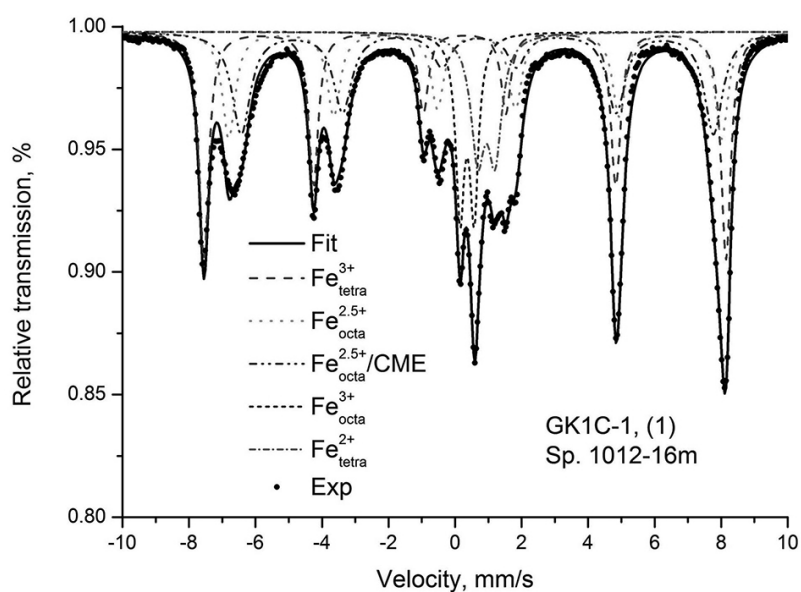| Sample	Components	IS, mm/s	QS, mm/s	H_{eff}, T	FWHM, mm/s	G, %	$Fe^{3+}/\Sigma Fe$
GK1C-1	Sx1-Fe^{3+}-tetra	0.29	0.01	48.75	0.35	30	0.645
	Sx2-$Fe^{2.5+}$-octa	0.62	-0.04	46.02	0.47	23	
	Sx3-$Fe^{2.5+}$-octa (CME)	0.70	-0.06	44.11	0.66	26	
	Db1-Fe^{3+}-octa	0.36	0.42	–	0.31	10	
	Db2-Fe^{2+}-tetra	0.94	0.52		0.49	11	
GK1A-7	Db1-Fe^{3+}-octa	0.32	0.56	–	0.50	37	0.37
	Db2-Fe^{2+}-tetra	0.84	1.07	–	0.34	20	
	Db3-Fe^{2+}-tetra	1.10	1.00	–	0.52	43	

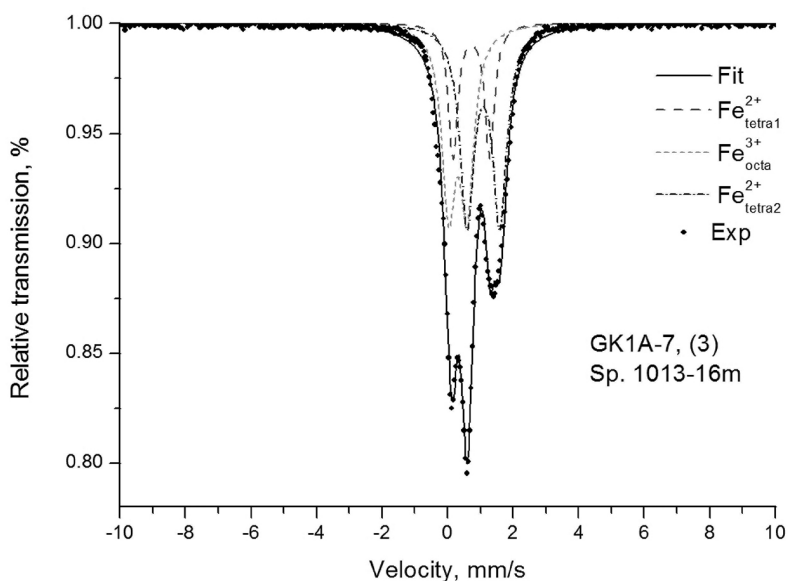**Fig. 6.** Mössbauer spectrum of homogeneous Cr-spinel.

Fig. 7. Mössbauer spectrum of zonal Cr-spinel.

Powder diffraction and Rietveld analysis

Powder X-ray diffraction analysis of the studied Cr-spinels shows that the investigated samples contain only spinel phases. Diffraction patterns for both samples are characterized with some differences, considering intensities, peak positions, FWHM of the peaks and the background level. The homogeneous sample shows narrow peaks and high background, witnessing of good crystallinity and high iron contents. Diffraction pattern of the zonal sample, in contrast, shows spectacular splitting of Bragg reflections, especially observed at high 2θ angles. This splitting reflects the compositional variability already confirmed by EPMA data. Because of strong peak overlapping, however, approximation of profile parameters was very hard. This sample was modeled with 3 phases, despite of indications for four spinel phases. Rietveld refinement was carried out with pseudo-Voigt profile function for zonal sample and TCH (Thompson, Cox and Hastings) pseudo-Voigt function with asymmetry correction by FCJ (Finger, Cox and Jephcoat) for the homogeneous sample. Rietveld plots are shown in Figures 8 and 9. The results from the Rietveld refinement are presented in Table 3.

Single crystal structure refinement

The structure refinement was performed, assuming fully ionized cations and neutral scattering for the oxygen. The distribution of main chemical species and constrained minor elements (Mn, Ni, Ti and V) in tetrahedral or octahedral sites was initially set, according to their site preferences [21]. The results of the refinement are represented in Table 4.

Final cation distributions, based on the procedure of Lavina et al. [21] are given in Table 5.

Intracrystalline geothermometry

In the present study we applied geothermometry calculations decribed by Princivalle et al. [25], which consider the Al and Mg intersite exchange and the chemical composition. The estimated temperatures for some of the studied Cr-spinels are in the range 796–1073°C (Table 5). For the zonal Cr-spinel (with preserved pristine cores) this temperature range could reflect the stage of reequlibration on cooling.

DISCUSSION

The two X-ray diffraction methods used – powder and single crystal, operate with slightly different material. The powder samples use bulk material, while crystal fragments used for single crystal studies, may belong to separate crystal zones. Since these particular zones differ in composition, they can give slightly different X-ray patterns. This is why the results from the single crystal study are slightly spread around the powder (bulk) results. This is well visible on Fig. 10, where solid squares and circles reflect powder and single crystal results, respectively. As seen, regardless of the slight displacements, two kinds of results coincide within rather narrow limits. This coincidence gives us a
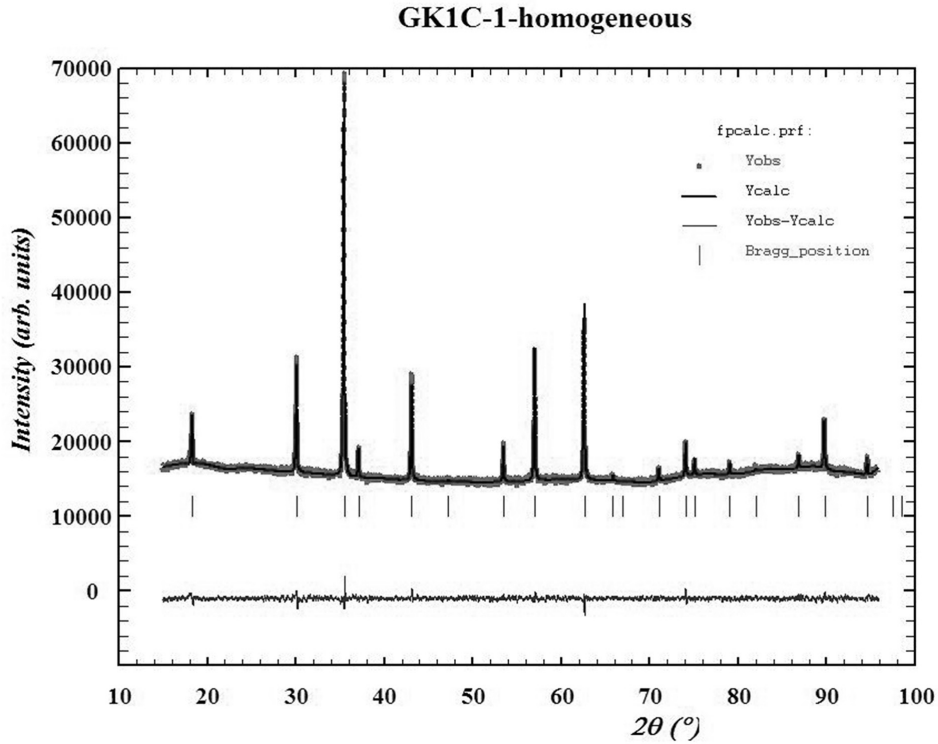
GK1C-1-homogeneous

Fig. 8. Rietveld plot of homogeneous Cr-spinel. Vertical bars denote Bragg positions; the dotted curve – experimental diffraction pattern; solid line is the calculated curve and the differences plot is presented at the bottom.
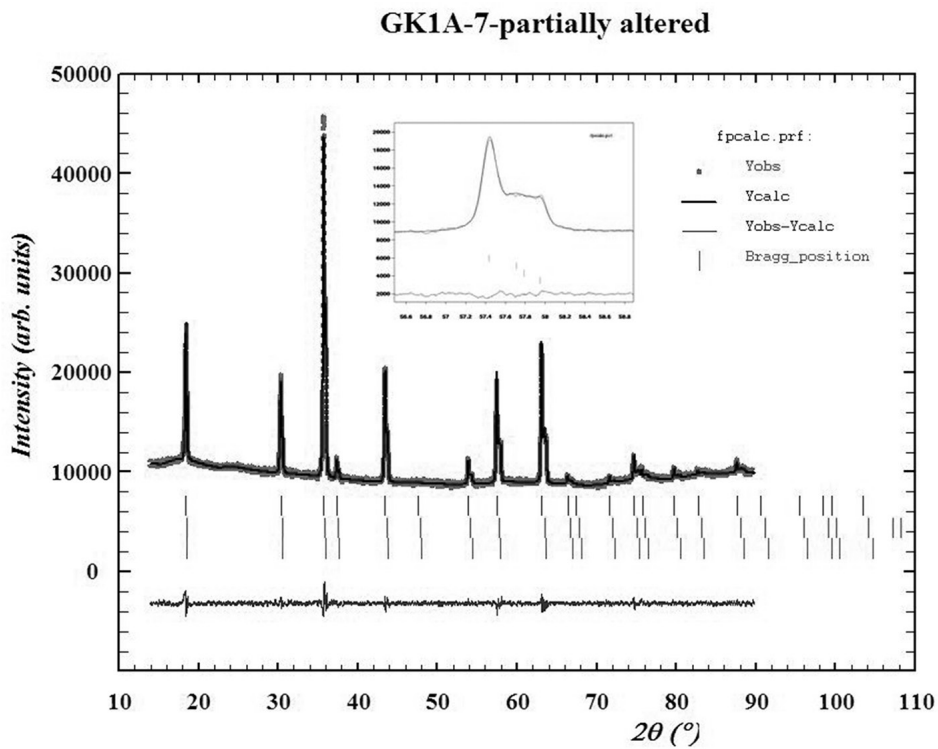
GK1A-7-partially altered

Fig. 9. Rietveld plot of zonal Cr-spinel. Inset shows splitting of the peaks. Line legend as in Fig. 8.

Table 3. Refined structural parameters from Rietveld refinement of the Cr-spinels studied. *a*: unit cell parameter (Å); *u*: oxygen positional parameter; Td-O and Oh-O: tetrahedral and octahedral bond lengths (Å); $Td_{m.a.n.}$ and $Oh_{m.a.n.}$: mean atomic number for tetrahedral and octahedral sites; B_O, B_{Td} and B_{Oh}: isotropic thermal displacement parameters; x: inversion parameter; the standard deviation is denoted in the brackets

	Rietveld refinement for powder samples			
Sample	GK1A-7 core	GK1A-7 rim1	GK1A-7 rim2	GK1C-1
a (Å)	8.25974 (5)	8.29103 (7)	8.32591 (5)	8.38598 (1)
u	0.26261 (9)	0.26205 (16)	0.26258 (9)	0.25809 (14)
Vol	563.506 (0)	569.933 (0)	577.159 (5)	589.742 (2)
Dcal *g/cm³*	4.398	4.447	4.482	4.873
Td-O (Å)	1.9687 (12)	1.9689 (6)	1.9840 (4)	1.9331 (6)
Oh-O (Å)	1.9663 (10)	1.9776 (5)	1.9823 (3)	2.0309 (7)
RB	3.69	2.55	2.76	4.35
RF	3.85	2.22	2.72	5.51
Chi2	2.26	2.26	2.26	2.42
GoF	1.5	1.5	1.5	1.6
Rp	22.3	22.3	22.3	22.3
Rwp	10.7	10.7	10.7	13.2
Rexp	7.1	7.1	7.1	8.51
Td m.a.n.	16.89	17.64	17.86	23.65
Oh m.a.n.	20.29	20.91	21.63	24.08
B_O	1.15 (2)	0.92 (9)	0.21 (5)	1.18 (5)
B_{Td}	0.67 (2)	0.69 (6)	0.08 (4)	0.86 (3)
B_{Oh}	0.39 (1)	0.57 (4)	0.64 (3)	0.51 (2)
	Site occupancy			
	Td site			
Mg	0.611 (2)	0.583 (2)	0.547 (1)	0.239 (1)
Fe^{2+}	0.357 (2)	0.397 (2)	0.420 (1)	0.260 (1)
Mn	0.011	0.013	0.015	0.020
Fe^{3+}	0.000	0.000	0.000	0.520 (1)
Al	0.000	0.000	0.000	0.000
total	0.979	0.992	0.982	1.039
vacancy	0.021	0.008	0.018	
∑	1.000	1.000	1.000	
	Oh site			
Al	0.649 (2)	0.573 (2)	0.419 (1)	0.019
Fe^{3+}	0.113 (2)	0.112 (2)	0.099 (1)	0.636 (1)
Fe^{2+}	0.023 (2)	0.000	0.000	0.465 (1)
Mg	0.000	0.000	0.000	0.000
Cr	1.182 (2)	1.302 (2)	1.460 (1)	0.786 (1)
Ni	0.004	0.003	0.003	0.007
Ti	0.002	0.002	0.002	0.007
V	0.004	0.003	0.003	0.003
total	1.977	1.994	1.986	1.923
vacancy	0.023	0.006	0.014	0.077
∑	2.000	2.000	2.000	2.000
x	0.000	0.000	0.000	0.52

reason to trust both study results. Moreover, both results comply well with EPMA and Mössbauer results.

The same figure shows clear clustering of data points from the homogeneous (black symbols) and zonal (gray symbols) Cr-spinels.

The homogeneous Cr-spinel points cluster close to magnesioferrite position (MgFt), giving us reason to classify this sample as such. Its *u* value below 0.26 witnesses for partially inverse character. This fact well corresponds to its high Fe content (both Fe^{2+} and Fe^{3+} derived from Mössbauer results).

Table 4. Single crystal structure refinement results. *a*: unit cell parameter (Å); *u*: oxygen positional parameter; Td-O and Oh-O: tetrahedral and octahedral bond lengths (Å); $Td_{m.a.n.}$ and $Oh_{m.a.n.}$: mean atomic number for tetrahedral and octahedral sites; U_{11} and U_{12}: anisotropic thermal displacement parameters for Td, Oh and O (oxygen) sites

	SHELXL refinement - Sheldricks 2013					
Sample	GK1A-7m -1a	GK1A-7m -1b	GK1A-7m -1c	GK1C-1-3a	GK1C-1-3b	GK1C-1-3c
a (Å)	8.2483 (4)	8.2936 (3)	8.2827 (4)	8.3784 (4)	8.3854 (5)	8.4021 (5)
u	0.26256 (14)	0.26201 (14)	0.26170 (18)	0.2577 (3)	0.2591 (5)	0.2588 (6)
cell vol	561.17 (8)	570.47 (6)	568.22 (8)	588.14 (8)	589.62 (11)	593.15 (11)
Td-O	1.965 (2)	1.968 (2)	1.961 (3)	1.926 (5)	1.948 (8)	1.9473 (8)
Oh-O	1.9639 (10)	1.9788 (10)	1.9785 (13)	2.032 (3)	2.023 (4)	2.0292 (4)
O-Oh-O shared	83.80 (7)	84.09 (7)	84.25 (9)	86.31 (17)	85.6 (3)	86.2 (2)
O-Oh-O unshared	96.20 (7)	95.91 (7)	95.75 (9)	93.69 (17)	94.4 (3)	93.8 (2)
Td m.a.n	15.89	16.86	16.98	23.48	22.38	25.50
Oh m.a.n.	18.57	19.75	19.82	24.12	24.98	25.16
U_{11}(Td)	0.0050 (6)	0.0065 (5)	0.0075 (7)	0.0048 (12)	0.0060 (13)	0.0064 (13)
U_{11}(Oh)	0.0034 (4)	0.0030 (3)	0.0044 (4)	0.0041 (9)	0.0118 (13)	0.0127 (13)
U_{12}(Oh)	0.00014 (16)	-0.00025 (14)	-0.0003 (2)	-0.0003 (5)	-0.0003 (5)	-0.0004 (7)
U_{11}(O)	0.0076 (7)	0.0087 (7)	0.0091 (9)	0.007 (2)	0.012 (3)	0.009 (3)
U_{12}(O)	0.0006 (4)	0.0003 (4)	-0.0001 (6)	0.0006 (17)	0.0006 (17)	0.0021 (19)
N refl	49	50	51	53	54	55
R all	0.0152	0.0137	0.0203	0.0193	0.0497	0.0619
R1	0.0146	0.0128	0.0195	0.0157	0.0477	0.0525
wR2	0.0334	0.0291	0.0371	0.0951	0.1424	0.1555
GoF	1.171	1.11	1.256	0.953	1.304	1.318
ext *coeff*	0.0074 (11)	0.0006 (5)	0.0000 (6)	0.0005 (14)		
abs *coeff* μ	3.576	3.518	3.532	3.354	3.346	3.326
Z	8	8	8	8	8	8

Points from the zonal Cr-spinel show much wider spread of *a* unit cell values, at almost constant *u*. This means that compositional differences (registered also by EPMA) between crystal core and rims result in different unit cells, but do not significantly affect the oxygen positional parameter. This behavior is not surprising. It was registered before by Lenaz and Princivalle [6] and allows pretty precise determination of *u*, regardless of possible spread in *a* values within certain limits.

Clear clustering of the two samples well apart is also visible on the tetrahedral (Td-O) vs. octahedral (Oh-O) bond length diagram (Fig. 11). The homogeneous Cr-spinel points (black symbols) cluster again close to the magnesioferrite position, but show somewhat larger tetrahedral and shorter octahedral bonds. This perfectly makes sense since extra Fe^{2+} (introduced during alteration) in tetrahedral position has much larger ionic radius than Mg. Chromium in octahedral position is smaller than Fe^{3+}, but the difference here is smaller, which well explains smaller deviation from magnesioferrite values.

The zonal sample (gray symbols) shows abrupt increase in octahedral bond length in core to rim direction, followed by bilateral spread in tetrahedral distances between different rims. The first change reflects the growing Cr/Al ratio, in octahedral position. Intra-rim differences are entirely due to variations in Fe^{2+}/Mg ratio, in tetrahedral position.

Finally, calculated cation distribution values were used for calculation of system closure temperatures, in accordance with the geothermometric procedure of Princivalle et al. [25]. Obtained temperatures for the zonal Cr-spinel were in the range 796–1073°C. Slightly lower temperatures were calculated for the homogeneous Cr-spinel 940–955°C. These temperatures are completely acceptable for a reequilibration stage (pristine cores) and very close to the temperatures reported for chromites from the Outer Dinarides [6]. Outer alteration rims of zonal sample are expected to have formed at much lower temperatures, during regional metamorphism (700–450°C) [26], but they were not calculated in this study, since used geothermomeric procedure is based on melt crystallization concepts, inapplicable for hydrothermal environment of the metamorphic stage.

Table 5. Final cation distributions refined according to the procedure of Lavina et al. [21]

Sample	GK1C-1 powder	GK1C-1-3c	GK1A-7m-1a	GK1A-7m-1b	GK1A-7m-1c
	Calculated cation distribution				
a (Å)	8.385869	8.402383	8.2483	8.2936	8.2827
u	0.258089	0.258796	0.26254	0.26200	0.2617
Td-O	1.93309	1.947189	1.965	1.9680	1.9611
Oh-O	2.030906	2.029386	1.9641	1.9789	1.9785
Td m.a.n.	22.75	22.75	15.82	16.69	16.09
Oh m.a.n.	24.62	24.98	18.87	20.09	20.30
Total charges	7.97	7.97	7.95	7.85	7.90
	Site occupancy				
	Td site				
Mg	0.229	0.232	0.677	0.617	0.643
Fe^{2+}	0.235	0.350	0.247	0.320	0.258
Mn	0.020	0.005	0.011	0.012	0.01
Fe^{3+}	0.515	0.413	0.012	0.000	0.022
Al	0.000	0.000	0.053	0.051	0.065
Sum	0.999	1.000	1.000	1.000	0.998
Vacancy	0.001	0.000	0.000	0.000	0.002
	Oh site				
Al	0.019	0.022	0.903	0.687	0.698
Cr	0.809	0.866	0.873	1.109	1.115
Fe^{3+}	0.647	0.650	0.109	0.003	0.000
Fe^{2+}	0.461	0.455	0.054	0.151	0.175
Mg	0.029	0.000	0.055	0.040	0.006
Ni	0.007	0.002	0.002	0.002	0.002
Ti	0.007	0.005	0.001	0.002	0.001
V	0.002	0.000	0.003	0.002	0.002
Sum	1.980	2.000	2.000	1.996	1.999
vacancy	0.020	0.000	0.001	0.004	0.001
x	0.515	0.413	0.065	0.051	0.087
T°C	940	955.15	796.00	982.86	1073.41
$Fe^{3+}/\Sigma Fe$	0.625	0.569	0.287	0.006	0.048

CONCLUSIONS

Based on structural, chemical and Mössbauer data collected, the two samples used in this study were identified as:

- Magmatic Cr-spinels, with high Al cores and progressively depleted in Al and less Mg alteration rims.
- High chromian magnesioferrite, which is a partially inverse Cr-spinel, not described previously in this locality. This determination was only possible with structural refinement, combined with Mössbauer data and demonstrated the importance of such studies for the correct mineral species identification in metamorphosed ophiolite sequences.

The two X-ray diffraction approaches – powder and single crystal gave comparable results, which makes them interchangeable for the purposes of this kind of studies. However some aspects of the structural characterization are better revealed by one or the other method and using them both gives best results.

REFERENCES

1. R. J. Hill, J. R. Craig, G. V. Gibbs, *Phys. Chem. Minerals,* **4**, 317 (1979).
2. F. Bosi, G. B. Andreozzi, V. Ferinni, S. Lucchesi, *Amer. Miner.*, **89**, 1367 (2004).
3. G. B. Andreozzi, *Per. Mineral.*, **68** (1), 43 (1999).
4. D. Lenaz, H. Skogby, F. Princivalle, U. Hålenius, *Phys. Chem. Minerals.*, **31**, 633 (2004).
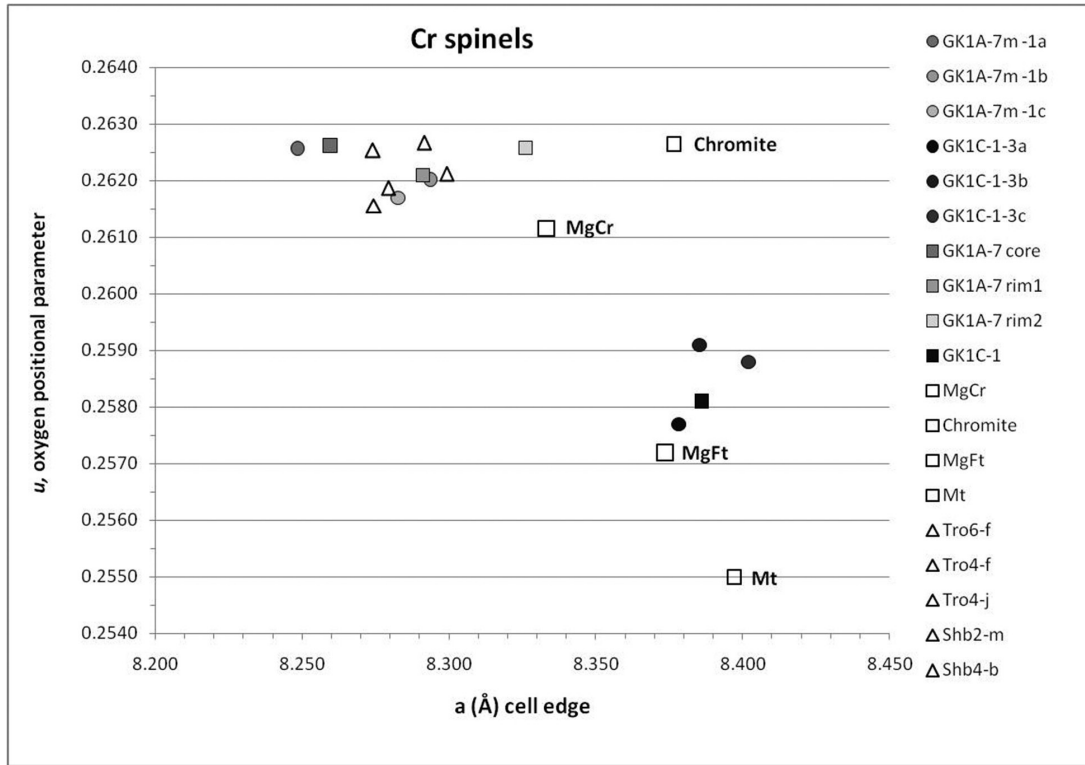5. R. O. Sack, M. S. Ghiorso, *American Mineralogist*, **76**, 827 (1991).

Fig. 10. Oxygen positional parameter vs. unit cell edge. Synthetic and natural Cr-spinels fom literature sources are presented for comparison too. Solid circles = single crystal data; solid squares = Rietveld refinement data; empty squares = chromite, magnesiochromite, magnesioferrite [30], and magnetite [31]; empty triangles = Albanian chromite [2]); MgCr = magnesiochromite; Mt = magnetite; MgFt = magnesioferrite.
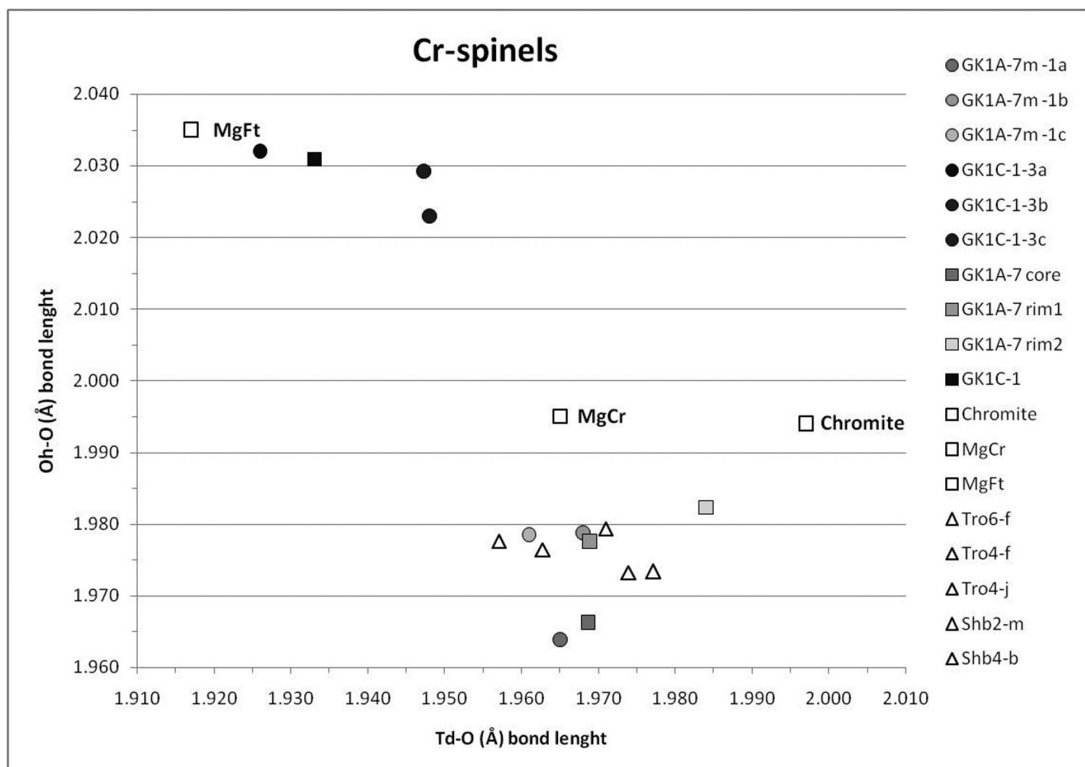

Fig. 11. Tetrahedral (Td-O) and octahedral (Oh-O) bond lengths. The symbols and notations are same as in Fig. 10.

19

6. D. Lenaz, F. Princivalle, *The Canadian Mineralogist*, **43**, 1305 (2005).
7. B. Lavina, B. Cesare, A. M. Álvarez-Valero, Hinako Uchida, R. T. Downs, A. Koneva, P. Dera, *American Mineralogist*, **94**, 657 (2009).
8. K. Kolcheva, I. Haydoutov, L. Daieva, *Geochem Mineral Petrol*, **37**, 25 (2000).
9. I. Haydoutov, K. Kolcheva, L. A. Dieva, I. Savov, C. Carrigan, *Ofioliti*, **29** (2), 145 (2004).
10. N. Bonev, in: Geol Soc Am Special Paper, Dilek Y, Pavlides S (eds). **49**, 211 (2006).
11. E. Mposkos, A Liati, *Can Mineral*, **31**, 401 (1993).
12. L. Macheva, *Geochem Mineral Petrol*, **35**, 17 (1998).
13. E. Mposkos *Bull Geol Soc Greece*, **32**, 59 (1998).
14. E. Mposkos, *Bull Geol Soc Greece*, 34, 2126 (2002).
15. E. Kozhoukharova, *Geochem Mineral Petrol*, **35**, 29 (1998).
16. S. Sarov, B. Yordanov, V. Valkov, S. Georgiev, D. Kamburov, E. Raeva, V. Grozdev, E. Balkanska, L. Moskovska, G. Dobrev, E. Voynova, M. Ovcharova (2007) Geological map of the republic of Bulgaria 1:50000: scheet K-35-88-V (Krumovgrad) and K-35-100-A (Egrek). Ministry of Environment and Water, Bulgarian geological Survey, project Nr. 425/20.07.2004, Geology and Geophysics JSCo., Apis 50 Ltd. printhouse. Sofia.
17. C-J De Hoog, *Geochem Geophys Geosyst*, **10**: Q10014 (2009).
18. T. Žák, Y. Jirásková, *Surf. Interface Anal.* **38**, 710 (2006).
19. MATCH!, Crystal Impact, H.Putz & K.Brandenburg GbR, Bonn, Germany, 2003-2016.
20. J. Rodriguez-Carvajal, *Physica* B., **55**, 192 (1993).
21. B. Lavina, G. Salviulo, A. Della Giusta, *Phys Chem. Minerals.*, **29**, 10 (2002).
22. H. O`Neill, A. Navrotsky, *American Mineralogist*, **68**, 181 (1983).
23. Oxford Diffraction. CrysAlis PRO, Oxford Diffraction Ltd, yarnton, England, 2010.
24. G. M. Sheldrick, *Acta Crystallographica A*, **64**, 112 (2008).
25. F. Princivalle, A. Della Giusta, A. De Min, E. M. Piccirillo, *Mineral. Mag.*, **63** (2), 257 (1999).
26. F. Gervilla, J. A. Padron-Navarta, T. Kerestedjian, I. Sergeeva, J. M. Gonzalez Jimenez, I. Fanlo, *Contrib. Mineral. Petrol.,* **164**, 643 (2012).
27. D. Lenaz, G.B. Andreozzi, M. Bidyananda, F. Princivalle, *Periodico di Mineralogia,* **83** (2), 241, 10.2451/2014PM0014, (2014).
28. H. C. Verma, J. K. Mohanty, R. P. Tripathi, *Journal of Alloys and Compounds*, **326**, 132 (2001).
29. Y. L. Chen , B. F. Xu , J. G. Chen and Y. Y. Ge, *Phys Chem Minerals*, (**19**), 255 (1992).
30. D. Lenaz, H. Skogby, *Per. Mineral.*, **72**, 69 (2003).
31. H. St. C. O'Neill and W. A. Dollase, *Phys Chem Minerals*, (**20**), 541 (1994).

КРИСТАЛОХИМИЯ И СТРУКТУРНО ХАРАКТЕРИЗИРАНЕ НА ПРИРОДНИ ХРОМШПИНЕЛИДИ

И. С. Сергеева[1*], Т. Н. Керестеджиян[1], Р. П. Николова[2],
З. П. Черкезова-Желева[3], Ф. Хервия[4]

[1] *Геологически институт „Страшимир Димитров“, Българска академия на науките, бл. 24, 1113 София*

[2] *Институт по минералогия и кристалография, Българска академия на науките, бл. 107, 1113 София*

[3] *Институт по катализ, Българска академия на науките, „Акад. Г. Бончев“ бл. 11, 1113 София, България*

[4] *Университет на Гранада, Катедра по минералогия и петрология, 18002 Гранада, Испания*

(Резюме)

Изследвани са два образеца от природни хром шпинелиди посредством рентгеноспектрален микроанализ, прахова и монокристална рентгенова дифракция и Мьосбауерова спектроскопия, с цел установяване на някои аспекти от взаимовръзката между химичният състав и кристалоструктурните параметри. Образците се различават значително в текстурно, химично и структурно отношение. Единият е богат на хром и може да се отнесе като хром шпинелид, докато другият е с високи съдържания на желязо доближавайки се до магнезиоферитовия член от шпинелова група. Различният химизъм поражда отчетливи разлики и в структурните параметри – параметър на елементарната клетка и кислороден параметър, които отразяват различни условия на образуване и/или промяна. Кислородният параметър е индикативен за термичната история на вместващите скали (температура на затваряне на системата) и е пряко свързан с катионното разпределение в структурата – основа за геотермометрични изчисления. Получените температури на затваряне на системата за двата образеца показват стойности в интервала 796–1073 °C, които са приемливи за преуравновесяване на хром шпинелида по време на охлаждане.

Synthesis and characterization of copper-manganese ferrites with composition $Cu_{1-x}Mn_xFe_2O_4$ supported on activated carbon

T. M. Petrova[1]*, N. I. Velinov[1], I. G. Genova[2], T. S. Tsoncheva[2],
D. G. Kovacheva[3], N. V. Petrov[2], I. G. Mitov[1]

[1] *Institute of Catalysis, Bulgarian Academy of Sciences, Acad. G. Bonchev str., bl. 11, 1113 Sofia, Bulgaria*
[2] *Institute of Organic Chemistry with Centre of Phytochemistry, Bulgarian Academy of Sciences,*
Acad. G. Bonchev str., bl. 9, 1113 Sofia, Bulgaria
[3] *Institute of General and Inorganic Chemistry, Bulgarian Academy of Sciences, Acad. G. Bonchev str.,*
bl. 11, 1113 Sofia, Bulgaria

The present study is addressed to the synthesis of mixed copper-manganese ferrite catalysts $Cu_{1-x}Mn_xFe_2O_4$ (x=0; 0.2; 0.4; 0.6; 0.8; 1) supported on activated carbon from peach stones. The samples were characterized by X-ray diffraction, Mössbauer spectroscopy and methanol decomposition to CO and hydrogen was used as a catalytic test. The formation of ferrite catalysts with cubic and partially inverse spinel structure was established. Significant changes under the reaction medium of the ferrite materials with the formation of magnetite and carbide of Haag were registered. The presence of copper in the manganese ferrites improves the catalytic activity at the low-temperature and this tendency increases with the increase of copper content.

Keywords: copper-manganese ferrites, activated carbon, Mössbauer spectroscopy, methanol decomposition.

INTRODUCTION

Ferrite materials are attractive area for intensive research due to their wide application in electronics [2], catalysis [3], biology and medicine [4], etc. Depending on the location of the cations in the crystal lattice the spinel type ferrites are classified in three main groups: normal, inverse and partially inverse. In the normal spinels all two-valent cations are located only on tetrahedral positions, while in the inverse spinels all two-valent cations occupy only octahedral positions and in the partially inverse spinels, the two-valent cations are located partially at tetrahedral and octahedral positions. It is well-known that various metallic ions may preferably occupy various coordination positions [5]. Moreover, the distribution of the ions in the structure of the spinel affects both the physical and catalytic features [6, 7]. Spinel ferrites are effective catalysts for photo-splitting of methanol/water solution [8], methane reforming [9], steam reforming of methanol

and ethanol [10, 11] and methanol decomposition [12–17]. It has been established, that mixed ferrites such as $Cu_{1-x}Co_xFe_2O_4$ and $Cu_{1-x}Zn_xFe_2O_4$ exhibit better catalytic activity in methanol decomposition than the mono-component ones [13, 14], [16], [18, 19]. In the recent years the activated carbons based on low-cost agricultural wastes are widely used as adsorbents and supports for catalysts due to their textural characteristics, surface functionality and stability which could be easily controlled during the process of the pyrolysis and carbon treatment [20–24]. Iron modified activated carbon from various agriculture wastes were tested as catalysts in methanol decomposition in ref. [20]. During the reaction the larger particles easily transformed to Fe and/or Fe_3C that resulted in low catalytic activity and high selectivity to CO [20]. The predominant effect of the surface functionality over the texture characteristics of the activated carbon on the state of loaded iron phase was discussed. The aim of the present investigation is synthesis and characterization of supported on activated carbon from peach stones mixed copper-manganese ferrite catalysts with different composition. Their behaviour as catalysts in methanol decomposition is also in the focus of the study.

---
* To whom all correspondence should be sent:
e- mail: silberbarren@abv.bg

EXPERIMENTAL

Synthesis

Activated carbon support was obtained by pyrolysis of waste peach stones at 550°C (heating rate of 5°C/min) at atmospheric pressure and further activation with water vapor at 800°C for 1 h. The activated carbon was impregnated by aqueous solution of $Cu(NO_3)_2.3H_2O$, $Mn(NO_3)_2.4H_2O$ and $Fe(NO_3)_3.9H_2O$ using ultrasonic treatment on a BANDELIN SONOPULS HD 2200. The samples were dried at 50°C for 24 hours and then heated at 500°C for 2 hours in a nitrogen atmosphere. The obtained materials contained 8 wt% metal are denoted as $Cu_{1-x}Mn_xFe_2O_4$/ACP, where x=0; 0.2; 0.4; 0.6; 0.8 and 1.

Methods of characterization

Powder X-ray diffraction (XRD) patterns were collected within the range of 10° to 80° 2θ on a Bruker D8 Advance diffractometer with Cu K$_\alpha$ radiation and LynxEye detector. Phase identification was performed using ICDD-PDF2 Database. The average crystallites size (D), the degree of microstrain (e) and the lattice parameters (a) of the studied ferrites were determined from the experimental XRD profiles by using the PowderCell-2.4 software and appropriate corrections for the instrumental broadening.

The Mössbauer spectra were obtained in air at room temperature (RT) with a Wissel (Wissenschaftliche Elektronik GmbH, Germany) electromechanical spectrometer working in a constant acceleration mode. A ^{57}Co/Rh (activity $\cong$ 50 mCi) source and α-Fe standard were used. The experimentally obtained spectra were fitted using CONFIT2000 software [25]. The parameters of hyperfine interaction such as isomer shift (δ), quadrupole splitting (ΔE_q), effective internal magnetic field (B), line widths (Γ_{exp}), and relative weight (G) of the partial components in the spectra were determined.

Catalytic experiments

Methanol conversion was carried out in a fixed bed flow reactor (0.055 g of catalyst), argon being used as a carrier gas (50 cm^3 min^{-1}). The methanol partial pressure was 1.57 kPa. The catalysts were tested under conditions of a temperature-programmed regime within the range of 80–500°C with heating rate of 1°C.min^{-1}. On-line gas chromatographic analyses were performed on HP apparatus equipped with flame ionization and thermo-conductivity detectors, on a PLOT Q column, using an absolute calibration method and a carbon based material balance.

RESULTS AND DISCUSSION

The X-Ray diffraction patterns are presented in Figure 1 and the corresponding data are listed in Table 1. Diffraction maxima of cubic spinel phase (S.G. Fd-3m) are observed in all spectra. In addition diffractions of small quantities of CuO (PDF 80-1917), Cu_2O (PDF 78-2076) and Cu (PDF 4-0836) are also registered. The increase of Mn content in binary ferrites leads to the increase in the lattice parameter, which was 8.34 Å and 8.45 Å for $CuFe_2O_4$ and $MnFe_2O_4$, respectively. This is probably due to the larger ionic radius of Mn^{2+} than this of Cu^{2+}. According to [26] the crystal radius in octahedral coordination of Mn^{2+} is 0.97 Å, while that of Cu^{2+} is 0.87 Å. No linear dependence of the average crystallite size of ferrites on their composition is observed. The largest crystallite size, which was detected for $Cu_{0.5}Mn_{0.5}Fe_2O_4$/ACP could be attributed to the inhomogeneous surface of the activated carbon, which probably reflects on the mechanisms of the formation of the primary microcrystals. There are no simple relation between the spinel composition and microstrain degrees.
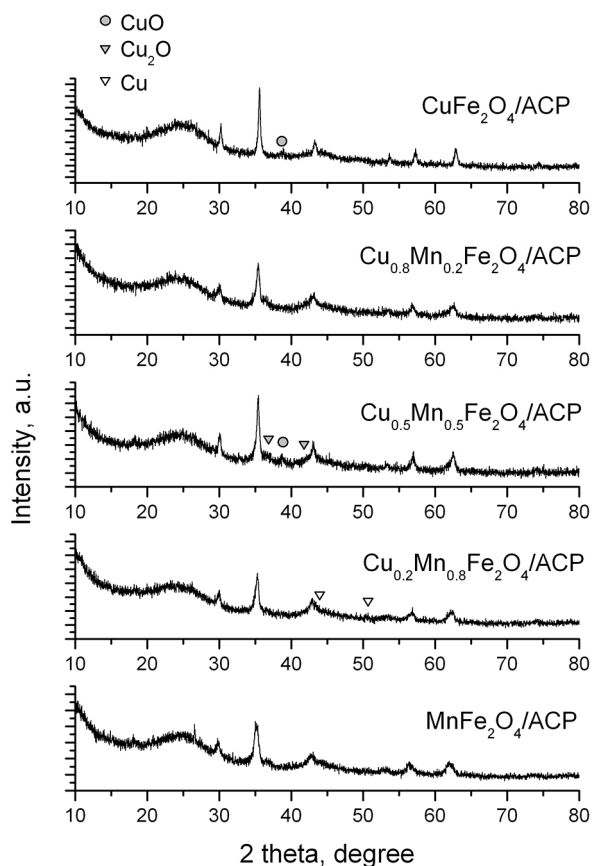

Fig. 1. X-ray diffraction patterns of samples of $Cu_{1-x}Mn_xFe_2O_4$ supported on activated carbon thermally treated at 500°C.

Table 1. Average crystallites size (D), degree of microstrain (e) and lattice parameter (a) of the ferrite phase in samples treated at 500°C determined from the experimental XRD profiles

Sample	Phase	D, nm	e_*10^3, a.u.	a, Å	Additional phases
$CuFe_2O_4$ /ACP	Spinel	18.79	2.14	8.34	CuO
$Cu_{0.8}Mn_{0.2}Fe_2O_4$ /ACP	Spinel	19.83	5.17	8.41	–
$Cu_{0.5}Mn_{0.5}Fe_2O_4$ /ACP	Spinel	47.27	5.07	8.40	CuO, Cu_2O
$Cu_{0.2}Mn_{0.8}Fe_2O_4$ /ACP	Spinel	22.58	2.05	8.43	Cu
$MnFe_2O_4$/ACP	Spinel	17.65	6.67	8.45	–

The Mössbauer spectra of samples obtained after drying are shown in Figure 2 and the calculated parameters of the spectra are presented in Table 2. All of the spectra are quadrupole doublets which parameters are typical of Fe^{3+} in octahedral coordination. The experimental spectra of the samples after thermal treatment at 500°C (Figure 3, Table 3) are well fitted with a model of three sextets and one doublet. The sextet (Sx1) corresponds to iron in tetrahedral position and the two sextets (Sx2 and Sx3), for iron in octahedral coordination. The sextet with higher values of magnetic field (Sx2) is due to stronger magnetic interactions between iron ions, which have smaller number non-magnetic neighbor ions (Cu^{2+}, Mn^{2+}), while the sextet with lower magnetic field (Sx3) corresponds to iron ions with more copper and manganese neighbors ions. It was observed increased isomer shift of the sextet components of iron in octahedral positions for the mixed copper-manganese ferrite. This indicates the presence of mixed-valence iron in octahedral coordination. The presence of a doublet component could be due to the presence of paramagnetic component, formed by iron ions located in the medium of hydrocarbon functional groups from the activated carbon surface. Alternatively, this component could be due to pres-
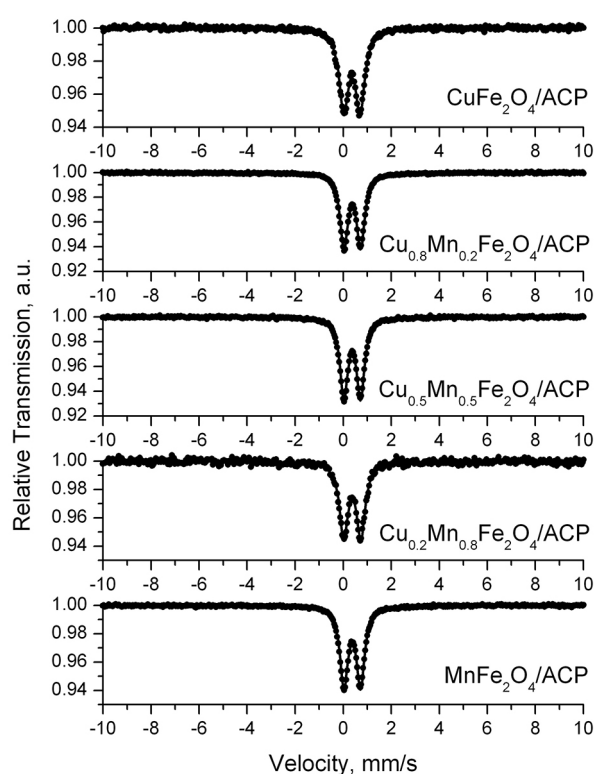
Fig. 2. Mössbauer spectra of samples of $Cu_{1-x}Mn_xFe_2O_4$ supported on activated carbon after drying at 50°C.
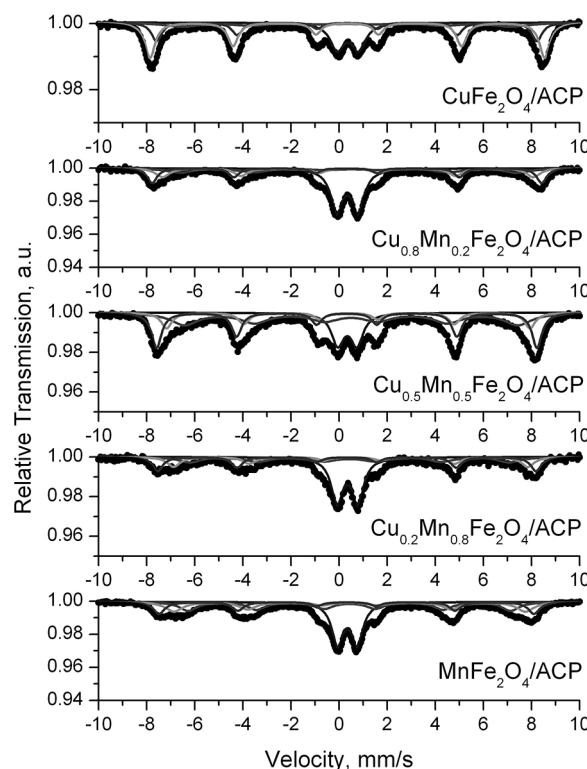
Fig. 3. Room temperature Mössbauer spectra of samples of $Cu_{1-x}Mn_xFe_2O_4$ supported on activated carbon thermally treated at 500°C.

Table 2. Mössbauer parameters of samples of $Cu_{1-x}Mn_xFe_2O_4$ supported on activated carbon after drying at 50°C (δ – isomer shift, ΔE_q – quadrupole splitting, B – effective internal magnetic field, Γ_{exp} – line widths, G – relative weight of the partial components in the spectra)

Sample	Components	δ, mm/s	ΔE_q, mm/s	B, T	Γ_{exp}, mm/s	G, %
$CuFe_2O_4$/ACP	Db-Fe^{3+}	0.36	0.68	–	0.46	100
$Cu_{0.8}Mn_{0.2}Fe_2O_4$/ACP	Db-Fe^{3+}	0.38	0.70	–	0.40	100
$Cu_{0.5}Mn_{0.5}Fe_2O_4$/ACP	Db-Fe^{3+}	0.38	0.70	–	0.39	100
$Cu_{0.2}Mn_{0.8}Fe_2O_4$/ACP	Db-Fe^{3+}	0.38	0.72	–	0.43	100
$MnFe_2O_4$/ACP	Db-Fe^{3+}	0.38	0.70	–	0.40	100

Table 3. Mössbauer parameters of samples of $Cu_{1-x}Mn_xFe_2O_4$ supported on activated carbon thermally treated at 500°C (δ – isomer shift, ΔE_q – quadrupole splitting, B – effective internal magnetic field, Γ_{exp} – line widths, G – relative weight of the partial components in the spectra, LNT – spectra measured at liquid nitrogen temperature)

Sample	Components	δ, mm/s	ΔE_q, mm/s	B, T	Γ_{exp}, mm/s	G, %
$CuFe_2O_4$/ACP	Sx1- Fe-tetra	0.33	−0.01	49.2	0.51	22
	Sx2- Fe-octa	0.34	0.00	51.0	0.52	41
	Sx3- Fe-octa	0.33	−0.02	42.6	1.74	16
	Db-Fe^{3+}	0.37	0.89	–	0.71	21
$Cu_{0.8}Mn_{0.2}Fe_2O_4$/ACP	Sx1- Fe-tetra	0.32	0.00	50.3	0.50	21
	Sx2- Fe-octa	0.38	−0.02	47.9	0.68	21
	Sx3- Fe-octa	0.45	−0.10	43.1	1.53	21
	Db-Fe^{3+}	0.35	0.88	–	0.62	37
$Cu_{0.5}Mn_{0.5}Fe_2O_4$/ACP	Sx1- Fe-tetra	0.32	0.00	49.2	0.50	31
	Sx2- Fe-octa	0.39	−0.03	47.0	0.54	16
	Sx3- Fe-octa	0.51	0.01	43.1	1.37	36
	Db-Fe^{3+}	0.34	0.80	–	0.62	17
$Cu_{0.2}Mn_{0.8}Fe_2O_4$/ACP	Sx1- Fe-tetra	0.32	0.00	48.9	0.53	23
	Sx2- Fe-octa	0.51	−0.05	45.7	0.63	18
	Sx3- Fe-octa	0.43	0.00	41.0	1.15	22
	Db-Fe^{3+}	0.35	0.86	–	0.59	37
$MnFe_2O_4$/ACP	Sx1- Fe-tetra	0.31	0.00	48.4	0.57	19
	Sx2- Fe-octa	0.44	0.01	45.4	0.85	23
	Sx3- Fe-octa	0.44	−0.02	41.7	0.85	26
	Db-Fe^{3+}	0.34	0.82	–	0.57	32
$Cu_{0.8}Mn_{0.2}Fe_2O_4$/ACP-LNT	Sx1- Fe-tetra	0.44	0.00	51.5	0.39	21
	Sx2- Fe-octa	0.47	0.03	53.0	0.35	15
	Sx3- Fe-octa	0.46	−0.09	49.4	0.95	27
	Db-Fe^{3+}	0.45	0.93	–	0.56	37
$Cu_{0.2}Mn_{0.8}Fe_2O_4$/ACP-LNT	Sx1- Fe-tetra	0.45	0.00	51.2	0.41	24
	Sx2- Fe-octa	0.47	0.02	52.7	0.36	14
	Sx3- Fe-octa	0.52	−0.11	49.0	0.98	28
	Db-Fe^{3+}	0.45	0.92	–	0.55	34
$MnFe_2O_4$/ACP-LNT	Sx1- Fe-tetra	0.45	0.00	51.0	0.39	22
	Sx2- Fe-octa	0.48	0.04	52.4	0.42	24
	Sx3- Fe-octa	0.51	−0.10	49.2	0.72	25
	Db-Fe^{3+}	0.45	0.86	–	0.56	29

ence of particles exhibiting superparamagnetic behaviour at room temperature. This supposition was supported by the Mössbauer spectra of the samples at the temperature of liquid nitrogen (Figure 4 and Table 3), where no significant changes with the doublet part of the spectra were detected.

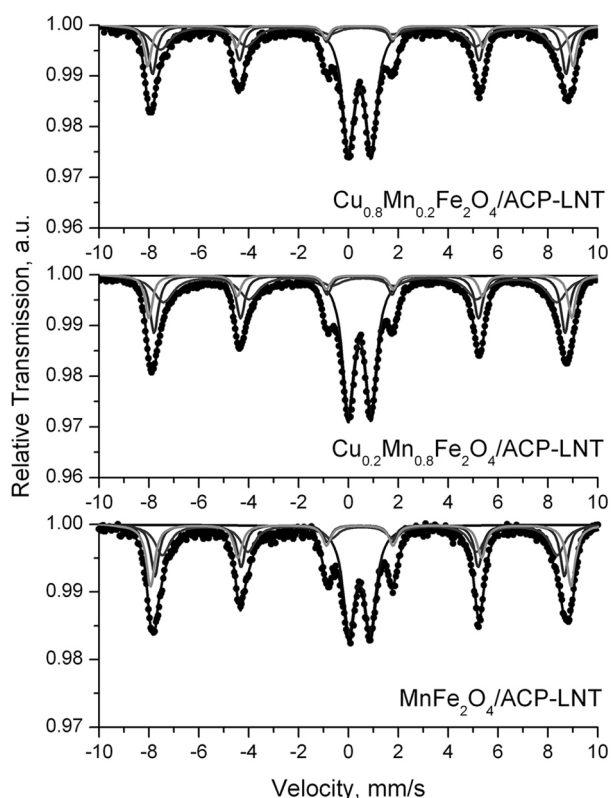The temperature dependencies of methanol decomposition on various ferrite materials are pre-

Fig. 4. Liquid nitrogen temperature Mössbauer spectra of samples of $Cu_{1-x}Mn_xFe_2O_4$ supported on activated carbon thermally treated at 500°C.

sented in Figure 5a. The selectivity to CO, which formation is directly related to the ability of catalysts to release hydrogen, is shown in Figure 5b. Methane (up to 26%) and CO_2 (up to 27%) are also registered as by-products. $MnFe_2O_4$/ACP sample exhibits catalytic activity just above 340°C and 80% conversion is achieved at 440°C. All copper containing materials demonstrate catalytic activity at about 100–150°C lower temperature. Among them, $CuFe_2O_4$/ACP possesses the lowest catalytic activity and well defined tendency of deactivation above 410°C. The catalytic activity of binary materials is higher than the mono component ones and this feature is most pronounced with the increase of copper content in them. Note the specific course of the temperature dependencies for all $Cu_{1-x}Mn_xFe_2O_4$ mixed ferrites. They all characterise with a slope at 260–350°C and a steep increase in the catalytic activity above it.

The Mössbauer data of the samples after the catalytic test are presented in Figure 6 and Table 4. All spectra of samples after test are changed in different degree. The best fitting of $CuFe_2O_4$/ACP, $Cu_{0.5}Mn_{0.5}Fe_2O_4$/ACP and $Cu_{0.2}Mn_{0.8}Fe_2O_4$/ACP spectra after test was done using a model consists of two sextets and one doublet. The absence of the third sextet in spectra of these samples after catalysis could be explain with partial reduction of Cu^{2+} to
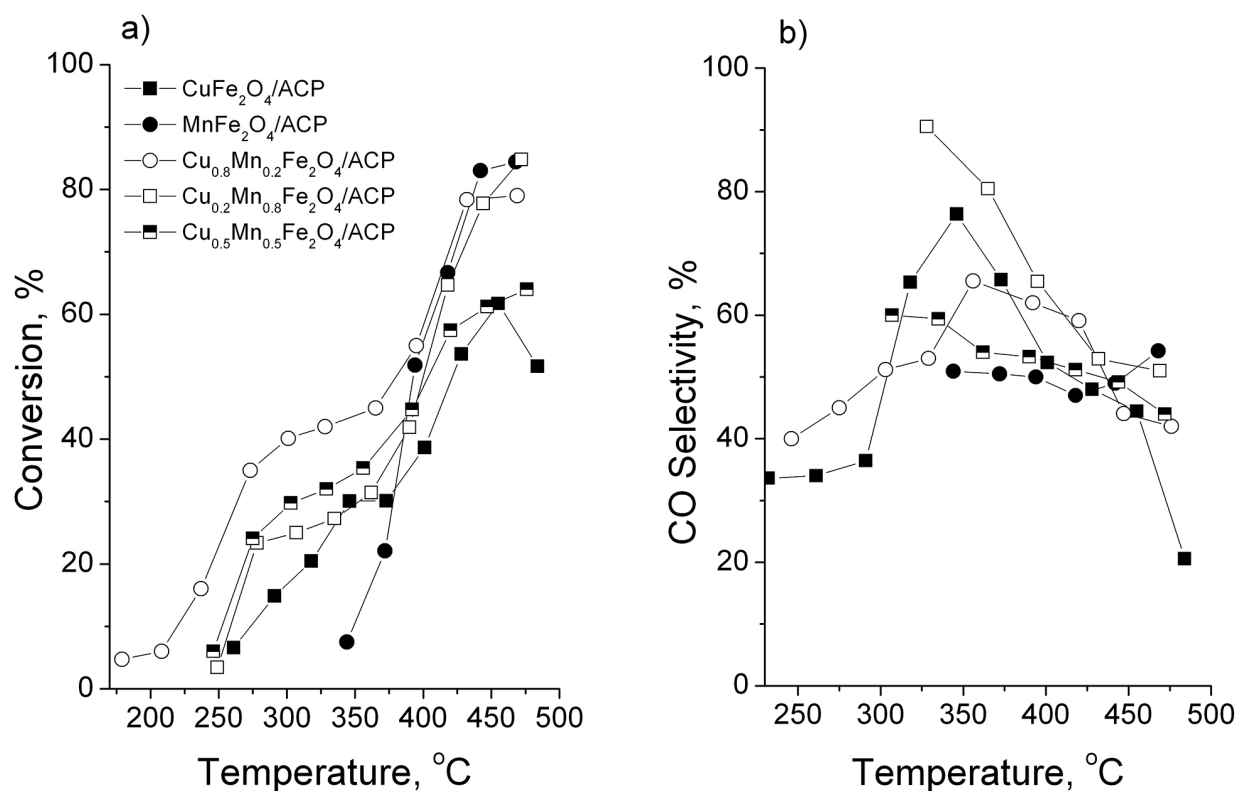
Fig. 5. Temperature dependencies of conversion (a) and CO selectivity (b) in methanol decomposition of thermally treated at 500°C samples.

Table 4. Mössbauer parameters of samples of $Cu_{1-x}Mn_xFe_2O_4$ supported on activated carbon after methanol decomposition test (δ – isomer shift, ΔE_q – quadrupole splitting, B – effective internal magnetic field, Γ_{exp} – line widths, G – relative weight of the partial components in the spectra)

Sample	Components	δ, mm/s	ΔE_q, mm/s	B, T	Γ_{exp}, mm/s	G, %
$CuFe_2O_4$/ACP-MD	Sx1-Fe-tetra	0.34	0.00	49.9	0.50	31
	Sx2-Fe-octa	0.38	−0.02	47.1	1.66	38
	Db1-Fe^{3+}	0.35	0.86	–	0.92	31
$Cu_{0.8}Mn_{0.2}Fe_2O_4$/ACP-MD	Sx1-χ-Fe$_5$C$_2$	0.19	0.06	20.6	0.45	37
	Sx2-χ-Fe$_5$C$_2$	0.15	0.07	18.5	0.33	12
	Sx3-χ-Fe$_5$C$_2$	0.26	0.09	10.9	0.35	3
	Db1-Fe^{3+}	0.34	0.83	–	0.62	48
$Cu_{0.5}Mn_{0.5}Fe_2O_4$/ACP-MD	Sx1-Fe-tetra	0.33	0.00	49.3	0.50	31
	Sx2-Fe-octa	0.48	0.05	45.5	1.17	40
	Db1-Fe^{3+}	0.35	0.76	–	0.71	29
$Cu_{0.2}Mn_{0.8}Fe_2O_4$/ACP-MD	Sx1-Fe-tetra	0.31	0.00	49.3	0.48	23
	Sx2-Fe-octa	0.58	0.03	45.4	1.02	26
	Db1-Fe^{3+}	0.32	0.78	–	0.64	51
$MnFe_2O_4$/ACP-MD	Sx1-χ-Fe$_5$C$_2$	0.19	0.05	21.1	0.38	35
	Sx2-χ-Fe$_5$C$_2$	0.17	0.03	19.5	0.36	12
	Sx3-χ-Fe$_5$C$_2$	0.23	0.00	11.0	0.35	3
	Db1-Fe^{3+}	0.35	0.77	–	0.56	50

Cu^0 and therefore decrease of number of octahedral iron with non-iron neighbors. The spectra of $Cu_{0.8}Mn_{0.2}Fe_2O_4$/ACP and $MnFe_2O_4$/ACP after catalysis are changed significantly and are well fitted with a model including three sextets and one doublet. The calculated parameters of the sextets correspond to carbide of Haag (χ-Fe$_5$C$_2$). In all spectra of the samples after catalytic test are present doublets corresponding to Fe^{3+} ions with similar parameters to doublets in the spectra of the samples before test, but with higher relative weight. This suggest that doublets correspond to an unchanged during reaction phase or due to a new one with high content of non- iron ions. The comparison of these Mössbauer results with the catalytic data clearly indicate that the reduction changes with the ferrites under the reaction medium leads to their complex catalytic behaviour. The high catalytic activity for all binary samples at lower temperature seems to be facilitated by the copper ions in the vicinity of manganese ones, which is realized in the ferrite structure. However at higher temperatures the catalytic behaviour is probably promoted by the activity of Mn^{2+}-Fe^{3+} couples and the formation of carbide phase during the reaction, as well.
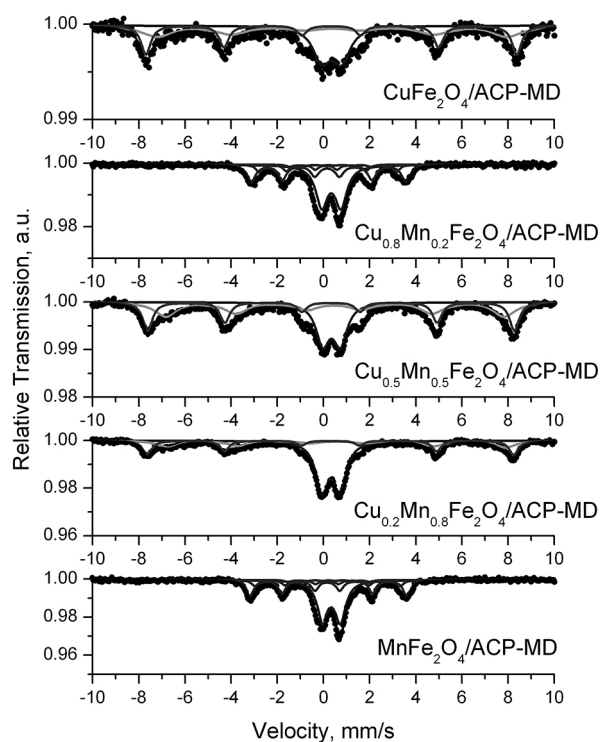
Fig. 6. Mössbauer spectra of samples of $Cu_{1-x}Mn_xFe_2O_4$ supported on activated carbon after methanol decomposition test.

CONCLUSIONS

Copper-manganese ferrite catalysts $Cu_{1-x}Mn_xFe_2O_4$ supported on activated carbon was synthesized. The formation of cubic spinel ferrite with partial inverse structure was established. Binary ferrites possess higher catalytic activity at lower temperature in comparison with their mono-component analogues. They are significantly change under the reaction medium and at higher temperatures the catalytic

behaviour is probably promoted by the activity of Mn^{2+}-Fe^{3+} couples and the formation of carbide phase.

REFERENCES

1. M. N. Ashiq, F. Naz, M. A. Malana, R. S. Gohar, Z. Ahmad, *Mater. Res. Bull.*, **47**, 683 (2012).
2. K. Mukherjee, S. B. Majumder, *Sensor Actuator B-Chem*, **162**, 229 (2012).
3. R. Benrabaa, H. Boukhlouf, S. Barama, E. Bordes-Richard, R. N. Vannier, A. Barama, *Catal. Lett.*, **142**, 42 (2012).
4. K. E. Scarberry, E. B. Dickerson, Z. J. Zhang, B. B. Benigno, J. F. McDonald, *Nanomed-Nanotechnol*, **6**, 399 (2010).
5. P. V. Kovtunenko, *Glass Ceram.*, **54**, 143 (1997).
6. T. A .S. Ferreira, J. C. Waerenborgh, M. H. R. M. Mendoca, M. R. Nunes, F. M. Costa, *Solid State Sci.*, **5**, 383 (2003).
7. J.-P. Jacobs, A. Maltha, J. G. H. Reintjes, J. Drimal, V. Ponec, H. H. Brongersma, *J. Catal.*, **147**, 294 (1994).
8. H. S. Kim, D. Kim, B. S. Kwak, G. B. Han, M.-H. Um, M. Kang, *Chem. Eng. J.*, **243**, 272 (2014).
9. R. Benrabaa, H. Boukhlouf, A. Löfberg, A. Rubbens, R.-N. Vannier, E. B.-Richard, A. Barama, *J. Nat. Gas Chem.*, **21**, 595 (2012).
10. Y.-H. Huang, S.-F. Wang, A.-P. Tsai, S. Kameoka, *Ceram. Int.*, **40**, 4541 (2014).
11. S. Hull, J. Trawczyński, *Int. J. Hydrog. Energy*, **39**, 4259 (2014).
12. E. Manova, T. Tsoncheva, C. Estournes, D. Paneva, K. Tenchev, I. Mitov, L. Petrov, *Appl. Catal. A Gen.*, **300**, 170 (2006).
13. N. Velinov, K. Koleva, T. Tsoncheva, D. Paneva, E. Manova, K. Tenchev, B. Kunev, I. Genova, I. Mitov, *Cent. Eur. J. Chem.*, **12**, 250 (2014).
14. N. Velinov, K. Koleva, T. Tsoncheva, E. Manova, D. Paneva, K. Tenchev, B. Kunev, I. Mitov, *Catal. Commun.*, **32**, 41 (2013).
15. N. Velinov, E. Manova, T. Tsoncheva, C. Estournès, D. Paneva, K. Tenchev, V. Petkova, K. Koleva, B. Kunev, I. Mitov, *Solid State Sci.*, **14**, 1092 (2012).
16. T. Tsoncheva, E. Manova, N. Velinov, D. Paneva, M. Popova, B. Kunev, K. Tenchev, I. Mitov, *Catal. Commun.*, **12**, 105 (2010).
17. E. Manova, T. Tsoncheva, D. Paneva, I. Mitov, K. Tenchev, L. Petrov, *Appl. Catal. A Gen.*, **277**, 119 (2004).
18. K. Koleva, N. Velinov, T. Tsoncheva, I. Mitov, *Hyperfine Interact.*, **226**, 89 (2014).
19. K. Koleva, N. Velinov, T. Tsoncheva, I. Mitov, B. Kunev, *Bulg. Chem. Commun.*, **45(4)**, 434 (2013).
20. T. Tsoncheva, N. Velinov, R. Ivanova, I. Stoycheva, B. Tsyntsarski, I. Spassova, D. Paneva, G. Issa, D. Kovacheva, I. Genova, I. Mitov, N. Petrov, *Microporous and Mesoporous Materials*, **217**, 87 (2015).
21. F. Rodriguez-Reinoso, *Carbon*, **36**, 159, (1998).
22. H. Juntgen, *Fuel*, **65**, 1436 (1986).
23. C. Moreno-Castilla, F. Carrasco-Marin, C. Parejo-Perez, M. V. Lopez Ramon, *Carbon*, **39**, 869 (2001).
24. F. Rodriguez-Reinoso, M. Molina-Sabio, M. A. Munecas, *J. Phys. Chem.*, **96**, 2707 (1992).
25. T. Žák, Y. Jirásková, *Surf. Interface Anal.*, **38**, 710 (2006).
26. R. D. Shannon, *Acta Cryst.*, **A 32**, 751 (1976).

СИНТЕЗ И ОХАРАКТЕРИЗИРАНЕ НА МЕД-МАНГАНОВИ ФЕРИТИ СЪС СЪСТАВ $Cu_{1-x}Mn_xFe_2O_4$, НАНЕСЕНИ ВЪРХУ АКТИВЕН ВЪГЛЕН

Т. М. Петрова[1]*, Н. И. Велинов[1], И. Г. Генова[2], Т. С. Цончева[2],
Д. Г. Ковачева[3], Н. В. Петров[2], И. Г. Митов[1]

[1] *Институт по катализ, Българска академия на науките, 1113, София, България*
[2] *Институт по органична химия с център по фитохимия, Българска академия на науките, 1113, София, България*
[3] *Институт по обща и неорганична химия, Българска академия на науките, 1113 София, България*

(Резюме)

Целта на настоящото проучване е да се синтезират смесено оксидни мед манганови феритни катализатори със състав $Cu_{1-x}Mn_xFe_2O_4$ (x=0; 0.2; 0.4; 0.6; 0.8 and 1), нанесени върху активен въглен, получен от костилки от праскови. За охарактеризиране структурата и катийонното разпределение на синтезираните образци са използвани Рентгенова дифракция, Мьосбауерова спектроскопия и е проведен каталитичен тест в реакция на разлагане на метанол. Резултатите от анализите дават доказателства, че са получени нанесени феритни катализатори с кубична симетрия и частично инверсна шпинелна структура. Установи се, че катализаторите претърпяват съществени редукционни промени с формиране на магнетит или карбид на Хааг под действието на реакционната среда. Доказа се, че присъствието на мед в манганови ферити подобрява каталитичната активност в нискотемпературната област като тази тенденция нараства с повишаване съдържанието на мед в образците.

Sol-gel SiO$_2$ coatings doped with Nd$_2$O$_3$

S. I. Yordanov[1]*, I. D. Stambolova[2], L. I. Lakov[1], V. N. Blaskov[2], B. T. Jivov[1],
M. K. Aleksandrova[1], S. T. Valkanov[1], A. E. Eliyas[3]

[1] *Institute of Metal Science, Equipment and Technologies with Hydro- and Aerodynamics Centre*
"Acad. A. Balevski", Bulgarian Academy of Science, 67, "Shipchenski Prohod" Blvd, 1574 Sofia, Bulgaria
[2] *Institute of General and Inorganic Chemistry – BAS, 1113 Sofia, "Acad. Georgi Bonchev" str. bld.11*
[3] *Institute of Catalysis – BAS, 1113 Sofia, "Acad. Georgi Bonchev" str., bld.11*

Non-doped and doped with Nd$_2$O$_3$-SiO$_2$ protective layers have been spin coated on low-carbon content constructions steel plates by the sol-gel method. The deposition-drying cycles have been repeated seven times and thereafter the coatings have been thermally treated at 300°C. Scanning electron microscopy (SEM) has been applied to investigate the surface morphology. The resistance of SiO$_2$ coated steels were examined in NaCl corrosive medium. It has been demonstrated that Nd$_2$O$_3$ dopant exerts positive effect upon the chemical resistance of the SiO$_2$ coatings.

Keywords: sol-gel coatings, chemical resistance, silica, Nd$_2$O$_3$.

INTRODUCTION

Unprotected metal surfaces are being exposed to the continuous or periodically unfavorable effect of severe external factors: hard abrasive particles, different aggressive chemical agents, extreme thermal variations, increased pressure and others. It is necessary to prevent the corrosion processes occurring in metals [1, 2] and this requires appropriate technology solutions, providing effective protection of load-bearing metal constructions, manufacturing equipment and factory installations in various fields of technology and industry.

Variety of technological methods to prepare coatings with diverse structures such as CVD, PVD, electrophoresis, sol-gel methods etc. have been applied so far [3–10]. The coatings possess specific thermal [11], optical [12], anti-corrosion and other properties [7, 8, 13–15], which are useful under various operating conditions. The specific features of the metals, the state of the surface, the peculiarities of working environment and the other factors determine the appropriate type of coverage and the optimal preparation method.

The coatings obtained by sol-gel process are suitable for effective protection of metallic surfaces from corrosion [16]. They significantly prolong the long-term durability of metals [17–19]. The sol-gel technology has been applied to the preparation of anticorrosive protective coatings on a steel [16], aluminium [20] and other metals.

There appear many advantages when using sol–gel coatings, several of the most important features are: (i) Sol–gel processing temperature is generally low, frequently close to room temperature. Thus thermal volatilization and degradation of entrapped species, such as organic inhibitors, is minimized. (ii) It is possible to cast coatings in complex shapes. (iii) The sol–gel method is waste-free so it does not require a stage of washing away impurities.

Several oxides possessing good chemical and thermal stability such as SiO$_2$, CeO$_2$, ZrO$_2$, TiO$_2$, Al$_2$O$_3$ are suitable for achieving corrosion protection [21].

Vasconcelos et al. [22] have been investigating the acidic corrosion resistance of sol–gel silica films deposited on AISI 304 stainless steel. In view of previous corrosion investigation experience it is well known that adding small amounts of dopants – for example rare earth elements (Ce, La etc.) greatly improves the corrosion resistance [23]. We have not found in the available literature information concerning the resistance of Nd$_2$O$_3$ doped SiO2 films in the NaCl medium.

_____
* To whom all correspondence should be sent:
E-mail: stancho14@abv.bg

The aim of this work is to investigate the effect of neodymium dopant in SiO_2 sol-gel coatings on the structure and their chemical resistance in corrosive NaCl medium.

EXPERIMENTAL

The substrates for sol-gel coatings were low carbon content constructions steel USt 37-1 plates (DIN 17 100) with perlite – ferrite type of structure. They were degreased in hot acetone for 5 min in ultrasonnic bath, then they were dried at 60°C in furnace. Ethanolic solution of tetraethyl orthosilicate (TEOS, 99.5%, Merck),was hydrolyzed with water-ethanol mixture, (sol A) at a molar ratio $TEOS:H_2O=4.7$. Hydrochloric acid (37%) was used to catalyse the hydrolysis process. This solution was used for deposition of non-doped SiO_2 coatings. Sol B was prepared by dissolving of Nd_2O_3 in small quantity of HNO_3, followed by dissolving it into deionized water in order to obtain final concentration of neodimum salt 0.01 mol/L. The Nd_2O_3 doped SiO_2 coatings were produced using a mixtures of sol A and sol B. The concentration of the metal dopant was calculated in such a way as to give 0.14 wt% and 0.28 wt% Nd_2O_3 with respect to SiO_2 amount.

The substrates were coated by spin-on technique at a constant speed of 800 rpm for 20 s. The coating was then dried at 100°C for 20 min.These steps were repeated 7 times in order to obtain desirable films thickness. The final thermal treatment step was carried out in temperature-programmable oven at 300°C. The temperature was increased at a constant rate of 3°C/min. After 1 hour the samples were cooled naturally down to room temperature.

The surfaces of the so prepared samples were investigated by scanning electron microscope JCXA 733 JEOL (SEM).

The investigated samples were exposed to the action of salty solution of 3.5% NaCl at 35°C (EN ISO 10289/2006) in the course of 12 hours in order to study their chemical resistance.

RESULTS

The surfaces of SiO_2 films were examined using a Scanning Electron Microscope. Figure 1 shows SiO_2 films doped with 0.28 wt% Nd_2O_3. The surface of the film is relatively dense without any visible cracks. The SEM micrographs of the coatings after carrying out resistance test in NaCl are shown in Fig. 2. It can be seen that on the surface of non-doped SiO_2 there appear numerous visible cracks and the film is detached in some places (Fig. 2a). The Nd_2O_3 doped silica coatings exhibit restricted

Fig. 1. SEM photograph of SiO_2 fresh films doped with 0.28% Nd_2O_3.
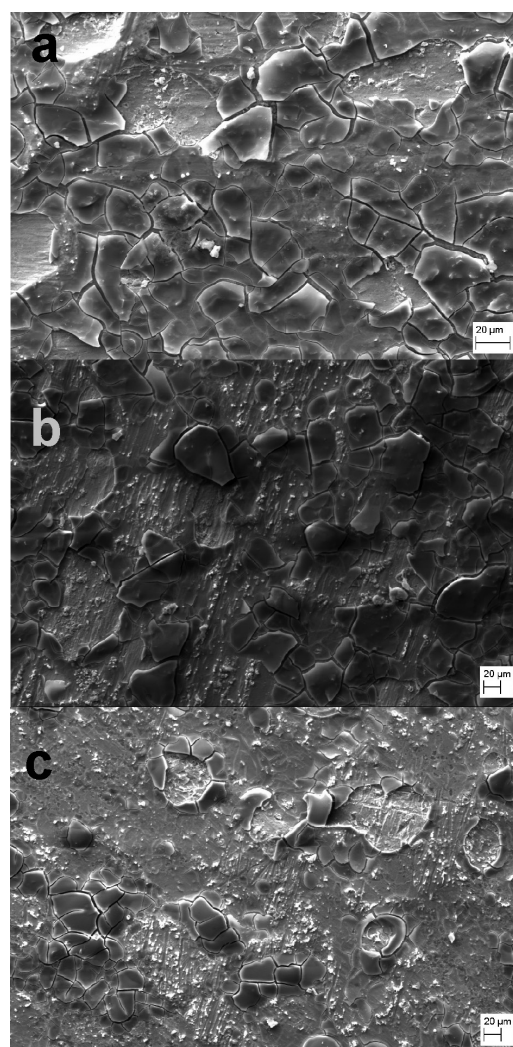
Fig. 2. SEM photograph of a) SiO_2 films after chemical resistance test, b) SEM photograph of SiO_2 films doped with 0.14% Nd_2O_3 after chemical resistance test and c) SEM photograph of SiO_2 films doped with 0.28% Nd_2O_3 after chemical resistance test.

lower number of cracks having smaller size. The films are more strongly adhered to the steel substrate surface in comparison with the non-doped SiO$_2$ coatings (Fig. 2b, c).

On the basis of the above mentioned results it can be concluded that the Nd$_2$O$_3$ doped silica coatings resist better to the NaCl corrosive attack than the non-doped coatings, which fact is probably due to the corrosion inhibiting effect of Nd^{3+} ions in the SiO$_2$ coatings similar to that of cerium ions [24] .These preliminary results about the chemical resistance of doped SiO$_2$ coatings are promising and they give us the reason to extend the scope of the experiments further involving electrochemical measurements for estimation of corrosion resistance.

CONCLUSIONS

The sol–gel spin-coating technique was successfully applied to obtain Nd$_2$O$_3$ doped SiO$_2$ coatings on steel substrates. The scanning electron photographs of the doped films reveals smoother surface in comparison with the non-doped films after chemical resistance test in corrosive NaCl medium. It has been revealed that Nd$_2$O$_3$ doped silica coatings can provide a higher chemical resistance.

REFERENCES

1. R. G. Buchheit, R.P. Grant, P. F. Hlava, B. Mcjebzue, G.L. Zender, *J. Electrochem. Soc.*, **144**, 2621 (1997).
2. T. L. Metroke, R.L. Parkhill, E. T. Knobbe, *Prog. Org. Coat.*, **41**, 233 (2001).
3. T. Kubota, N. Akao, N. Har, K. Sugimoto, *J. Jpn. Instrum. Methods*, **60**, 980 (1996).
4. K. Ohashi, K. Miyake, *Mater. Chem. Phys.*, **54**, 365 (1998).
5. F. Perdomo, P. De Lima-Neto, M.A. Aegerter, L.A. Avaca, *J. Sol-Gel Sci. Technol.*, **15** , 87 (1999).
6. B. Ferrari, R. Moreno, *J. Electrochem. Soc.*, **147**, 2987 (2000).
7. L. Fedrizzi, F. J. Rodriguez, S. Rossi, F. Deflorian, R. Di Maggio, *Electrochim. Acta*, **46**, 3715 (2001).
8. J. P. Holgado, M. Perez-Sánchez, F. Yubero, J. P. Espinós, A. R. González-Elipe, *Surf. Coat. Technol.*, **151–152**, 449 (2002).
9. R. López Ibáñez, J. R. Ramos Barrado, F. Martín, F. Brucker, D. Leinen, *Surf. Coat. Technol.*, **188 – 189**, 675 (2004).
10. R. Romero Pareja, R. López Ibáñez, F. Martín, J.R. Ramos-Barrado, D. Leinen, *Surface & Coatings Technology*, **200**, 6606 (2006).
11. P. K. Wright, A. G. Evans, *Curr. Opin. Solid State Mater. Sci.*, **4**, 255 (1999).
12. Q. Zhang, J. Shen, J. Wang, G. Wu, L. Chen, *Int. J. Inorg. Mater.*, **2**, 319 (2000).
13. H. Hasuyama, Y. Shima, K. Baba, G.K. Wolf, H. Martín, F. Stippich, *Nucl. Instrum. Methods Phys. Res.*, **B 127–128**, 827 (1997).
14. A. R. Di Giampaolo, Y. González, D. Gutiérrez-Campos, *Adv. Perfom. Mater.*, **6**, 39 (1999).
15. F. Martín, M.C. López, P. Carrera, J.R. Ramos-Barrado, D. Leinen, *Surf. Interface Anal.*, **36**, 8 (2004).
16. Duhua W., Gordon P., Bierwagen, *Sol-gel coatings for corrosion protection, Progress in Organic Cotings*, **64**, 327 (2009).
17. G.P. Bierwagen, L. He, J. Li, L. Ellingson, D.E. Tallman, *Progress in Organic Coatings*, **39**, 67 (2000).
18. C. J. Brinker, A.J. Hurd, P.R. Shunrk, *J. Non-Cryst. Solids*, **147**, 424 (1992).
19. J. D. Wright, N. A. J. Sommerdijk, *Sol–Gel Materials Chemistry and Applications*, CRC Press, OPA Overseas Publishers Association (2001).
20. M. Guglielmi, *J. Sol–Gel Sci. Technol.*, **8**, 443 (1997).
21. D. Wang, G. P. Bierwagen, *Progress in Organic Coatings*, **64**, 327 (2009).
22. D. C .L. Vasconcelos, J. A. N. Carvalho, M. Mantel, W. L. Vasconcelos, *J. Non-Cryst. Sol.*, **273**, 135 (2000).
23. M. Garcia-Heras, A. Jimenez-Morales, B. Casal, J.C. Galvan, S. Radzki, M.A. Villegas, *J. Alloys Comp.*, **380**, 219 (2004).
24. A. Pepe, M. Aparicio , A. Dur´an, S. Cer´e, *J. Sol-Gel Sci Technol.*, **39,** 131 (2006).

ЗОЛ-ГЕЛНИ ПОКРИТИЯ ОТ SiO$_2$, ДОТИРАНИ С Nd$_2$O$_3$

С. И. Йорданов[1], И. Д. Стамболова[2], Л. И. Лаков[1], В. Н. Блъсков[2], Б. Ц. Живов[1], М. К. Александрова[1], С. Т. Вълканов[1], А. Е. Елиаз[3]

[1] *Институт по металознание, съоръжения и технологии с Център по хидро- и аеродинамика „Акад. А. Балевски" – БАН, бул. „Шипченски проход" 67, 1574 София, България*
[2] *Институт по обща и неорганична химия – БАН, Акад. Г. Бончев, бл. 11, 1113 София, България*
[3] *Институт по катализ – БАН, Акад. Г. Бончев, бл. 11, 1113 София, България*

(Резюме)

Недотирани и дотирани с Nd$_2$O$_3$ – SiO$_2$ защитни покрития са отложени върху нисковъглеродни стоманени подложки чрез зол-гел метод. Циклите на отлагане/сушене бяха повторени седем пъти, след което покритията са термично третирани при 300°C. Сканираща електронна микроскопия е приложена за изследване на морфологията на повърхността. Устойчивостта на покритията върху стомана е изучена в корозионна среда от NaCl. Демонстрирано е, че въвеждането на допант Nd$_2$O$_3$ в покритията от SiO$_2$ има положителен ефект върху химическата им устойчивост.

Structural and morphological characterization of heat-activated nickel-titanium archwires

I. Ilievska[1]*, V. Petrov[2], L. Andreeva[2], D. Kovacheva[3], A. Zaleski[4], M. Drozd[4], E. Bukowska[4], V. Mikli[5], A. Stoyanova-Ivanova[1]

[1] Institute of Solid State Physics, BAS, 72 Tzarigradsko Chaussee Blvd., 1784 Sofia, Bulgaria
[2] Faculty of Dental Medicine, Medical University Sofia, St. Georgi Sofiiski Blvd., 1431 Sofia, Bulgaria
[3] Institute of General and Inorganic Chemistry, 1113 Sofia „Acad. Georgi Bonchev" str. bld.11
[4] Institute of Low Temperature and Structure Research, Polish Academy of Sciences,
ul. Okolna 2, 50-422 Wroclaw, Poland
[5] Centre for Materials Research, Tallinn University of Technology, Ehitajate 5, Tallinn 19086, Estonia

Heat-activated nickel-titanium (Ni-Ti) archwires are widely used in the initial stages of orthodontic treatment. These alloys exhibit a shape memory effect which can be related to displacive (martensitic) transformation, which can be induced by temperature variation or mechanical influence (stress).

Here we explored the changes of archwires microstructure, chemical composition and phase transition temperatures due to prolonged regular usage. Three forms of dental archwires with dimensions 0.016" x 0.022" (3M Unitek, Monrovia, CA, USA) were investigated: as-received, as-received + autoclaved (sterilized) and used during treatment heat-activated Ni-Ti archwires. The three forms of archwires were analyzed by powder X-ray diffraction analysis (XRD), Scanning Electronic Microscopy (SEM) in combination with Energy Dispersive Spectroscopy (EDX) and Differential Scanning Calorimetry (DSC).

The room temperature the XRD pattern of the archwires show typical peaks for a Ni-Ti alloy with austenite type structure. The DSC measurements were conducted in the –50°C to +50°C temperature range. The DSC analyses of the Ni-Ti archwires revealed three phase transitions. Upon heating from –50°C to +50°C a phase transition occurs at ~12°C. No additional *endo/exo* effects are registered. Upon cooling the DSC registers a phase transition around 10°C and around –40°C. The first effect is due to the formation of an intermediate rhombohedral phase (R phase) while at –40°C Ni-Ti structure transforms to martensite. The results from EDX demonstrate that there is no pronounced change in the chemical composition on the surface of the investigated orthodontic archwires. Though SEM micrographs show some changes on the surface of the wires after usual use.

The results obtained within this study contribute to the establishment of some peculiarities related to the thermal behavior and the shape-memory effect of the investigated archwires.

Keywords: Ni-Ti heat-activated orthodontic archwires, XRD, SEM, DSC.

INTRODUCTION

Nickel-titanium (Ni-Ti) archwires are used in the initial stages of orthodontic treatment due to their properties of exerting light constant forces that are appropriate for alignment and leveling and good super-elasticity. [1–3]

An interesting feature of these heat-activated archwires is their thermoelastic behavior and the so-called shape memory effect, which has remark- able clinical applications. During bending and repeated temperature cycles, orthodontic archwires in the austenitic phase are able to „remember" a pre-formed shape, including specific shape of the dental arch [4]. The Ni-Ti archwires transform from martensitic to austenitic phase at oral temperature (35 degrees). At lower temperatures the martensitic phase is fully present in the alloy, which allows the orthodontist to easily put the orthodontic arch into the slot of the bracket. At higher temperatures the alloy turns to the austenite phase and starts exerting larger forces, due to the return to its original shape. These forces make teeth move in a certain direction [5, 6].

* To whom all correspondence should be sent:
E-mail: ivannyilievska@gmail.com

During orthodontic treatment, Ni-Ti archwires in the patient's mouth are exposed to frequent temperature changes, which are more complex than those observed in the in - vitro studies [7]. Accordingly, the orthodontic archwires will be subjected to loads, complex temperature fluctuations, as well as interaction with the brackets, which are with different metal composition. The wires can also interact with electrolytes, fluoride, proteins, etc., and that leads to formation of new compounds on the surface. The combination of these factors could affect the properties and structure of archwires, although there is little information in the literature about the effects of these factors on clinically used orthodontic archwires [8].

In our previous studies we examine the chemical composition of the surface of thermally activated copper-nikel-titanium archwires [9].

In this study we concentrate not only on investigating the chemical composition and the structure, but also on investigating the thermal phase transition on as-received, as-received autoclaved (sterilized) and used heat-activated Ni-Ti archwires, because their action is influenced by temperature. The process of autoclaving (sterilization) has also been studied. The results obtained within this study contribute to the establishment of some peculiarities of the thermal behavior and the shape-memory effect of the archwires.

MATERIALS AND METHODS

Three types of dental orthodontic archwires with a rectangular cross section and dimensions 0.016" × 0.022" (0.406 mm × 0.558 mm) were chosen: as-received, as-received autoclaved (sterilized) and used (up to 5 and 8 weeks) heat-activated Ni-Ti archwires, produced by the company 3M Unitek, Monrovia, CA, USA. The analyses were carried out by the following techniques: X-ray diffraction analysis (XRD), Scanning Electronic Microscopy (SEM), Energy Dispersive Spectroscopy (EDX) and Differential Scanning Calorimetry (DSC).

To determine the structure of the material we use an X-ray Powder Diffractometer X'Pert Pro with a high-temperature closed attachment HTK 1200 from Anton Paar.

Surface morphology and elemental composition were studied using a ZEISS HR FESEM Ultra 55 Scanning Electron Microscope (SEM) with Bruker EDX system ESPRIT 1.8. The elemental composition was determined by energy-dispersive X-ray microanalysis (EDX) method using Bruker Esprit 1.8 system. Quantification of the EDX results was performed by the help of interactive PB-ZAF standardless method. The acceleration voltage for SEM measurements was 4.0 kV and for EDX 7.0 kV.

The analyses by Differential Scanning Calorimetry (DSC) were performed using a DSC Perkin-Elmer – 8000 with TGA attachment, model PE-TGA4000. Before introducing the sample in the DSC apparatus for each individual test a calibration with indium was made. The temperature range of the DSC apparatus is from –170°C to +600°C. The samples were scanned from –50°C to +50°C for the heating process and from +50°C to –50°C for the cooling process, with a heating/cooling rate of 20°C per minute. The onset and endset temperatures along with enthalpy of all investigated archwires were calculated for various phase transformations.

RESULTS AND DISCUSSIONS

Information about the presence or absence of the martensitic and austenitic phases is received by XRD analyses of the Ni-Ti heat-activated orthodontic wires [10]. On Fig. 1, the XRD pattern made at room temperature on as-received, as-received sterilized and used up to 5 and up to 8 weeks orthodontic archwires, we observed typical peaks for Ni-Ti alloy with austenite type structure. The austenitic phase has an ordered base-centered cubic structure, which occurs at high temperature [11]. It can be seen that there is a presence of a surface amorphization of the material, which can be due to surficial interaction with saliva or contamination. Similar behavior is seen in the Cu-Ni-Ti heat-activated archwires [9].

Information about the surface morphology of the Ni-Ti heat-activated orthodontic archwires is obtained by Scanning Electron Microscopy (Fig. 2.)

The results demonstrate that there is no remarkable change on the surface of as-received and as-
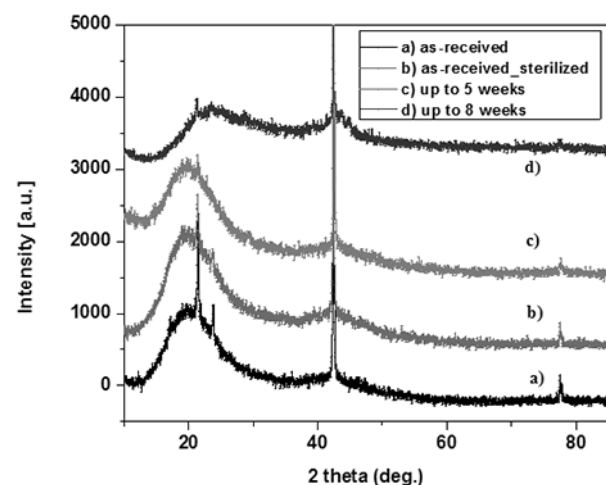

Fig. 1. XRD pattern of investigated Ni-Ti archwires at different stages of treatment.
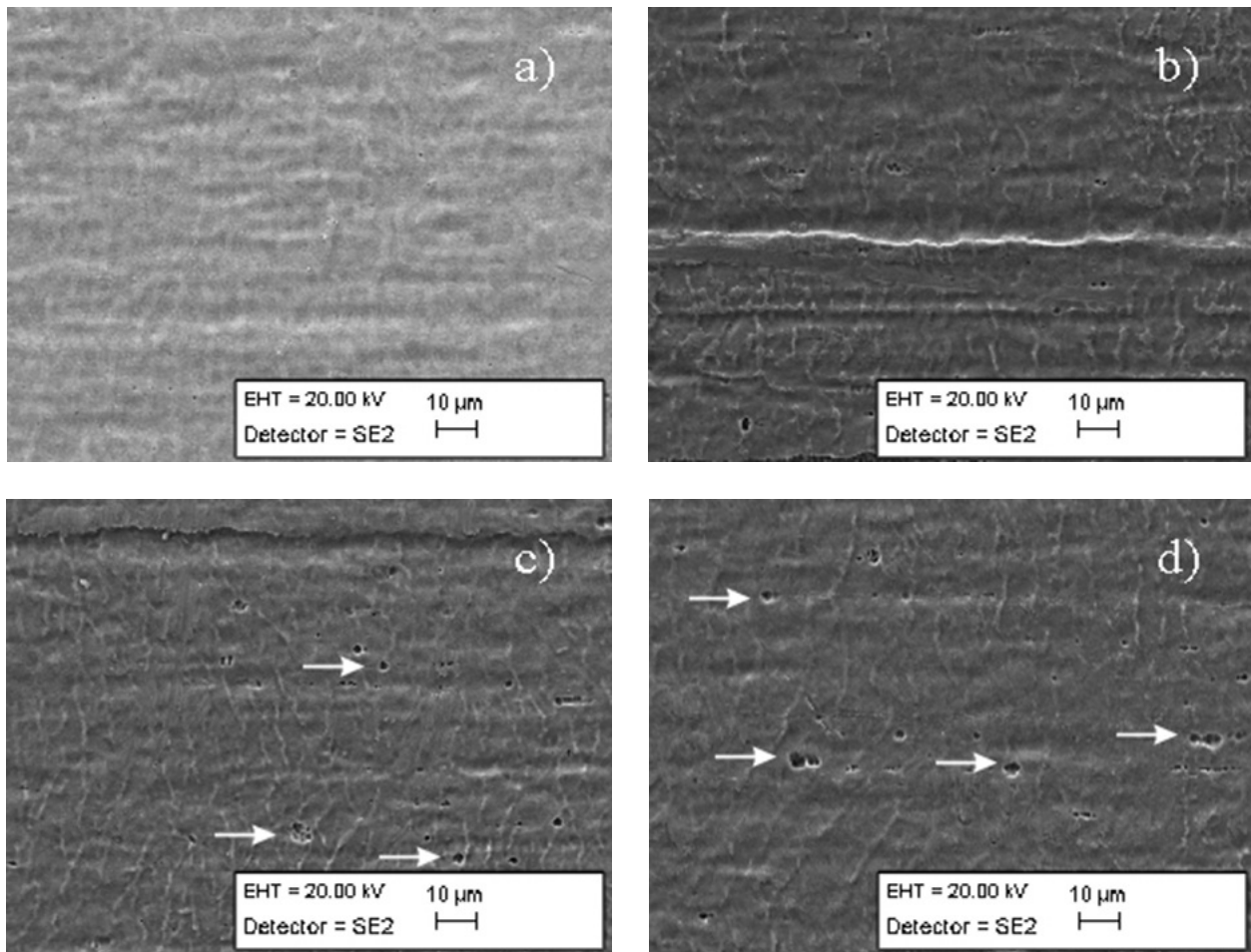
Fig. 2. SEM images of as-received a), as-received sterilized b), used up to 5 weeks c), used up to 8 weeks d) Ni-Ti heat-activated orthodontic archwires.

received sterilized archwires. Autoclaving process seems to have no effects on archwires' structure. On the surface of the archwires that have been used for treatment up to 5 and up to 8 weeks it can be seen that there is a change after use. The presence of the bigger pores can be observed on the surface of the used archwires, which can be the result of an aggressive environment in the mouth during treatment and masticatory action.

Also the EDX was used to analyze the surface of the archwires and to make quantitative identification of the chemical composition by elements. The average values of the element composition are shown in Table 1.

The results show that as-received Ni-Ti heat-activated archwire has average Ni – 54.36 wt% and Ti – 45.64 wt%. The period of residence in the mouth has no significant effect on the proportion of elements in the tested orthodontic archwires and the ratio Ni to Ti is kept. The analysis confirms the presence of only the main components of the alloy.

Ni-Ti archwires are heat-activated orthodontic archwires with shape-memory properties. Phase transformations (austenite − martensite) in these archwires are of big importance due to their clinical applications. That's why we chose the DSC method for investigating phase transformations and because this method provides information about the entire sample [12].

DSC can give information about the thermal transitions of the material, in our case we measured our samples in the temperature range from –50°C to +50°C and back to –50°C with heating/cooling of 20°C per minute to see the transformation temperatures and associated transformation enthalpy changes, respectively. The transition temperature range (TTR) in Ni-Ti alloys, which happens when phase transition occurs, should correspond to the temperature variations in the oral environment to be beneficial for the orthodontic treatment [13]. Information about TTR for rectangular Ni-Ti archwires with dimensions 0.016" × 0.022", are in need because

Table 1. Elements content of investigated Ni-Ti archwires

Ni-Ti archwires	Elements, weight %				
Spectrum	Ni	Error	Ti	Error	Total Ni-Ti
Ni-Ti as-received	54.36	+/– 0.8%	45.64	+/– 0.8%	100.00
Ni-Ti as-received sterilized	54.41	+/– 0.8%	45.59	+/– 0.8%	100.00
Ni-Ti up to 5 weeks	54.13	+/– 0.8%	45.87	+/– 0.8%	100.00
Ni-Ti up to 8 weeks	54.19	+/– 0.8%	45.81	+/– 0.8%	100.00

there is no enough studies about it. The manufacturers do not provide complete information about the produced archwires as well.

The transformation from austenite to R-phase and from R-phase to martensite has been investigated by DSC method [14], where As (austenite start), Rs (R-phase start) and Ms (martensite start) are the onset temperatures when the transition begins. Respectively, Af (austenite finish), Rf (R-phase finish) and Mf (martensite finish) are the endset temperatures when the transition ends.

Table 2 and table 3 show our results obtained by DSC: transformation temperatures (onset, endset), enthalpy of the transition (ΔH), the peak and the area under the curve, which were measured for all investigated archwires. An intermediate tetragonal phase between austenite and martensite called R-phase can occur as a result of a rhombohedral distortion of the cubic parent phase [10] and the lower temperature phase is rhombohedral. The R-phase transition is a kind of martensitic transformation with a very small thermal hysteresis [15]. In our case, we observed the intermediate R-phase in the cooling process.

In as-received Ni-Ti archwire, from the DSC analyses made in the temperature range from –50°C

Table 2. DSC results for heating process of the investigated archwires

Ni-Ti heat-activated archwires	Heating				
	Onset [°C]	Delta H [J/g]	Peak [°C]	Area [mJ]	Endset [°C]
	As				Af
As-received	4.35	6.3539	10.91	79.048	17.57
As-received sterilized	6.97	7.8037	10.93	33.056	13.86
Used up to 5 weeks	12.90	10.0995	18.20	37.934	21.34
Used up to 8 weeks	6.21	9.3893	11.43	49.979	15.52

Table 3. DSC results for cooling process of the investigated archwires

Ni-Ti heat-activated archwires	Cooling									
	Onset [°C]	Delta H [J/g]	Peak [°C]	Area [mJ]	Endset [°C]	Onset [°C]	Delta H [J/g]	Peak [°C]	Area [mJ]	Endset [°C]
	Rs				Rf	Ms				Mf
As-received	11.93	–2.1860	3.01	–27.19	–3.16	–	–	–	–	–
As-received sterilized	24.19	–2.9258	3.46	–12.394	–1.38	–42.59	–0.8540	–46.62	–3.618	–49.34
Used up to 5 weeks	24.89	–3.5700	11.28	–13.409	3.94	–35.91	–4.7536	–41.66	–17.85	–47.19
Used up to 8 weeks	9.03	–2.9202	3.40	–15.544	–2.61	–42.78	–0.7760	–47.08	–4.131	–49.74

to +50°C and back to –50°C, it can be observed that there is a transition from austenite to R-phase, without the presence of martensite phase (Fig. 3a). For the as-received sterilized Ni-Ti archwire, in the cooling process there are two peaks which are attributed to an austenite to R-phase followed by an R-phase to martensite transition. (Fig. 3b). The Af in the heating process for as-received and used archwires, is changing during treatment from 17.57°C to 15.52°C. The Af is particularly important, since it indicates the temperature in which the material will entirely return to the original shape and consequently acquire greater rigidity [13].

Brantley et al. reported that the R-phase may always be present in some Ni-Ti heat-activted archwires [16]. DSC analyses of investigated as-received Ni-Ti archwire do not show presence of martensite phase in the measured temperature interval.

On Figure 4 results from DSC for the used archwires (up to 5 weeks (a) and up to 8 weeks (b)) are shown. The presence of the R-phase is observed in the cooling process for the used archwires as well. The Ms temperature for as-received sterilized and used archwires is below –30°C. It can be seen that every phase transition has different transition temperatures for investigated archwires. Other studies of orthodontic archwires produced form other companies used for the same purpose show differences from our results [1]. This requires prolonged study of applied orthodontic archwires in each step of treatment.
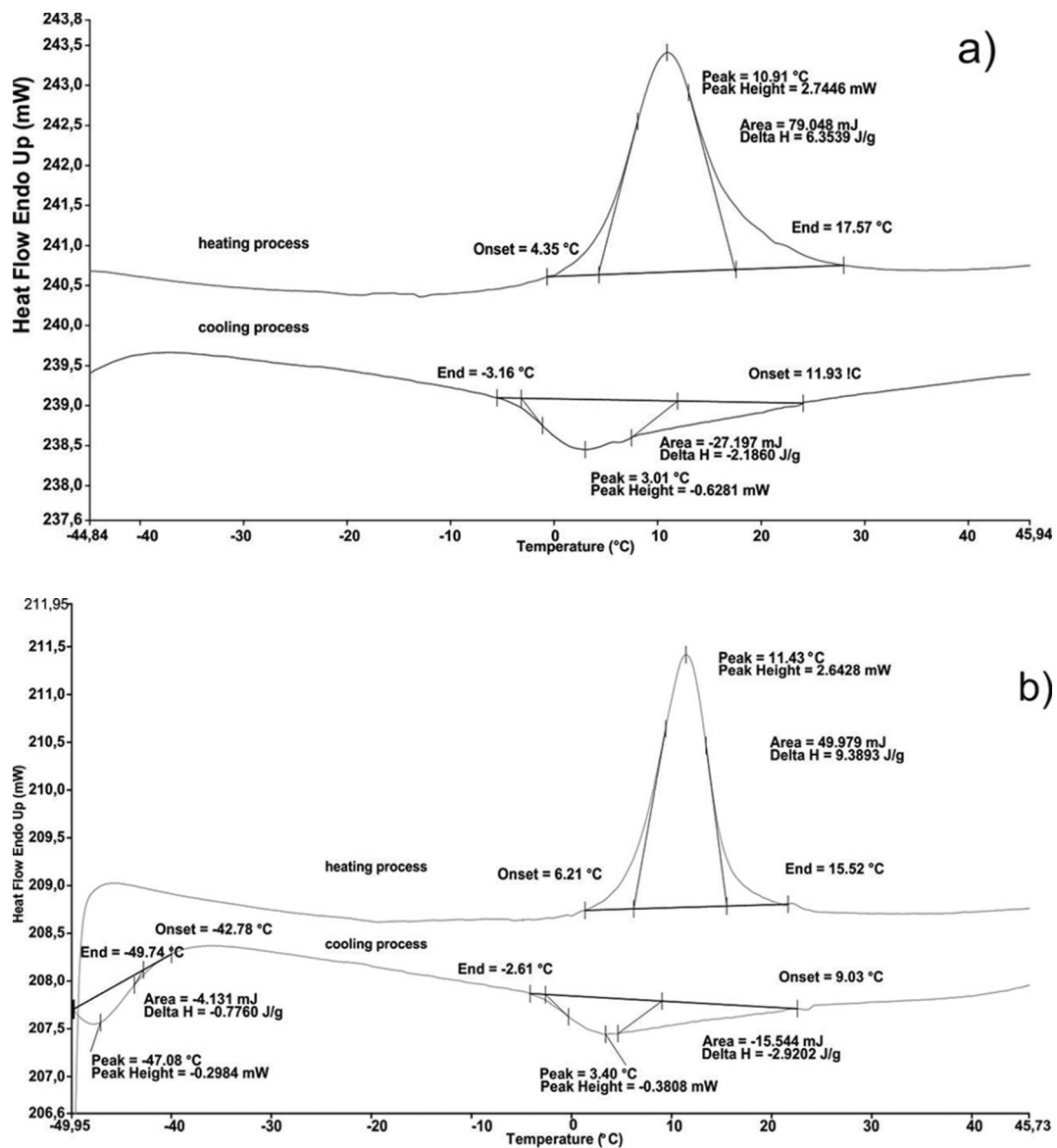
Fig. 3. DSC analyses on as-received a) and as-received sterilized b) Ni-Ti archwires.
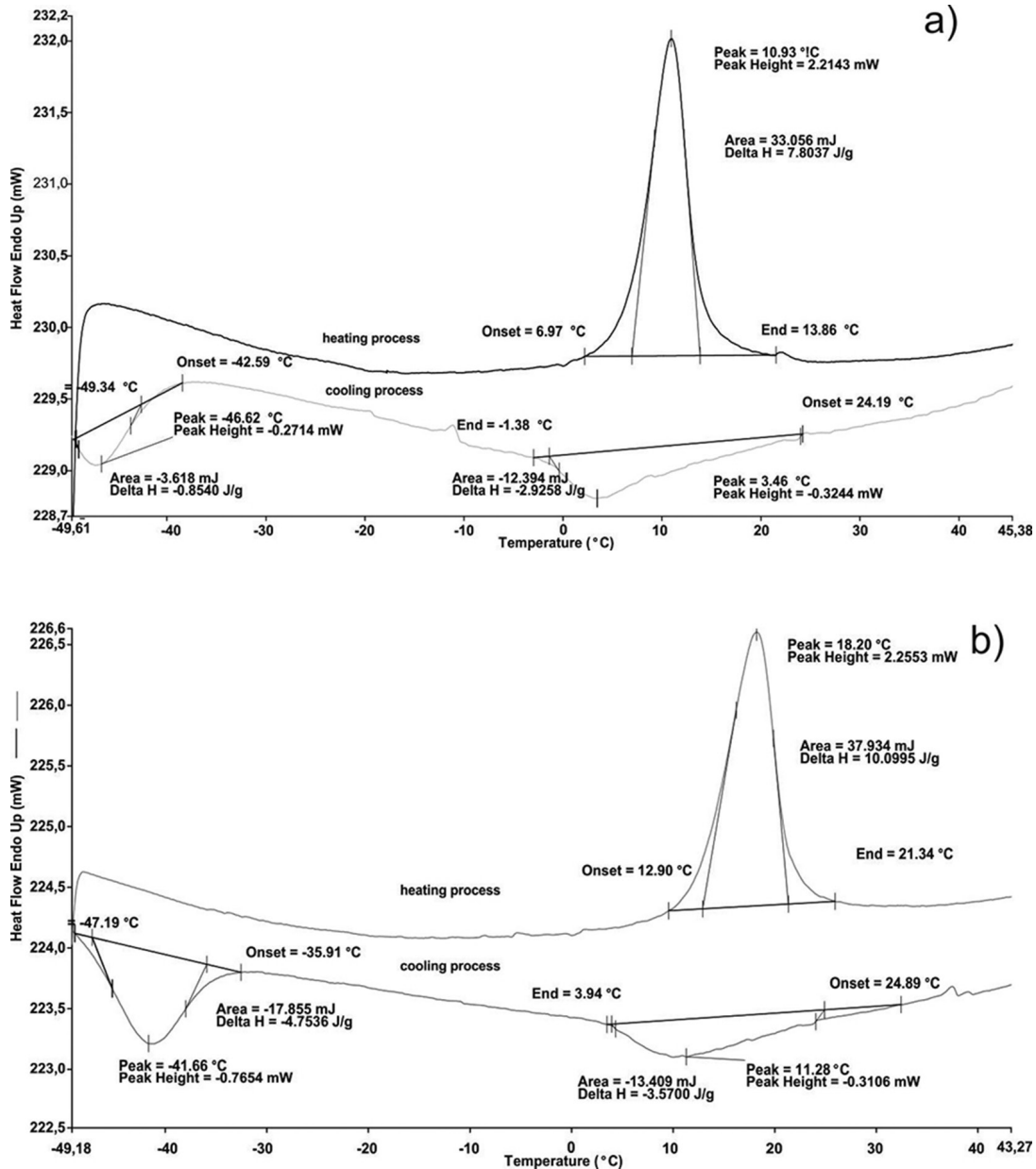
Fig. 4. DSC analyses on Ni-Ti archwires used up to 5 weeks a) and up to 8 weeks b)

CONCLUSION

The results obtained within this study contribute to the establishment of some peculiarities of thermal behavior and the shape-memory effect of the archwires. We have demonstrated that after a prolonged period of time in the patient's month, the archwires have no significant changes in the proportion of elements in the tested wires: Ni – 54.36 +/– 0.8 wt% and Ti – 45.64 +/– 0.8 wt%. The DSC analyses made in the temperature range from –50°C to +50°C and back to –50°C, indicate that Ms temperature for as-received sterilized and used archwires is below –30°C. The results will be useful for clinicians to make a choice for using the proper archwire during treatment.

REFERENCES

1. D. W. Berzinsa, H. W. Roberts, *Dent. Mater.,* **26**, 666-674, (2010).
2. http://www.scielo.br/scielo.php?pid=S2176-94512016000100083&script=sci_arttext
3. C. Ren, Y. Bai, H. Wang, Y. Zheng, S. Li, *Chin. Med. J.*, **121(20)**, 2060-2064, (2008).
4. C. L. Hurst, M. G. Duncanson, R. S. Nanda, P. V. Angolkar, *Am J Ortho. Dent.,* **98**, 72-6, (1990).
5. T. W. Duerig, R. Zadno, *Eng. Asp. of Shape Mem. All.,* 369-93, (1990).
6. G. Airoldi, G. Bellini, C. Di Francesco, *J Phys.*, **14**, 1983-7, (1984).
7. R. J. Moore, J. T. Watts, J. A. Hood, D. J. Burritt, *Eur. J. Orthod.,* **21**, 249–61, (1999).
8. M. C. Biermann, D. W. Berzins, T. G. Bradley, *Angle. Ortho.,* **77**, 499–503, (2007).
9. V. G. Petrov, S. D. Terzieva, V. G. Tumbalev, V. Mikli, L. S. Andreeva, A. K. Stoyanova-Ivanova, *Bul. Chem. Commun.*, **47**, 54–58, (2015).
10. D. J. Fernandes, R. V. Peres, A. M. Mendes, C. N. Elias, *ISRN Dent.,* **2011,** (2011).
11. T. Eliades, A. E. Athanasiou, *Angle Ortho.*,**72**, 3, (2002).
12. W. A. Brantley, T. Eliades, *Ortho. Mater. Sci. Clin. Asp.,* 173–189, (2001).
13. T. Sobottka, F. P. Valarelli, R. H. Cancado, K. M. S. Freitas, D. J. Villarinho, *J App. Oral Sci.*, **22** 109–117, (2014).
14. M. Taya, Y. Liang, O. C. Namli, H. Tamagawa, T. Howie, *Smart Mater. Struct.*, **22**, 10, (2013).
15. T. W. Duerig, K. N. Melton, D. StÖCkel, C. M. Wayman, *Eng. Asp. Shap. Mem. All.*, (1990).
16. W. A. Brantley, M. Iijima, T. H. Grentzer, *Thermochim. Acta*, **392–393**, 1-416, (2002).

ОХАРАКТЕРИЗИРАНЕ НА СТРУКТУРАТА И МОРФОЛОГИЯТА НА ТОПЛОАКТИВИРАЩИ НИКЕЛ-ТИТАНОВИ ОРТОДОНТСКИ ДЪГИ

И. Илиевска[1*], В. Петров[2], Л. Андреева[2], Д. Ковачева[3], А. Залески[4], М. Дрозд[4], Е. Буковска[4], В. Микли[5], А. К. Стоянова-Иванова[1]

[1] *Институт по физика на твърдото тяло „Акад. Георги Наджаков", Българска Академия на Науките*
[2] *Факултет по дентална медицина, Медицински Университет – София, бул. „Св. Георги Софийски" 1*
[3] *Институт по обща и неорганична химия, Българска Академия на Науките*
[4] *Институт по ниски температури и структурни изследвания, Полска Академия на Науките*
[5] *Център за изследване на материали към Талински Технологичен Университет – Талин, Естония*

(Резюме)

Топлоактивиращите никел-титанови (Ni-Ti) ортодонстки дъги са широко използвани в първия етап на ортодонтското лечение. Направени са от сплави които проявяват свойството памет на формата, което се свързва с мартензитна трансформация, проявяваща се при промяна на температурата или механично въздействие (стрес). Целта на това изследване е да се охарактеризира структурата, химичния състав и температури на фазовите преходи на топлоактивиращи никел-титанови ортодонтски дъги при редовната употреба.

За тази цел, три вида топлоактивиращи никел-титанови (Ni-Ti) ортодонстки дъги с размери 0.016" x 0.022" (0.406 x 0.558 mm) бяха изследвани: неизползвани (фабрични), неизползвани автоклавирани и използвани по време на лечение, произведени от фирмата 3M Unitek, Монровия, Калифорния, САЩ. Анализите са проведени със следните методи: рентгенноструктурен анализ (XRD), сканираща електронна микроскопия (SEM), рентгенов микроанализ (EDX) и диференциална сканираща калориметрия (DSC).

Рентгенноструктурният анализ направен при стайната температура показва типични пикове за Ni-Ti сплав с аустенитна тип структура. Фазовите преходи са изучавани с метода на диференциална сканираща калориметрия при температура от –50°C до +50°C. Показано е че при Ni-Ti топлоактивиращи дъги освен аустенит към мартензит преход, има наличие и на междинна R фаза. При процеса нагряване (–50°C до +50°C) тремична фазова транформация се наблюдава при ~12°C. Не са регистрирани допълнителни ендотермични/екзотермични ефекти. При процеса охлаждане, DSC резултатите показват термични фазови преходи при около 10°C се наблюдава формиране на R-фаза, докато при около –40°C, Ni-Ti структура се трансформира до мартензит.

Резултатите получени от енергийно-дисперсиония анализ показват че няма значителни промени на химичния състав на повърхността на изследваните дъги. Сканиращата електронна микроскопия показва промени в морфологията на дъгите след клинично им използване.

Резултатите получени в хода на изследването допринасят за установяване на някои особености в термичното поведение и ефекта на запаметяване на формата на изследваните дъги.

Synthesis and characterization of samarium doped zinc borophosphate glasses

G. I. Patronov*, I. P. Kostova, D. T. Tonchev

Department of Chemical Technology, Plovdiv University "Paisii Hilendarski", 4000 Plovdiv, Bulgaria

This paper is focusing on the synthesis and characterization of the optical, mechanical and thermal properties of samarium doped ZnO-rich borophosphate glasses. Two series of samples have been synthesized – non doped with composition: $(68+x)ZnO - 18B_2O_3 - (14–x)P_2O_5$ and doped – $(67.5+x)ZnO - 18B_2O_3 - (14–x)P_2O_5 - 0.5Sm_2O_3$, where x = 0, 2, 4, 6 mol%. The obtained materials have been investigated by powder X-ray diffraction, differential scanning calorimetry, infrared spectroscopy and photoluminescence analysis. Furthermore, the density has been measured and the chemical durability in acid, neutral and alkaline medium has been determined. The obtained samples are amorphous, homogeneous and transparent glasses except for the samples with the highest content of ZnO. Samarium doped samples exhibit strong visible immediate photoluminescence signal under UV light. The synthesized samarium doped ZnO-rich borophosphate glasses may find applications for preparation of energy converters, solar cells, X-ray dosimeters and for protection of valuable documents.

Key words: zinc borophosphate glasses, samarium doping, x-ray powder diffraction, differential scanning calorimetry, photoluminescence.

INTRODUCTION

The developments of industry and technology in recent decades led to the search and application of new technologies and materials in order to meet the ever increasing economic and environmental demands. The phosphate glasses known for their unique properties such as the wide compositional range of glass forming, high thermal expansion, low melting point, high UV transparency are causing growing interest. Introduction of metal oxides improves their properties and expands the scope of their applications [1, 2]. Additional doping with rare earths elements provides the new materials with unique optical and electrical properties and associated fluorescent effects. These materials have high potential application as an active bearer for laser fibres, optical amplifiers, sensors, LEDs, semiconductors and insulators in optoelectronics and others. Such compositions may be prepared either as stoichiometric compounds or as alloys with a polycrystalline, amorphous or amorphous-crystalline structure [3–8].

In this work we present synthesis and characterization studies of samarium doped ZnO-rich borophosphate glasses. Two series of samples have been synthesized: non doped with a composition $(68+x)ZnO - 18B_2O_3 - (14–x)P_2O_5$ and doped – $(67.5+x)ZnO - 18B_2O_3 - (14–x)P_2O_5 - 0.5Sm_2O_3$, where x = 0, 2, 4, 6 mol%.

EXPERIMENTAL

Sample preparation

All samples were prepared by conventional melt-quenching method. The ratio of the main components (ZnO, B_2O_3 and P_2O_5), the content of the dopant rare earth element (Sm as Sm_2O_3) and the conditions of synthesis and analysis were set on the basis of literature data and our previous studies [2, 9, 10]. The reagents were thoroughly mixed, placed in alumina crucibles and heated at 950 °C for 3 hours in a muffle furnace. Samples were quenched out of the melt to room temperatures and annealed at 250 °C for two hours. The obtained materials are predominantly homogeneous, non-hygroscopic, transparent and easily reproducible glasses as seen in Fig. 1.

---

* To whom all correspondence should be sent:
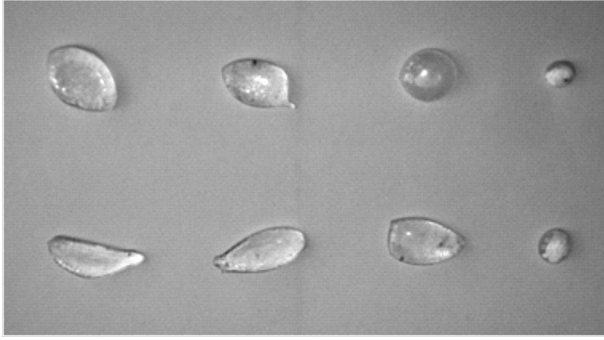E-mail: patron@uni-plovdiv.bg

Fig. 1. Photo of the synthesized doped (upper row – samples 5–8) and non doped samples (bottom row – samples 1–4).

time of 0.2 s/strip (total of 35 s/step). The phase in the XRD patterns was identified using the Diffract Plus EVA v.12 program and ICDD PDF-2 (2009) database – PDF 01-070-8070 (ZnO) [12, 13].

Infrared spectroscopy analysis

The Infrared spectroscopy studies were conducted using the Perkin Elmer 1750 Infrared Fourier Transform Spectrometer.

Differential Scanning Calorimetric analysis

DSC measurements were performed using TA Instruments DSC Q100 and DSC 2910 with attached Fast Air Cooling System (FACS) and Refrigerating Cooling System (RCS). The samples (20–22 mg) were placed in aluminium hermetic pans. A heating rate of 10 K/min was used.

Photoluminescence measurements

The photoluminescence spectra were measured by optical CCD Aventes spectrometer Ave spec – 2048. The set-up consists of a light source, a sample and a detection system. The light source is a combination of a Deuterium and a Halogen lamp, providing a spectrum with the 250–1100 nm range for transmission and absorption measurements and semiconductor light emitting diode (LED), emitting at 395 nm to pump directly the sample under study for photoluminescence measurements.

Analytical procedures:

Density measurements

Density measurements were carried out according to the Archimedes method using deionized water of density $1 g/cm^3$ as an immersion liquid.

Chemical durability

The chemical durability was evaluated from the dissolution rate (D_r) of synthesized samples in alkaline, neutral and acidic aqueous solutions at 98 °C for 1, 2 and 3 hours, correspondingly. The following solutions were used for this purpose – 0,1M NaOH + 0,5M Na_2CO_3 (pH = 12.2), deionized water (pH = 7) and 0,1M HCl (pH = 1). The samples were placed for up to three hours in each solution. The change in weight and area of the samples was reported every hour. The dissolution rate D_r of the respective compositions was calculated from the obtained results:

$$(1) \qquad D_r = \frac{\Delta W}{t}, [g.cm^{-2}.s^{-1}]$$

where ΔW is the weight loss in relation with the surface area of the immersed sample and t is the time that the sample was immersed in the test solution [11].

Powder X-ray diffraction analysis

Structural characterization was carried out by powder X-ray diffraction (XRD) using a Bruker D8 Advance powder diffractometer with Cu – Kα radiation source (l = 1.5406 nm) and Lynx Eye PSD detector. XRD spectra were recorded at room temperature. Data were collected in the 2θ range from 10° to 80° 2θ with a step of 0.04° 2θ and counting

III. RESULTS AND DISCUSSION

List of the synthesized two series zinc borophosphate compositions with theirs thermal (glass transition temperature) and physical properties (density and molar volume) is presented in Table 1. As can be seen from the results, the values of density of the synthesized materials increase with increasing the content of zinc. Samarium doped samples have higher density. Enhancing the density is probably due to the consolidation of the structure of the compositions.

The results obtained for the chemical durability of the synthesized samples are presented in Table 2. Data about the behaviour of the samples in a neutral aqueous solution are not represented. No change has been observed under these conditions and the dissolution rate is equal to zero. The values for the rate of decomposition in an alkaline medium are in the range of 10^{-8} g.cm^{-2}.s^{-1}, which is comparable with the resistance of the phosphate glass [11, 14]. The most significant changes occur in an acid medium, wherein the samples have been dissolved in

Table 1. Composition, thermal and physical properties of samarium doped zinc borophosphate samples

Sample, №	ZnO, mol%	B$_2$O$_3$, mol%	P$_2$O$_5$, mol%	Sm$_2$O$_3$, mol%	Tg, °C	ρ, g/cm^3	V$_m$, cm^3
1	68.00	18.00	14.00	–	535.87	2.262	38.798
2	70.00	18.00	12.00	–	541.79	2.727	31.739
3	72.31	18.00	9.69	–	544.57	2.935	28.940
4	74.00	18.00	8.00	–	534.94	2.907	29.011
5	67.50	18.00	14.00	0.50	544.72	3.921	22.726
6	69.50	18.00	12.00	0.50	551.10	4.236	20.749
7	71.81	18.00	9.69	0.50	533.98	4.433	19.510
8	73.50	18.00	8.00	0.50	533.99	4.889	17.482

Table 2. Dissolution rate (D$_r$) of synthesized samples in alkaline and acidic aqueous solutions at 98 °C for different time

Sample, №	Alkaline resistance			Acid resistance
	D$_{r60}$, g.cm^{-2}.s^{-1}	D$_{r120}$, g.cm^{-2}.s^{-1}	D$_{r180}$, g.cm^{-2}.s^{-1}	D$_{r40}$, g.cm^{-2}.s^{-1}
1	2,7778.10^{-8}	2,7778.10^{-8}	0	9,9904.10^{-5}
2	0	0	0	7,8381.10^{-5}
3	0	0	0	9,2571.10^{-5}
4	0	2,7778.10^{-8}	0	6,7524.10^{-5}
5	0	0	0	6,9208.10^{-5}
6	0	0	0	6,7.10^{-5}
7	2,7778.10^{-8}	2,7778.10^{-8}	0	8,25.10^{-5}
8	0	0	0	7,3083.10^{-5}

less than one hour. It is evident that the synthesized samples are stable both in neutral and in alkaline medium, but are not stable in the acidic medium.

The results obtained from Powder X-ray diffraction analysis show that the samples are predominantly amorphous, except for the samples with the highest content of zinc oxide (Fig. 2). The crystalline phase identified in these samples is indexed as ZnO (PDF 01-070-8070 from ICDD PDF-2 database using DiffractPlus EVA v.12 program (2009)) [12, 13].

Figure 3 presents the infrared spectra of the as-synthesized zinc borophosphate materials – non-doped sample (№1) and doped sample (№8), respectively. The absorption band at about 1250 cm^{-1} is due to the asymmetrical stretching vibration of P = O, the peak around 995 cm^{-1} – vibration of the structural unit BO$_4$. The absorption band at about 730 cm^{-1} is determined by the symmetrical vibration P-O-P, those about 560 cm^{-1} – by stretching vibration P-O- and peaks about 500 cm^{-1} – from the structural unit PO$_4$. The results are in agreement with the existing literature data on the structure of borophosphate glasses [2, 9, 15].

DSC analysis of the as-synthesized glass samples in accordance with XRD results are showing
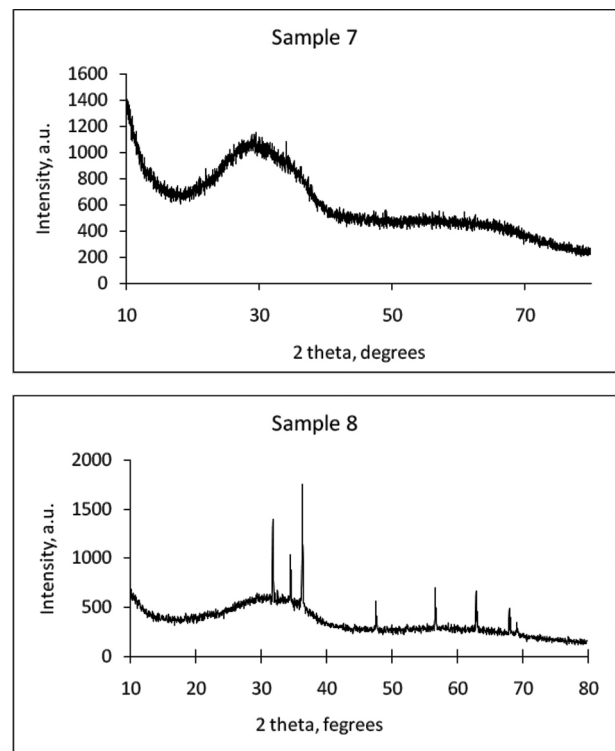
Fig. 2. Powder X-ray diffraction patterns for samples No 7 and No 8.
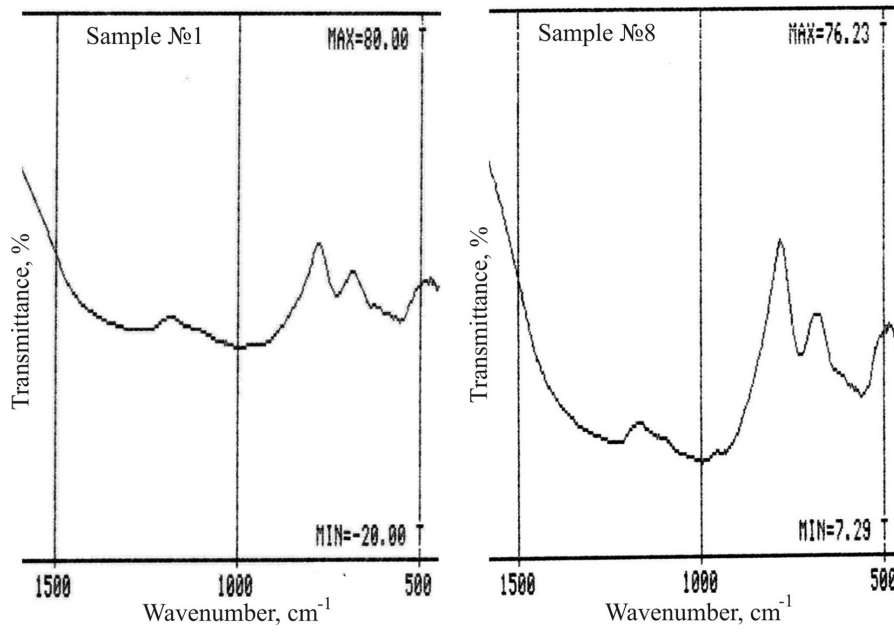
Fig. 3. Infrared spectra of samples №1 and No 8.
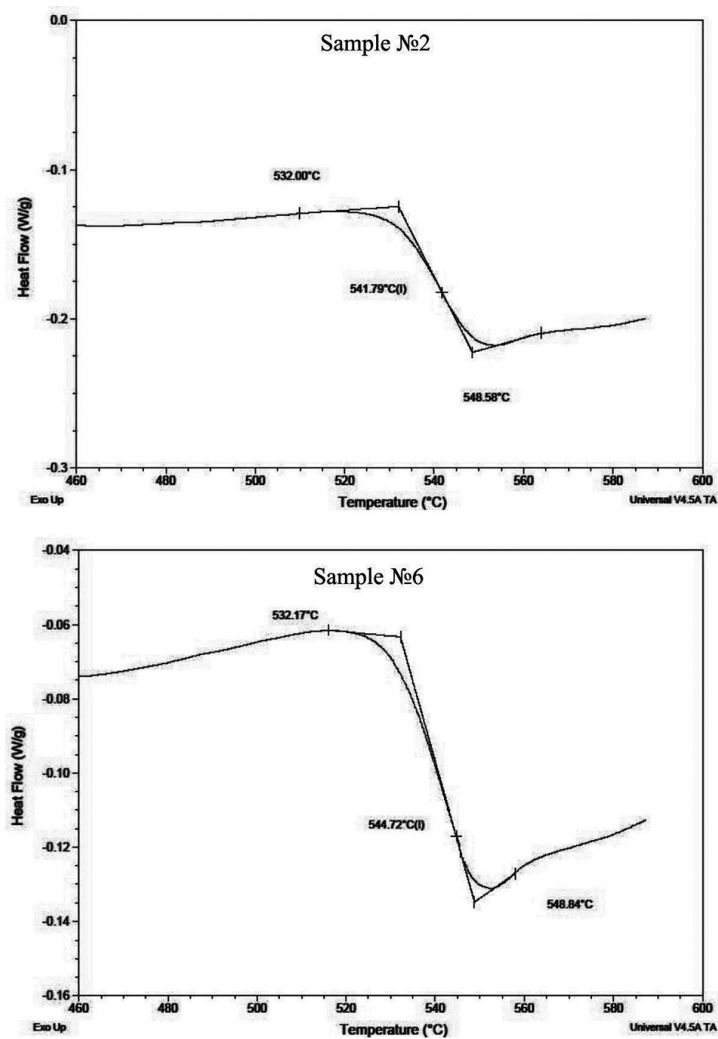
Fig. 4. DSC data of the samples No 2 and No 6.

that partially crystallized samples keep showing an amorphous phase (i.e. it is possible to evaluate glass transition Tg but with reduced relaxation) as shown in Figure 4. The high glass transition temperature is an indication of the stability of the glass (Table 1).

The most efficient LED for pumping the glasses is the one at 395 nm according to our previous research [16]. Representative emission spectra for synthesized samples are illustrated in Fig. 5. The observed spectra depict three pronounced peaks at wavelengths of 560 nm, 600 nm and 645 nm, respectively. There is a fourth peak at 704 nm, which is much less intense than the others. These four peaks are characteristic of Sm^{3+} ions and correspond to transitions [17]:

$$560 \text{ nm} - {}^4G_{5/2} \rightarrow {}^6H_{5/2}$$
$$600 \text{ nm} - {}^4G_{5/2} \rightarrow {}^6H_{7/2}$$
$$645 \text{ nm} - {}^4G_{5/2} \rightarrow {}^6H_{9/2}$$
$$704 \text{ nm} - {}^4G_{5/2} \rightarrow {}^6H_{11/2}$$
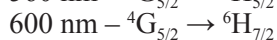
Therefore, samarium ions effectively activate the zinc borophosphate matrix. This evidences the opportunity to use the as-synthesized samarium doped zinc borophosphate compositions for application in optical devices.

Fig. 5. Photoluminescence spectra for doped samples at an excitation wavelength 395 nm.

CONCLUSIONS

Samarium doped ZnO-rich borophosphate glasses with varying content of ZnO have been synthesized and investigated by powder X-ray diffraction, IR spectral analysis, differential scanning calorimetry (DSC) and photoluminescence spectroscopy.

The obtained samples are amorphous, homogeneous and transparent glasses except for those ones with the highest content of ZnO. The data from the IR spectral analysis and the DSC confirmed the results obtained from the XRD analysis.

Samarium doped samples exhibit strong visible (orange to red) immediate photoluminescence (scintillation) signal under UV light.

The content of zinc and doping of materials play an important role in the structural and thermal properties of glass, as evidenced from the presented here results.

The synthesized samarium doped ZnO-rich borophosphate glasses may successfully be applied for preparation of energy converters for solar cells, X-ray dosimeters and for protection of valuable documents.

REFERENCES

1. P. Pascuta, G. Borodi, N. Jumate, I. Vida-Simiti, D. Viorel, E. Culea, *J. Alloys and Compounds*, **504**, 479 (2010).
2. Yong-Seok Kim, Won-Gyu Choi, Bong-Ki Ryu, *Glass Physics and Chemistry,* **40(4)***,* 408 (2014).
3. M. Seshadri, M. Radha, D. Rajesh, L.C. Barbosa, C.M.B. Cordeiro, Y.C. Ratnakaram, *Physica B*, **459**, 79 (2015).
4. Siti Amlah M. Azmi, M.R. Sahar, S.K. Ghoshal, R. Arifin, Journal of Non-Crystalline Solids, 411, 53 (2015).
5. Q. Sheng, Y. Shen, S. Liu, W. Li and D. Chen, *Applied Physics Letters*, 101, 061904 (2012).
6. G. Lakshminarayana, R. Yang, M. Mao, J. Qiu, I. Kityk, *Journal of Non-Crystalline Solids* **355**, 2668 (2009).
7. M. Elfayoumi, M. Farouk, M.G. Brik, M.M. Elokr, *Journal of Alloys and Compounds***, 492**, 712 (2010).
8. M. Elisa, B.A. Sava, I.C. Vasiliu, R. Monteiro, J.P. Veiga, L. Ghervase, I. Feraru, R. Iordanescu, *Journal of Non-Crystalline Solids***, 369**, 55 (2013).
9. Koudelka, P. Mosnerr, *Materials Letters*, **42**, 194 (2000).
10. G. Patronov, I. Kostova, D. Tonchev, *Bulgarian Chemical Communications*, **45(4),** 536 (2013).
11. Meng Xianfeng, Zhang Qitu, Lu Chunhua, Xu Zhongzi, *Journal of rare earths,* **25** 125 (2007).
12. DiffractPlus EVA v.12 program and ICDD (The International Centre for Diffraction Data) PDF-2 database (2009).
13. K. Yoshio, A. Onodera, H. Satoh, N. Sakagami, H. Yamashita, *Ferroelectrics*, **264,** 133 (2001).

14. J. Massera, K.Bourhis, L.Petit, M.Couzi, L.Hupa, M.Hupa, J.J.Videau, T.Cardinal, *Journal of Physics and Chemistry of Solids*, **74** 121 (2013).
15. P. Chen, S. Li, W. Qiao and Y. Li, *Glass Physics and Chemistry*, **37(1)** 29 (2011).
16. I. Kostova, T. Pashova, G. Patronov, D. Tonchev,

T. Eftimov, *Proceedings of ICYS 2013 Plovdiv, Scientific researches of the Union of Scientists in Bulgaria – Plovdiv, Series C. Natural Sciences and Humanities,* **16**, 231 (2013).
17. G. Lakshminarayana, H. Yang, Y. Teng, J. Qiu, *J. Luminesc.,* **129**, 59 (2009).

СИНТЕЗ И ХАРАКТЕРИСТИКА НА ЦИНК БОРОФОСФАТНИ СТЪКЛА, ДОТИРАНИ СЪС САМАРИЙ

Г. И. Патронов, И. П. Костова, Д. Т. Тончев

Катедра Химична технология, Пловдивски университет „Паисий Хилендарски",
4000 Пловдив, България

(Резюме)

Статията насочва вниманието върху синтеза и охарактеризирането на оптичните, механичните и термичните свойства на богати на ZnO борофосфатни стъкла, дотирани със самарий. Синтезирани са две серии проби – недотирани със състав: $(68+x)ZnO – 18B_2O_3 – (14–x)P_2O_5$ и дотирани – $(67,5+x)ZnO – 18B_2O_3 – (14–x)P_2O_5 – 0,5Sm_2O_3$, където x = 0, 2, 4, 6 mol%. Получените материали са изследвани чрез рентгенодифракционен анализ, диференциална сканираща калориметрия, инфрачервена спектроскопия и фотолуминесцентен анализ. Освен това е измерена плътността и определена химическата устойчивост в кисела, неутрална и алкална среда. Получените проби са аморфни, хомогенни и прозрачни стъкла с изключение на тези с най-високо съдържание на ZnO. Дотираните със самарий проби показват силен видим непосредствен фотолуминесцентен сигнал под ултравиолетова светлина. Синтезираните богати на ZnO борофосфатни стъкла, дотирани със самарий, могат да намерят приложение при изготвяне на енергийни преобразуватели, соларни клетки, рентгенови дозиметри и за защита на ценни документи.

Structural study of Tl-exchanged natural clinoptilolite using Rietveld refinement

L. T. Dimowa*, O. E. Petrov, M. P. Tarasov, M. K. Kadiyski

Institute of Mineralogy and Crystallography, Bulgarian Academy of Sciences, "Acad. Georgi Bonchev" str., building 107, 1113 Sofia, Bulgaria

This study presents the exchange of thallium cations in the clinoptilolite channels. Used material is clinoptilolite tuff from Beli Plast deposit, Bulgaria. Fully exchanged thallium forms of HEU–type zeolites have not been reported so far. Here, the ion exchange procedure was performed at 90 °C with 1N solution of $TlNO_3$ for 3 days. The EDS analysis detected major thallium content and small amounts of Ca and Mg. Structural details obtained by PXRD Rietveld refinement reveal thallium positions in the three channels of clinoptilolite microporous structure. Thus, thallium cations are located in three sites: Tl1, (Tl2 and Tl2′ – close to each other), and Tl3 in the channels. Site Tl1 is in the 10-member ring channel A and is occupied by 0.78 Tl cations. This position is shifted towards the centre in comparison with the original sodium position in the channel A. Site Tl2 is in the centre of the 8-member ring channel B, where H_2O molecule usually stays and is occupied by 1.18 Tl cations. A small amount of Tl cations (0.72) are located in site Tl2′ close to Tl2 (distance – 2.42 Å). Site Tl3 with occupation of 2.80 Tl cations is in the 8-member ring channel C near to the original potassium position.

Keywords: clinoptilolite, Tl exchange, Rietveld refinement, EDS.

INTRODUCTION

The mineral group of natural zeolites has a potential for large application and also it is of great interest for crystal-chemical studies related with porous materials [1–3]. The ions exchange is among the important and promising peculiarities of the zeolite porous structure [4]. The spectrum of applications of these minerals covers various branches of industry, ecology, medicine [5–10]. In the exchange process the cations are replaced one another and the incoming ones are integrated and adjusted themselves in various positions into the channel systems. The modified zeolites commonly retain unaffected their microporous structures. The ion-exchanging process in zeolites is typically carried out by replacing Na^+, K^+, and Ca^{2+} with different ions, such as Ag^{2+}, K^+, Cs^+ and Sr^{2+}, etc [11–13]. One of the main methods of purification of toxic and radioactive waste is adsorption deactivation. The most abundant and effective natural zeolite which is used for toxic and radioactive waste-treatment is clinoptilolite. Clinoptilolite has been a focus of researchers for its applications in environmental protection, chemical and other industries because it is stable up to ~650–700 °C and more, and remains unaffected over a wide pH range [14, 15]. Clinoptilolite also has a great potential to keep in its structure toxic and radioactive elements. Different ion-exchanged clinoptilolites are obtained and studied so far [16–23]. Thallium is an extremely toxic metal which contaminates soils and is readily taken up by plants [24]. Fully exchanged thallium forms of HEU–type zeolites have not been reported so far. Detailed description of thallium positions is reported for ZSM5 [25].

The purpose of the present study is to perform structural investigation on the distribution of Tl cations in the structure of ion-exchanged clinoptilolite in order to consider the potential of this zeolite for collector of dangerous polluting cations like Tl^+ and to provide additional crystal-chemical information about the ion-exchange properties of clinoptlolite.

EXPERIMENTAL

The used material is clinoptilolite from Beli Plast deposit, East Rhodopes, Bulgaria.

Ion exchange: 1 g of clinoptilolite, 50 ml 1N $TlNO_3$ solution were placed in a Teflon autoclave

---

and heated at 90 °C for 3 days. The autoclave was shaken 5 times daily and the solution of 1N TlNO₃ was renewed every day. The Tl-exchanged material was filtered, washed with distilled water (6×200 ml) and dried at room temperature. This Tl-exchanged clinoptilolite was labeled as Tl-cpt.

The chemical composition of natural clinoptilolite was obtained by Inductively Coupled Plasma optical emission spectroscopy (ISP-OES) on a Varian Vista MPX CCD.

The chemical composition of Tl-cpt was determined by EDS microanalysis using a ZEISS SEM LS 25 equipped with an EDAX Trident system. The material under study was preliminary pressed into pellet and then coated with carbon. Series of area EDS analyses were performed in a scanning area regime at acceleration voltage of 15 kV. Sanidine (for Al and Si), diopside (for Ca and Mg), hematite (for Fe) were used as standards. There was a problem to find appropriate standard for thallium. In this study, the pure intensity for TlMa line in the standard file was calculated using linear approximation (R²=0.99) of the relationship between the pure intensity of Mα line and atomic number of the neighbour to Tl elements in the periodic table - Au, Hg, Pb and Bi. For these calculations, preliminary measurements of intensity of AuMα, HgMα, PbMα and BiMα lines were carried out in metal Au, cinnabar (HgS), galena (PbS) and bismuthinite (Bi₂S₃), respectively.

The obtained analyses were normalized to 100% in view of the uncertainty of water content as determined by the applied method. Then, the obtained compositions were averaged into one average normalized composition which was further used for processing of X-Ray diffraction data and structural refinement of Tl-cpt.

Powder X-ray analyses: Powder X-ray diffraction (PXRD) data were collected at room temperature on a PANalytical X'Pert MPD diffractometer equipped with a Cu X-Ray source (40 kV/40 mA) and an X'Celerator detector. Automatic divergence slits and 0.02 radian soller slits were used. Patterns were collected from 5 to 80° 2θ with a step size of 0.016° 2θ/step at 5 s/step.

The Rietveld method was applied for structural refinement of the sample Tl-cpt. The unit-cell parameters and the atomic coordinates of extra framework cations and H₂O molecules were refined using Bruker AXS Topas v. 4.0 [26] suite of programs. The background was fitted by a Chebyshev polynomial with 20 coefficients and the pseudo-Voigt peak function was applied for peak modelling. The refinement was conducted with the clinoptilolite structural model of ICSD #37061 [27]

RESULTS AND DISCUSSION

The comparison between natural clinoptilolite powder pattern and Tl-cpt (Fig. 1) reveals that the intensity change of the 020 reflection decreased and approached a negligible value. The line 020 is the most influenced one by cation exchange as it was discussed by Petrov 1995 [28]. The lowering of {F(020)}² can be achieved if clinoptilolite under-
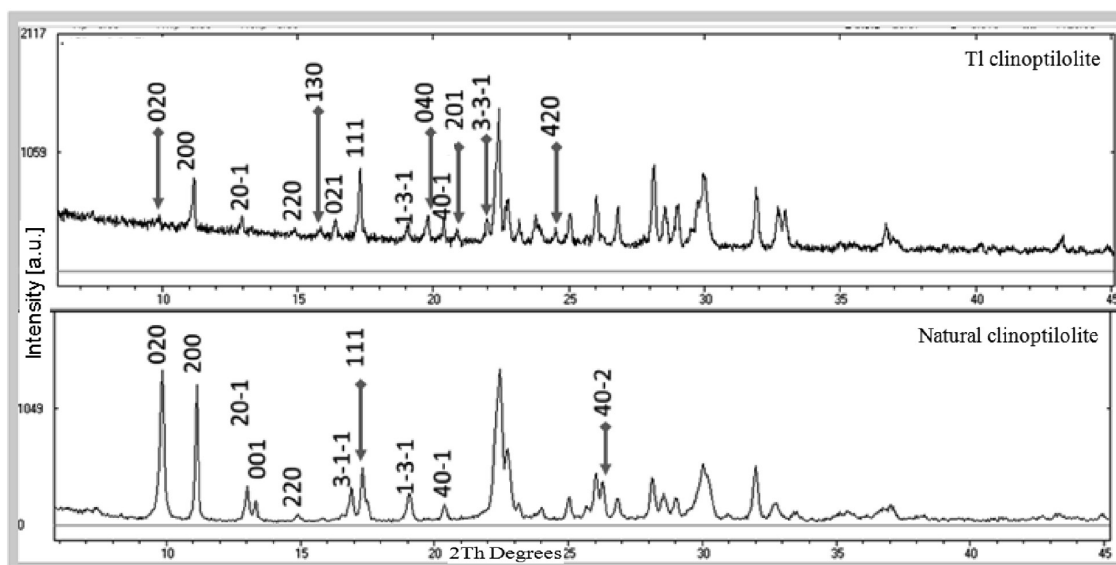

Fig. 1. PXRD patterns of natural (down) and Tl-exchanged clinoptilolite (upper).

goes ion exchange with heavy cations. It was calculated that Tl exhanged cations lower the peak 020 toward zero value of the intensity. Due to the incorporation of Tl cations in the channels other notable differences in intensity of peaks are also observed in the pattern like 001, $3\bar{1}\bar{1}$ and $40\bar{2}$ which decrease (peaks become invisible), while 130, 021, 111, 040, 201, $33\bar{1}$, 420 and others increase their intensity.

The obtained chemical formulae for natural clinoptilolite using ICP OES data is:

$$(Na_{0.23}Ca_{1.83}K_{1.52}Mg_{0.46})Al_{6.31}Fe_{0.07}Si_{29.65}O_{72} \times 20\ H_2O$$

The EDS analysis shows the following composition of the Tl-exchanged clinoptilolite (in wt.%, normalized to 100% without water): SiO_2 – 44.94, Al_2O_3 – 11.64, CaO – 0.90, Tl_2O – 42.00, MgO – 0.20, Fe_2O_3 – 0.32. This composition gives the following crystal chemical formulae of the phase:

$$(Tl_{5.47}Ca_{0.44}Mg_{0.14})Fe_{0.11}Al_{6.32}Si_{29.57}O_{72} \times H_2O.$$
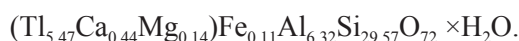
There is a possibility that Mg and Fe are related to mechanical inclusions of other phases. Exclusion of these elements gives the following formulae of the Tl-exchanged clinoptilolite:

$$(Tl_{5.49}Ca_{0.44})Al_{6.34}Si_{29.66}O_{72} \times H_2O.$$

Thus the intensity changes in the PXRD pattern of Tl-cpt and EDS analysis shows that Tl cations almost fully exchange the original cations in clinoptilolite channels.

The structural refinement of clinoptilolite for sample Tl-cpt was performed in several consecutive stages. The first stage of refinement used Tl cations in the extra-framework positions of the model. The framework atomic coordinates were kept fixed. During the next stage of the refinement the extra-framework atomic coordinates were refined and were gradually adjusted to the occupancy obtained from the running refinement and the chemical data. Then, H_2O sites were located and their coordinates and occupancies were also refined. Several times extra-framework and H_2O positions (atomic coordinates) and occupancies were refined and fitted to the experimental data. During the final stage of the refinement isotropic displacement parameters are also refined: first framework positions, then cations and H_2O molecules.

The sites, Wyckoff positions, atomic coordinates, occupancies and isotropic displacement parameters for sample Tl-cpt are listed in Table 1.

The reliability factors and a difference plot showed good agreement between the experimental data and the refined model (Fig. 2, Table 2).

Table 1. Sites, Wyckoff positions, atomic coordinates, occupancies and isotropic displacement parameters Tl exchanged clinoptilolite sample Tlcpt

| Site	Wp	x	y	z	Atom	Occ.	Biso.
T1	8j	0.1794	0.1686	0.0978	Si^{4+}	1	1.4(3)
T2	8j	0.2146	0.4108	0.5063	Si^{4+}	1	1.5(3)
T3	8j	0.2083	0.1912	0.7161	Si^{4+}	1	1.3(3)
T4	8j	0.0668	0.2983	0.4176	Si^{4+}	1	1.5(4)
T5	4g	0	0.2173	0	Si^{4+}	1	1.6(3)
O1	4i	0.1981	0.5	0.4565	O^{2-}	1	1.1(3)
O2	8j	0.2330	0.1213	0.6144	O^{2-}	1	1.7(6)
O3	8j	0.1882	0.1535	0.8902	O^{2-}	1	1.8(4)
O4	8j	0.2304	0.1008	0.2473	O^{2-}	1	1.6(4)
O5	4h	0	0.3257	0.5	O^{2-}	1	1.5(3)
O6	8j	0.0805	0.1614	0.0499	O^{2-}	1	1.8(5)
O7	8j	0.1226	0.2296	0.5515	O^{2-}	1	1.8(5)
O8	8j	0.0142	0.2709	0.1891	O^{2-}	1	1.7(6)
O9	8j	0.2153	0.2492	0.1928	O^{2-}	1	1.8(4)
O10	8j	0.1208	0.3708	0.4225	O^{2-}	1	1.8(6)
Tl1	4i	0.548(1)	0	0.182(2)	Tl^+	0.194(3)	1.5(6)
Tl2	2d	0	0.5	0.5	Tl^+	0.593(4)	1.4(5)
Tl2`	4i	0.515(2)	0	0.190(2)	Tl^+	0.180(4)	2.4(3)
Tl3	4i	0.229(3)	0	0.310(2)	Tl^+	0.701(3)	1.1(3)
O12	4i	0.412(2)	0.5	0.287(2)	O^{2-}	1.003(5)	2.6(4)
O13	8j	0.430(3)	0.085(3)	0.106(3)	O^{2-}	0.501(2)	2.2(5)
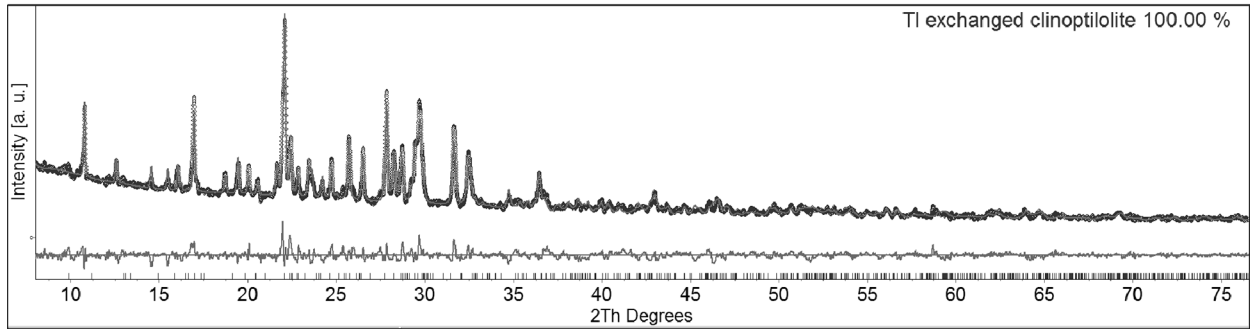
Fig. 2. PXRD difference plot of Tl clinoptilolite.

Structure description and crystal-chemical features of Tl-cpt

Three cationic positions are located in the channels of sample Tl-cpt, namely Tl1, Tl2 (Tl2 and Tl2′ are close to each other) and Tl3 (Fig. 3, Fig. 4). Position Tl1 is in the 10-member ring channel A. This position is shifted toward the centre of the channel in comparison with sodium positions (M1) [29] in the clinoptilolites. The occupation is 0.78 Tl

Table 2. Agreement factors space group and unit cell parameters of Tl-cpt

R_{exp}	6.59	SG	$C2/m$
R_{wp}	7.84	a[Å]	17.696(1)
R_{-p}	5.78	b[Å]	17.949(1)
R_B	4.01	c[Å]	7.412(1)
GOF	1.19	β[°]	116.224(2)
DW	1.12	V[Å]	2112.1(2)
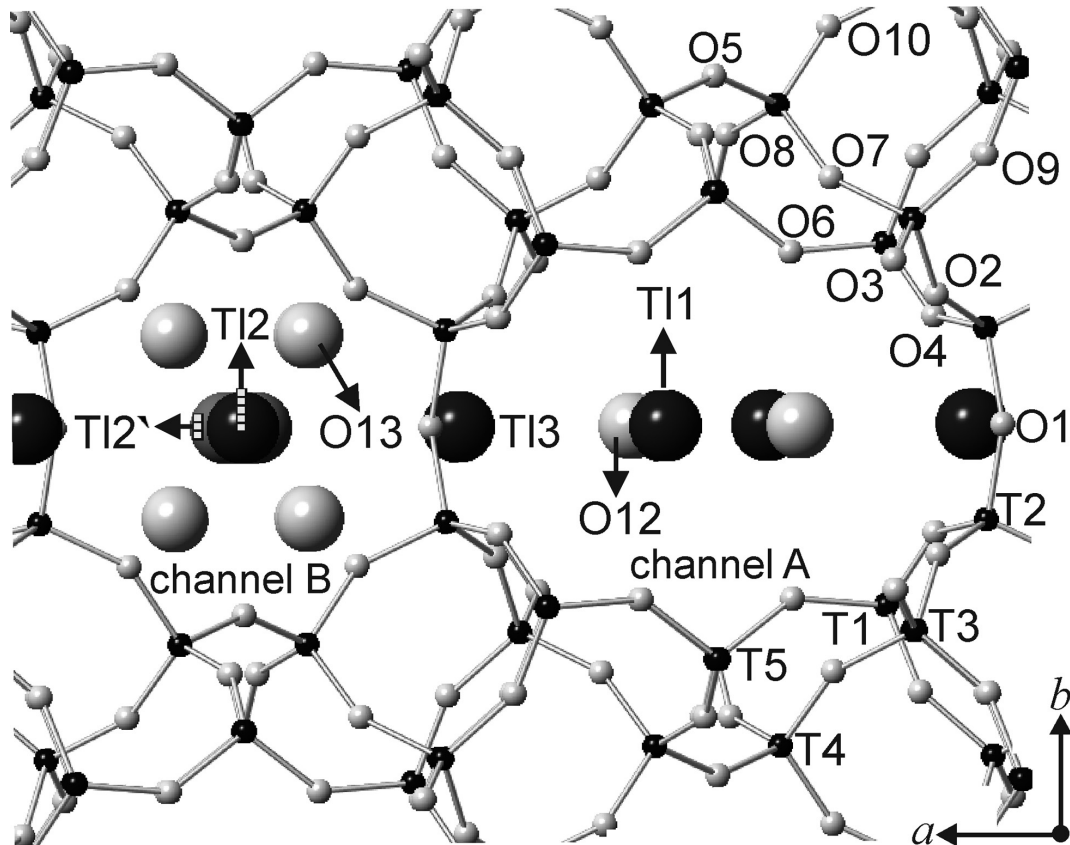
Fig. 3. The tetrahedral framework, positions of cations and H_2O molecules in channel A and B of Tl-exchanged clinoptilolie.
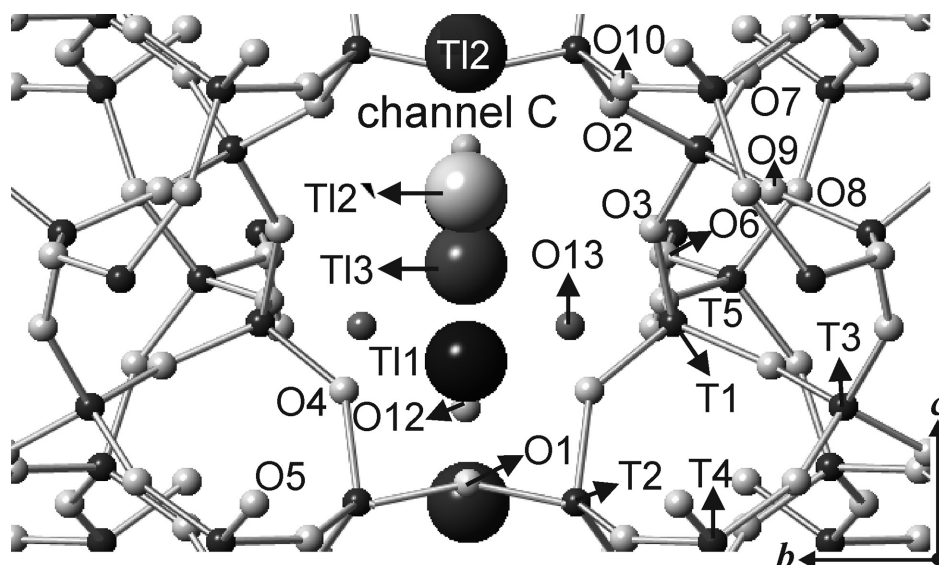
Fig. 4. The tetrahedral framework, positions of cations and H_2O molecules in channel C of Tl-exchanged clinoptilolie.

cations per unit cell. The distances between Tl positions and H_2O molecules as well some of framework oxygen positions are represented in Table 3. The H_2O molecule named O12 (4 molecules per unit cell) coordinate Tl1.

Position Tl2 takes 1.18 Tl$^+$ per unit cell and locates in the centre of channel B where H_2O molecule usually stays [29]. The H_2O molecules in appropriate distance O13 coordinate position Tl2. Small amounts of Tl$^+$ 0.72 per unit cell are detected in site Tl2′ close to Tl2 (at a distance of 2.42 Å) and mutual occupation of Tl2 and Tl2′ is forbidden. Position Tl2′ is coordinated by framework oxygens O1 and O10.

Comparison of ion-exchanged zeolites is important both from fundamental point of view sorption

(structural modification) and utilization properties (sorption of polluting cations in nature). In the case of Cs exchanged clinoptilolite in channel B, Cs cations are located almost close to the centre [30, 31], or just in the centre [32]. Thallium and cesium are large monovalent cations and they tend to show similarity when occupy the channel B.

Position Tl3 is near to site M3 [29] (channel C) where potassium is usually situated and it is the most occupied by thallium cations (2.1 per unit cell) position. Position Tl3 is coordinated by H_2O molecules in positions O12 and O13 (amounting 4 molecules per unit cel).

The Tl-cpt formula obtained by the refinement is:

$$(Tl_{5.5}Ca_{0.42})Al_{6.35}Si_{29.65}O_{72} \times 8.1\ H_2O$$
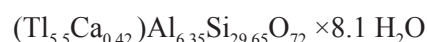
Table 3. Selected bond distances between positions of thallium cations, H_2O molecules and framework oxygen

Atom1	Atom2	No	d(Å)	Atom1	Atom2	No	d(Å)
Tl1	Tl1	1x	2.539(24)	Tl2′	O1	1x	2.956(28)
	O12	1x	2.953(43)		O10	2x	2.999(34)
	O6	2x	3.155(23)		O13	2x	3.162(58)
Tl2	Ti2′	2x	2.426(22)	Tl3	O12	1x	2.942(30)
	O13	4x	3.035(38)		O13	2x	2.961(54)
	O5	2x	3.128(31)		O3	2x	3.053(32)
Tl2′	O13	2x	2.042(49)		O4	2x	3.058(29)
	Tl2	1x	2.425(25)	O13	O8	1x	2.906(38)
	Tl2`	1x	2.628(39)		O13	1x	3.062(68)

CONCLUSIONS

Ion exchange of thallium cations in the clinoptilolite channels is studied on clinoptilolite from Beli Plast deposit, Bulgaria. The exchange proceeds almost totally – 5.5 Tl^+ replace about 90% of the original cations in the channels of clinoptilolite. Structural details obtained by PXRD Rietveld refinement reveal thallium positions in the three channels of clinoptilolite microporous structure. Thallium cations are located in three sites: Tl1 (in channel A), Tl2 and Tl2′ in channel B, and Tl3 in channel C. Such structural investigation on the distribution of Tl cations in the structure of ion-exchanged clinoptilolite is important to consider the potential of this zeolite for collector of dangerous polluting cations like Tl^+ and to provide additional crystal-chemical information about the ion-exchange properties of clinoptlolite towards large monovalent cations.

REFERENCES

1. C. Colella, *Surface Science and Catalysis*, **125**, 641 (1999).
2. R. Gläser, *Chem. Eng. Technol.*, **30**, 5, 557 (2007).
3. G. D. Gatta, V. Kahlenberg, R. Kaindl, N. Rotiroti, P. Cappelletti, M. De' Gennaro, *American Mineralogist*, **95**, 495, (2010).
4. A. Top, S. Ulku, *Applied Clay Science*, **27**, 13 (2004).
5. P. B. Venuto, *Microporous Mater.*, **2**, 297 (1994).
6. W. F. Höderich, H van Bekkum, in: Introduction to Zeolite Science and Practice, H van Bekkum, E. M. Flaningen, J. C. Jansen (eds), Vol. 58, Elsevier – Amsterdam, 1991, p 631.
7. A. Baiker, *Chem. Rev.*, **99**, 453 (1999).
8. J. D. Grunwaldt, R. Wandeler, A. Baiker, *Catal. Rev. Sci. Eng.*, **45**, 1 (2003).
9. K. Takai, T. Ohtsuka, Y. Senda, M. Nakao, K. Yamamoto, J. Natsuoka-Junji, Y. Hirai, *Immunology*, **46**, 2, 75 (2002).
10. T. Tanimoto, K. Nakajima, *Zeolites*, **16**, 1, 82 (1996).
11. A. Langella, M. Pansini, P. Cappelleti, B. de Gennaro, M. de. Gennaro, C. Collela, *Microporous Mesoporous Materials*, **37**, 337 (2000).
12. T. Armbruster, P. Simoncic, N. Dobelin, A. Malsy, P. Yang, *Microporous and Mesoporous Materials*, **57**, 121 (2003).
13. J. Stolz, P. Yang, T. Armbruster, *Microporous and Mesoporous Materials*, **37**, 233 (2000).
14. F. A. Mumpton, *American Mineralogist*, **45**, 351 (1960).
15. J. R. Boles, *American Mineralogist*, **57**, 1463 (1972).
16. E. Uzunova, H. Mikosch, *Microporous and Mesoporous Materials*, **177**, 113 (2013).
17. A. Langella, M. Pansini, P. Cappelleti, B. de Gennaro, M. de. Gennaro, C. Collela, *Microporous and Mesoporous Materials*, **37**, 337 (2000).
18. A. Godelitsas, T. Armbruster, *Microporous and Mesoporous Materials*, **61**, 3 (2003).
19. M. E. Gunter, T. Armbruster, T. Kohler, C. R. Knowles, *Am. Mineral.*, **79**, 675 (1994).
20. O. E. Petrov, L. D. Filizova, G. N. Kirov, *Compt. Rend. Acad. Bulg. Sci.*, **38**, 5, 603 (1985).
21. O. E. Petrov, L. D. Filizova, G. N. Kirov, *Compt. Rend. Acad. Bulg.* Sci., **44**, 12, 77 (1991).
22. L. Dimova, O. Petrov, M. Kadiyski, N. Lihareva, A. Stoyanova-Ivanova, V. Mikli, *Clay Minerals*, 46, 205 (2011).
23. L. T. Dimowa, O. E. Petrov, N. I. Djourelov, B. L. Shivachev, *Clay Minerals*, **50**, 41 (2015).
24. K. Scheckel, R. Hamon, L. Jassogne, M. Rivers, E. Lombi, *Plant and Soil*, **290**, 1, 51 (2007).
25. N. H. Heo, C. W. Kim, H. J. Kwon et al., *J. Phys. Chem.* C **113** (46), 19937 (2009).
26. Topas V4.2: General Profile and Structure Analysis 17. Software for Powder Diffraction. Bruker AXS, Karlsruhe, Germany.
27. E. Galli, G. Gottardi, H. Mayer, A. Preisinger, E. Passaglia, *Acta Crystallographica B*, **39**, 189 (1983).
28. O. E. Petrov, in: Natural Zeolites '93: Occurrence, Properties, Use (Proc. 4th Intern Conf.), D. W. Ming and F. A. Mumpton (eds), International Committee on Natural Zeolites, Brockport, New York, 1995, p. 271.
29. K. Koyama, Y. Takeuchi, *Zeitschrift für Kristallographie*, **145**, 216 (1977).
30. J. R Smyth, A. T. Spaid, D. L. Bish, *American Mineralogist*, **75**, 522 (1990).
31. M. Johnson, D. O'Connor, P. Barnes, C. R. A. Catlow, L. Owens, G. Sankar, R. Bell, S.J. Teat, R. Stephenson, *J. Phys. Chem. B*, **107**, 942 (2003).
32. O. E. Petrov, L. D. Filizova, G. N. Kirov, *Dokl. Bulg. Akad. Nauk.*, **44(12)**, 77 (1991).

СТРУКТУРНО ИЗСЛЕДВАНЕ НА Tl-ОБМЕНЕН ПРИРОДЕН КЛИНОПТИЛОЛИТ С ИЗПОЛЗВАНЕ МЕТОДА НА РИТВЕЛД

Л. Т. Димова*, О. Е. Петров, М. П. Тарасов, М. К. Кадийски

¹ Институт по Минералогия и Кристалография, Българска Академия на Науките, ул. „Акад. Георги Бончев“, бл. 107, София 1113, България

(Резюме)

Изследван е обмен на талиеви катиони в каналите на клиноптилолитовата структура. Използваният материал е клиноптилолит от находище „Бели пласт“, България. Данни за напълно обменени на талий форми от HEU–тип зеолити не са съобщавани досега. Йонният обмен е проведен при 90 °C, с използване на 1N разтвор на $TlNO_3$ в продължение на 3 дни. При EDS анализа е установено значително количество талий и малки съдържания на Ca и Mg. Структурните данни са уточнени чрез PXRD по метода на Ритвелд. Анализът показа талиевите позиции в трите типа канали на клиноптилолитовата микропореста структура. Талиевите катиони са разположени в три позиции: Tl1, (Tl2 и Tl2′ близо една до друга) и Tl3. Позиция Tl1 е в канал A, изграден от 10-членни пръстени и е заета от 0.78 Tl катиони. При сравнение с натриевата позиция (канал A) в природните клиноптилолити, Tl1 се измества в посока към центъра на канала. Позиция Tl2 е в центъра на канал B, изграден от 8-членни пръстени, където обикновено застава водна молекула, и е заета от 1.18 Tl катиони. Малко количество от Tl катиони (0.72) се намира в положение Tl2′, близо до позиция Tl2 (разстояние – 2.42 Å). Позиция Tl3 е със заетост 2.80 Tl катиони. Тя е в канал C, изграден от 8-членни пръстени и се намира близо до калиевата позиция при природните клиноптилолити.

New data on the crystal morphology of brazilianite
(Galiléia, Minas Gerais, Brazil)

R. I. Kostov[1]*, S. Dencheva[2]

[1] University of Mining and Geology "St. Ivan Rilski", Prof. Boyan Kamenov Str., Sofia 1700
[2] Sofia University "St. Kliment Ohridski", 15 Tsar Osvoboditel Blvd., Sofia 1504

Morphology of brazilianite $NaAl_3(PO_4)_2(OH)_4$ crystals from the Galiléia area, Minas Gerais, Brazil (collection Ilia Deleff; Museum of Unique Crystals "Ilia Deleff", University of Mining and Geology "St. Ivan Rilski", Sofia) is studied by goniometry in order to determine the crystal forms. On 29 samples are decribed 25 crystallographic forms, among them 14 new forms. The majority of crystals are single terminated, spearhead-shaped, elongated along the [001] zone, with dominant crystal forms for the majority of the studied crystals: a {100}, b {010}, w {$\bar{2}$01}, i {210}, q {121}, γ {$\bar{2}$21} and δ {$\bar{2}$23}. In several cases are found the faces of the following forms x {$\bar{1}$01}, z {101}, θ {301}, μ {230}, g {$\bar{1}$11}, o {111}, ε {$\bar{3}$21}, ι {253} and ρ {122}. Crystal forms found in single cases are: for sample N4 v {012}; for sample N10 c {001}, ζ {332}, η {546}, κ {$\bar{1}$32}; λ {$\bar{5}$32}; for sample N26 ξ {130}, n {011}; for sample N27 π {223}. A new specific for the area prismatic crystal habit of brazilianite is described – spearhead shaped long-prismatic habit. Brazilianite has a $2a/(b+c)$ = 1.29 ratio, which is representative for the (I)^a structural type, according the crystal habit types of the paragenetic and crystal and chemical systematic of minerals. For the studied crystals the dominant crystal habit can be denoted as (I)$^a_{[001]}$.

Keywords: brazilianite, crystal habit, morphology.

INTRODUCTION

Brazilianite $NaAl_3(PO_4)_2(OH)_4$ has been reported for the first time from the Córrego Frio pegmatites, in the district of Linópolis, Minas Gerais in Brazil [1-6], and later on from several other occurrences in the country [7]: Minas Gerais – Araçuaí pegmatite district – Jenipapo[8], Conselheiro Pena pegmatite district – Divino das Laranjeiras [9], Telírio pegmatite, near Linópolis [5, 8, 10] as well as Gentil, Mendes Pimentel pegmatites [11, 8] and São Geraldo do Baxio pegmatites [8]; Espírito Santo – Santa Teresa and Mantena [12]; Paraíba – Pedra Lavrada – Alto Patrimônio; Rio Grande do Norte – Equador (Alto do Giz pegmatite) and Parelhas (Boqueirão or Boqueirãozinho pegmatite). Beside Brazil, the mineral is reported from pegmatites in several countries worldwide [13]. Brazilianite belongs to the class of phosphates and crystallizes in the $P2_1/n$ space group of the Monoclinic System,

with a=11.233 (6) Å, b=10.142 (5) Å, c=7.097 (4) Å and β=97.37 (2)° [14].

EXPERIMENTAL

Brazilianite crystals and aggregates from the Galiléia pegmatites in the Rio Doce Valley, about 40 km southeast from Governador Valadares, south of Divino das Laranjeiras, Minas Gerais, are on display at the Museum of Unique Crystals "Ilia Deleff" at the University of Mining and Geology "St. Ivan Rilski" in Sofia (labeled Galiléia, Minas Gerais; collection Ilia Deleff). The Galiléia mine area includes also the type locality for brazilianite Córrego Frio mine. The pegmatites belong to the pegmatite district Conselheiro Pena, which is part of the Eastern Brazilian Pegmatite Province in the state of Minas Gerais. Most of the pegmatites in that region are hosted in the quartz biotite-schist of the São Tomé formation linked to the Urucum granite – they are orientated in most cases in the NW-SE direction [8]. Brazilianite is described as a hydrothermal mineral in phosphate-rich zones of the granite pegmatites. The mineral association for the Córrego Frio type

_____

* To whom all correspondence should be sent:
E-mail: rikostov@yahoo.com
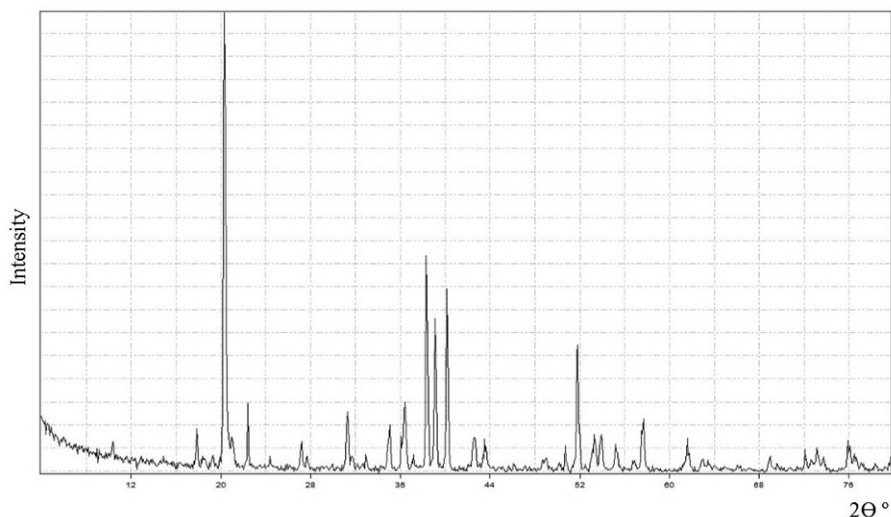
Fig. 1. X-ray powder diffraction of brazilianite

pegmatite is: muscovite, albite, quartz, fluorapatite, souzalite, scorzalite, arsenopyrite, beraunite, childrenite, dufrenite, frondelite, garnet, jahnsite, roscherite, sabugalite, strunzite, tapiolite, tourmaline, uraninite, wyllieite and zircon [5].

Twenty nine brazilianite crystals from the Galiléia area, Conselheiro Pena district, state of Minas Gerais in Brazil were chosen for study. The majority of brazilianite crystals are not double terminated. Most of the brazilianite samples are fragments of crystals or such of a poor termination. They are transparent to semi-transparent (Fig. 2–3). In some of the large brazilianite aggregates the crystals are whitish and not transparent. The brazilianite crystals (University of Mining and Geology – mainly from inv. N K222; Sofia University N M6229), were measured on a optical contact (Optische Universal-Winkelmesser, Carl Zeiss) and one-circle (E. Fluess, Steglitz, Berlin) goniometer to determine crystal morphology. The average dimensions for the largest 16 crystals are: 3.6×2.2×1.3 cm.

X-ray data were received on a TUR-M62 (Faculty of Geology and Geography, University of Sofia "St. Kliment Ohridski") powder diffractometer in the region 2Θ 4–80°, $Co_{K\alpha}$ radiation, 40 kV, 15 mA and on a Bruker-D2 Phaser (with a Diffrac.eva V4.0 search-match software) in the region 2Θ 5–70°, $Cu_{K\alpha}$ radiation, 30 kV, 10 mA (University of Mining and Geology "St. Ivan Rilski").

RESULTS AND DISCUSSION

The X-ray pattern of brazilianite (Fig. 1) corresponds to the standard one [15]. The X-ray patterns of the Palermo and Brazilian material also cor-

respond – for the Palermo mine, New Hampshire, USA d (Å): 5.04 (10), 2.98 (8), 2.73 (8), 2.68 (8), 2.87 (7), 1.44 (5), 3.77 (4) [16]. The X-ray powder pattern in several crystals yielded a peculiarity in the range of 4–64°: the °2Θ diffraction lines 311, 122, 231, 510, 142, 251, 611 and 433 are widened or even doubled in all investigated samples, with additional lines of smaller intensity on lower °2Θ (e.g. on ~31° 2Θ) [8].

Twenty five crystallographic forms were recorded (Table 1). Dominant are the forms: *a* {100}, *b* {010}, *w* {$\bar{2}$01}, *i* {210}, *q* {121}, *γ* {$\bar{2}$21}, and *δ* {$\bar{2}$23} (Fig. 2, 4). Drawings are made with the help

Fig. 2. Brazilianite crystal with double termination faces (sample N5; 4×2×1.5 cm)

Table 1. Distribution of more than one observed crystal forms on the studied brazilianite crystals

N	a {100}	b {010}	w {$\bar{2}$01}	x {$\bar{1}$01}	z {101}	θ {301}	i {210}	μ {230}	q {121}	g {$\bar{1}$11}	o {111}	γ {$\bar{2}$21}	δ {$\bar{2}$23}	ε {$\bar{3}$21}	ι {253}	ρ {122}
1	+		+				+		+			+				
2	+	+	+				+		+			+				
3	+	+	+				+		+			+	+			
4	+		+				+		+		+	+	+			
5	+	+	+				+		+			+	+			
6	+		+				+					+				
7	+		+				+		+		+	+	+	+		
8	+	+	+	+			+		+	+		+	+			
9	+	+	+				+		+			+	+			
10	+						+									
11	+	+	+			+	+		+				+	+		
12	+	+	+	+		+	+		+	+		+	+			
13	+	+	+	+		+	+		+	+		+	+			
14	+		+	+			+		+	+		+	+			
15	+	+	+				+		+			+	+			
16	+		+				+		+			+	+			
17	+	+	+	+			+		+	+		+	+			
18	+	+	+	+			+		+	+		+	+			
19	+		+	+			+		+	+		+	+			
20	+		+				+		+			+	+			
21	+		+	+			+		+			+	+			
22	+		+				+		+			+	+			
23	+		+	+			+		+	+		+	+			
24	+	+	+				+		+				+			
25	+	+	+				+					+				
26	+					+?	+	+								+
27	+					+	+	+								+
28	+	+	+		+	+	+								+	
29	+		+		+	+	+								+	

of a VESTA program [17]. Some faces in the [001] zone are striated along the crystallographic axis *c* or display striations in a curvilinear pattern. All striated forms in the [001] zone exhibit multiple signals. Crystals are typically prismatic, or spearhead-shaped, elongated along the [001] zone, with large faces of the forms *w* {$\bar{2}$01}, *i* {210}, and *γ* {$\bar{2}$21}, and subordinate or rare forms as *a* {100}, *c* {001}, *b* {010}, *q* {121}, as well as *x* {$\bar{1}$01}, *g* {$\bar{1}$11}, *o* {111}, *ε* {$\bar{3}$21}, *ζ* {332}, *η* {546}, *θ* {301}, *ι* {253} and *z* {101}. The front (1st) pinacoid *a* {100} and 2nd pinacoid *b* {010} are represented by elongated narrow faces in the prism zone. The basal (3rd) pinacoid *c* {001}, as a tiny face, is rarely observed. Two brazilianite crystals (N28-29) display a similar prismatic zone morphology with the majority of crystals, but with a different termination including forms *θ* {301}, *ι* {253} and *z* {101}. They can represent a morphological subtype (Fig. 3, 5). Sample N10 also displays a different bipyramidal-type habit. In several cases are found the faces *x* {$\bar{1}$01},

Fig. 3. Brazilianite crystal with single termination faces (rare crystal habit; sample N1; 4×3×2 cm)

Fig. 4. Drawing of a typical crystal habit with common crystal forms for the majority of the studied brazilianite crystals in standard orientation (VESTA program)

Fig. 5. Drawing of the rare crystal habit for brazilianite (VESTA program)

z {101}, θ {301}, μ {230}, g {$\overline{1}$11}, o {111}, ε {$\overline{3}$21} ι {253}, and ρ {122}. Crystal forms found in single cases are: for sample N4 v {012}; for sample N10 c {001}, ζ {332}, η {546}, κ {$\overline{1}$32} and λ {$\overline{5}$32}; for sample N26 ξ {130} and n {011}; for sample N27 π {223}.

In the first publication on brazilianite 18 crystal forms have been distinguished, but some crystallographic descriptions (as "bipyramid"; "dome") turn to be incorrect, including the spherical coordinates for the m {110} form [1]. Several different habits of investigated brazilianite crystals have been distinguished, primarily on the basis of the elongation and orientation of the crystal, but relative development of the forms was considered as well [8]: the first group of crystal habits is represented by the elongation along [101] (this group could be divided into four subgroups on the basis of different form development); the second habit is represented with crystals from the Jenipapo pegmatite, Araçuaí district, which are elongated along [001] and terminated with a large {011} form, giving the crystal the form of a sharp column; the third group (new habit)

is represented with crystals from the Gentil pegmatite (G5) and the São Geraldo do Baixio group (S1) – the crystal S1 is tabular, flattened along [001] with a large development of {101}, while crystal G5 exhibits a similar, although slightly less flattened habit; the fourth group (new habit) is represented by a crystal from the São Geraldo do Baixio group (S3) which appears somewhat isometric, due to the large development of {110} prism as well as {010}; the fifth group is represented with crystals from the Rapid Creek, Yukon, Canada, with an extremely elongated along [001] crystal habit.

In another morphological overview four types of crystal habits are distinguished: short-prismatic to the c-axis with the crystal forms {100}, {010} and {110} parallel to the c-axis ("Brazil habit"); short-prismatic to the a-axis with crystal forms {100}, {110}, {$\overline{1}$01}, {$\overline{3}$01}, {011}, {111}; "dipyramidal" on the a-axis with crystal forms {011}, {111} ("Palermo habit"); "dipyramidal" on the c-axis [13].

The arrow-like or spearhead shaped prismatic habit is also a new crystal habit among the described brazilianite habits from Brazil. Such prismatic habit can be placed between the S3 short prismatic brazilianite type habit from São Geraldo do Baixio group pagmatites in Brazil and the extremely long prismatic habit of crystals from Rapid Creek area, Yukon, Canada [8].

According to its structural anisometricity, brazilianite can be regarded as of a pseudo-isometric type structure – one can compare the forms of the similar in symmetry monacite-(Ce) in the monoclinic system [18]. The structure of brazilianite with a $2a/(b+c) = 1.29$ ratio is representative for the $(I)^a$ structural type. For the studied crystals the dominant crystal habit can be denoted as $(I)^a_{[001]}$ according the crystal habit types of the paragenetic and crystal and chemical systematic of minerals [18].

CONCLUSIONS

Goniometric studies of 29 crystals of brazilianite from the Galiléia area (Minas Gerais, Brazil) revealed 25 crystallographic forms, among them 14 new forms. The majority of crystals are single terminated, spearhead-shaped, elongated along the [001] zone, with dominant crystal forms a {100}, b {010}, w {$\bar{2}$01}, i {210}, q {121}, γ {$\bar{2}$21} and δ {$\bar{2}$23}. In several cases are found the forms x {$\bar{1}$01}, z {101}, θ {301}, μ {230}, g {$\bar{1}$11}, o {111}, ε {$\bar{3}$21}, ι {253} and ρ {122}, and in single cases the forms v {012}, c {001}, ζ {332}, η {546}, κ {$\bar{1}$32}; λ {$\bar{5}$32}, ξ {130}, n {011} and π {223}. A new specific for the area prismatic crystal habit of brazilianite is described – spearhead-shaped long-prismatic habit, denoted as $(I)^a_{[001]}$.

REFERENCES

1. F. H. Pough, E. P. Henderson, *American Mineralogist,* **30**, 572 (1945).
2. M. Godoy, *Min. e Met.*, **8**, 385 (1945).
3. C. Palache, H. Berman, C. Frondel, Dana's System of Mineralogy, John Wiley, New York, 1951.
4. J.-P. Cassedanne, *Revue de Gemmologie*, **68**, 9, 14 (1981).
5. J.-P. Cassedanne, *Mineralogical Record*, **14**, 227 (1983).
6. R. B. Cook, *Rocks & Minerals*, **75**, 40 (2000).
7. C. Cornejo, A. Bartorelli, Minerals and Precious Stones of Brazil, Solaris, Sao Paulo, 2010.
8. A. Čobić, V. Zebec, R. Scholz, V. Bermanec, S. de Brito Barreto, *Natura Croatica,* **20**, 1 (2011).
9. V. Bermanec, N. Tomašić, G. Kniewald, R. Scholz, G. M. Da Costa, A. H. Horn, J. Karfunkel, *32nd International Geological Congress, Abstracts, Part 1, Firenze, IUGS,* 215 (2004).
10. G. D. Gatta, P. Vignola, M. Meven, R. Rinaldi, *Amer. Mineral.*, **98**, 1624 (2013).
11. M. L. de Sa C. Chavez, R. Scholz, *Geociencias, REM: R. Esc. Minas*, **61**, 141 (2008).
12. G. Niedermayr, *Ann. Naturhistor. Mus. Wien*, **76**, 605 (1972).
13. K.-L. Weiner, R. Hochleitner, *Lapis*, **22**, 1, 8 (1997).
14. B. M. Gatehouse, B. K. Miskin, *Acta Cryst.*, **30**, 1311 (1974).
15. JCPDS International Center for Diffraction Data, Power Diffraction File, Swarthmore, PA, 1991.
16. C. Frondel, M. L. Lindberg, *Amer. Mineral.*, **33**, 135 (1948).
17. K. Momma, F. Izumi, *J. Appl. Crystallogr.*, **44**, 1272 (2011).
18. I. Kostov, R. I. Kostov, Crystal Habits of Minerals (Bulgarian Academic Monographs, 1), Co-published by Pensoft Publishers and Prof. Marin Drinov Academic Publishing House, Sofia, 1999.

НОВИ ДАННИ ВЪРХУ КРИСТАЛОМОРФОЛОГИЯТА НА БРАЗИЛИАНИТ (ГАЛИЛЕЯ, МИНАС ЖЕРАИС, БРАЗИЛИЯ)

Р. И. Костов[1], С. Денчева[2]

[1] *Минно-геоложки университет „Св. Иван Рилски", ул. „Проф. Боян Каменов", 1700 София*
[2] *Софийски университет „Св. Климент Охридски", бул. „Цар Освободител" № 15, 1504 София*

(Резюме)

Изучена е кристаломорфологията на 29 кристали от бразилианит $NaAl_3(PO_4)_2(OH)_4$ от района Галилея в щат Минас Жераис в Бразилия (колекция на Музея на уникалните кристали „Илия Делев" при Минно-геоложкия университет „Св. Иван Рилски", София). Установени са 25 кристални форми, от които 14 нови кристални форми. Повечето от бразилианитовите кристали са еднокрайни, копиевидно оформени, удължени по [001] зоната, с доминиращи кристални форми i {210}, a {100}, w {$\bar{2}$01}, γ {$\bar{2}$21}, q {121}, δ {$\bar{2}$23} и b {010}. Описан е нов дългопризматичен хабитус за този минерал, който съгласно парагенетичната и кристалохимичната класификация на минералите може да се отнесе към $(I)^a_{[001]}$ хабитусния тип.

Powder XRD microstructural analysis of thermally treated synthetic fluor-hydroxylapatite

V. V. Kostov-Kytin[1]*, V. Petkova[1,2], T. Kaljuvee[3]

[1] *Bulgarian Academy of Sciences, Institute of Mineralogy and Crystallography, 1113 Sofia, Acad. Georgi Bonchev Str., Bl. 107, Bulgaria*
[2] *New Bulgarian University, Department of Natural Sciences, 21 Montevideo Str., 1618 Sofia, Bulgaria*
[3] *Tallinn University of Technology, Lab. of Inorg. Materials, Ehitajate tee 5, 19086, Tallinn, Estonia*

Samples of nano-sized synthetic Fluor-hydroxylapatite (SFHA) heated within the temperature range 400–910 °C are studied by powder X-ray diffraction (PXRD) analysis. Description of the microstructural characteristics at different temperatures as well as their evolution during the thermal treatment is in the focus of the investigations. The analysis of diffraction-line broadening is performed using Rietved refinement and applying various size and strain models to handle the distinct anisotropy observed in certain crystallographic directions. Trends and consistencies of patterns in terms of domain sizes and microstrain have emerged for the studied material upon heating. The obtained results are explained and interpreted in the light of the up-to-date views and theories on crystal growth and imperfections and modern PXRD microstructural approaches.

Keywords: apatite, Rietveld refinement, microstructural analysis, crystal growth.

INTRODUCTION

Apatite is the name of a group of phosphate minerals, usually referring to hydroxylapatite – $Ca_{10}(PO_4)_6(OH)_2$, fluorapatite – $Ca_{10}(PO_4)_6(F)_2$, and chlorapatite $Ca_{10}(PO_4)_6(Cl)_2$ [1]. As a major source of phosphorus for the plants its primary use is in the manufacture of fertilizer for the purposes of agriculture. Synthetic hydroxylapatite and fluorapatite have been extensively used as a bone implant material, because of its similarity with human bone composition and ability to form strong bond to the human hard tissue. Prior to bringing into use both natural and synthetic representatives of these materials are frequently subjected to various procedures like mechanoactivation and heating in order to improve their functionality and properties. Numerous investigations have contributed to obtain better knowledge about the apatite crystal structure, its compositional diversity and thermal stability [2, 3]. The following structural and physicochemical features of this material are of interest for the present study: i) the apatite structure can be presented as sheets lying in the (001) plane and comprising approximate hexagonally packed spheres each one represented by a tetrahedral PO_4^{3-} ion and containing also two different sized holes, the larger ones, where Ca^{2+}, reside being midway between the sheets [3]; ii) like all phosphate compounds, apatite refers to the anisodesmic compounds, which is a prerequisite for the emergence of zones of weak bonding along certain crystallographic planes and directions; iii) the apatite structure is known to manifest weak and imperfect cleavage along {001} and {100}.

Unlike the structural and macro-structural characterization of apatite less attention has been paid to the description and quantification of its microstructural parameters like crystallite size and various lattice imperfections for better understanding this material evolution upon various treatments in the nanoscale range.

Powder X-ray diffraction (PXRD) has actively come into use for the purposes of microstructural analysis during the last decades. An intrinsic feature of the XRD line profile analysis originating from its physical grounds is that it gives information for the bulk properties of a powder or a polycrystalline solid. When the PXRD data are processed by a software package involving the facilities of Rietveld refinement the obtained results provide information as

---

* To whom all correspondence should be sent:
E-mail: vkytin@abv.bg

for the crystal-chemical changes, phase transitions, and quantity of phases as well as for certain microstructural characteristics of the investigated crystalline matter like the coherently diffracting domain sizes and the microstrains distribution. Although the inspection of the line broadening is not yet a standard and universally adopted procedure, various size and strain models can be tested including also anisotropy of the microstructural distribution in terms of the reciprocal lattice vectors.

Apatite microstructural characteristics have already been object of investigation by local methods and PXRD.

Studying the effects of nanoindentation on natural and synthetic apatite crystals Chaikina has summarized that the greatest concentration of dislocation sites marked by the amount of etch pits as manifestation of their outlet is on the faces of dipyramides {10–11} and prism {10–10} [4]. Only isotropic, predominantly structureless size and strain models have been applied in the majority of works where PXRD analysis is applied to study the microstructural characteristics of apatite [5–8]. In their work Lala et al. [9] have focused attention on the pertinent explanation of the crystal growth mechanism of β-TCP on the account of nanocrystalline hydroxyapatite (HAp) upon its sintering to 1000 °C. They have also provided data for the anisotropy of the size and strain characteristics. Certain contradictions however emerge between the illustrative material presented by these authors and the interpretation of the obtained results e.g. their statement that "The maximum particle size is found along the plane (002) which is exactly perpendicular to c axis. Whereas, the planes parallel to c-axis have small particle sizes indicating the hindrance of growth of such planes parallel to c-axis" vs. the evidenced by the HRTEM images of a nano-sized HAp single crystal elongation along [002] in Fig 7b (inset) and data in Table 1 [9].

A well-known fact for the specialists in materials science is that heat treatment alters the physical properties of a material and is often accompanied by decrease of strain and stress in terms of various kinds of point, linear, and plane defects and increase of crystallite size. First attempts in terms of XRD to develop a phenomenological line-broadening theory were made referring to plastically deformed metals and alloys [10, 11]. The theory identifies two main types of diffraction line broadening: the size and strain components. The former depends on the size of coherent domains, which is not limited to the grains but may include effects of stacking and twin faults and small-angle boundaries caused by any lattice imperfection (dislocations and different point defects). The theory is general and was successfully applied to other materials, including oxides

and polymers. In 2008, T. Ungár [12] has presented the dislocation model of strain anisotropy postulating that strain broadening can only be caused by dislocation-type lattice defects. On the other hand, from the theories of crystal growth it is known that the growth rate of the entire face is determined by the driving force at the point of emergence of the predominant point of growth (e.g. a dislocation, a foreign particle, or crystal twin) [13]. Thus, the dislocations spatial distribution and migration ability on the account of atomic bonds rearrangement that may occur upon heating of a crystalline material is closely related and can provoke crystal growth in certain crystallographic directions.

This study presents results from the microstructural characterization of nanosized synthetic Fluor-Hydroxylapatite performed using the facilities of the FullProf (FP) program [14] on collected PXRD patterns of samples heated within the temperature range 400–910 °C. Isotropic and various anisotropic size and strain models have been applied in order to achieve best whole profile fitting (WPF). Crystal-chemical control has been hold in all stages of the refinement. Certain trends and consistencies of patterns in terms of domain sizes and microstrain anisotropic appearance have emerged for the studied material upon heating and explanation for them is suggested in the light of the existing theories and models for crystal growth and deformations.

EXPERIMENTAL

Synthesis

Synthetic Fluor-HydroxylApatite (SFHA) was synthesized using a procedure reported by Nathanael *et al.*, (2013) with only minor variations [15]. Calcium nitrate $(Ca(NO_3)_2.4H_2O)$ and ammonium dihydrogen phosphate $((NH_4)H_2PO_4)$ instead of $((NH_4)_2HPO_4)$ were used as calcium (Ca) and phosphate (P) sources, respectively. Both sources mixed separately with distilled water were prepared in a way as to maintain the overall Ca/P ratio equal to 2. Ammoniumfluoride (NH_4F) was dissolved in water and added to the phosphate containing solution as a fluorine (F) source keeping the ratio P/F = 2. The pH of the phosphate containing solution was increased to 9 by adding ammonium hydroxide (30%). During the reaction the phosphate containing solution was added dropwise into the calcium containing solution with vigorous stirring for 1 h. The mixed solution was transferred to the Teflon beaker of the stainless steel autoclave and placed in the oven at 180 °C for 16 h. After the reaction the autoclave was cooled down to room temperature and the final precipitate was washed several times

with distilled water and ethanol and dried at 100 °C overnight.

Subsequently, portions of the as-synthesized material were heated in an oven at equal temperature intervals chosen in accordance with the TGA-DTG-DTA data up to 400 °C; 530 °C; 660 °C; 790 °C; and 910 °C, kept for 2 hours each one and cooled gradually to room temperature.

Analytical Procedure

Powder X-ray diffraction patterns of the samples were collected using a Bruker D2Phaser diffractometer with Ni-filtered CuKα radiation in the 2θ range from 5 to 70° and in a step-scan regime (step 0.015° and time 10 s per step). Thermogravimetric and differential thermal analyses (TGA-DTG-DTA) were performed on a SETSYS2400 thermal analyzer (SETARAM, France) in the temperature range 20–1200 °C, at a heating rate of 10 °C.min^{-1} in static air.

Structure and microstructural refinements

The theoretical XRD pattern has been simulated with Fluor-HydroxylApatite (FHA) (ICSD # 182890, hexagonal, S. G. P63/m, a = 9.3970 Å, c = 6.8820 Å) [16, 17].

The microstructural effects within FullProf [14] are treated using the Voigt approximation: both instrumental and sample intrinsic profiles are supposed to be described approximately by a convolution of Lorentzian and Gaussian components. The TCH pseudo-Voigt profile function is used to mimic the exact Voigt function. The integral breadth method to obtain volume averages of sizes and strains is used to output a microstructural file where an analysis of the size and strain contribution to each reflection is written if the user has provided an input file containing the instrumental resolution function (IRF) [18].

Initially, the crystal structures of the SFHA samples heated at different temperatures have been refined without applying any microstrucutral model just to confirm the materials phase purity and plausibility of the final crystal-chemical parameters. No substantial changes in the reflection positions or appearance of new ones have been detected and it is assumed that within the studied temperature interval the material has not undergone structural transformations or phase transitions. The profile parameters obtained for the sample heated to 910 °C have been incorporated in an IRF file that has later been used for the microstructural analysis.

Several isotropic size and strain models in terms of the Gaussian and Lorentzian components of the profile have been checked for each sample and the best results in terms of reliability factors and crys-

tal-chemical plausibility are presented in the following section. Subsequently, the WPF continued with applying the General Size formulation model: Generalised size parameters (quadratic form) and preserved isotropicity of the Lorenzian strain model. Finally, pattern fitting has been performed using the Generalized Strain formulation model: Anisotropic Lorenzian Size Broadening Spherical Harmonics (SH) and Strain Broadening Model (quartic form). This actually presents a refinement procedure with simultaneous application of anisotropic size and anisotropic strain models in it. In all cases, the whole pattern fitting procedures have ended including in the refinement all those structural and profile parameters that would allow checking the plausibility of the obtained crystal-chemical characteristics.

RESULTS

Figure 1 gives notion about certain crystallographic planes and directions in apatite crystals being of interest for this study. Figure 2 demonstrates the anisotropy of line broadening, as well as the advantages of the anisotropic model used as compared with the isotropic one in the WPF procedure. Table 1 presents selected structural parameters of the studied samples obtained according to the applied refinement procedure and size and strain models using FullProf. The standard deviations appearing in the global average apparent size and strain is calculated
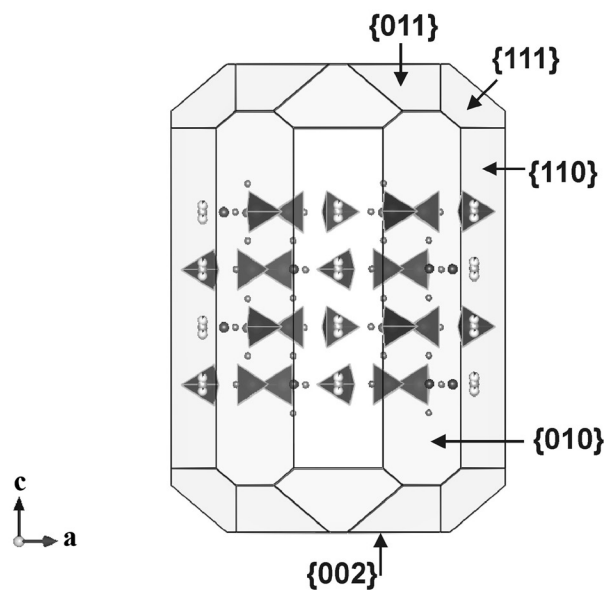
Fig. 1. Some of the most abundant forms of apatite crystals: pinacoid {002}; first-order prism {010}; second-order prism {110}; first-order dipyramid {011}; second-order dipyramid {111}.

Table 1. Selected structural parameters of the studied samples obtained according to the applied refinement procedure and size and strain models using FullProf (FP)

Samples of synthetic fluor-hydroxyl apatite (SFHA)

FP pattern fitting without microstructural model – Standard approach

	As-synth	400 °C	530 °C	660 °C	790 °C	910 °C
Lattice	$a = b = 9.3886(14)$ Å $c = 6.8914(11)$ Å $V = 526.1(1)$ Å³ *ATZ= 1041.277	$a = b = 9.3750\,(9)$ Å $c = 6.8852\,(7)$ Å $V = 524.1(1)$ Å³ ATZ= 1035.852	$a = b = 9.3670(6)$ $c = 6.8872(5)$ $V = 523.6(1)$ Å³ ATZ= 1036.590	$a = b = 9.3703(4)$ Å $c = 6.8849(3)$ Å $V = 523.5(0)$ Å³ ATZ= 1019.408	$a = b = 9.3705(3)$ Å $c = 6.8850(2)$ Å $V = 523.6(0)$ Å³ ATZ= 1002.544	$a = b = 9.3704(1)$ Å $c = 6.8833(1)$ Å $V = 523.4(0)$ Å³ ATZ= 1003.352
Fit	$\chi^2 = 2.572$ Rp = 17.3 Rwp = 21.9 Bragg R-factor = 4.99	$\chi^2 = 1.944$ Rp = 15.1 Rwp = 17.9 Bragg R-factor = 3.07	$\chi^2 = 1.73$ Rp = 14 Rwp = 16.7 Bragg R-factor = 2.89	$\chi^2 = 1.457$ Rp = 12.7 Rwp = 15.3 Bragg R-factor = 2.51	$\chi^2 = 1.309$ Rp = 11.5 Rwp = 14.3 Bragg R-factor = 2.81	$\chi^2 = 1.618$ Rp = 12.5 Rwp = 15 Bragg R-f-r = 3.41

FP pattern fitting with Isotropic Lorenzian size (Å) and Lorenzian strain model (10^{-4})

	As-synth	400 °C	530 °C	660 °C	790 °C	910 °C
Lattice	$a = b = 9.3902(5)$ Å $c = 6.8927(4)$ Å $V = 526.3(1)$ Å³	$a = b = 9.3730(10)$ Å $c = 6.8879(8)$ Å $V = 524.1(1)$ Å³	$a = b = 9.3697(3)$ Å $c = 6.8872(2)$ Å $V = 523.6(0)$ Å³	$a = b = 9.3705(2)$ Å $c = 6.8852(1)$ Å $V = 523.6(0)$ Å³	$a = b = 9.3705(3)$ Å $c = 6.8852(2)$ Å $V = 523.5(0)$ Å³	$a = b = 9.3703(1)$ Å $c = 6.8830(1)$ Å $V = 523.4(0)$ Å³
Fit	$\chi^2 = 2.130$ Rp = 16.1 Rwp = 19.3 Bragg R-factor = 3.84	$\chi^2 = 3.418$ Rp = 18.5 Rwp = 22.5 Bragg R-factor = 4.38	$\chi^2 = 1.727$ Rp = 14 Rwp = 16.6 Bragg R-factor = 2.92	$\chi^2 = 1.476$ Rp = 12.7 Rwp = 15.2 Bragg R-factor = 2.52	$\chi^2 = 1.341$ Rp = 11.6 Rwp = 14.4 Bragg R-factor = 2.93	$\chi^2 = 4.949$ Rp = 22.7 Rwp = 25.8 Bragg R-f-r = 6.36
Size/Strain	App. Size = 212.65 (0.25) Max Strain = 12.280 (0.0078)	App. Size = 145.86 (0.16) Max Strain = 41.473 (0.0494)	App. Size = 289.21 (0.20) Max Strain = 11.745 (0.0175)	App. Size = 456.42 (0.50) Max Strain = 7.2754 (0.0044)	App. Size = 790.93 (0.70) Max Strain = 8.7402 (0.0111)	App. Size = 2779.49 (2.92) ** Max Strain = 4.5818 (0.007) **

(Table 1 continued)

FP pattern fitting with General size formulation Model (GSzfM): Generalised Size parameters (quadratic form), (Å)

$a = b = 9.3898(3)$ Å $c = 6.8908(2)$ Å $V = 526.2(0)$ Å³	$a = b = 9.3748(3)$ Å $c = 6.8852(2)$ Å $V = 524.0(0)$ Å³	$a = b = 9.3697(2)$ Å $c = 6.8868(2)$ Å $V = 523.6(0)$ Å³	$a = b = 9.3707(2)$ Å $c = 6.8852(1)$Å $V = 523.6(0)$ Å³	$a = b = 9.3705(1)$ Å $c = 6.8849(1)$ Å $V = 523.6(0)$ Å³
$\chi^2 = 1.244$ $Rp = 12.3$ $Rwp = 14.8$ Bragg R-factor = 3.24	$\chi^2 = 1.265$ $Rp = 12.0$ $Rwp = 14.5$ Bragg R-factor = 3.45	$\chi^2 = 1.302$ $Rp = 11.8$ $Rwp = 14.5$ Bragg R-factor = 3.29	$\chi^2 = 1.252$ $Rp = 11.3$ $Rwp = 14.0$ Bragg R-factor = 2.91	$\chi^2 = 1.257$ $Rp = 11.1$ $Rwp = 14.0$ Bragg R-factor = 2.78
Av. App. Size = 206.94 (77.28) and Table 2 Average max strain = 18.095 (0.0234)	Av. App. Size = 203.94 (58.66) and Table 2 Average max strain = 19.235 (0.0146)	Av. App. Size = 292.67 (70.12) and Table 2 Average max strain = 11.745 (0.0175)	Av. App. Size = 456.43 (80.97) and Table 2 Average max strain = 7.2754 (0.0044)	Av. App. Size = 859.00 (97.74) and Table 2 Average max strain = 8.7402 (0.0117)
				Resolution limited

FP pattern fitting with the General Strain formulation Model: Anisotropic Lorenzian Size Broadening (SH), (Å) and Strain Broadening Model (Quartic form), (10⁻⁴)

$a = b = 9.3895(3)$ Å $c = 6.8906(2)$ Å $V = 526.1(0)$ Å³ ATZ= 1006.847	$a = b = 9.3743(3)$ Å $c = 6.8850(2)$ Å $V = 524.0(0)$ Å³ ATZ= 1006.667	$a = b = 9.3682(2)$ Å $c = 6.8856(2)$ Å $V = 523.3(0)$ Å³ ATZ= 1002.950	$a = b = 9.3707(2)$ Å $c = 6.8851(1)$ Å $V = 523.6(0)$ Å³ ATZ= 1005.880	$a = b = 9.3706(1)$ Å $c = 6.8849(1)$ Å $V = 523.6(0)$ ATZ= 1003.204 Å³
$\chi^2 = 1.204$ $Rp = 12$ $Rwp = 14.6$ Bragg R-factor = 3.02	$\chi^2 = 1.233$ $Rp = 11.8$ $Rwp = 14.4$ Bragg R-factor = 3.25	$\chi^2 = 1.257$ $Rp = 11.5$ $Rwp = 14.2$ Bragg R-factor = 3.19	$\chi^2 = 1.209$ $Rp = 11$ $Rwp = 13.8$ Bragg R-factor = 2.87	$\chi^2 = 1.249$ $Rp = 11$ $Rwp = 13.9$ Bragg R-factor = 2.73
Av. App. Size = 220.27 (64.98) and Table 3	Av. App. Size = 197.77 (43.53) and Table 3	Av. App. Size = 305.06 (32.28) and Table 3	Av. App. Size = 516.27 (82.07) and Table 3	Av. App. Size = 856.89 (90.73) and Table 3
Av. max Strain = 29.5348 (11.7310) and Table 4	Av. max Strain = 24.5140 (7.9247) and Table 4	Av. max Strain = 20.4704 (5.0513) and Table 4	Av. max Strain = 14.1595 (3.0045) and Table 4	Av. max Strain = 8.4299 (0.5542) and Table 4
				Resolution limited

*ATZ – Coefficient to calculate the weight percentage of the phase. $ATZ = Z\ M_w\ f^2/\ t$ (FullProf_Manual, [14])

**Data obtained when IRF file created with SiO_2 as a standard sample was used.
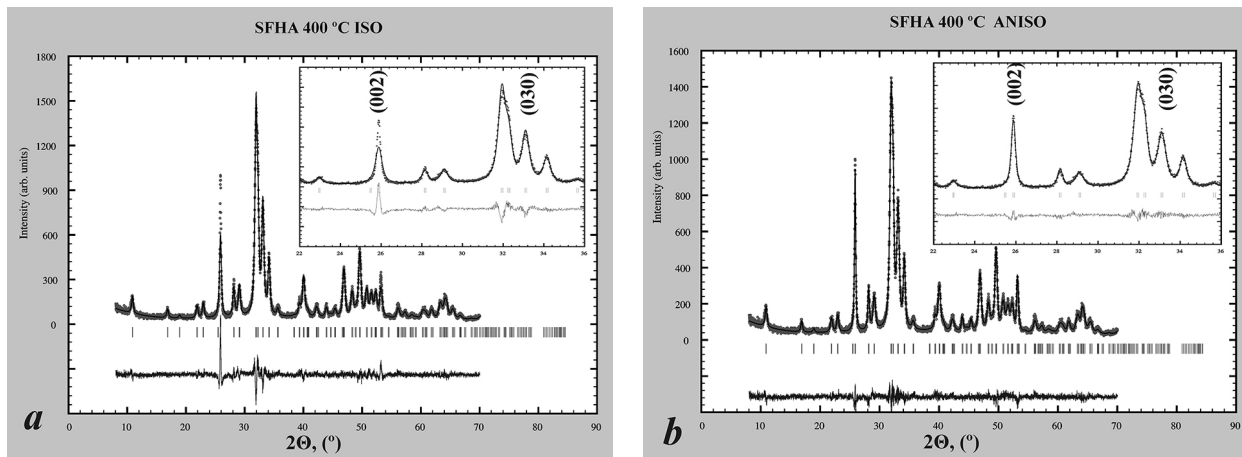
Fig. 2. Rietveld refinements for the SFHA sample heated at 400 °C: a) pattern fitting with isotropic Lorenzian size and Lorenzian strain model; b) pattern fitting with the Generalized Strain formulation model: Anisotropic Lorenzian Size Broadening (SH) and Strain Broadening Model (Quartic form). The circles are the experimental XRD data and the line through the markers is the result from the refinement. The Bragg positions are shown as short vertical lines. At the bottom is the difference plot between the data and the calculated profile.

using the different reciprocal lattice directions. It is a measure of the degree of anisotropy, not of the estimated error. Table 2 and Table 3 present apparent sizes along certain reciprocal lattice vectors according to the applied size and strain models, accordingly. Table 4 gives maximum strains values for selected crystallographic families after the corresponding refinement procedure has been used. Interestingly, when applying only the anisotropic Lorenzian size broadening (SH) for the sample heated to 530 °C FullProf refinement provides results for the (00l) reflections (data in bold in Table 3). However, when the anisotropic strain broadening model is included in the fitting procedure both size and strain results appear to be resolution limited (data in bold in Table 4). We do not have appropriate explanation for this. Figure 3 and Figure 4 present visualizations of the averaged crystallite shape and sizes obtained for the material heated to 660 °C (Table 3) and of the average maximum strain distribution tendencies
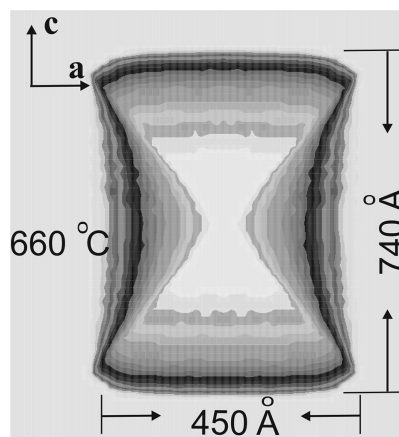
Fig. 3. Visualization of the average crystallite shape from refinement of the pattern with the Generalized Strain formulation model: Anisotropic Lorenzian Size Broadening (SH) and Strain Broadening Model (Quartic form) for the studied material heated to 660 °C as received by the GFOURIER module in FullProf.

Table 2. FullProf apparent sizes along selected Bragg reflections (*hkl*) (Å) of the studied samples after the General size formulation Model (GSzfM) was applied

	As-synth	400 °C	530 °C	660 °C	790 °C
(*0k0*)	159.91	171.31	248.14	398.10	781.63
(*0kk*)	211.03	208.33	300.11	491.98	901.47
(*hh0*)	171.21	179.86	253.55	401.49	820.98
(*hhh*)	190.64	188.85	284.16	438.31	852.21
(*00l*)	543.09	456.29	549.82	728.45	1168.56
(*00l*) / (*0k0*)	3.396	2.664	2.216	1.830	1.495

Table 3. Apparent sizes along selected Bragg reflections orders (*hkl*) after the General Strain formulation Model: Anisotropic Lorenzian Size Broadening (SH) and Strain Broadening Model (Quartic form) were applied in the FullProf refinement, (Å)

	As-synth	400 °C	530 °C	660 °C	790 °C
(010)	175.35	173.22	286.08	448.13	786.03
(020)	174.21	164.75	285.27	445.28	781.41
(030)	188.48	177.92	286.11	448.01	786.54
(040)	193.08	178.45	286.36	448.12	786.73
(050)	183.55	173.37	285.84	447.11	784.85
(060)	189.17	178.56	286.16	448.14	786.77
(0k0) averaged	183.97	174.38	285.97	447.47	785.39
(011)	237.00	208.62	339.12	541.51	880.56
(022)	237.00	208.62	339.12	541.51	880.56
(033)	223.01	197.35	338.40	539.07	876.63
(0kk) averaged	232.34	204.86	338.88	540.67	879.25
(110)	228.81	197.63	299.27	488.76	842.87
(220)	243.38	208.80	299.83	490.74	846.45
(330)	232.01	200.09	299.40	489.22	843.69
(hh0) averaged	234.73	202.17	299.5	489.58	844.34
(111)	217.12	192.01	303.14	500.41	836.59
(222)	212.48	188.26	302.92	499.62	835.24
(hhh) averaged	214.8	190.14	303.03	500.02	835.92
(002)	502.79	377.31	535.08	738.70	1118.60
(004)	502.79	377.31	535.08	738.70	1118.60
(00l) averaged	502.79	377.31	**535.08***	738.70	1118.60
averg. app. size, Å³, Table 1	220.27 (64.98)	197.77 (43.53)	305.06 (32.28)	516.27 (82.07)	856.89 (90.73)
(00l) averaged / (0k0) averaged	2.87	2.16	1.75	1.65	1.42

* see RESULTS

Table 4. Maximum-strains for selected crystallographic families {hkl} after the General Strain formulation Model: Anisotropic Lorenzian Size Broadening (SH) and Strain Broadening Model (Quartic form) were applied in the FullProf refinement, (10^{-4})

	As-synth	400 °C	530 °C	660 °C	790 °C
{0k0}	41.1863	33.2999	25.2034	17.2382	9.0697
{0kk}	12.2812	15.2440	11.7062	11.2760	7.8054
{hh0}	41.1863	33.2999	25.2034	17.2382	9.0697
{hhh}	25.7652	22.7116	18.2267	13.9017	8.2619
{00l}	10.2422	13.4004	**res. lim.***	7.9346	7.5815
av. max Strain	29.5348 (11.7310)	24.5140 (7.9247)	20.4704 (5.0513)	14.1595 (3.0045)	8.4299 (0.5542)

* see RESULTS

upon heating (Table 4), respectively. Figure 5 is a schematic presentation of the average for all crystalline domains apparent sizes at a particular temperature, scaled along the normal to the scattering planes (0*k*0) and (00*l*). Table 5 contains selected interatomic distances for the coordination polyhedra in SFHA material at different temperatures upon applying the simultaneous anisotropic size and strain refinement procedure. Obviously, all obtained re-

sults concerning the size and strain characteristics of the studied samples are model-dependent (Tables 1–3). Despite some differences in the magnitudes of the refined parameters a clear tendency is observed in the behavior of the title material upon heating and namely – crystal domain enlargement and microstrain diminishment with the increase of temperature. Some deviations from this trend within the interval around 400–550 °C are accompanied by

←
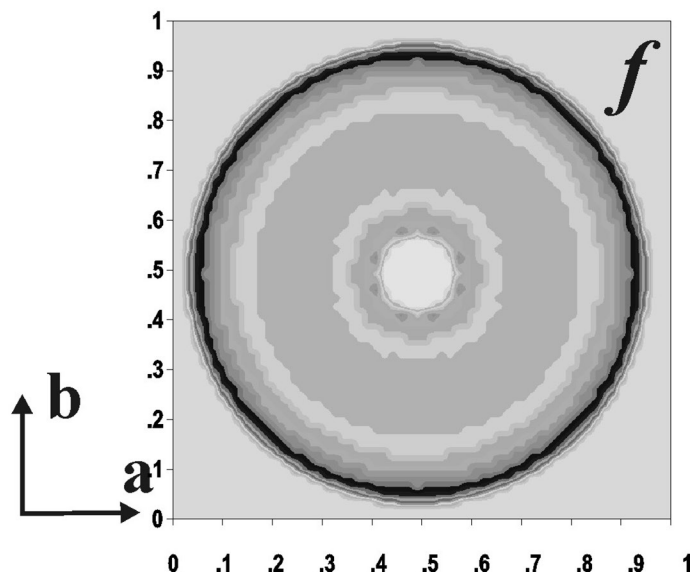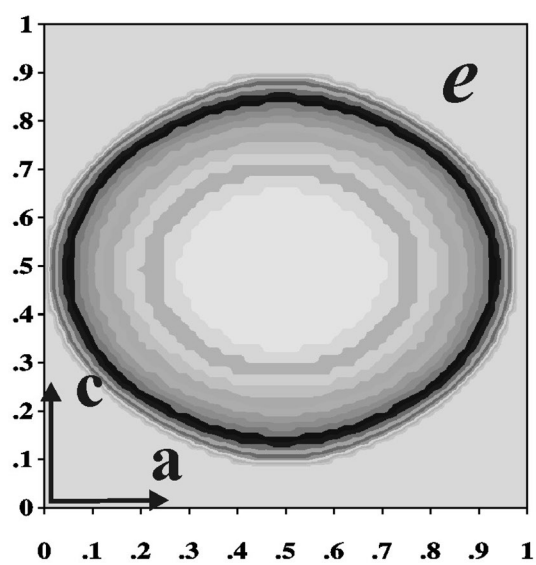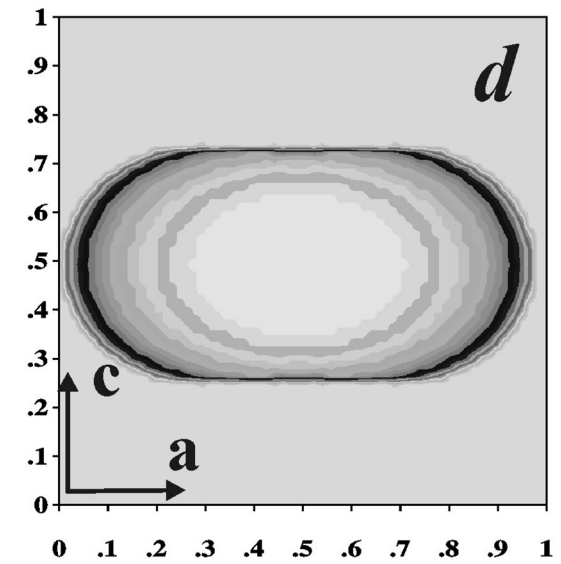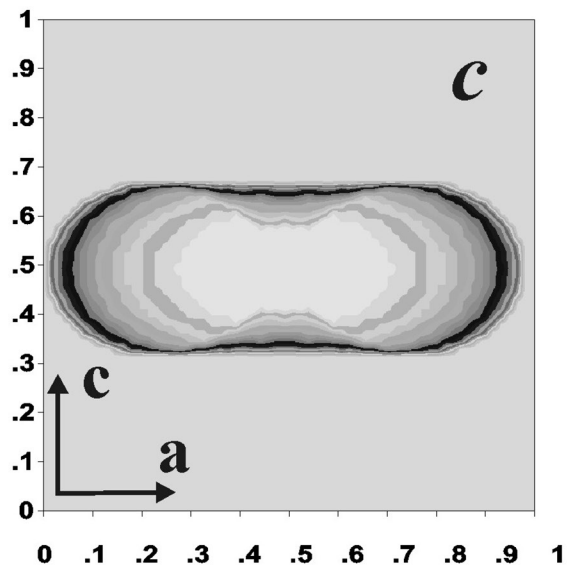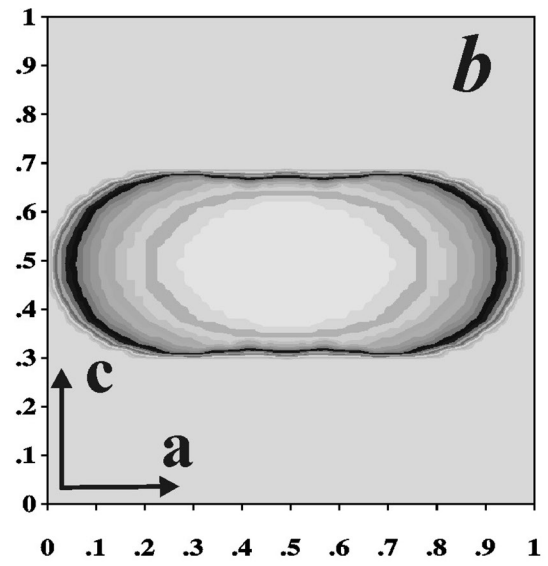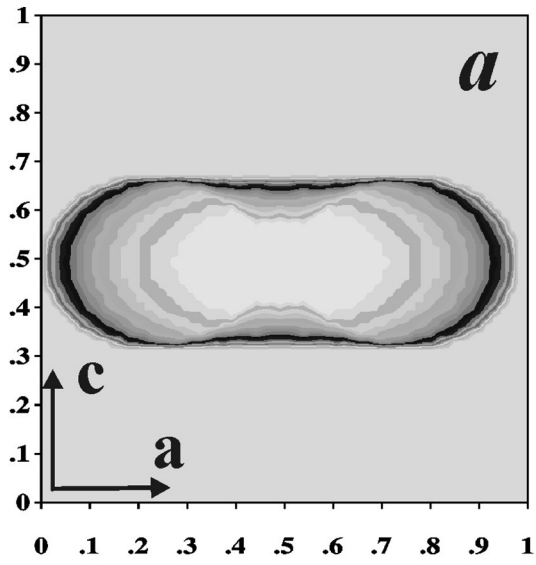
Fig. 4. Visualization of the average maximum strain from refinement of the patterns with the Generalized Strain formulation model: Anisotropic Lorenzian Size Broadening (SH) and Strain Broadening Model (Quartic form) for the studied material: a) as-synthesized; b) 400 °C; c) 530 °C, d) 660 °C, e) 790 °C, and f) strain in the **ab** plane equal for all samples as received by the GFOURIER module in FullProf.

Table 5. Selected interatomic distances (Å) for the coordination polyhedra in SFHA material at different temperatures after the General Strain formulation Model: Anisotropic Lorenzian Size Broadening (SH) and Strain Broadening Model (Quartic form) were applied in the FullProf refinement, (Å)

	As-synth	400 °C	530 °C	660 °C	790 °C
Ca1O9 polyhedron					
Ca1 – O1 x 3	2.411(6)	2.425(7)	2.420(7)	2.399(6)	2.402(5)
Ca1 – O2 x 3	2.443(7)	2.429(7)	2.430(6)	2.450(5)	2.448(5)
Ca1 – O3 x 3	2.832(5)	2.836(6)	2.826(4)	2.824(4)	2.827(4)
Ca2O6F polyhedron					
Ca2 – O1 x 1	2.701(9)	2.656(9)	2.684(8)	2.680(7)	2.682(5)
Ca2 – O2 x 1	2.397(9)	2.407(9)	2.406(7)	2.386(6)	2.377(6)
Ca2 – O3 x 2	2.500(6)	2.526(7)	2.501(5)	2.489(5)	2.483(4)
Ca2 – O3 x 2	2.321(5)	2.306(5)	2.318(4)	2.333(4)	2.344(4)
Ca2 – (O4,F) x 1	2.309(4)	2.301(4)	2.295(3)	2.302(3)	2.303(2)
PO4 tetrahedron					
P – O1	1.510(11)	1.501(12)	1.497(10)	1.529(9)	1.528(7)
P – O2	1.542(9)	1.540(9)	1.530(8)	1.526(7)	1.533(6)
P – O3	1.559(5)	1.559(5)	1.562(4)	1.551(4)	1.540(4)
P – O4	1.559(5)	1.559(5)	1.562(4)	1.551(4)	1.540(4)
max Δ(cc-l)*	0.049	0.058	0.065	0.022	0.012

* see DISCUSSION

weight loss registered in the TG-DTG-DTA curves for the as-synthesized sample (Fig. 6) and are discussed in the following section.

DISCUSSION

In this work the microstrain presence and orientation are accepted as almost entirely being due to the availability and the spatial distribution of dislocation defects. The dislocation density is strongly influenced by symmetrical and physicochemical considerations peculiar for the studied material (space group requirements and zones of weak atom bonding due to anisodesmicity). Thermal treatment facilitates the dislocations ability to migrate as a rule within the plane aligned by their directions and their Burgers vectors. The occurring upon this process atomic bonds rearrangement provokes atomic ordering in certain crystallographic directions and corresponding spatial increase of the coherently diffracting domains.
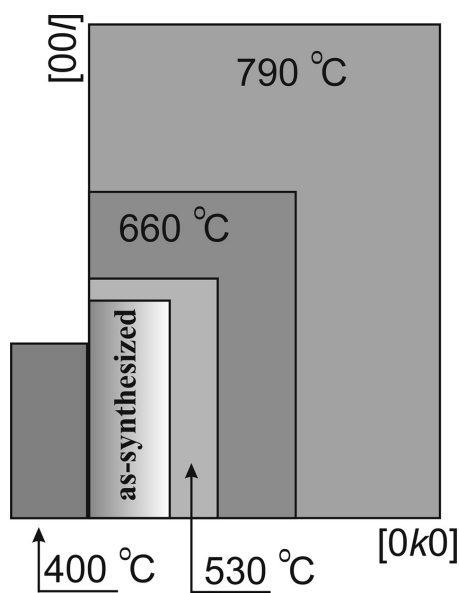
Fig. 5. Schematic presentation of the average for all crystalline domains apparent sizes at a particular temperature scaled along the normal to the scattering planes (0k0) and (00l).
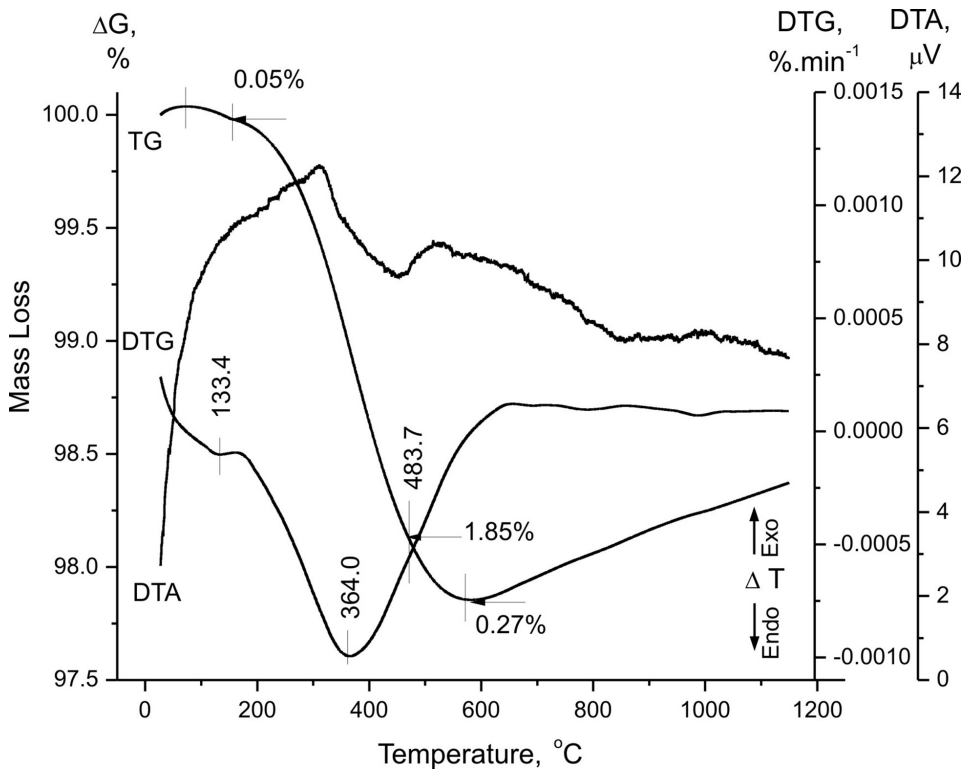
Fig. 6. TG-DTG-DTA curves of as-synthesized SFHA.

Indeed, such assumptions find evidence in the presented illustrative material (Fig. 3, 4; Tables 3, 4). Both size and strain manifest anisotropic distributions. The longest dimensions (41.186 10⁻⁴, Table 4) of the initial almost disk-shaped form of the average maximum strain obtained for the as-synthesized SFHA lie in the crystallographically most symmetrical a-b plane (Fig.4 a, f) and parallel to the indistinct cleavage reported for the {001} crystal form. In contrast, the strain magnitude along the *c*-axis is nearly four times smaller (10.242, Table 4). Upon heating, maximum strains tend to diminish in all directions; however the process goes faster in the **ab** plane (Table 4). Figure 4e depicts almost isotropic dislocation distribution for the sample heated to 790 °C. Although the average crystallite shape manifests opposite to the strain distribution form (Table 3 and Fig. 3) its thermal evolution in terms of domain sizes in certain crystallographic directions is similar to that one observed for the strain. Thus domains increase more rapidly along [100] and [110] and less pronouncedly along [001] facilitated by the "healing" effect of the heating over the migration and cancellation of the dislocations in those directions. In other words the initial long prismatic crystallites turn into short-prismatic ones at the end of the process (Table 3, Fig. 5).

Some deviations from this trends are registered in the temperature interval around 400–530 °C. Certain decrease of domain size for the sample heated to 400 °C is obtained (Table 3, Fig. 4c). Overall decrease of the average maximum strain is observed when a refinement procedure with simultaneous application of anisotropic size and anisotropic strain models is applied however this is not the case when other refinements models have been used (Table 1 and Table 4). Besides, relative strain increase is detected along [001] and some other directions for the sample heated to 400 °C. A plausible explanation for this can be the fact that being a product of wet chemistry SFHA has comprised in its structure an extra amount of hydroxyl groups. Within the mentioned temperature interval their motion and rearrangement is provoked and they start to act like additional (point or line) defects, simultaneously hampering the migration of the existing dislocations and causing their spatial ordering possibly into arrays within the weak bonding zones. It is suggested now that for a while by causing slight misorientations within the crystalline domains these arrays play the role of small-angle grain boundaries that cause splitting and subsequent size decrease as registered by FullProf. Upon temperature increase a dehydroxylation occurs as evidenced by the mass

loss of 2.12% which equals the amount of approximately one molecule of water per unit cell (Fig. 6). After its liberation the crystalline material continues its evolution in the common pathway by size increase and microstrain diminishment. Additional facts supporting this suggestion are the ATZ values obtained from the whole pattern fitting without applying any microstructural model (Table 1) and the degree of the phosphorous coordination polyhedron distortion in terms of the maximal difference of the bond lengths central cation-ligand established for each temperature (max Δ(cc-l), Table 5).

CONCLUSIONS

The performed PXRD microstructural analysis reveals distinct anisotropy in the patterns line-broadening of nano-sized SFHA samples heated within the temperature range 400–910 °C. Profile broadening is caused as from the presence of nano-sized crystalline domains as well as from the occurring microstructural effects.

Both microstructural characteristics manifest opposite trends in their evolution upon thermal treatment. Whereas, in general, size tends to increase most pronouncedly along [110] and [010] (4-fold) and to a less extend along [001] (2-fold), strain diminishes with similar in intensity and directions manner until reaching a nearly isotropic spatial distribution. The deviation from this pathway between *ca*. 400–550 °C is explained with atomic rearrangements and mass-loss of nearly one H_2O molecule per formula unit.

Assuming that microstrain effect is due mainly to the presence of dislocations and dislocation-type defects a plausible explanation can be found for the interrelated behavior of size and strain parameters in the light of the up-to-date views for crystal growth and imperfections. Heating provokes dislocations migration and cancelation preferably within zones of weak atomic bonding. This process is accompanied by crystal growth occurring in the corresponding directions. For apatites such zones appear to coincide with the **ab** crystallographic planes in which the indistinct cleavage {001} has also been observed for this material.

This study provides a reliable and easy to apply approach for specialists in materials science to investigate through PXRD the bulk properties of a powder or a polycrystalline solid in terms of their microstructural characteristics.

REFERENCES

1. The New IMA (International Mineralogical Association) List of Minerals – A Work in Progress – Updated: July 2016 - http://nrmima.nrm.se//IMA_ Master_List _%282016-07%29.pdf
2. J. C. Elliott, Structure and Chemistry of the Apatites and Other Calcium Orthophosphates (Studies in Inorganic Chemistry, vol. 18), Elsevier, Amsterdam-London-New York-Tokyo, 1994.
3. J. C. Elliott, R. M. Wilson and S. Dowker, Apatite structures, JCPDS-International Centre for Diffraction Data 2002, Advances in X-ray Analysis, Volume 45, 2002.
4. M. V. Chaikina, Mechanochemistry of Natural and Synthetic Apatites, Novosibirsk Publishing House of SB RAS, Branch "Geo", 2002 (in Russian).
5. A. A. Baig, J. L. Fox, R. A. Young, Z. Wang, J. Hsu, W. I. Higuchi, A. Chhettry, H. Zhuang, M. Otsuka, *Calcif Tissue Int*, **64**, 437 (1999).
6. K. Venkateswarlu, A. Chandra Bose, N. Rameshbabu, *Physica B* **405**, 4256 (2010).
7. K.D. Rogers, P. Daniels, *Biomaterials* **23**, 2577 (2002).
8. K. Venkateswarlu, D. Sreekanth, M. Sandhyarani, V. Muthupandi, A. C. Bose, and N. Rameshbabu, *International Journal of Bioscience, Biochemistry and Bioinformatics*, **2**, **6**, (2012).
9. S. Lala, B. Satpati, S.K. Pradhan, *Ceramics International*, **42**, 13176 (2016).
10. B. E. Warren, *Progr. Metal Phys.*, **8**, 147 (1959).
11. B. E. Warren, B. L. J. Averbach, *Appl. Phys.*, 21, 595 (1950).
12. T. Ungár, Dislocation Model of Strain Anisotropy, JCPDS-International Centre for Diffraction Data, 2008.
13. Frank, F. C. *Discussions of the Faraday Society*. **5**, 48 (1949).
14. J.R. Carjaval, *Physica B*, **192**, 55, (1993).
15. A. J. Nathanael, D. Mangalaraj, S. I. Hong, Y. Masuda, Y.H. Rhee, H. W. Kim, Materials Chemistry and Physics, 137, 3, 967 (2013).
16. Inorganic Crystal Structure Database (ICSD), Karlsruhe: Gmelin institute fur anorganische Chemie, 2005.
17. M. Rossi, M. R.Ghiara, G.Chita, F.Capitelli, American Mineralogist, 96, 1828 (2011).
18. J. R. Carvajal, Study of Micro-Structural Effects by Powder Diffraction Using the Program FULLPROF, https://www.ill.eu/fileadmin/users_files/documents/ news_and_events/workshops_events/2015/FP School- 015/Microstructural_effects_FP.pdf.

ПРАХОВ РЕНТГЕНО-ДИФРАКЦИОНЕН МИКРОСТРУКТУРЕН АНАЛИЗ НА ТЕРМИЧНО ОБРАБОТЕН СИНТЕТИЧЕН ФЛУОР-ХИДРОКСИЛ АПАТИТ

В. В. Костов-Китин[1]*, В. Петкова[1,2], Т. Калювий[3]

[1] Институт по минералогия и кристалография „Акад. Ив. Костов", Българска академия на науките, София 1113, ул. Акад. Г. Бончев, бл. 107, България
[2] Нов Български Университет, Факултет Природни Науки, София 1618, ул. Монтевидео 21, България
[3] Талински Технологичен Университет, Лаборатория по Неорганични Материали, Ehitajate tee 5, 19086, Талин, Естония

(Резюме)

Образци от нано-размерен флуор-хидроксил апатит, отгрявани в температурния интервал 400–910 °C са изучавани чрез прахов рентгено-дифракционен анализ. Във фокуса на изследванията са описание на микроструктурните характеристики при различни температури, както и тяхното развитие по време на термичната обработка. Анализът на профилните уширения на дифракционната линия е осъществен чрез метода на Ритвелд, като са прилагани различни модели за размерност и напрежение при третирането на отчетливата анизотропност, наблюдавана в определени кристалографски направления. При нагряването се проявяват тенденции и закономерности по отношение на големината на кристалните домени и микронапреженията в изучавания материал. Получените резултати са обяснени и интерпретирани съгласно сега съществуващите възгледи и теории за кристален растеж и дефектност на структурата и в светлината на модерните разбирания за прахов рентгено-дифракционен микроструктурен анализ.

Influence of the structure and morphology of MnO_2 on the electrochemical performance of supercapacitor systems

G. D. Ivanova[1]*, A. E. Stoyanova[1], L. S. Soserov[1], D. G. Kovacheva[2], D. B. Karashanova[3]

[1] Institute of Electrochemistry and Energy Systems – Bulgarian Academy of Sciences,
G. Bonchev Street, bl.10, 1113 Sofia, Bulgaria
[2] Institute of General and Inorganic Chemistry – Bulgarian Academy of Sciences,
G. Bonchev Street, bl.11, 1113, Sofia, Bulgaria
[3] Institute of Optical Materials and Technologies – Bulgarian Academy of Sciences,
G. Bonchev Street, bl.109, 1113 Sofia, Bulgaria

In the present work three type nanosized manganese oxides are structurally and morphologically characterized using X-Ray diffraction, Scanning electron microscopy and Transmission electron microscopy. A supercapacitor cells are composed by a positive electrode - a composite with teflonized acetylene black (XC-35) and 50 wt.% MnO_2, negative electrode of activated carbon (Cabot CGP Super, 1800 m^2g^{-1}) with addition of polytetrafluoroethylene (PTFE) and carbon black (Cabot SC2) and alkaline electrolyte (7M KOH with addition of 35 gl^{-1} LiOH) and subjected to electrochemical tests at different current loads (30–420 mAg^{-1}) and prolong cycling (up to 350 cycles) using Arbin BT2000 apparatus.

The results show that the structure and morphology of MnO_2 play a significant role on the supercapacitor performances. The highest discharge capacity (180–200 Fg^{-1}) and most stable cycle ability at prolong cycling are observed for a single phase MnO_2 with akhtenskite type structure and crystallites sizes about 5–6 nm.

Key words: supercapacitors, manganese dioxide, electrode materials, structure, morphology.

INTRODUCTION

Supercapacitors have a lower energy density, but a higher power density, and longer shelf and cycle life than batteries [1]. Due to these properties, supercapacitors have potential applications in various power and energy systems, such a hybrid vehicles, portable computers, mobile phones, micro-grids and others. In addition, supercapacitors possess much potential to serve as a device energy buffer in the data storage industry [2].

In order to improve the energy density at long life of energy source are developed hybrid electrochemical systems (e.g. asymmetric supercapacitors) at which both electrodes are made of different materials. The supercapacitors require porous and stable electrodes. Carbon-based active materials (AC) are the most widely used electrode materials

in these systems thanks to their physical and chemical properties [3].

Transition metal oxides, such as hydrous RuO_2, NiO and MnO_2 have been identified as possible composite materials for a high power and higher energy density supercapacitor [4–7]. They represent a type of attractive material with high specific capacitance, wide operational potential window and stability through charge–discharge cycling. Ruthenium oxide (RuO_2), as an early example, can deliver relatively constant and appreciable capacitance of 600–1000 Fg^{-1} with a potential window of 1.0–4.0 V. However, the rarity of ruthenium in the earth's crust and hence the high market price of RuO_2 limits its applications mostly in military and aerospace [8].

Manganese, as the twelfth most abundant element on the earth, is an inexpensive material with various oxidation states. Manganese oxides (MnO_x) are a class of environmentally friendly material compared with other metal oxides, only harmful by excessive inhalation or imbibing. Throughout the years, MnO_x

* To whom all correspondence should be sent:
E-mail: galia_ivanova2000@yahoo.co.uk

in various forms has been widely studied as the electrode materials in various energy storage systems, such as alkaline batteries, lithium ion batteries and supercapacitors and has been proven to be a reliable electrode material with high performance [9].

Manganese dioxide is demonstrated to be one of the most promising electrode materials for supercapacitors because of such superior characteristics as large specific capacitance, environmental benignity nature, natural abundance and low cost [10]. It was found that the textural characteristics, crystal forms and ion conductivity of MnO$_2$ strongly influence the electrochemical performances [11, 12]. Because of this there are a lot of reports on MnO$_2$ preparation technologies, such as a co-preparation method, a thermal decomposition method, a sol-gel method and so on [13–16].

Nano-structured MnO$_2$ has the advantages of large specific area, wider charge/discharge potential range, higher specific capacitance, and good environmental compatibility, which attracts many attentions in the world as electrode material for supercapacitors in recent years. One powerful and straightforward approach is to incorporate uniform MnO$_2$ nanostructures into an electrical conductive substrate, which is demonstrated to be an effective method to improve the electrochemical performance [17–22].

The effect of MnO$_2$ loading on the electrochemical performance was investigated by cyclic voltammeter and galvanostatic charging/discharging technique. The results showed than an ultra thin MnO$_2$ deposits were indispensable to achieve better electrochemical performance. The theoretical specific capacitance of MnO$_2$ is estimated to be 1370 Fg^{-1}. This ultrahigh value has only been obtained in nanoscale MnO$_2$ (1380 Fg^{-1}) [23], however, the capacitance decreases rapidly with the increase in the MnO$_2$ mass.

In the present work the effect of the structure and morphology of three type nanoscale manganese dioxide on its characteristics as electrode material in hybrid supercapacitors is discussed. The investigated samples were characterized by means of physicochemical (X-Ray diffraction, Scanning electron microscopy and Transmission electron microscopy) and electrochemical (charge/discharge galvanostatic cycling) methods.

EXPERIMENTAL

For the purposes of this study two types commercial nanoscale MnO$_2$ (Faradizer FW and Faradizer FM), Sedema company, Belgium and one type MnO$_2$ produced from company Fluka, USA are tested. Faradizer type manganese oxides are inves-

tigated previously as electrode material in lithium-ion batteries and showed a good electrochemical properties [24, 25].

These materials are structurally characterized by X-diffraction (XRD) method. The powder X-ray diffraction patterns are collected in the range from 10 to 80° 2θ with a constant step of 0.02° 2θ angle on Bruker D8 Advance diffractometer with Cu Kα radiation and Lynx Eye detector. Phase identification was performed with the Diffractplus EVA using ICDD-PDF2 Database. The powder diffraction patterns are evaluated with the Topas-4.2 software package using the fundamental parameters peak shape description including appropriate corrections for the instrumental broadening and diffractometer geometry.

The surface morphology of the electrode materials are examined by JEOL JSM-5510 and JEOL Superprobe 733 scanning electron microscope (SEM) and JEOL 2100 Transmission electron microscope (TEM). The specimens are prepared by grinding the samples in an agate mortar and dispersing them in ethanol by ultrasonic treatment for 5 min. A droplet of each suspension is dropped on standard Cu grid, covered by amorphous carbon film and dried in pure atmosphere at room temperature.

The hybrid supercapacitor cell is composed by a positive electrode – a composite with teflonized acetylene black (XC-35) and different types MnO$_2$ (50 wt.%), and a negative electrode of activated carbon (Cabot CGP Super, 1800 m^{2}g^{-1}) with addition of carbon black (Cabot SC2) and polytetraflourethylene (PTFE) as a binder. PTFE is added previously to the activated carbon under standardized methodology. The formed sheet electrodes (surface area 1,75 cm^2) are dried at 140 °C for 12 hours and pressed under pressure of 20 MPa. The obtained electrodes are soaked in the electrolyte (7M KOH with 35 gl^{-1} LiOH) under vacuum and then mounted in a coin-type cell with Viledor 700/18F separator and filled with electrolyte. The capacitor cells are subjected to galvanostatic charge-discharge cycling using an Arbin Instrument System BU-2000 [26]. The test program is carried out at constant current mode at different current load (from 30 to 360 mAg^{-1}) at 25 cycles and room temperature. Some cells are subjected to continuous cycling charge/discharge at current rate 60 mAg^{-1} up to 350 cycles.

The value of the specific capacity C is obtained from the charge-discharge cycling measurements according to the following equation [27]:

$$C = 4 \, I \, \Delta t \, / \, m \, \Delta V \qquad (1),$$

where I, Δt, ΔV and m are respectively, the constant current applied, charge/discharge time, voltage range and the total mass of the electrode material.

RESULTS AND DISCUSSION

Physicochemical characterization

The results of X-ray diffraction characterization show that the investigated manganese oxides differ in their phase composition and size of the crystallites. MnO$_2$, produced from Fluka company contains a single phase MnO$_2$ – akhtenskite type structure with crystallites sizes about 5–6 nm. The both other samples MnO$_2$ FW and MnO$_2$ FM are composites of two type structures – akhtenskite and pyrolusite and Ni, respectively with larger crystalline sizes and a non-homogeneous structure (Fig. 1, Table 1).

The crystallite sizes of different MnO$_2$ samples are determined on the basis of broadening of diffraction peaks and are shown in Table 1.

In order to clarify the role of morphology in electrochemical performance, SEM and TEM are utilized to observe the morphology of the different types Mn-oxides.

The SEM images of the samples reveal a great difference in the morphological characteristics and correspond very well with X-ray diffraction patterns. From Fig. 2c it can be seen that MnO$_2$ FM shows a strongly inhomogeneous structure with a large difference in crystal sizes and thus less developed surface area.
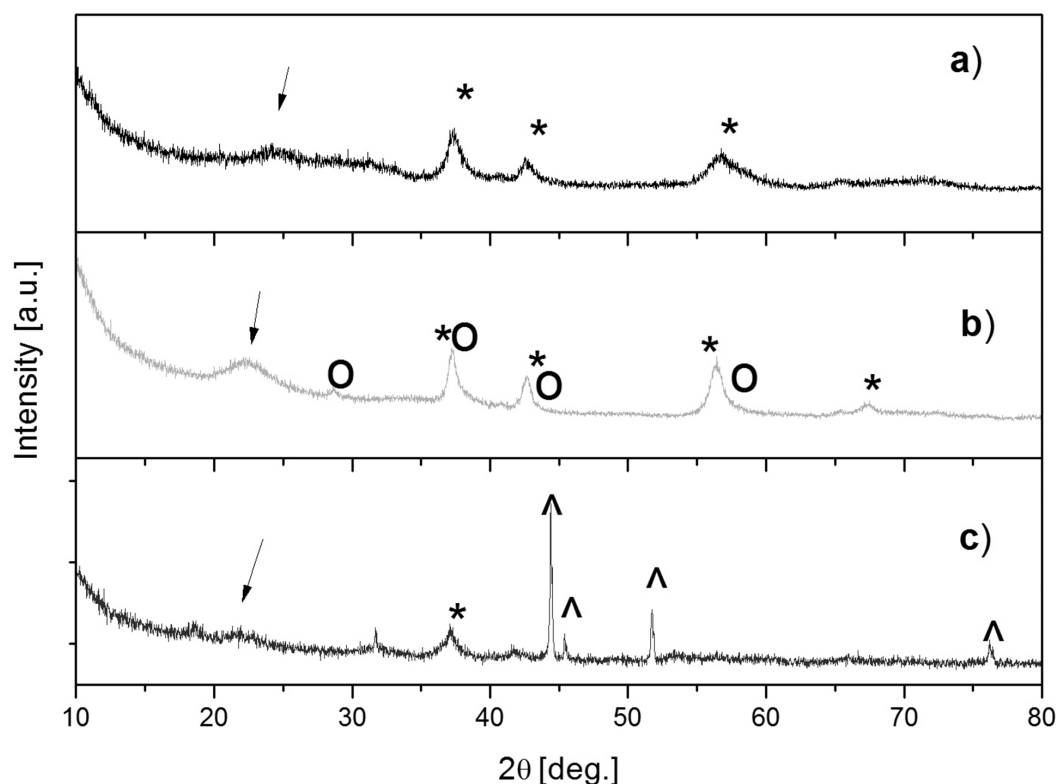
Fig. 1. Powder XRD patterns of different manganese oxides: a) MnO$_2$, b) MnO$_2$ FW and c) MnO$_2$ FM. The different phases were denoted as follows: ∗ – α-MnO$_2$ akhtenskite, o – MnO$_2$, pyrolusite, ∧ – metallic Ni. With arrows are pointed the amorphous humps.

Table 1. Determined crystallite size of investigated MnO$_2$ samples

Type	Crystallite size, nm		
	Akhtenskite	Pyrolusite	Ni
MnO$_2$	6	–	–
MnO$_2$ FW	4	14	–
MnO$_2$ FM	10	–	124
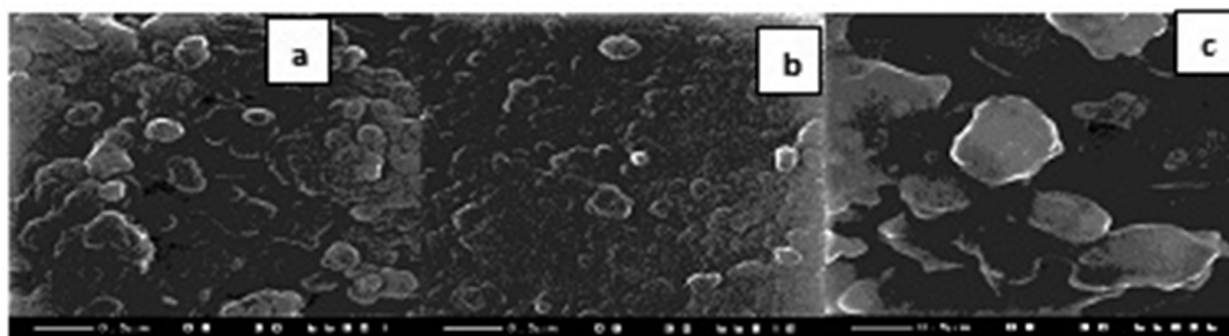
Fig. 2. SEM images of MnO$_2$ (a), MnO$_2$ FW (b) and MnO$_2$ FM (c).
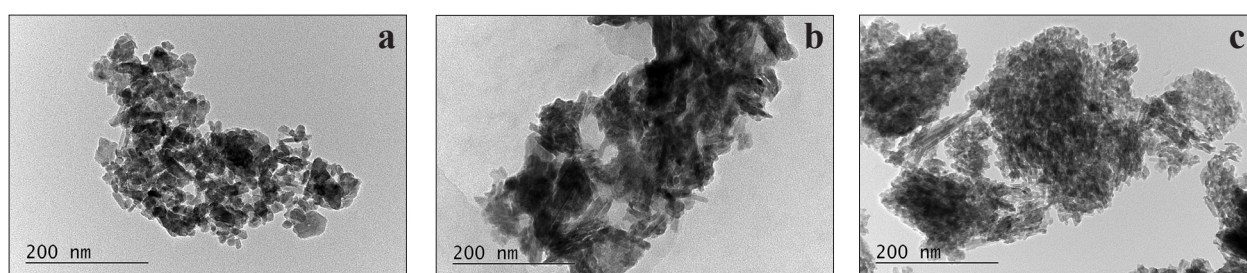
Fig. 3. TEM images of MnO$_2$ (a), MnO$_2$ FW (b) and MnO$_2$ FM (c).

The TEM observation provides additional information on lattice distortion, the size and the distribution of Mn particles and in Figure 3 are displayed the TEM images of the studied MnO$_2$ samples.

The TEM micrographs of MnO$_2$ (Fig. 3a) show that the particles are nanosized and homogeneous in size, while in MnO$_2$ FW and MnO$_2$ FM samples (Figs. 3b and 3c) dominate large formations, separated by layered structures and small clusters. There is also a significant difference in the form of crystalline particles. The micrographs of both samples (MnO$_2$ and MnO$_2$ FW) show needle-shaped particles, while the MnO$_2$ FM consists of round particles (Fig. 3).

In our previous study the physicochemical characteristics of used activated carbon Cabot CGP Super are examined in detail and it is found that this material has a very high specific surface area (1800 m^{2}g^{-1}) and small particles clusters [28].

Electrochemical characterization

The electrochemical performance of the two-electrode hybrid capacitor cells are studied by charge-discharge cycling test and are presented in Figures 4–6.

Figure 4 gives the dependences of the discharge capacitance as a function of discharge current density for studied composite electrodes fabricated by using three types MnO$_2$. It can be seen the signifi-
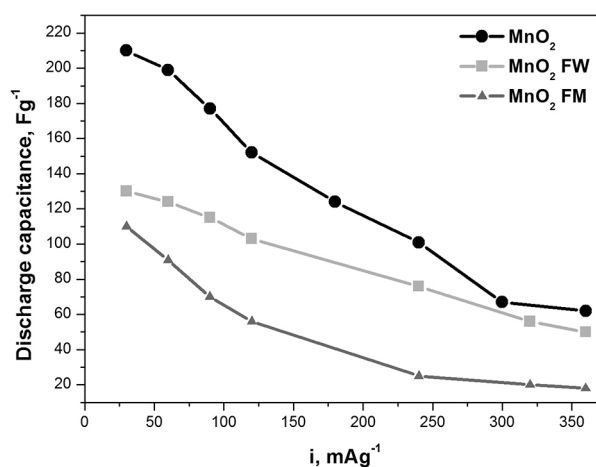
Fig. 4. Dependence of the discharge capacitance of hybrid supercapacitor cells with different types MnO$_2$ on the current loads.

cant role on the structure and morphology of the active composite material on its electrochemical performances. The analysis of the cycling behaviors shows that all three hybrid supercapacitor cells demonstrate good reproducibility of the charge/discharge process and high specific discharge capacity, which is best expressed using MnO$_2$. Substantially lower capacity indicates the cell with MnO$_2$ FM, which possesses inhomogeneous structure with very large crystal sizes.

To illustrate still better the effect of the structure on the metal oxide in composite electrode on its electrochemical performance, Figure 5 shows the charge-discharge profile curves of all studied samples fabricated in electrodes with different MnO$_2$, measured at 60 mAg^{-1}. The electrodes with MnO$_2$ and MnO$_2$ FW active material show that approximately linear voltage varies with time during both charge and discharge process which indicates that these oxides with such a structure and morphology behave as capacitors and have a good cycling stability. The electrode with MnO$_2$ demonstrates the lowest voltage drop during the discharge process, giving high values of charge/discharge efficiency [2].

The cycle life of the investigated hybrid capacitors cells is also illustrated in Figure 6, where the specific discharge capacitances of electrode materials are given as a function of cycle number. This test of cycle life is performed under constant current load (60 mAg^{-1}) conditions.

The analysis of the cycling behaviors shows that the MnO$_2$ – akhtenskite type structure demonstrates the highest discharge capacity (around 180 Fg^{-1}) and most stable cycleability at prolong cycling. The both other structures of MnO$_2$ also exhibit a long

Fig. 6. Dependence of the specific capacitance of hybrid supercapacitor cells with different types MnO$_2$ on the number of cycles at current rate 60 mAg^{-1}.

cycle life under shallow depth of discharge, but significantly worse capacitor properties (especially MnO$_2$ FM).

CONCLUSION

In this paper, three type nanosized manganese oxides are structurally and morphologically characterized and investigated as composite electrode materials in hybrid supercapacitors in alkaline electrolyte. The highest discharge capacity (180–200 Fg^{-1}) and most stable cycle ability at prolong cycling demonstrates MnO$_2$ which contains a single phase akhtenskite type and homogenous structure with crystalline sizes about 5–6 nm. The others two tested oxides (Faradizer FW and FM) with two phase structure and significant difference in the crystal sizes and pronounced lack of homogeneity (especially manganese MnO$_2$ FM) demonstrate stable, but considerably lower discharge capacitance. The obtained results confirm the positive effect of application of MnO$_2$ with defined structure and morphology as active electrode material in supercapacitors.

Fig. 5. Galvanostatic charge and discharge curves of hybrid supercapacitor cells with different types MnO$_2$ at current load of 60 mAg^{-1}.

REFERENCES

1. A. Burke, *J. Power Sources,* **91,** 37 (2000).
2. Jun Li, H. Wang, Q. Huang, S. Gamboa, P. Sebastian, *J. Power Sources,* **160**, 1501 (2006).

3. T. Cottineau, M. Toupin, T. Delahaye, T. Brousse, D. Bélanger, *Appl. Phys*., **A 82 (4)**, 599 (2006).
4. C. Portet, P. L. Taberna, P. Simon, E. Flahaut, C. Laberty-Robert, *Electrochim. Acta*, **50**, 4174 (2005).
5. W. C. Chen, C. C. Hu, C. C.Wang, *J. Power Sources*, **125,** 292 (2004) .
6. P.R. Kalakodimi, M. Nono, Electrochem., *Solid State Lett*., **7–11,** 425 (2004) .
7. W. Gui-Xin, Z. Bo-Lan, Y.Zuo-Long, *Solid State Ionics*, **176**, 1169 (2005).
8. B. E. Conway, Electrochemical supercapacitors: scientific fundamentalsand technological applications, Kluwer Academic/Plenum Publishers, New York, 1999.
9. A. A. Francis and C. Forsyth: available at: http://rais.ornl.gov/tox/profiles/mn.shtml.
10. W. Wei, X. Cui, W. Chen, D. G. Ivey, *Chem. Soc. Rev*., **40,** 1697 (2011).
11. S. Devaraj, N. Munichandraiah, *J. Phys. Chem*., **C 112**, 4406 (2008).
12. O. Ghodbane, J. L. Pascal, F. Favier, *ACS Appl. Mater. Interfaces*, **1**, 1130 (2009).
13. N. R. Redly, G. R. Reddy, *J. Power Sources*, **124**, 330 (2003).
14. Y. U. Jeong, A. Mantiram, *J. Electrochem. Soc*., **149**, 1419 (2002).
15. X. Y. Chen, X. Li, Y. Jank, *Solid State Commun.*, **136**, 94 (2005) .
16. J. Li, X. Y. Wang, Q. H. Huang, S. Gamboa, P. J. Sebastian, *J. Power Sources*, **160**, 1501 (2006).
17. S. C. Pang, M. A. Anderson, T. W. Chapman, *J. Electrochem. Soc.*, **147**, 444 (2000).
18. R. N. Reddy, R. G. Reddy, *J. Power Sources,* **132**, 315 (2004).
19. Y. S. Chen, C. C. Hu, Y. T. Wu, *J. Solid State Electrochem*., **8**, 467 (2004).
20. K. R. Prasad, N. Miura, *Electrochem. Commun.* **6**, 1004 (2004).
21. Y. Kuzuoka, C. Wen, J. Otomo, M. Ogura, T. Kobayashi, K.Yamada, H. Takahashi, *Solid State Ionics*, **175**, 507(2004).
22. Chen Ye, Zhang Mi Lin, Shi Zhao Hui, *J. Electrochem. Soc*., **15**, A 1272 (2005).
23. M. Toupin, T. Brousse, D. Belanger, *Chem. Mater.*, **16**, 3184 (2004).
24. V. Manev, N. Ilchev, A. Nassalevska, *J. Power of Sources*, **25**, 167 (1989).
25. N. Ilchev, V. Manev, *J. Power of Sources*, **35**, 175 (1991).
26. M. Mladenov, K. Alexandrova, N. Petrov, B. Tsynsarski, D. Kovacheva, N. Saliyski, R. Raicheff, *J. Solid State Electrochem.*, **17**, 2101 (2013).
27. M. Stoller and R. Ruoff, *Energy& Environment Sci.*, **3**, 1294 (2010).
28. Ch. Girginov, L. Stoyanov, S. Kozhukharov, A. Stoyanova, M. Mladenov, R. Raicheff, in: Chemical Technologies (Proceedings of RU&SU'15, Ruse, 2015), University of Ruse Angel Kanchev Proceedings, 2015, **54**, 10.1, p. 89.

ВЛИЯНИЕ НА СТРУКТУРАТА И МОРФОЛОГИЯТА НА MnO_2
ВЪРХУ ЕЛЕКТРОХИМИЧНИТЕ ХАРАКТЕРИСТИКИ
НА СУПЕРКОНДЕНЗАТОРНИ СИСТЕМИ

Г. Д. Иванова[1]*, А. Е. Стоянова[1], Л. С. Сосеров[1], Д. Г. Ковачева[2], Д. Б. Карашанова[3]

[1] Институт по Електрохимия и Енергийни Системи – Българска Академия на Науките
[2] Институт по Обща и Неорганична Химия – Българска Академия на Науките
[3] Институт за Оптични Материали и Технологии – Българска Академия на Науките

(Резюме)

В представената работа структурно и морфологично са охарактеризирани три типа наноразмерен манганов оксид с помощта на рентгенова дифракция, сканираща електронна микроскопия и трансмисионна електронна микроскопия.

Суперкондензаторните клетки са съставени от положителен електрод – композит на основата натефлонизирани въглени сажди (ХС-35) и 50 тегл.% MnO_2 и отрицателен електрод, съставен от активен въглен (Cabot CGP Super, 1800 m^2g^{-1}) с добавка на политетрафлуоретилен (ПТФЕ) и въглени сажди (Cabot SC2). Използван е алкален електролит (7М КОН с 35 gl^{-1} LiOH) и така асемблираните клетки са подложени на електрохимични изпитания при различни токови натоварвания (30–420 mAg^{-1}) и продължително циклиране (до 350 цикъла) с помощта на електрохимична система Arbin BT2000.

Резултатите показват, че структурата и морфологията на MnO_2 играят важна роля за характеристиките на суперкондензаторите. Най-висок разреден капацитет (180–200 Fg^{-1}) и най-стабилна циклируемост при продължително циклиране се наблюдава за еднофазен MnO_2 с актенскитов тип структура и размери на кристалитите 5 nm.

CeO$_2$ and TiO$_2$ obtained by urea assisted homogeneous hydrolyses method as catalysts for environmental protection: Effect of Ti/Ce ratio

A. Mileva[1]*, G. Issa[1], J. Henych[2], V. Štengl[2], D. Kovacheva[3], T. Tsoncheva[1]

[1] Institute of Organic Chemistry with Centre of Phytochemistry, BAS, Bulgaria
[2] Materials Chemistry Department, Institute of Inorganic Chemistry AS CR
[3] Institute of General and Inorganic Chemistry, BAS, Bulgaria

In present study mesoporous titanium–cerium oxide materials with different composition were prepared by homogeneous precipitation with urea. The samples were characterized by nitrogen physisorption, XRD, UV–Vis, Raman, temperature programmed reduction and their catalytic properties were studied in methanol decomposition and oxidation of ethyl acetate. The effect of phase composition on the texture, structure and redox properties was discussed in close relation with their catalytic activity. It was found that the catalytic behavior of the samples in the methanol decomposition and ethyl acetate oxidation, could be successfully controlled by the Ti/Ce ratio.

Keywords: nanostructured oxides, ethyl acetate combustion, methanol decomposition.

INTRODUCTION

Recently, titanium oxide has received much attention in technological areas due to its superior electrical, optical, and photo-catalytic properties [1, 2]. The application of titania as catalyst or catalyst support is strongly related to its crystal structure, surface density of hydroxyl groups, specific surface area, porosity, particle size, etc. [2, 3]. A lot of data in the literature have demonstrated that catalytic activity of TiO$_2$ materials could be increased by the introduction of various additives due to improved dispersion and redox properties of the mixed nano-composites. Among them, the titania-ceria binary oxides have been intensively studied in various reactions, such as total oxidation, steam reforming, decomposition of nitrogen oxides, etc [4]. Monteros at al. [5] show that the isomorphic substitution of Ce ions into TiO$_2$ lattice generates oxygen vacancies, which stabilizes the anatase phase, increases the specific surface area and the dispersion of the metal oxide particles. Dutta et al. [6] demonstrated enhanced reducibility of ceria–titania solutions. Yang et al. [7] reported higher catalytic activity of ceria–titania catalysts than the pure oxides in aqueous-phase oxidations. It has been also demonstrated that

the homogeneous co-precipitation method favors the deposition of finely dispersed CeO$_2$ on TiO$_2$, which makes it highly active in selective oxidation of nitrogen oxides. The aim of current investigation is to obtain series of Ti-Ce composites with different composition by urea assisted homogeneous hydrolyses method. The obtained materials were characterized by nitrogen physisorption, XRD, UV–Vis, Raman- spectroscopies and TPR. The relation between the phase composition, structure, texture and surface properties of the obtained materials and their catalytic behaviour in methanol decomposition as a source of syngas and total oxidation of ethyl acetate as a representative VOCs was discussed.

EXPERIMENTAL

The ceria-titania samples were synthesized by urea assisted homogeneous hydrolyses method as was described in [8]. The samples were denoted as TixCey, where x:y was the metal mol ratio, which in bi-component samples was 2:8, 5:5 or 8:2. The textural characteristics were collected from nitrogen adsorption-desorption isotherms measured at 77 K using a Quantachrome NOVA 1200 apparatus. Powder X-ray diffraction patterns were collected on a Bruker D8 Advance diffractometer with Cu Kα radiation using a LynxEye detector. The UV–Vis spectra were recorded on a Jasco V-650 UV-Vis spectrophotometer equipped with a diffuse

---

* To whom all correspondence should be sent:
E-mail: aleksandra_bunalova@abv.bg

reflectance unit. Raman spectra were acquired with a DXR Raman microscope using a 780 nm laser. The TPR/TG analyses were performed on a Setaram TG92 instrument using a flow of 50 vol.% H$_2$ in Ar. The catalytic oxidation of ethyl acetate was performed in a flow type reactor (0.030 g of catalyst) with a mixture of ethyl acetate in air (1.21 mol %) and WHSV of 100 h^{-1}. Methanol conversion was carried out in a fixed bed flow reactor (0.055 g of catalyst), argon being used as a carrier gas and methanol partial pressure of 1.57 kPa. On-line gas chromatographic analyses were performed for both reactions using an absolute calibration method and carbon based material balance.

RESULTS AND DISCUSSION

Textural characterization of the obtained materials was carried out by low temperature nitrogen physisorption (Fig. 1a, Table 1). All samples exhibited type IV isotherms with a sharp inflection of adsorbed nitrogen volume at a relative pressure (P/P$_0$) of about 0.8 (type H2 hysteresis loop), indicating the existence of mesopores. The shape of the hys-

teresis loop changed with the samples composition indicating domination of cage-like pores for TiO$_2$ and all bi-component Ti-Ce and slit-like pores for CeO$_2$. The addition of cerium to TiO$_2$ leads to an increase in the surface area, pore volume and average pore volume and this effect is most pronounced for 8Ti2Ce sample (Table 1). The observed improved textural parameters significantly overcame the expected ones if the samples were considered as a mechanical mixture of the individual oxides.

The XRD patterns of the prepared mesoporous Ti-Ce oxides are shown in Figure 1b. Diffraction peaks typical of highly crystalline TiO$_2$ with average crystallite size of about 13 nm and anatase structure are observed for the mono-component titania [1] (Fig. 1b). The XRD pattern of ceria consists of reflections typical of face centered cubic fluorite phase with average crystallite size about 13 nm [4]. Anatase phase was only registered when titania was doped with small amount of ceria (8Ti2Ce), but the reflections were broader as compared to pure TiO$_2$, which evidences higher dispersion of TiO$_2$. For the samples with higher ceria content, the characteristic of ceria reflections were only registered. The observed slight decrease of unit cell parameters for the
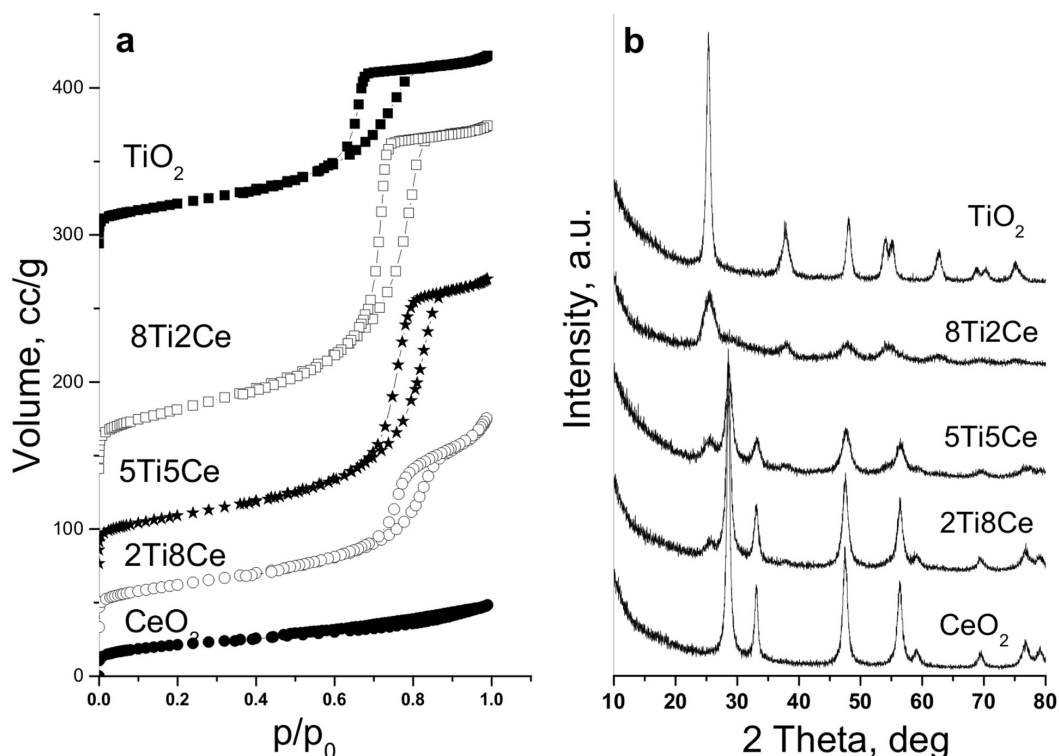
Fig. 1. Nitrogen physisorption isotherms (a) and XRD patterns (b) of TiCe materials. (The curves are shifted in y direction for better comparison).

Table 1. Nitrogen physisorption data of mono- and bi-component TiCe materials

Sample	BET m^{2}g^{-1}	Vt cm^{3}g^{-1}	Average pore diameter, nm	SA, EA mol.m^{-2}	SA, MD mol.m^{-2}
TiO$_2$	97	0.19	5.91	0.23	0.54
8Ti2Ce	146	0.36	7.98	0.31	0.36
5Ti5Ce	117	0.30	9.05	0.65	0.53
2Ti8Ce	107	0.21	3.23	0.78	0.60
CeO$_2$	76	0.07	3.80	1.09	0.60

*BET-surface areas; Vt – pore volume; *SA – specific catalytic activity (600K)

ceria component in binary materials as compared to the individual CeO$_2$ sample does not exclude substitution of Ce^{4+} ion by smaller Ti^{4+} ion [5].

Diffuse reflectance UV–Vis spectra of all Ti-Ce materials were presented in Figure 2a. The spectrum of CeO$_2$ represents a well visible absorption band in the 300–500 nm range, which is typical of pure ceria phase. The absorption at 355 nm in the TiO$_2$ spectrum is related to presence of anatase phase. It is clearly seen, that ceria doping of titania results in shift of the adsorption edge to the visible region which is slightly influenced by the Ti/Ce ratio. In accordance with the XRD and nitrogen physisorption data, the increasing absorption feature for all mixed materials could be assigned to changes in the environment of both metal ions due to the better dispersion of metal oxides and/or to the appearance of strong interaction between them. The

structural changes in the bi-component materials as compared to the individual oxides are well illustrated by Raman spectra (Fig. 2b). Raman spectrum of pure TiO$_2$ represent bands at about 141, 198, 398, 515 and 644 cm^{-1} typical of anatase phase [7]. The observed slight blue shift of the main mode to 151 cm^{-1} could be an indication for the changes in the environment of titanium ions in anatase lattice. The decrease in the intensity of this peak accompanied with its slight broadening for all bi-component samples could be due to particle size decrease, which is in accordance with the XRD data. The strong peak at 460 cm^{-1} in the spectrum of CeO$_2$ is attributed to its fluorite type structure [4]. In the mixed oxides spectra the intensity of the main peak of ceria significantly decreased. In accordance with the XRD and UV-Vis data this could be assigned to the improved metal oxide dispersion and formation of
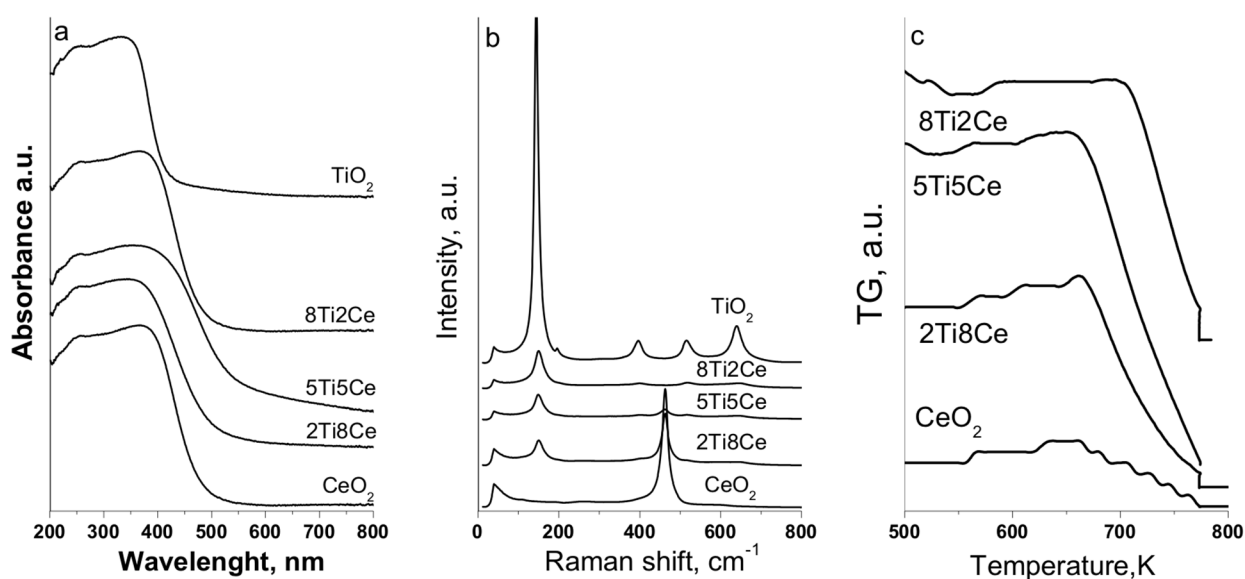
Fig. 2. UV-Vis spectra (a), Raman spectra (b) and TPR-TG profiles (c) of TiCe materials.

mixed oxide phases, due to the incorporation of Ti^{4+} ions into the ceria lattice. In order to study the nature of the obtained metal oxide species in detail, TPR measurements were carried out. In case of pure ceria (Fig. 2c), the reduction was initiated just above 657 K. Here, the observed weight loss up to 773 K corresponded to about 4% reduction of Ce^{4+} to Ce^{3+} ions. The reduction effect for bi-component material with high ceria content (2Ti8Ce) was significantly shifted to lower temperature, which was combined with an increase in the reduction degree (about 10%). The increase in titania content (5Ti5Ce) leaded to the increase of the reduction ability, which was clearly demonstrated both with the shift of the reduction profile to lower temperature as well as by the increase in the overall reduction degree (up to 13%).

However the reduction of 8Ti2Ce material significantly decreases (8%), despite it is still easier as compared to pure CeO_2. Thus, TPR results clearly demonstrate the existence of interaction between different metal oxide species in bi-component materials, which results in the presence of more readily reducible and finely dispersed metal oxide crystallites interacted with titania. In accordance with the XRD and Raman analyses, the improved reducibility of the mixed oxides could be due to the incorporation of Ti^{4+} ions into the ceria lattice, but this effect strongly depends on the Ti/Ce ratio.

The temperature dependencies of catalytic activity for all mono- and bi-component materials in total oxidation of ethyl acetate are presented in Figure 3a. Beside CO_2 which is the most important product of EA oxidation, ethanol (EtOH), acetaldehyde (AA) and acetic acid (AcAc) are also registered as by-products (Figure 3b). Among all materials, pure mono-component ceria compound exhibit the highest catalytic activity, but low selectivity to CO_2 due to the formation of ethanol as byproduct. The pure titania sample demonstrated significantly low catalytic activity combined with high ability to formation of by-products, mainly AA, EtOH and ethane. All bi-component materials exhibit higher catalytic activity than pure TiO_2 and this tendency increases with the increase of Ce content in them. However their activity was less than the observed one for pure CeO_2 sample. With the exception of 2Ti8Ce, the selectivity to CO_2 formation for the binary materials remained relatively low (about 50% at 50% conversion) and very close to that one of the individual oxides. In order to elucidate the effect of different specific surface area of the samples on their catalytic behaviour (Table 1), the specific catalytic activity was calculated as conversion at selected
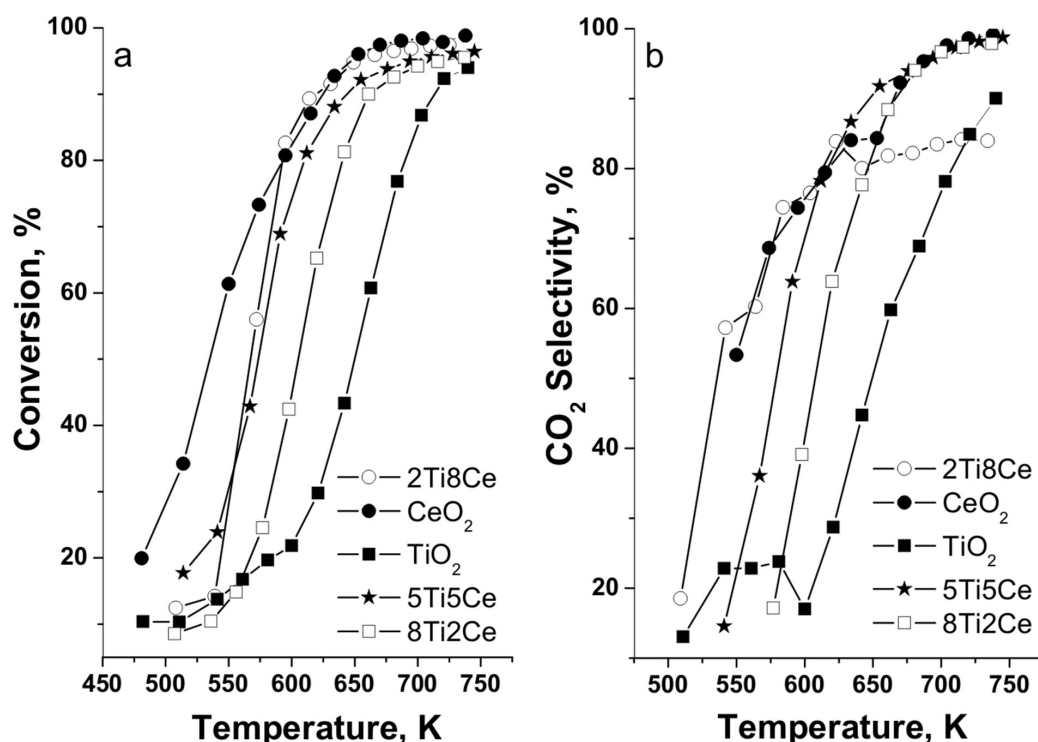
Fig. 3. Ethyl acetate conversion (a) and selectivity to CO_2 (b) of TiCe materials.

temperature (600 K) per unit surface area. The obtained results demonstrate well defined tendency of its increase with ceria content in the bi-component samples and the highest value is observed for pure CeO$_2$. However, the deviation from the linear dependency of the specific catalytic activity vs Ce content urge the authors to assume that the improvement of the catalytic activity in binary materials is not simply related to their higher surface area as a result of the improved dispersion. We can not fully exclude the contribution of the improved mobility of lattice oxygen in ceria due to the incorporation of Ti^{4+} ions in it, which was well illustrated by the TPR measurements (Fig. 2c). This promotes ethyl acetate oxidation via Mars van Krevelen mechanism [9]. Obviously small additives of titania to ceria (sample 2Ti8Ce) ensures optimal concentration of these defects and minimum segregation of pure titania phase, which provides not only high specific catalytic activity but also an increase in the selectivity in total oxidation of ethyl acetate to CO$_2$ as compared to the individual CeO$_2$.

The temperature dependencies of methanol decomposition are presented in Figure 4. Methanol decomposition provides with the formation of CO and hydrogen as the main product and CO$_2$, CH$_4$, dimethyl ether (DME) and C$_2$-C$_3$ hydrocarbons are registered as by-products. Methanol conversion is typically observed above 500–570 K. For most of the samples, the conversion increased with the temperature and reached 70–80% at 750 K.

The appearance of well defined maximum of about 50% conversion at 675 K was observed only for TiO$_2$ which clearly indicates trend to deactivation. Among the tested materials, highest catalytic activity was registered for CeO$_2$. Note that all binary materials initiate the methanol decomposition at about 50-100 K higher temperature, but the conversion exceeds about 80% in a very narrow temperature interval (about 680 K) and no trend of deactivation is observed. To elucidate the contribution of texture parameters on the catalytic behaviour of the samples, the specific catalytic activity per unit surface area (SA) was calculated (Table 1). With the exception of 8Ti2Ce, the specific activity was very similar for all materials, which indicates the important role of both, texture and structure parameters. This was also confirmed by the changes in the selectivity during the methanol decomposition to CO and hydrogen. CO$_2$ was the main by-product on CeO$_2$ and here the highest selectivity to CO was realized. Dimethyl ether (DME) formed in
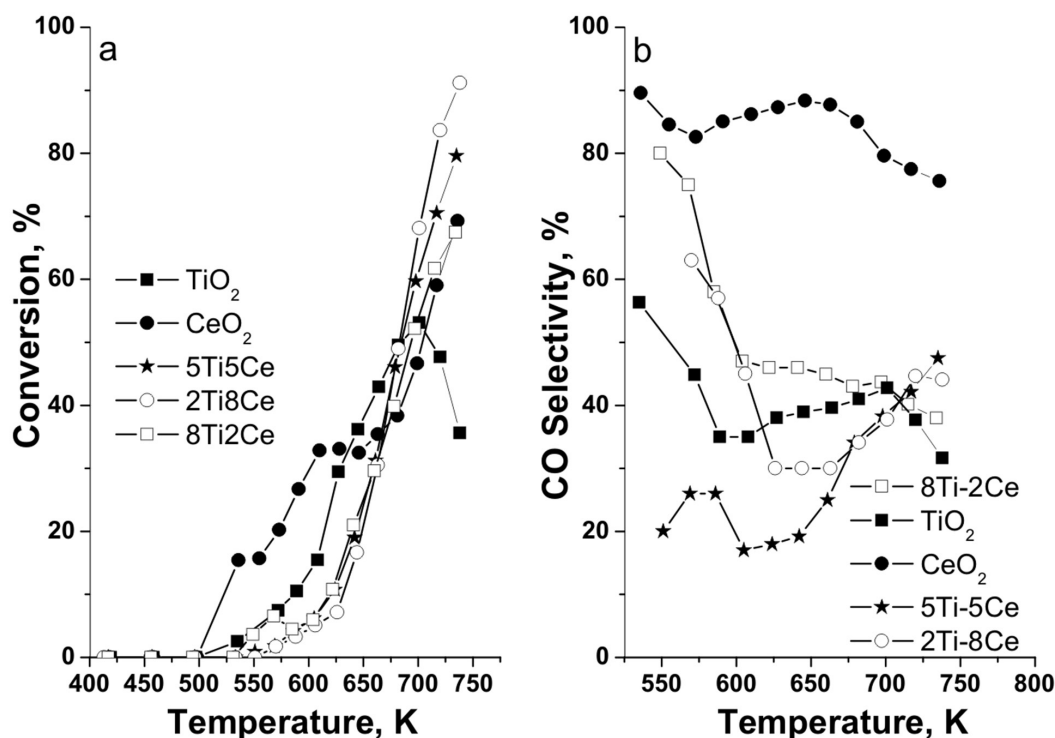
Fig. 4. Methanol conversion (a) and selectivity to CO (b) of TiCe materials.

high amount on TiO_2, indicating its high acidity. A mixture of DME and CH_4 was registered for the binary samples but their proportion was not changed in a regular way with the samples composition. The formation of CO_2 can be provided in two different reaction (1) and (2), in the presence of oxygen particles on the catalyst surface:

$$CO + H_2O \text{ (g)} \rightarrow CO_2 + H_2 \text{ (1) } \Delta Ho = -41 \text{ kJ mol}^{-1}$$

$$CH_3OH + O \text{ (lattice)} \rightarrow CO_2 \text{ (2)}$$
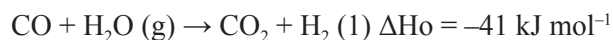
The strongly acidic solids, such as TiO_2, the surface methoxy groups act as methylating agents, which can react with methanol to form dimethyl ether. The α-H abstraction from the surface methoxide groups with the participation of basic oxygen ions of the solid provides the formation of aldehyde intermediates[10]. They can be bonded to the surface either *via* O and C atom through the carbonyl π* orbital (η2(C,O configuration) or *via* the oxygen lone pair orbital (η1(O) configuration). Obviously, the changes in the surface electron properties of the catalyst can readily control the formation of various aldehyde species. It seems that the Lewis acidic sites, which surface density is the highest for TiO_2, facilitates the η2(C,O) configuration. The aldehyde intermediates can transform to acyl intermediate *via* hydrogen abstraction, which further decomposes to CO and H_2. Note that the η2(C,O) configuration can be stabilized on the surface in higher extent than η1(O) configuration, which leads to desorption of the later at lower temperatures combined with decomposition to CO and H_2.

The observed specific features of the binary materials in methanol conversion clearly indicate that they are not only a result of the improved textural characteristics. The changes in the redox and acid-base properties of the samples due to the incorporation of Ti^{4+} in the ceria lattice probably reflects on their catalytic activity and on the selectivity to various products and this seems to be controlled in a complex way by the Ce/Ti ratio in the samples.

CONCLUSION

By using homogeneous precipitation with urea, mesoporous mono- and bi-component

Ti-Ce materials with high specific surface area and pore volume were successfully prepared. All bi-component materials demonstrate higher dispersion and improved porous characteristics in comparison with the mono-component oxides. TPR results clearly demonstrate the existence of interaction between different metal oxide species in binary materials, which results in the presence of more readily reducible and more finely dispersed metal oxide crystallites. All bi-component oxides demonstrate specific catalytic behaviour in methanol decomposition and total oxidation of ethyl acetate, in comparison with the mono-component ones. The observed effects are in a complex relation to the improved textural characteristics of binary materials and to the specific interaction between the individual oxides, which could be successfully controlled by the Ti/Ce ratio.

REFERENCES

1. O. Cap, C. L. Huisman, A. Reller, *Prog. Solid State Chem.*, **32**, 33 (2004).
2. G. Schmid, M. Baumle, M. Greekens, I. Heim, C. Osemann, T. Sawatowski, *Chem. Soc. Rev.*, **28**, 179 (1999).
3. C. T. Fleaca, M. Scarisoreanu, I. Morjan, R. Alexandrescu, F. Dumitrache, C. Luculescu, I. P. Morjan, R. Birjega, A.-M. Niculescu, G. Filoti, V. Kuncser, E. Vasile, V. Danciu, M. Pop, *Appl. Surf. Sci.*, **302**, 198 (2014).
4. W. Shan, F. Liu, H. He, X. Shi, C. Zhang, *Catal. Today*, **184**, 160 (2012).
5. A. Espinosa de los Monteros, G. Lafaye, A. Cervantes, G. Del Angel, J. Barbier Jr., G. Torres, *Catal. Today*, **258**, 564 (2015).
6. G. Dutta, U. V. Waghmare, T. Baidya, M. S. Hegde, K. R. Priolkar, P. R. Sarode, *Chem. Mater.*, **18**, 3249 (2006).
7. S. Yang, W. Zhu, Z. Jiang, Z. Chen, J. Wang, *Appl. Surf. Sci.*, **252**, 8499 (2006).
8. J. Subrt, V. Stengl, S. Bakardjieva, L. Szatmary, *Powder Technol.*, **169**, 33 (2006).
9. P. -O Larsson, A. Andersson, *Appl. Catal.* B, **24**, 175 (2000).
10. M. Mavrikakis, M. A. Barteau, *J. Mol. Catal. A: Chemical*, **131**, 135 (1998).

CeO$_2$ И TiO$_2$, ПОЛУЧЕНИ ЧРЕЗ МЕТОД НА ХОМОГЕННА ХИДРОЛИЗА С УРЕА, КАТО КАТАЛИЗАТОРИ ЗА ОПАЗВАНЕ НА ОКОЛНАТА СРЕДА: ЕФЕКТ НА СЪОТНОШЕНИЕ Ti/Ce

А. Милева[1]*, Г. Исса[1], И. Хених[2], В. Щенгъл[2], Д. Ковачева[3], Т. Цочева[1]

[1] *Институт по Органична химия с Център по Фитохимия, БАН, България*
[2] *Институт по неорганична химия, Чехия*
[3] *Институт по обща и неорганична химия, БАН*

(Резюме)

В настоящото изследване бяха получени мезопорести Ti-Ce оксидни материали чрез хомогенно отлагане с уреа с различен състав. Образците бяха характеризирани чрез физична адсобция на азот, XRD, UV-Vis и Раман спектроскопии, TPR, а каталитичните им свойства бяха изследвани в реакции на разлагане на метанол и окисление на етилацетат. Ефектът от фазовия състав върху текстурните, структурни и редокс свойства на образците беше дискутиран в тясна връзка с тяхната каталитична активност. Беше установено, че каталитичното поведение на образците в разлагане на метанол и окисление на етилацетат може да бъде успешно контролирано от отношението Ti/Ce.

Influence of the hydrothermal treatment temperature on the properties of mixed ceria-zirconia catalysts for ethyl acetate combustion

R. N. Ivanova[1]*, M. D. Dimitrov[1], D. G. Kovacheva[2], T. S. Tsoncheva[1]

[1] *Institute of Organic Chemistry with Centre of Phytochemistry, BAS, Sofia, Bulgaria*
[2] *Institute of General and Inorganic Chemistry, BAS, 1113 Sofia, Bulgaria*

A series of nanosized ceria-zirconia mixed oxides were prepared by an original procedure using template-assisted precipitation with urea followed by a hydrothermal treatment step at two different temperatures (373 K or 413 K). The obtained materials were characterized by X-ray diffraction, nitrogen physisorption, UV-Vis spectroscopy, temperature-programmed reduction (TPR) with hydrogen and their potential application in catalysis was tested in ethyl acetate combustion as a model reaction for total oxidation of volatile organic compounds. The results show that mixed oxide samples prepared using higher hydrothermal treatment temperature (413 K instead of 373 K) possess more finely dispersed tetragonal zirconia particles and significantly higher total pore volumes due to larger pore sizes, while the BET specific surface areas remains similar. Thus improved textural characteristics favor the higher catalytic activity found with the mixed ceria-zirconia samples synthesized by using the higher hydrothermal treatment temperature.

INTRODUCTION

CeO_2-ZrO_2 system is one of the most studied mixed metal oxides in the literature due to its important role in the operation of automotive catalysts [1]. To enhance the redox properties and thermal stability of pure ceria, zirconia is often mixed as an additive to form solid solutions [2]. Density functional theory calculations [3] indicate that the difference in size of Ce^{4+} (0.97 Å) and Zr^{4+} (0.87 Å) is quite important for the local structure of the metal cations. Upon the addition of Zr to CeO_2, the Zr positive charge in $Ce_{1-x}Zr_xO_2$ is smaller than in pure ZrO_2, whereas the Ce positive charge is larger than in pure CeO_2. The perturbations in the Zr-O coordination sphere could be responsible for the high oxygen mobility seen in ceria-zirconia mixed oxides [2, 4]. The excellent ability for oxygen absorption/release observed with ceria-zirconia system leads to the enhancement in its redox-properties in comparison with pure ceria [4]. The enhanced reducibility is likely to lead to improved catalytic properties for some reactions such as volatile organic compounds (VOC) combustion [5]. Besides, in case of nanosized mixed metal oxides the surface to volume ratio is high and large part of the surface is exposed, however, the presence of additional porosity coming from either the use of template or some specific treatment during synthesis could have a beneficial effect on the overall catalytic activity of the obtained materials. In the present study, a series of nanosized ceria-zirconia mixed oxides were prepared by co-precipitation of the corresponding metal chlorides with urea in the presence of hexadecyl-trimethyl ammonium bromide (CTAB), followed by a hydrothermal treatment step at either 373 K or 413 K. The obtained materials were characterized by X-ray diffraction, nitrogen physisorption, UV-Vis spectroscopy, temperature-programmed reduction (TPR) with hydrogen and their potential application in catalysis was tested in ethyl acetate combustion as a model reaction for total oxidation of volatile organic compounds. Special attention was paid on the influence of the hydrothermal treatment temperature on the textural and structural characteristics of the obtained nanocomposites and their role in the studied reaction.

---

* To whom all correspondence should be sent:
E-mail: radostinaiv@abv.bg

EXPERIMENTAL

Materials

Mono- and bi-component oxide samples were synthesized using precipitation technique in the presence of template followed by hydrothermal treatment (HT) step according to a procedure reported by Tsoncheva et al. [6]. Here, the difference is the use of urea as a precipitator instead of ammonia and the further overnight stirring of the solution under reflux conditions at 358 K before the following hydrothermal treatment, which has been conducted at either 373 K or 413 K for 24 h. The obtained mixed oxide samples are designated as follows: $xCeyZr(T)$ where x/y represents Ce/Zr mol ratio, and T is the temperature of hydrothermal treatment.

Methods of characterization

Powder X-ray diffraction patterns were collected on Bruker D8 Advance diffractometer equipped with Cu Kα radiation and LynxEye detector. The size of the crystalline domains in the samples was determined using Topas 4.2 software with Rietveld quantification refinement. Nitrogen sorption measurements were recorded on a Quantachrome NOVA 1200e instrument at 77 K. Before the physisorption measurements the samples were outgassed at 423 K overnight under vacuum. The UV–Vis spectra were recorded on a Jasco V-650 UV-Vis spectrophotometer equipped with a diffuse reflectance unit. The TPR/TG (temperature-programmed reduction/

thermogravimetric) analyses were performed in a Setaram TG92 instrument. Typically, 40 mg of the sample were placed in a microbalance crucible and heated in a flow of 50 vol.% H_2 in Ar (100 cm³min⁻¹) up to 773 K at 5 Kmin⁻¹ and a final hold-up of 1 h. The catalytic experiments were performed in a flow type reactor (0.030 g of catalyst) with a mixture of ethyl acetate (1.21 mol%) in air with WHSV – 335 h⁻¹. Gas chromatographic (GC) analyses were carried out on HP5850 apparatus using carbon-based calibration. The samples were pretreated in Ar at 423 K for 1 h and then the temperature was raised with a rate of 2 K/min in the range of 423–773 K.

RESULTS AND DISCUSSION

Some physicochemical characteristics of the obtained samples are presented in Table 1. X-ray diffraction technique (XRD) has been used for determination of samples crystallinity and phase composition (Fig. 1). Pure ceria as well as all cerium-containing samples show well defined reflections of cubic fluorite-like structure with particle sizes of about 12–14 nm (Fig. 1, Table 1). At the same time, monoclinic (P21/c) phase is registered for both pure zirconia samples. Here, an additional and more finely dispersed tetragonal (P42/nmc) phase is found only for $ZrO_2(373)$ sample (Fig. 1, Table 1). In case of mixed oxide samples, the intensity of ceria reflections decreases with zirconium content increase as expected, however, it should be noted that the unit cell parameter is smaller for the samples obtained at higher HT temperature (413 K), which could be
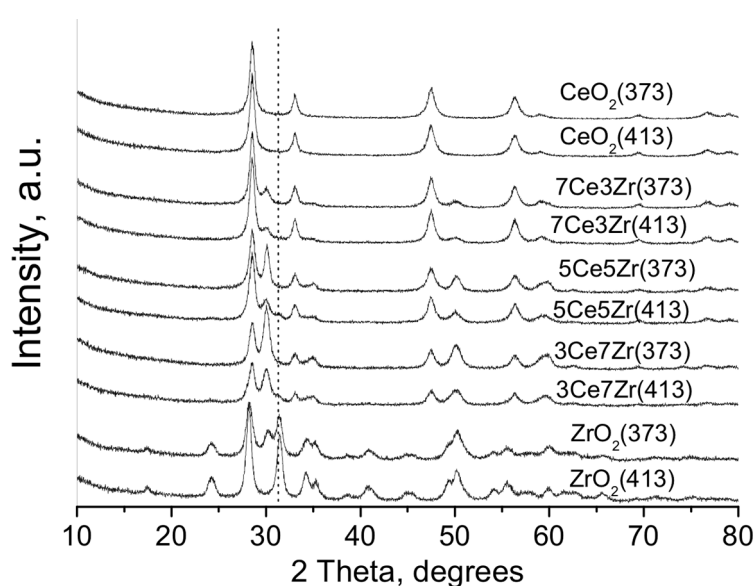
Fig. 1. XRD patterns of the studied samples.

Table 1. Texture and structure characteristics of the obtained materials

Sample	S_{BET}, m²/g	V_{total}, cc/g	S_{micro}, m²/g	V_{micro}, cc/g	Space Group	Unit cell, Å	Particles size, nm
CeO$_2$(373)	70.7	0.10	64.0	0.026	Fm–3m	5.4150(7)	12
CeO$_2$(413)	92.3	0.06	76.9	0.03	Fm–3m	5.4154(7)	13
7Ce3Zr(373)	67.4	0.09	26.5	0.01	Fm–3m P4$_2$/nmc	5.4128(8) a=3.616(1) c=5.204(4)	14 12
7Ce3Zr(413)	66.4	0.12	37.2	0.016	Fm–3m P4$_2$/nm	5.4115(7) a=3.618(2) c=5.193(2)	14 10
5Ce5Zr(373)	67.3	0.10	17.6	0.008	Fm–3m P4$_2$/nm	5.4118(8) a=3.618(1) c=5.208(3)	13 13
5Ce5Zr(413)	67.0	0.18	21.4	0.01	Fm–3m P4$_2$/nm	5.409(1) a=3.614(1) c=5.194(3)	13 9
3Ce7Zr(373)	66.8	0.12	1.3	0.0004	Fm–3m P4$_2$/nm	5.4138(9) a=3.617(1) c=5.206(2)	13 13
3Ce7Zr(413)	65.5	0.28	13.1	0.006	Fm–3m P4$_2$/nm	5.408(1) a=3.612(2) c=5.187(3)	12 9
ZrO$_2$(373)	59.3	0.11	–	–	P2$_1$/c	a=5.150(5) b=5.202(5) c=5.303(4) β=98.85(2)	13
					P4$_2$/nmc	a=3.592(5) c=5.19(1)	10
ZrO$_2$(413)	45.2	0.30	–	–	P2$_1$/c	a=5.146(2) b=5.202(2) c=5.306(2) β=99.12(1)	15

S_{BET} – BET specific surface area; V_{total} – total pore volume; S_{micro} – micropore specific surface area defined by t-plot method; V_{micro} – micropore volume.by t-plot method.

an indication of partial Zr introduction within ceria fluorite structure (Table 1). Simultaneously, a second tetragonal zirconia phase is found with all binary materials, however, its unit cell parameters are slightly expanded and we could assign this to partial cerium incorporation within the obtained tetragonal zirconia phase (Table 1). Besides, the latter phase is considerably more finely dispersed within the binary materials obtained at 413 K of HT treatment and for these samples traces of monoclinic zirconia phase is registered as well (Fig. 1, Table 1).

Nitrogen physisorption measurements were conducted in order to elucidate the textural properties of the studied samples (Fig. 2, Table 1). All isotherms are of type IV that is characteristic of mesoporous materials with the exception of pure ceria samples, which isotherms are combination of types I and IV with predominant presence of micropores (Fig. 2,

Table 1). On the other hand, both pure zirconia samples are exclusively mesoporous, but differ significantly in the shape of their isotherms according to the temperature of the conducted hydrothermal treatment – ZrO$_2$(373) is characterized with steep adsorption step within 0.6–0.8 relative pressure and H1 type hysteresis due to narrow pore size distribution (Fig. 2, Table 1), while ZrO$_2$(413) shows steep adsorption step just above 0.9 relative pressure due to the presence of non-uniform pores with very broad pore size distribution that gives almost three times higher total pore volume (Fig. 2, Table 1). In case of mixed oxide samples the shapes of their isotherms are similar to the ones obtained for pure zirconia samples with mesoporosity increasing with Zr content. All HT treated at 413 K binary materials are characterized with presence of non-uniform pores and broad pore size distributions, higher de-
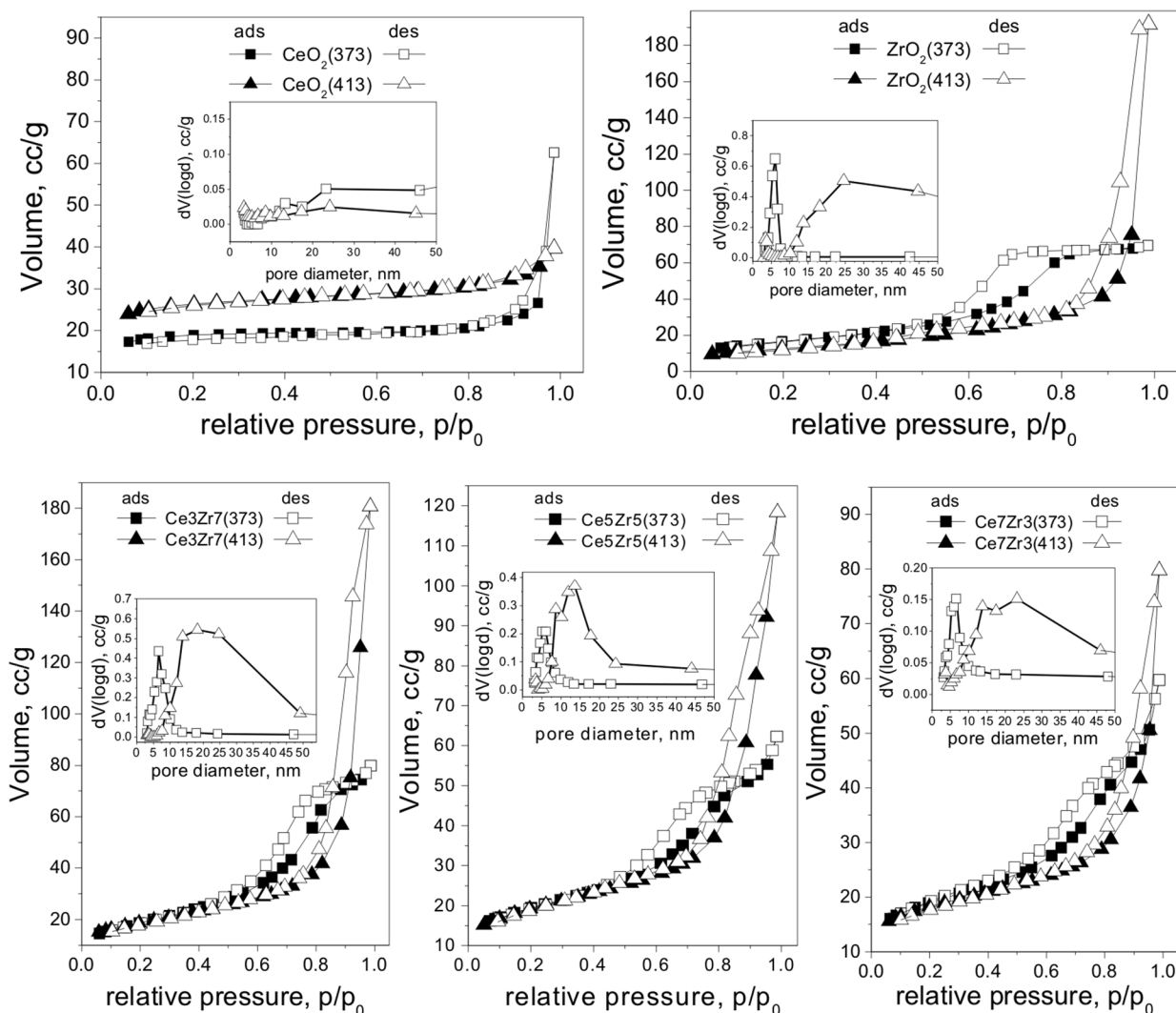
Fig. 2. Nitrogen physisorption isotherms with pore size distributions as insets for the studied pure and mixed metal oxide samples.

gree of microporosity and much higher total pore volumes in comparison to their analogues that were HT treated at 373 K, however, the BET specific surface areas remain similar (Fig. 2, Table 1).

Uv-Vis analysis has been used to obtain information for the coordination and oxidative state of metal ions. The spectra of both ZrO_2 samples show two absorption bands at around 215 and 230 nm, as expected for monoclinic ZrO_2. The second weaker broad absorption feature in their spectra positioned at around 320 nm arises from either transitions involving extrinsic states such as surface trap states and/or defect states and could be attributed to the presence of nanosized zirconia particles [7] or reveals the co-existence of tetragonal ZrO_2. For pure ceria samples, the strong absorption with maximum at about 250 nm is ascribed to $O^{2-} \rightarrow Ce^{3+}$ charge

transfer (CT) transitions, while that one at about 350–360 nm – to $O^{2-} \rightarrow Ce^{4+}$ CT transitions (Fig. 3). The overall absorption of the binary CeO_2-ZrO_2 materials is significantly higher as compared to the pure ZrO_2 samples and resembles that of the pure ceria samples. An absorption increase in the 450–550 nm region is also detected, especially for the samples with high Zr content (Fig. 3) that could be ascribed to the appearance of additional defects due to partial incorporation of Ce within zirconia lattice and vice versa.

Additional information for the redox properties of the studied materials was obtained by temperature-programmed reduction (TPR) with hydrogen (Fig. 4). No significant TG effect is observed for both ZrO_2 samples, indicating weak reduction transformations due to dehydroxylation. The reduction
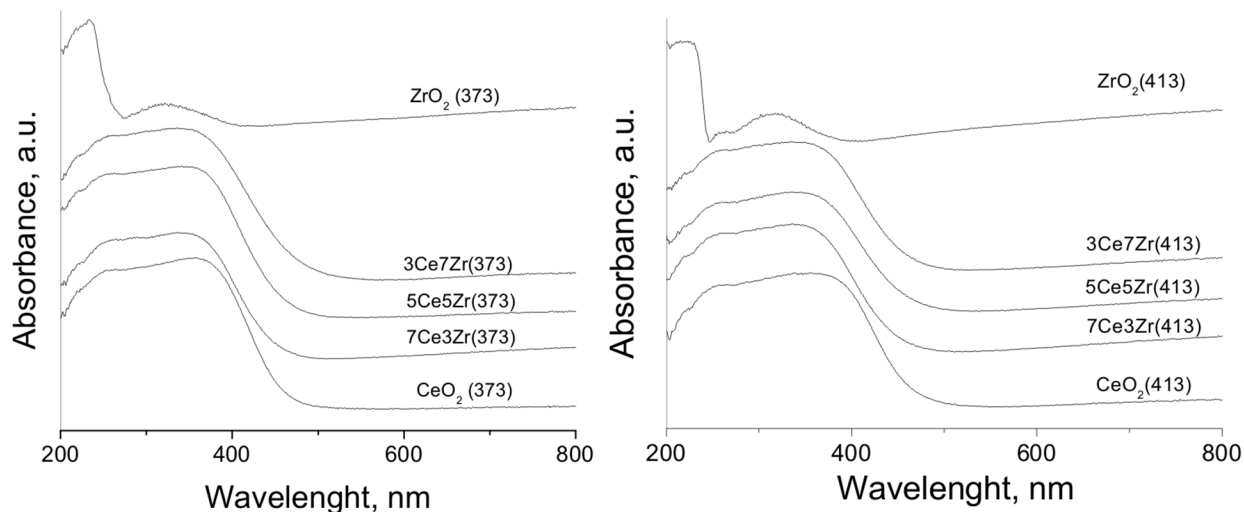
Fig. 3. UV-Vis spectra of the studied samples.

degree of Ce(IV)-Ce(III) transition for $CeO_2(373)$ is about 14%, while that for $CeO_2(413)$ is only about 9%. The reduction of all mixed oxide samples obtained at higher temperature of HT treatment (413 K) show facilitated reduction compared to $CeO_2(413)$ as well as increased reducibility (up to 25%) according to cerium content (Fig. 4). At the same time, more difficult start of reduction is observed for all samples prepared 373 K of HT treatment, but the reduction degree is significantly in-

creased, especially with Zr content above 30 mol% (Fig. 4).

The catalytic properties of the samples were studied in temperature-programmed regime within 423–773 K range (Fig. 5). Pure zirconia samples show catalytic activity just above 625–650 K with relatively low selectivity to CO_2 due to their strong acidic function and relatively low redox ability. At the same time, pure ceria samples are significantly more active and selective due to their superior re-
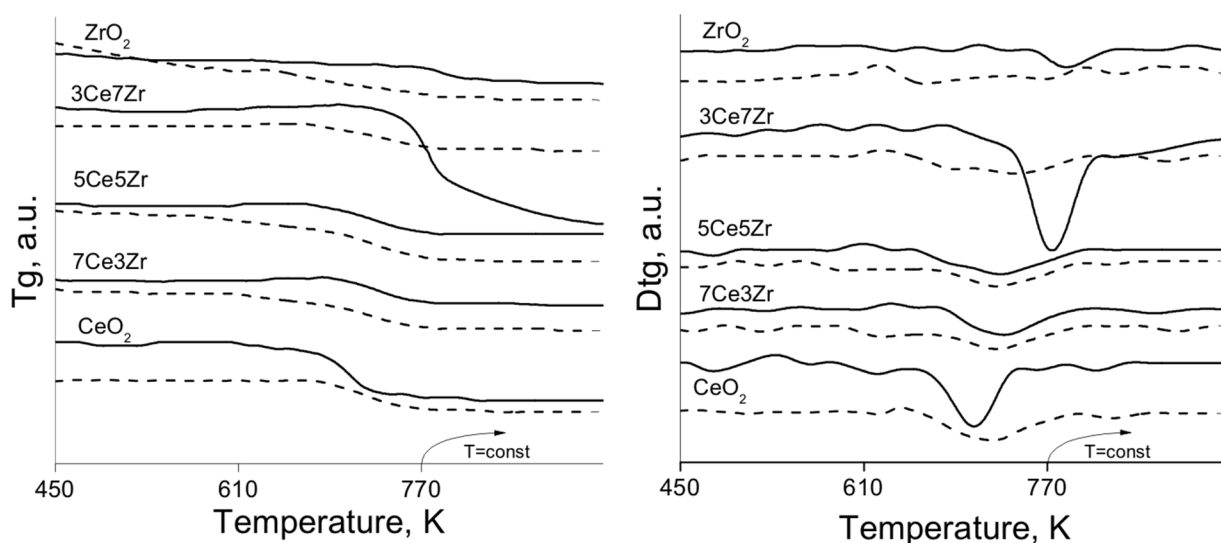
Fig. 4. TG (left) and DTG (right) data for the samples prepared at 373 K (solid lines) and 413 K (dash lines) temperature of hydrothermal treatment.
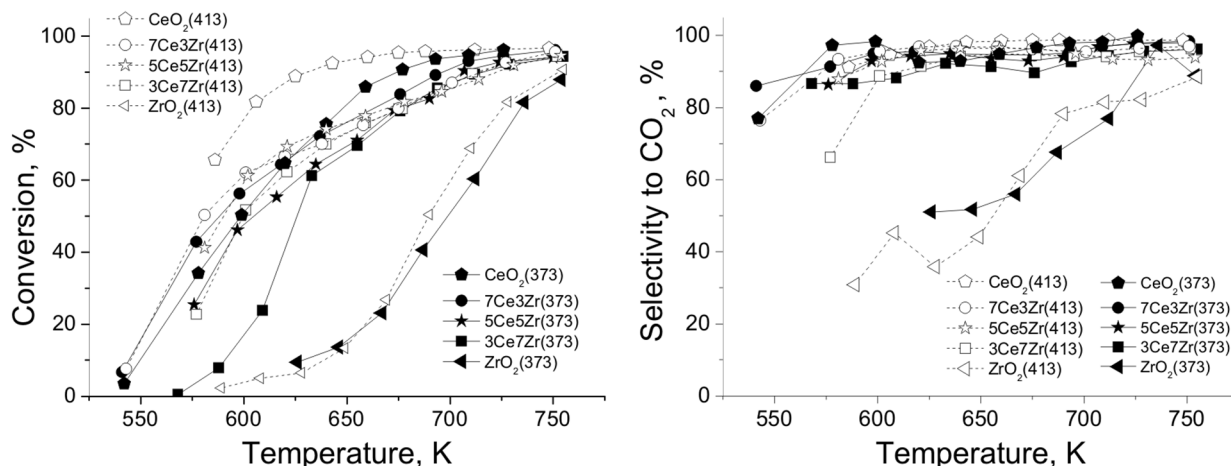
Fig. 5. Temperature dependency of ethyl acetate total oxidation for the studied samples.

dox properties (Fig. 5). The registered highest conversion ability of $CeO_2(413)$ we could assign to its much higher specific surface area compared to the other samples. All mixed oxide samples start to convert ethyl acetate at about 550 K with steeply increasing activity together with very high selectivity to CO_2 (Fig. 5). Here, the considerably higher total pore volumes and much broader pore size distributions of the HT treated at 413 K binary materials together with their improved redox properties at lower temperatures according to TPR data (Fig. 4) seems to favor their better catalytic performance.

CONCLUSION

Novel synthetic approach was applied for the synthesis of nanosized ceria-zirconia materials with micro-mesoporous structure as potential catalysts for VOCs elimination. The use of higher temperature of HT treatment (413 K instead of 373 K) during synthesis results in the development of larger and non-uniform pores which provides the higher total pore volume in the binary materials. The increased tendency for the substitution of Ce in zirconia and vice versa under the higher temperature of hydrothermal treatment facilitates the oxygen mobility in the solid. The improved textural and redox properties for the binary materials obtained under the higher temperature of hydrothermal treatment (413 K) ensures higher catalytic activity in total oxidation of ethyl acetate.

REFERENCES

1. M. Boaro, M. Vicario, C. Leitenburg, G. Dolcetti, A. Trovarelli, *Catal. Today*, **77**, 407 (2003).
2. S. Arai, S. Muto, J. Murai, T. Sasaki, Y. Ukyo, K. Kuroda, H. Saka, *Mater. Trans.*, **45**, 2951 (2004).
3. J. A. Rodriguez, J. C. Hanson, J.-Y. Kim, G. Liu, A. Iglesias-Juez, M. Fernandez-García, *J. Phys. Chem. B,* **107**, 3535 (2003).
4. H. Kaneko, S. Taku, Y. Tamaura, *Sol. Energy*, **85**, 2321 (2011).
5. M. V. Ganduglia-Pirovano, A. Hofmann, J. Sauer, *Surf. Sci. Rep.*, **62**, 219 (2007)
6. T. Tsoncheva, R. Ivanova, J. Henych, M. Dimitrov, M. Kormunda, D. Kovacheva, N. Scotti, V. Dal Santo, V. Štengl, *Appl. Catal., A*, **502,** 418 (2015).
7. M. R. Loghman-Estarki, R. S. Razavi, H. Edris, *Curr. Nanosci.*, **8**, 767 (2012).

ВЛИЯНИЕ НА ТЕМПЕРАТУРАТА НА ХИДРОТЕРМАЛНА ОБРАБОТКА ВЪРХУ СВОЙСТВАТА НА СМЕСЕНИ CeO$_2$-ZrO$_2$ КАТАЛИЗАТОРИ ЗА ИЗГАРЯНЕ НА ЕТИЛАЦЕТАТ

Р. Н. Иванова[1], М. Д. Димитров[1], Д. Г. Ковачева[2], Т. С. Цончева[1]

[1] Институт по органична химия с Център по фитохимия, БАН, 1113 София, България
[3] Институт по обща и неорганична химия, БАН, 1113 София, България

(Резюме)

Бяха получени по оригинална процедура в присъствие на темплейт серия наноразмерни CeO$_2$-ZrO$_2$ смесени оксиди, чрез използването на уреа като утаител и последваща хидротермална обработка при две различни температури (373 K или 413 K). Получените материали бяха характеризирани с помощта на прахова рентгенова дифракция, физична адсорбция на азот, UV-Vis спектроскопия, температурно-програмирана редукция (ТПР) с водород, а тяхното потенциално приложение в катализа беше изследвано в изгаряне на етилацетат, като моделна реакция за елиминиране на летливи органични съединения. Резултатите показаха, че смесените образци получени при използване на по-висока температура на хидротермална обработка съдържат по-фини ZrO$_2$ частици и значително по-голям общ обем на порите, дължащ се на наличието на по-големи пори, докато специфичната повърхност почти не се променя. Подобрените по този начин текстурни характеристики благоприятстват по-високата каталитична активност на смесените образци, получени при използването на по-високата температура на хидротермалната обработка.

Synthesis of nanosized pure and Cr doped $Sc_{2-x}In_x(WO_4)_3$ solid solutions

A. S. Yordanova[1]*, R. S. Iordanova[1], V. S. Nikolov[1], I. I. Koseva[1], P. T. Tzvetkov[1]

*[1] Institute of General and Inorganic Chemistry, Bulgarian Academy of Sciences,
Acad. G. Bonchev Str., Building 11, 1113 Sofia, Bulgaria*

Nanosized solid solutions with the formula $Sc_{2-x-y}In_xCr_y(WO_4)_3$, where x varies from 0 to 2 and y from 0.02 to 0.06 were synthesized for the first time by co-precipitation method. Phase and structural investigations were performed. By X-Ray analysis it was established that only by strict maintenance of pH between 2.7 and 5.7 a pure, monophase product can be obtained. It was found that at room temperature the solid solutions $Sc_{2-x}In_x(WO_4)_3$ at x value equal to 0 and 0.5 are orthorhombic and for x value between 1.0 and 2.0 are monoclinic. The lattice parameters of the obtained solid solutions were calculated. The conditions of thermal treatment of the amorphous precipitates were determined by preliminary DTA and TG analyses. The average crystallite dimensions of the obtained solid solutions, calculated from the X-ray data, are between 19 and 110 nm. The crystallite sizes depends on the ratio of Sc, In and Cr, and on the temperature of thermal treatment.

Keywords: Nanostructured materials, Tungstates, X-ray diffraction, DTA.

INTRODUCTION

Scandium tungstate $Sc_2(WO_4)_3$ and indium tungstate $In_2(WO_4)_3$ belong to a class of compounds with a general formula $Me_2(WO_4)_3$, where Me = Y, Sc, In, Al or lanthanides with a small ionic radius – Ho, Er, Tm, Yb, Lu. Normally, these compounds crystallize in an orthorhombic structure, space group Pnca [1]. As a result of phase transition, the structure transforms to monoclinic at lower temperatures, with space group $P2_1/a$. The phase transition of $In_2(WO_4)_3$ occurs at 258 °C [2], and of $Sc_2(WO_4)_3$ occurs at minus 263 °C [3].

The specificities of the orthorhombic structure, Pnca space group, determine a number of interesting properties and potential applications of the considered class of compounds. The orthorhombic modification is built of MeO_6 octahedrons, connected with WO_4 tetrahedrons in such a manner that they form a layered structure with a large tunnel size, where the Me^{3+} ions are sufficiently mobile, i.e. the compounds possess Me^{3+} ionic conductivity. The trivalent ionic conductivity of Al^{3+}, Sc^{3+}, Y^{3+}, Er^{3+} and In^{3+} in the corresponding tungstates is directly demonstrated and described in reference literature [4–7].

The increase of the lattice parameters by changes in the chemical composition would result in the increase of the ionic conductivity too. Similar behaviour has been already demonstrated in the system $Al_2(WO_4)_3 – Sc_2(WO_4)_3 – Lu_2(WO_4)_3$ [8–10].

Some of the $Me_2(WO_4)_3$ compounds possess unusually low thermal expansion coefficients, including zero and even negative ones, within a broad temperature range [11–14]. For example, a zero thermal expansion coefficient is reported for the $Al_{1.68}Sc_{0.02}In_{0.3}(WO_4)_3$ composition [15–17]

Another basic application of this class of compounds is as laser media for tunable lasers. The Me^{3+} situated in octahedral coordination may be easily substituted by a Cr^{3+} active ion, characterized by a broad absorption cross section, as well as by a broad emission, being incorporated in a structure with weak or intermediate type crystal field [18–20]. Our previous investigations on optical and phonon properties of nanocrystalline Cr doped $Al_2(WO_4)_3$ and solid solutions of $Al_{2-x}Sc_x(WO_4)_3$ revealed the presence of two chromium sites in these structures, one with intermediate type and another with weak crystal field strength, respectively. [21, 22].

An important advantage of this class of compounds is their aptitude to build their structure by accumulation of different trivalent ions. This provides the possibility to tailor the thermal expansion coefficient, ionic conductivity and laser emission to a desired value by varying the chemical composi-

* To whom all correspondence should be sent:
E-mail: a.yordanova@svr.igic.bas.bg

tion of solid solutions within the mentioned structures.

For the solid solutions with composition Sc$_{2-x}$In$_x$(WO$_4$)$_3$, pure or doped with chromium there is no data in the reference literature. This refers to both the methods for their production (as a rule using only the classical solid state synthesis) and the already discussed properties, important for their application.

This article presents the results of the synthesis of nanosized Sc$_{2-x}$In$_x$(WO$_4$)$_3$ solid solutions in the entire concentration range (for x values from 0 to 2), as well as the same solutions doped with 1 and 3 at.% Cr by co-precipitation method.

EXPERIMENTAL

The nanosized powders from solid solutions with a general formula Sc$_{2-x}$In$_x$(WO$_4$)$_3$ for x value equal to 0, 0.5, 1.0, 1.5 and 2 were obtained by co-precipitation method. In addition to the pure solid solutions, two series of solid solutions doped by Cr^{3+} with the same atomic ratio of Sc to In were also synthesized. These series of Cr^{3+} doped solid solutions was with general formula Sc$_{2-x-y}$In$_x$Cr$_y$(WO$_4$)$_3$ for values of y = 0.02 and 0.06. In other words, the obtained solid solutions were with concentration of In 0, 25, 50, 75 and 100 at.% (100, 75, 50, 25 and 0 at.% Sc respectively) and with concentration 0, 1 and 3 at.% of Cr^{3+} with respect to the sum of Sc and In. Each of the solid solutions was synthesized using two preliminarily prepared separate aqueous solutions: first solution of Na$_2$WO$_4$ in 50 ml of distilled water using Na$_2$WO$_4$.2H$_2$O (p.a.) as a reagent, and second solution of Sc(NO$_3$)$_3$, In(NO$_3$)$_3$ and Cr(NO$_3$)$_3$ in 50 ml of distilled water using Sc(NO$_3$)$_3$.4H$_2$O, In(NO$_3$)$_3$.3H$_2$O and Cr(NO$_3$)$_3$.9H$_2$O (p.a.) as a reagents. The quantity of the tungstates in the first solution and the total amount of nitrates in the second one corresponded to the stoichiometric composition for the progress of the co-precipitation reaction:

Mixing:

$$(2 - x - y)Sc(NO_3)_3 + xIn(NO_3)_3 + yCr(NO_3)_3 + 3Na_2WO_4$$
$$\rightarrow Sc_{2-x-y}In_xCr_y(WO_4)_3 + 6NaNO_3$$
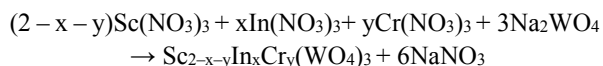
The two aqueous solutions were homogenized at room temperature until full clarification. The prepared solutions were mixed by simultaneous pouring in a third glass vessel and the obtained white substance was intensively mixed in the course of 1 hour. The solutions were adjusted to the desired pH value by adding diluted nitric acid (1:3), (HNO$_3$ p.a., 63.01 g/mol), or 1M sodium hydroxide (p.a.). The precipitation process was in the course of 24 hours.

The obtained precipitate was filtered, dried at 80 °C, then ground in an agate mortar, washed with deionised water and dried again. The amorphous precipitates of the solid solution were thermally treated in two single series: at 550 °C, 650 °C, 700 °C, 800 °C for 1 hour and at 900 °C for 3 hours. After treatment at 550 °C, 650 °C, 700 °C and 800 °C, the obtained powders were used to determine the crystallite sizes depending on the composition of the solid solutions and the temperature of thermal treatment. The well crystallized powders at 900 °C for 3 hours were used to determine structure, cell parameters and lattice volume depending on the composition of the solutions.

Structural characterization was carried out by powder X-ray diffraction (XRD) using a Bruker D8 Advance powder diffractometer with Cu Ka radiation and SolX detector. XRD spectra were recorded at room temperature. Data were collected in the 2θ range from 10 to 80 deg with a step 0.04 deg and 1s/step counting time. XRD spectra were identified using the Diffractplus EVA program. The obtained data were used for determining of the solid solution lattice parameters. The mean crystallite size and unit cell parameters were calculated from the integral breadth of all peaks (Pawley fit) using the TOPAS 3 program.3 – General profile and structure analysis software for powder diffraction data, 2005, Bruker AXS, Karlsruhe, Germany.

The thermal analysis was used for determination of crystallization temperature of some solid solution precipitate as well as for establishing of the phase transition temperature. The investigations were done by combined LABSYS™ EVO DTA/TG device of the SETARAM Company, France. The samples were investigated at a heating rate of 10°C/min in Ar flow at a flow rate of 20 ml/min.

RESULTS AND DISCUSSION

Our earlier investigations on synthesizing nanosized Al$_{2-x}$In$_x$(WO$_4$)$_3$ [23] and Al$_{2-x}$Sc$_x$(WO$_4$)$_3$ [24] by the co-precipitation method proved that aluminium − scandium solid solutions can be obtained without any special adjustment of the pH value of the mixed solution. Pure Sc$_2$(WO$_4$)$_3$ is obtained at pH equal at 5.7. In contrast for Al$_{2-x}$In$_x$(WO$_4$)$_3$, it was necessary to adhere to a strict pH value of the solution. A pure In$_2$(WO$_4$)$_3$ product was obtained only for pH values between 2.7 and 2.9. A two-phase product (In$_2$(WO$_4$)$_3$ and In$_6$WO$_{12}$ or In$_2$(WO$_4$)$_3$ and WO$_3$) was obtained for the other pH values [23]. Therefore it was logical to presume that for obtaining pure Sc$_{2-x}$In$_x$(WO$_4$)$_3$ solid solutions, it is necessary to adjust intermediate pH values between 5.7 and 2.8, proportionally diminishing with increasing

the concentration of indium in the solid solution. In this way, in order to obtain solid solutions of $Sc_{2-x}In_x(WO_4)_3$ with x equal to 0.5, 1.0, and 1.5, the chosen pH values of the solutions were 4.97, 4.25 and 3.53 respectively. The solutions were adjusted to the desired pH value by adding diluted nitric acid or sodium hydroxide.

Well crystallized samples of $Sc_{2-x}In_x(WO_4)_3$ were obtained after thermal treatment of the precipitates at 900 °C for 3 h. (t. 1). The X-ray pattern of the products for values of x equal to 2.0, 1.5 and 1.0 corresponds exactly to the reference literature data for the monoclinic symmetry with space group $P2_1/a$ and x values equal to 0.5 and 0 correspond to the orthorhombic symmetry (space group Pnca) [2, 3]. As pointed out in the literature data for $In_2(WO_4)_3$, the two structures are close to each other and in the X-ray pattern of monoclinic symmetry two additional peaks at $2\Theta = 23.6$ and 25.7 are observed. These peaks are marked by asterisk on the Figure 1b. There are not any additional peaks of impurities in the obtained solid solutions. The missing peaks of an admixture phase in the X-ray patterns and the shift of peaks at higher values 2Θ with the increasing of the In content is a proof that pure sol-

id solution compounds were obtained in the entire range from $Sc_2(WO_4)_3$ to $In_2(WO_4)_3$. The calculated lattice parameters of the pure $Sc_{2-x}In_x(WO_4)_3$ and Cr doped $Sc_{2-x-y}In_xCr_y(WO_4)_3$ (6–9) solid solutions are shown in Table 1.

As can be seen from Table 1, lattice parameters and cell volume of the solutions with orthorhombic symmetry slightly increase (solid solutions number 1,2 and 6,7) with addition of indium. These results are expected due to the small difference in ionic radii of scandium (0.745 Å) and indium (0.8 Å). On the other hand due to a big difference between the ionic radii of scandium (indium) and chromium (0.615 Å) ions, a clear tendency of lattice parameters decreasing was observed with the addition of Cr^{3+} in the orthorhombic (1, 2 and 6, 7) and monoclinic structure (3÷5 and 8÷10). The observed slight non – regular lattice parameters deviation of the of solid solutions with monoclinic symmetry is probably a result of the different sites Cr^{3+} ions (scandium or indium sites) could occupy into the solid solutions.

The aim of the second series of thermal treatment of the precipitates was to obtain nanosized powders from these solid solutions. The amorphous
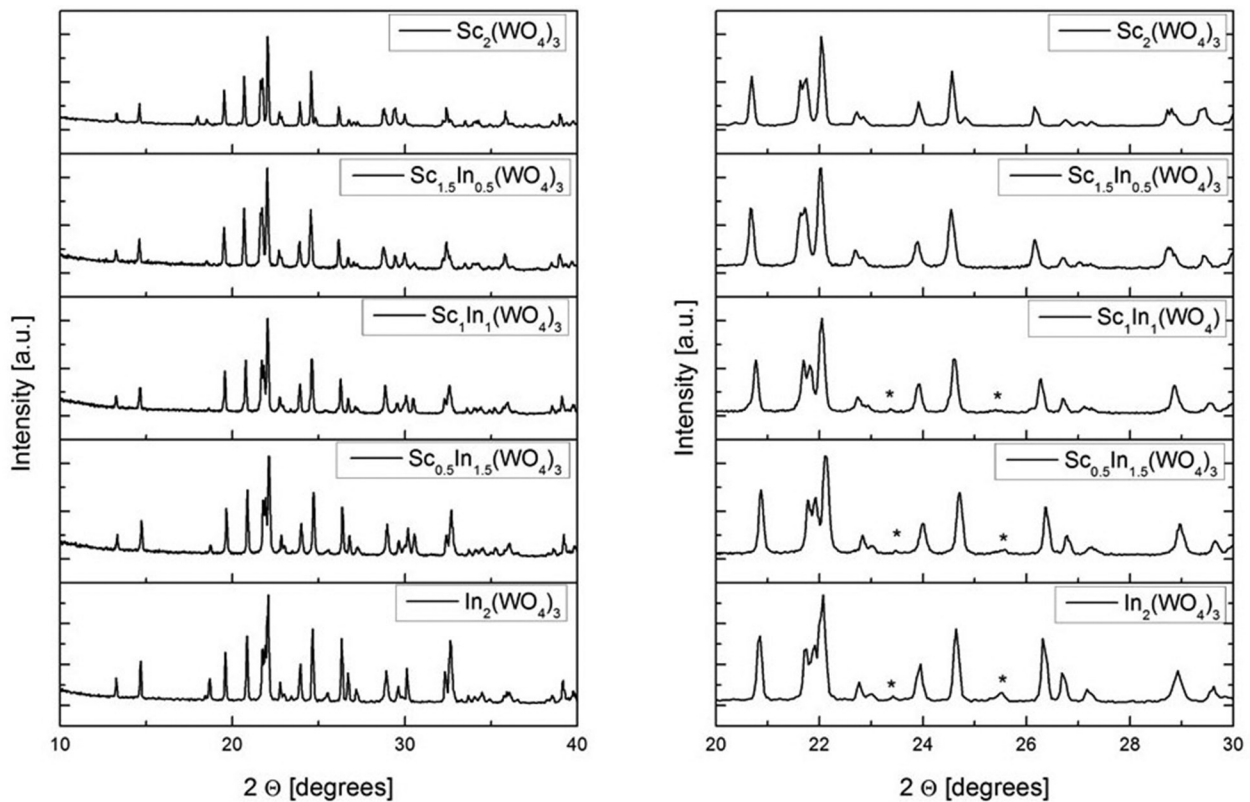
Fig. 1. a) X-ray patterns of non-doped $Sc_{2-x}In_x(WO_4)_3$ (x = 0÷2) precipitates obtained at different pH value and thermally treated at 900 °C for 3 h; b) The same X-ray pattern (narrow scale) with marked picks (*) corresponding to the monoclinic symmetry with space group $P2_1/a$ in the case of x = 1, 1.5 and 2.

Table 1. Cell parameters a, b, c, beta and cell volume, V of non-doped $Sc_{2-x}In_x(WO_4)_3$ (1–5) and of doped $Sc_{2-x-y}In_xCr_y(WO_4)_3$ (6–9) solid solutions

No	Solid solution composition	a [Å]	b [Å]	c [Å]	beta (°)	V [Å³]	Symmetry
1	$Sc_2(WO_4)_3$	9.677	13.325	9.586	90	1236.1	Pnca
2	$Sc_{1.5}In_{0.5}(WO_4)_3$	9.688	13.328	9.594	90	1238.3	Pnca
3	$Sc_1In_1(WO_4)_3$	16.355	9.637	19.038	125.38	2446.51	$P2_1/a$
4	$Sc_{0.5}In_{1.5}(WO_4)_3$	16.357	9.634	19.021	125.32	2445.52	$P2_1/a$
5	$In_2(WO_4)_3$	16.375	9.638	19.039	125.31	2452.15	$P2_1/a$
6	$Sc_2(WO_4)_3$: 3%Cr	9.676	13.324	9.584	90	1235.6	Pnca
7	$Sc_{1.5}In_{0.5}(WO_4)_3$: 3%Cr	9.681	13.317	9.585	90	1235.7	Pnca
8	$Sc_1In_1(WO_4)_3$: 3%Cr	16.361	9.632	19.050	125.45	2445.74	$P2_1/a$
9	$Sc_{0.5}In_{1.5}(WO_4)_3$: 3%Cr	16.341	9.622	19.010	125.36	2437.65	$P2_1/a$
10	$In_2(WO_4)_3$: 3%Cr	16.350	9.627	19.010	125.31	2441.56	$P2_1/a$

precipitates of the Cr^{3+} doped $Sc_{2-x}In_x(WO_4)_3$ solid solutions were subjected to DTA analysis to determine the temperature of phase crystallization. The results are shown on Fig. 2.

On the DTA curves a strong exothermic effects in the temperature range 536÷555 °C were observed. These effects indicate the beginning of the crystal-
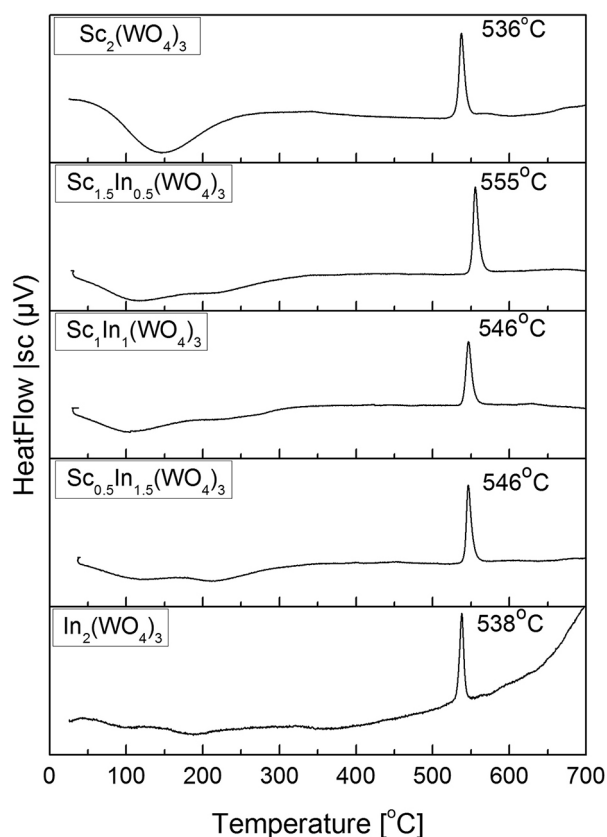
Fig. 2. Thermal behavior of the 3% Cr^{3+} doped $Sc_{2-x}In_x(WO_4)_3$ (x = 0÷2) amorphous precipitates.

lization processes in the precipitates. It can be seen that due to the more complex chemical composition of intermediate solid solutions ($Sc_{0.5}In_{1.5}(WO_4)_3$, $Sc_1In_1(WO_4)_3$ and $Sc_{1.5}In_{0.5}(WO_4)_3$) their initial temperature of crystallization is higher than that of $Sc_2(WO_4)_3$ and $In_2(WO_4)_3$. The endothermic effects at 100÷200 °C is related to H_2O release. The parallel TG and gas analyses proved that the weight losses are about 5%. The observed exothermic peaks defined the choice of the temperature of thermal treatment for crystallization of solid solutions.

Our previous investigations on obtaining nanosized particles from $Al_{2-x}Sc_x(WO_4)_3$ [24] and $Al_{2-x}In_x(WO_4)_3$ [23] proved that the main factor determining the growth of the particles is the temperature. We have also established that maintaining the same temperature for more than 1 hour has almost no impact on the particles growing. Therefore, the precipitates of non-doped and Cr^{3+} doped $Sc_{2-x}In_x(WO_4)_3$ solid solutions were thermally treated at 550, 650, 700, 800 °C and 900 °C in the course of 1 h. As an example, Fig. 3 shows the XRD data of 3% Cr^{3+} doped $Sc_{2-x}In_x(WO_4)_3$ solid solutions obtained at above mentioned temperatures for 1 h. As can be seen, after treatment at 550 °C the products contain negligible amorphous part, while after treatment at 650, 700, 800 and 900 °C the products are well crystallized. The increasing trend of peak tightening with the increasing the temperature of thermal treatment indicates the increase in average crystallites size. The average crystallite dimensions calculated from the X-ray data of the obtained solid solutions are presented in Table 2.

The average crystallite dimensions of the obtained solid solutions, calculated from the X-ray data, are between 19 and 110 nm, except for $Sc_2(WO_4)_3$ (Table 2). The influence of the temperature is weak and even at 900 °C, the average crystallites size reach only 110 nm. Higher in-
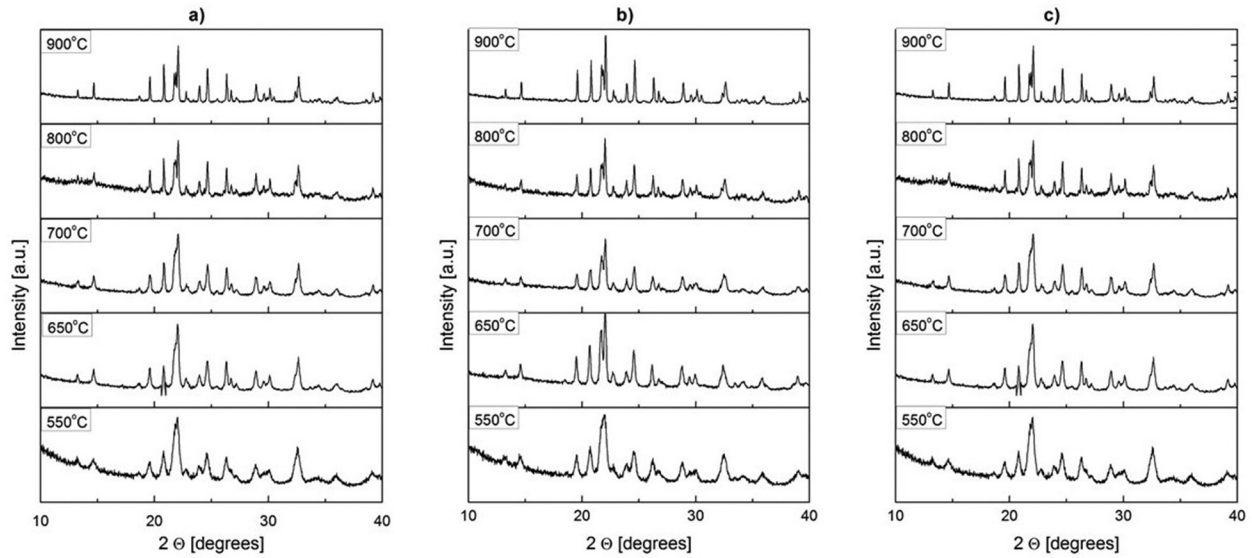
Fig. 3. X-ray powder diffraction patterns of the 3% Cr^{3+} doped precipitates, treated at different temperatures for 1 h: a) $Sc_{0.5}In_{1.5}(WO_4)_3$; b) $Sc_1In_1(WO_4)_3$; c) $Sc_{1.5}In_{0.5}(WO_4)_3$

dium content leads to decrease of crystallites size. The chromium influence depends on the temperature of thermal treatment. The thermal treatment of $Sc_{2-x-y}In_xCr_y(WO_4)_3$ solid solutions at 550, 650, 700 and 800 °C leads to a decrease of the crystallites sizes, while at 900 °C results in increasing the sizes. This result clearly showed that the velocity of phase nucleation in the temperature range 550÷ 900 °C is significantly higher than the speed of nuclei growth and indium and chromium enhance this effect. These results are in good agreement with our previous investigation on tungstate solid solutions from the same class of compounds with a general formula $Me_2(WO_4)_3$ [23–25]. An exception is Cr^{3+} doped $Sc_2(WO_4)_3$ with highest crystallites size –

250 nm at 550 °C, where the velocity of nuclei growth is very high. Due to this, thermal treatment at higher temperature of this sample was not performed. In our earlier investigation, we have established that the combination of high concentrations of Sc^{3+} and Cr^{3+} leads to a strong growth of the crystallite size, (up to the order of 200 nm) [24].

CONCLUSIONS

Nanosized solid solutions from $Sc_{2-x}In_x(WO_4)_3$ and $Sc_{2-x-y}In_xCr_y(WO_4)_2$ are synthesized for the first time by co-precipitation method. The obtained solid solutions possess orthorhombic symmetry for value

Table 2. Crystallites size dimension [nm] of $Sc_{2-x}In_x(WO_4)$ (1–5) and $Sc_{2-x-y}In_xCr_y(WO_4)_3$ (6–10) solid solution at different x and y = 0.06 (3% Cr^{3+}) after thermal treatment at 550, 650, 750, 800 °C and 900 °C

No	Solid solution composition	550 °C	650 °C	700 °C	800 °C	900 °C
1	$Sc_2(WO_4)_3$	65 nm	78 nm	86 nm	90 nm	110 nm
2	$Sc_{1.5}In_{0.5}(WO_4)_3$	30 nm	46 nm	57 nm	77 nm	90 nm
3	$Sc_1In_1(WO_4)_3$	30 nm	40 nm	50 nm	71 nm	89 nm
4	$Sc_{0.5}In_{1.5}(WO_4)_3$	29 nm	38 nm	45 nm	71 nm	88 nm
5	$In_2(WO_4)_3$	27 nm	37 nm	41 nm	55 nm	77 nm
6	$Sc_2(WO_4)_3$: 3 at% Cr^{3+}	250 nm				
7	$Sc_{1.5}In_{0.5}(WO_4)_3$: 3 at% Cr^{3+}	28 nm	45 nm	55 nm	80 nm	110 nm
8	$Sc_1In_1(WO_4)_3$: 3 at% Cr^{3+}	25 nm	38 nm	43 nm	70 nm	110 nm
9	$Sc_{0.5}In_{1.5}(WO_4)_3$: 3 at% Cr^{3+}	24 nm	36 nm	40 nm	68 nm	98 nm
10	$In_2(WO_4)_3$: 3 at% Cr^{3+}	19 nm	30 nm	38 nm	55 nm	85 nm

of x = 0 and 0.5 and monoclinic one for value of x greater than 1. Considering the results from the analyses, advantages of co-precipitation method is obvious. It gives the opportunity to obtain nanosized solid solutions in the temperature range 550÷800 °C. The crystallites size depends on the ratio of Sc^{3+}, In^{3+} and Cr^{3+}, and on the temperature of thermal treatment and are between 19 and 110 nm. The synthesized solid solutions give opportunity for systematic analyses of properties important for their application, defined by the difference of the two structures.

REFERENCES

1. K. Nassau, H. J. Levinstein, G. M. Loiacono, *J. Phys. Chem. Solids*, **26**, 1805 (1965).
2. V. Sivasubramanian, T. R. Ravindran, R. Nithya, A. K. Arora, *J. Appl. Phys.*, **96**, 387 (2004).
3. J. S. O. Evans, T. A. Mary, A. W. Sleight, *J. Solid State Chem.*, **137**, 148 (1998).
4. T. Suzuki, K. Yoshida, K. Uematsu, T. Kodama, K. Toda, Z.-G. Ye, M. Sato, *Solid State Ionics*, **104**, 27 (1997).
5. Y. Kobayashi, S. Tamura, N. Imanaka, G. Adachi, *Solid State Ionics,* **113–115**, 545 (1998).
6. N. Imanaka, G. Adachi, *J. Alloys Compd.*, **250**, 492 (1997).
7. Y. Kobayashi, T. Egawa, S. Tamura, N. Imanaka, G. Adachi, *Chem. Mater.*, **9**, 1649 (1997).
8. Y. Kobayashi, T. Egawa, S. Tamura, N. Imanaka, G. Adachi, *Solid State Ionics*, **118,** 325 (1999).
9. J. Kohler, N. Imanaka, G. Adachi, *Solid State Ionics*, **136–137**, 431 (2000).
10. G. Adachi, N. Imanaka, S. Tamura, *J. Alloys Compd.*, **323–324**, 534 (2001).
11. A. K. A. Pryde, K.D. Hammonds, M.T. Dove, V. Heine, J.D. Gale, M.C. Warren, *J. Phys.: Condens. Mater.*, **8**, 10973 (1996).
12. T. R. Ravindran, A.K. Arora, T.A. Mary, *Phys. Rev. Lett.*, **84**, 3879 (2000).
13. R. Mittal, S. L. Chaplot, H. Schober, T.A. Mary, *Phys. Rev. Lett.*, **86**, 4692 (2001).
14. Y. Yamamura, N. Nakajiama, T. Tsuji, M. Kayano, Y. Iwasa, S. Katayama, K. Saito, M. Sorai, *Phys. Rev. B,* **66**, 014301-1 (2002).
15. T. A. Mary, A. W. Sleight, *J. Mater. Res.*, **14**, 912 (1999).
16. J. S. O. Evans, T.A. Mary, A.W. Sleight, *J. Solid State Chem.*, **133**, 580 (1997).
17. R. K. Sviridova, V. I. Voronkova, S. S. Kvitka, *Crystallography (in Russ.)*, **15**, 1077 (1970).
18. K. Petermann, P. Mitzscherlich, *IEEE J. Quantum Electron.*, **23**, 1122, (1987).
19. J. Hanuza, M. Maczka, K. Hermanowicz, M. Andruszkiewicz, A. Pietraszko, W. Strek, P. Deren, *J. Sol. State Chem.*, **105**, 49 (1993).
20. D. Ivanova, V. Nikolov, P. Peshev, *J. Cryst. Growth*, **308**, 84 (2007).
21. M. Mączka, V. Nikolov, K. Hermanowicz, A. Yordanova, M. Kurnatowska, J. Hanuza, *Optical Materials*, **34 (7)**, 1048 (2012).
22. M. Maczka, K. Hermanowicz, A. Pietraszko, A. Yordanova, I. Koseva, *Opt. Mater.*, **36**, 685 (2014).
23. I. Koseva, A. Yordanova, P. Tzvetkov, V. Nikolov, D. Nihtianova, *Mater. Chem. Phys.*, **132 (2–3)**, 808 (2012).
24. A. Yordanova, I. Koseva, N. Velichkova, D. Kovacheva, D. Rabadjieva, V. Nikolov, *Mater. Res. Bull.*, **47 (6)**, 1544 (2012).
25. V. Nikolov, I. Koseva, R. Stoyanova, E. Zhecheva, *J. Alloys Compd.*, **505**, 443 (2010).

СИНТЕЗ НА НАНОРАЗМЕРНИ ЧИСТИ И ДОТИРАНИ С Cr ТВЪРДИ РАЗТВОРИ С ОБЩА ФОРМУЛА $Sc_{2-x}In_x (WO_4)_3$

А. С. Йорданова[1*], Р. С. Йорданова[1], В. С. Николов[1],
Й. И. Косева[1], П. Т. Цветков[1]

[1] *Институт по обща и неорганична химия, Българска академия на науките, ул. „Акад. Г. Бончев",
бл. 11, 1113 София, България*

(Резюме)

За първи път бяха синтезирани, наноразмерни твърди разтвори с обща формула $Sc_{2-x-y}In_xCr_y(WO_4)_3$, за стойности на x = 0÷2 и у 0,02 и 0,06, по метода на химичното съутаяване. Бяха проведени фазови и структурни изследвания. Чрез рентгенофазов анализ беше установено, че само чрез стриктно поддържане на pH между 2,7 и 5,7 могат да се получат монофазни продукти. На стайна температура, твърдите разтвори са с орторомбична симетрия за стойности на x = 0 и 0,5 и с моноклинна за стойности над 1,0. Бяха пресметнати параметрите на елементарната клетка на всички твърди разтвори. Чрез ДТА бяха определени условията на термично третиране на аморфните утайки. Средните размери на кристалите бяха изчислени от рентгенограмите и са със стойности между 19 и 110 nm. Беше установено, че размерът на кристалите зависи от температурата на термично третиране и от съотношението между скандий и индий.

Phase composition of multilayer system TiN/CrN deposited by DC magnetron sputtering

M. Ormanova[1]*, D. Dechev[1], R. Bezdushnyi[2], P. Petrov[1]

[1] Institute of Electronics of Bulgarian Academy of Sciences, Tzarigradsko Chausse 72, 1784 Sofia, Bulgaria
[2] Department of Solid State Physics and Microelectronics, Faculty of Physics, Sofia University
"St. Kliment Ohridski", 5 James Bouicher blvd., 1164 Sofia, Bulgaria

TiN/CrN multilayer coating system is a hard, wear resistant material which is widely used for cutting and forming tools and other components operating in an abrasive wear environment. This study offers a combined method of surface modification of tool steel including electron beam treatment (EBT), plasma nitriding (PN) and TiN/CrN multilayer deposition by DC (direct current) magnetron sputtering.

The phase composition and distribution, chemical composition and microstructure of the layers were investigated by X-ray diffraction (XRD); Scanning Electron Microscopy (SEM) and Dispersive X-ray Spectroscopy (EDX), respectively.

In this study was demonstrated the possibility of formation of multilayer coating of TiN/CrN on the substrate from tool steels.

Keywords: multilayer system TiN/CrN, magnetron sputtering, XRD.

INTRODUCTION

During the last decades many authors have worked on the development of methods and techniques for producing nanostructured and wear resistant coatings applicable in different fields of the modern industry [1–4].

Many investigations are concentrated on the improvement of the mechanical characteristics of tool steels and it has been shown that the deposition of nitride based coatings (e.g. TiN, VN, WN, CrN, etc.) is applicable for these purposes [5–8]. The TiN layer combine high hardness and low friction coefficient which is able to increase the lifetime of exploitation of different cutting and forming tools. The properties of other coatings have been also investigated as in the case of CrN the excellent mechanical and tribological properties and chemical and thermal stability of oxidation (700 °C) with application in different industrial branches was demonstrated [9].

Multilayer coatings for wear resistant applications, such as TiN/CrN, TiN/VN, TiN/NbN etc. are also subject of investigations in the modern material science [10–13]. Such multilayer coatings consist of alternately nanocoating with thickness from 7 to 100 nm. The effect of the deposition of large number of layers is related to additional strengthening and improving of the adhesion of the coating to the base material [14, 15]. It should be noted that multilayer nanostructured coatings are widely used for improving of the operational properties of different tools working in abrasive environments, as well as their hardness, wear resistance and resistance to corrosion. Due to the very low resistance to corrosion of TiN films (550 °C) it is widely combined with another nitridic layer (CrN, VN, NbN etc.) forming multilayer coating. In dependence of the conditions of the deposition, the hardness of the multilayer TiN/CrN coating varies from 18 to 41 GPa [16, 17].

There exist several technologies for obtaining of the discussed above coatings. The most common methods are chemical vapor deposition (CVD) which is applicable of the formation of thin and ultra-thin films widely used in the nanotechnologies. Another technique for developing of thin layers and coatings is physical vapor deposition (PVD) which includes arc deposition, electron-beam evaporation, radio-frequency and direct current magnetron sputtering [18–22].

---

* To whom all correspondence should be sent:
E-mail: maria_mecheva@abv.bg

During the last years the so called "combined methods" which includes a combination of two or more techniques is of great interest. The formation of CrN deposits by combination of plasma nitriding (PN) and PVD methods and application of resulted coatings were proposed and discussed [23].

The application of the combination of plasma nitriding and magnetron sputtered CrN layer on AISI 4140 steel is discussed [24]. The XRD investigations, conducted after PN process show the presence α-Fe and γ-Fe_4N phases. After the PVD process, a single phase with CrN structure has been registered. The authors have reported a significant increment, of the hardness after PN – 12.1 GPa, after PN+CrN – 21 GPa as the hardness of the base material is 10.2 GPa.

The process of high thermal oxidation of multilayer TiN/CrN coatings has been investigated [25]. It has been found that after the thermal treatment at 500 °C for 300 min the adhesion of the coating with the substrate is greatly improved. At this kind of treatments no changes of the hardness have been observed.

Other authors have found that the crystallographic parameters of the deposited TiN/CrN coatings significantly affect the mechanical and exploitation properties. They strongly depend on the phase composition and grain size [26, 27].

The aim of this study is to investigate the phase composition of the magnetron sputtered TiN and TiN/CrN coatings deposited on tool steel as the base material was preliminary treated by scanning electron beam followed by plasma nitriding.

EXPERIMENTAL

The experiments were conducted on samples of W320 (0.31 wt% C; 0.30 wt% Si; 0.35 wt% Mn; 2.9 wt% Cr; 2,8 wt% Mo; 0.5 wt% V) hot-work tool steel that were heat-treated in advance. The size of the substrates was 20×20×4 mm. In this work we combining three technologies for surface modification of hot work tool steel: electron-beam treatment (EBT) + plasma nitriding (PN) + direct current (DC) magnetron sputtering (MS). The TiN layer and multilayer TiN/CrN coating are deposited by magnetron sputtering.

The schematic diagram of electron beam treatment with scanning electron beam is presented on Figure 1. The electron beam, formed in an electron optical system (EOS), is scanned over the surface of the sample treated by means of electromagnetic lenses. The interaction between the electron beam and the surface of the treated specimen results in transformation of the kinetic energy to heat. After the achievement of the structural transformation

Table 1. Sequence of experiments

Sample	Treatment	Size
1	EBH + PN+ TiN	20×20×4 mm
2	EBH + PN + TiN/CrN	20×20×4 mm

temperature of the steels the sample is cooled down in a controlled way in order to reduce the residual stresses and the oxidation.

The electron beam treatment with scanning electron beam was performed on Leybold Heraus (EWS 300/15–60) at the following technological parameters: accelerated voltage – U = 55 kV, electron beam current – I = 40 mA, speed of the specimen movement – V = 4 cm/s, frequency of the electron beam – f = 1 kHz, diameter of the electron beam – d = 0.1 mm.

The plasma nitriding surface treatment was conducted on "ION 500" at 600 °C for 8–24 h, in a gas mixture of 70% N_2 + 30% H_2. After the nitriding process, the samples were cooled down at a high vacuum state in order to minimize the residual stresses and the oxidation.

The TiN and TiN/CrN coatings were deposited by direct current (DC) magnetron sputtering (MS). The diameter of the sputtered targets was 100 mm as the purity of Ti and Cr one was 99.8%. The process took place in Ar-N_2 atmosphere at working pressure of $1.2×10^{-1}$ Pa. The deposition time for TiN with thickness 2 μm is 120 minutes, 60 minutes for TiN with thickness 1 μm and 40 minutes for CrN with thickness 1 μm. In order to minimize the residual
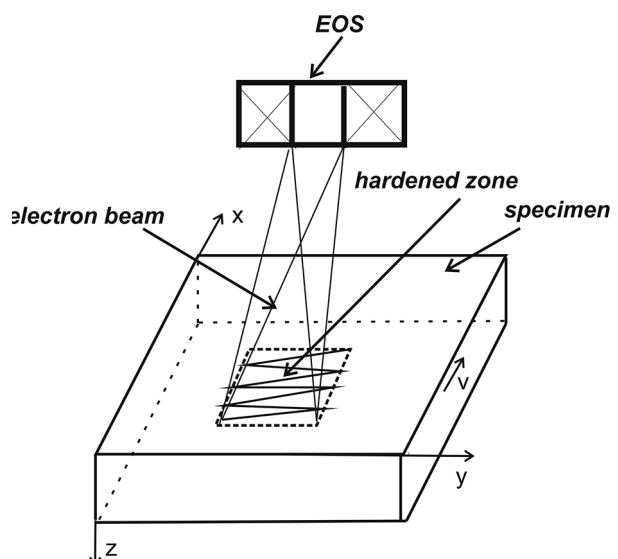
Fig. 1. Schematic diagram of scanning electron beam treatment.

stresses and the oxidation the samples with deposited coating were retrieved from the vacuum chamber after the achievement of room temperature.

X-ray diffraction experiments were performed on a URD6 Seiferd & Co diffractometer with Cu Kα radiation. The XRD patterns were recorded within the range from 30° to 80° at 2θ scale with a step 0.1°. The measurements were performed in symmetric (Bragg–Brentano) mode.

The microstructure of the obtained layers was investigated by Scanning Electron Microscopy (SEM EVO MA10 Carl Zeiss equipped with EDX detector – Quantax 200, Bruker), as secondary electrons have been used. The accelerated voltage was 20 kV.

RESULTS AND DISCUSSION

X-ray diffraction investigation of phase composition has been performed in Bragg-Brentano (B-B) mode. Fig. 2a and 2b represent XRD patterns of the samples with deposited TiN and TiN/CrN coatings. All diffractions maximums are indexed as both patterns demonstrate relatively low background. Phase identification was carried out with ICDD Database file PDF #38-1420 for TiN and PDF#11-0065 for CrN crystal phase. Fig. 2a shows presence face-centered cubic (fcc) TiN phase with space group Fm-3m (225) and reflections, corresponding to (111), (200), (220), (311) and (222) crystallographic planes. Fig. 2b represents XRD pattern of EBT+PN+TiN/CrN, where diffraction maximums of TiN and CrN (fcc and space group Fm$\overline{3}$m (225)) phases are identified. No peaks corresponding to Ti_2N, Cr_2N etc. are observed indicating that the coatings are made of single phase polycrystalline layers. The application of the preliminary treatments (electron-beam treatment (EBT) and plasma nitriding (PN)) on the sample of tool steel and technological parameters on the deposition of coatings it is possible to form TiN and TiN / CrN coatings which is of the greatest interest from practical point of view.

In the case of monolayer TiN coating, the calculated by the obtained diffraction lines parameter a is 4.254 (±0.003) Å. This result is in agreement with those from the ICDD database where the value of the lattice parameter of TiN is 4.241 Å. In many studies describing the formation of TiN coatings, the reported deviation of the calculated lattice parameter is much greater than in our case [28]. Therefore, the application of the discussed above technological conditions leads to formation of nanostructured coatings with small amount of residual stresses, microstrains, etc., because the obtained values for the lattice parameters of both phases are very similar to that applied in ICDD Database.
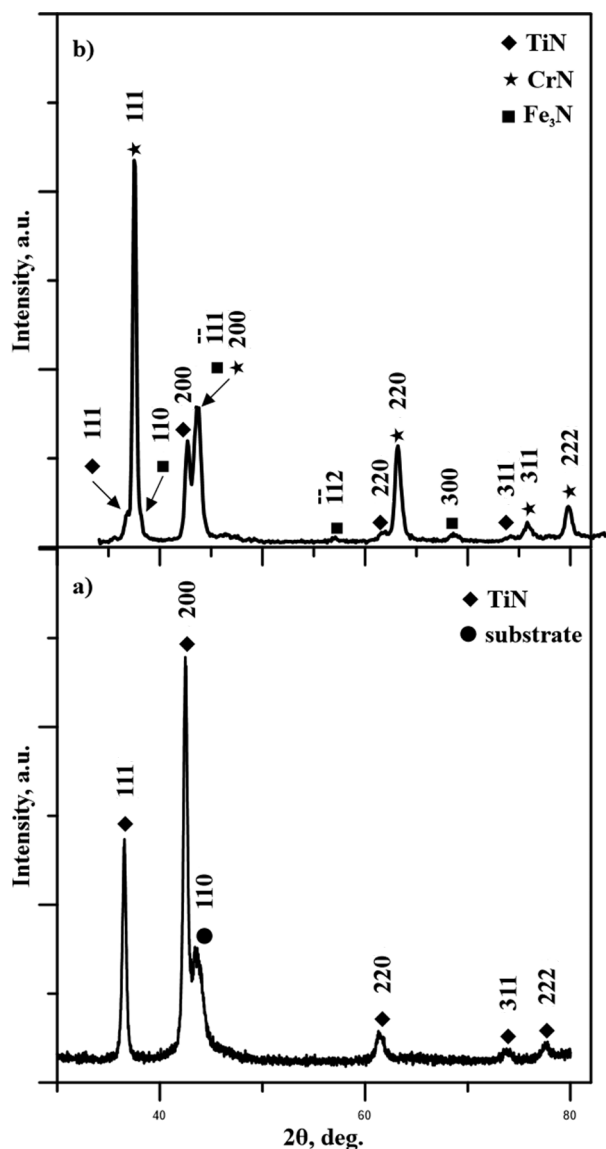
Fig. 2. XRD pattern of the samples with deposited TiN (a) and TiN/CrN (b) coatings.

In the case of multilayer TiN/CrN coating, the calculated lattice parameters are the following: a_{TiN} = 4.228 (±0.003) Å and a_{CrN} = 4.155 (±0.002) Å. It is clearly visible that for TiN it decreases while for CrN is closed to the theoretical one of 4.140 Å (PDF#11-0065). This means that the application of CrN layer on steel – TiN system is able to form additional residual stresses and microstrains in the TiN film but for the CrN coating it is monophasic with Cr-N stoichiometry. This problem has been investigated many times [29, 30, 31]. The possibility of formation of single phase structure of the deposited CrN coatings is able to reflect on significantly improved mechanical properties. Therefore, the application of the discussed above technology is able
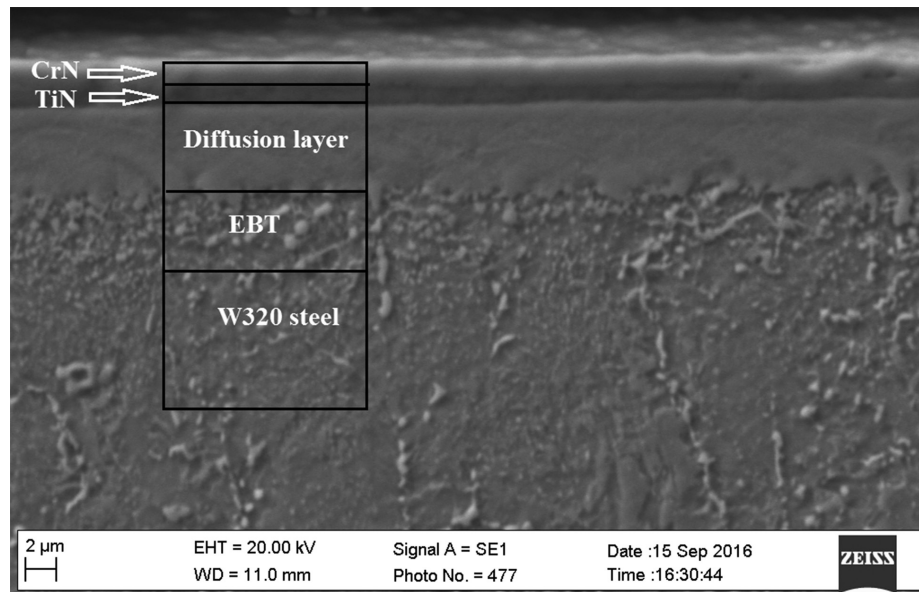
Fig. 3. Cross section SEM image of the sample with deposited TiN/CrN coatings.

to form single phase CrN coatings with improved exploitation properties.

A cross section SEM image of the sample with TiN/CrN coating is presented on Figure 3. The microstructure of the tool steel which acts as a substrate in the present particular case consists of equally-axes grains of ferrite. The grains become larger towards the core of the sample. The depth of the treated by electron-beam treatment zone is about 10–15 μm. Due to the plasma nitriding the diffusion layer with thickness of about 4–5 μm has been formed. The presence of the deposited TiN and CrN coatings is clearly visible as their thickness is about 1 μm for each layer.

CONCLUSIONS

DC magnetron sputtering system was used to deposit nanostructured TiN/CrN multilayer coatings on tool steel substrates. The control of the process parameters resulted in the deposition of a monolayer of TiN and multilayer TiN/CrN coatings with face-centered cubic structure. The obtained stoichiometry for the monolayer TiN coating is Ti-N, for the multilayer TiN/CrN it is Ti-N and Cr-N, which is of great interest from a practical point of view. The lattice parameters of TiN and CrN are similar with those from the ICDD database, which means that the amount of residual stresses and micro-strains is very low. The deposition of CrN coating on the preliminary deposited TiN layer is able to form monophasic CrN coating with the discussed above stoichiometry, which reflects on the improvement of the operational properties.

REFERENCES

1. O. V. Bondar, V. A. Stolbovoy, M. K. Kylyshkanov, S. V. Plotnikov, N. K. Erdybaeva, K. Piotrowska, K. Czarnacka, Czesław Karwat, *Prz. Elektr.*, **12**, 233 (2015).
2. S. Lin, K. Zhou, M. Dai, E. Lan, Q. Shi, F. Hu, T. Kuang, C. Zhuang, *Vacuum*, **122**, 179 (2015).
3. W. Aperador, A. Delgado, J. Duque, *Int. J. Electrochem. Sci.*, **8**, 10711 (2013).
4. M. Nordin, M. Larsson, S. Hogmark, *Surf. Coat. Technol.*, **106**, 234 (1998).
5. A. Cavaleiro, J. T. Hosson, *Nanostructure Coatings*, Springer Science+Business Media, LLC (2006).
6. F. Y. G. Silva, R. P. Martinho, A. P. M. Baptista, *Thin Solid Films*, **550**, 278 (2014).
7. M. Schlögl, J. Paulitsch, P. A. Mayrhofer, *Surf. Coat. Technol.*, **240**, 250 (2014).
8. C. Sabitzer, C. Steinkellner, C.M. Koller, P. Polcik, R. Rachbauer, P. H. Mayrhofer, *Surf. Coat. Technol.*, **275**, 185 (2015).
9. G. A. Zhang, P. X. Yan, P. Wang, Y. M. Chen, J. Y. Zhang, *Appl. Surf. Sci.*, **253**, 7353 (2007).

10. Q. Yang, C. He, L. R. Zhao, J-P. Immarigeon, *Scr. Mat.*, **46**, 293 (2002).
11. O. V. Sobol, A. A. Andreev, V. A. Stolbovoy, V. F. Gorban, N. V. Pinchuk, A. A. Meylekhov, *J. Nano-Electr. Phy.*, **7**, 01034-1 (2015).
12. A. D. Pogrebnjak, O. V. Bondar, G. Abadias, D. Eyidi, V. M. Beresnev, O. V. Sobol, B. O. Postolnyi, P. Zukowski, *Acta Phy. Pol. A*, **128**, 836 (2015).
13. H. C. Barshilia, K. S. Rajam, *Surf. Coat. Technol.*, **183**, 174 (2004).
14. S. Gallegos-Cantú, M. A. L. Hernandez-Rodriguez, E. Garcia-Sanchez, A. Juarez-Hernandez, J. Hernandez-Sandoval, R. Cue-Sampedro, *Wear*, **330–331**, 439 (2015).
15. P. Petrov, D. Dechev, V. Bondrachuk, D. Kozlenko, N. Ivanov, I. Martev, *J. Mat. Sci. Technol.* (in Bulgarian), **24**, 11 (2016).
16. S. Y. Lee, G. S. Kim, J. H. Hahn, *Surf. Coat. Technol.*, **177–178**, 426 (2004).
17. K. Rzepiejewska-Malyska, M. Parlinska-Wojtan, K. Wasmer, K. Hejduk, J. Michler, *Micron*, **40**, 22 (2009).
18. K. A. Aissa, A. Achur, J. Camus, L. Brizoual, P.Y. Jouan, M.A. Djonadi, *Thin Solid Films*, **550**, 264 (2014).
19. M. Hagarova, O. Blahova, J. Savkova, *Acta Metall. Sl.*, **15**, 221 (2009).
20. R. N. Ibrahim, M. A. Rahmat, R. H. Oskouei, R. K. Singh Raman, *Eng. Fract. Mech.*, **137**, 64 (2015).
21. D. Al. Colombo, M. D. Echeverría, S. Laino, R. C. Dommarco, J. M. Massone, *Wear*, **308**, 35 (2013).
22. R. Bayon, A. Igartua, X. Fernande, R. Martinez, R. J. Rodrıguez, J. A. Garcıa, A. Frutos, M. A. Arenas, J. Damborenea, *Trib. Inter.*, **42**, 591 (2009).
23. M. Sokovic, P. Panjan, R. Kirn, *J. Mater. Process. Technol.*, **157–158**, 613 (2004).
24. A. L. Bandeira, R. Trentin, C. Aguzzol, M. E. H. Maia da Costa, A. F. Michels, I. J. R. Baumvol, M. C. M. Farias, C. A. Figulroa, *Wear*, **301**, 786 (2013).
25. P. Panjan, B. Navinsek, A. Cvelbar, A. Zalar, J. Vlcek, *Surf. Coat. Technol.*, **98**, 1497 (1998).
26. Q. Yang, D. Y. Seo, L. R. Zhao, *Surf. Coat. Technol.*, **177–178**, 204 (2004).
27. I. Iordanova, P. J. Kelly, R. Mirchev, V. Antonov, *Vacuum*, **81**, 830 (2007).
28. V. Valvoda, *Surf. Coat. Technol.*, **80**, 61 (1996).
29. P. Petrov, M. Ormanova, D. Dechev, N. Ivanov, P. Chobanov, *J. Mat. Sci. Technol.*, 23, 153 (2015).
30. J. C. Avelar-Batista, E. Spain, J. Housden, G. G. Fuentes, R. Rebole, R. Rodriguez, F. Montala, L. J. Carreras, T. J. Tate, *Thin Solid Films*, **491**, 177 (2005).
31. O. V. Sobol, A. A. Andreev, V. A. Stolbovoy, N. V. Pinchuk, A. A. Meylekhov, *J. Nano- Electr. Phy.*, **7**, 01026-1 (2015).

ФАЗОВ СЪСТАВ НА МНОГОСЛОЙНО ПОКРИТИЕ TIN/CRN, ОТЛОЖЕНО ЧРЕЗ МАГНЕТРОННО РАЗПРАШВАНЕ

М. Орманова[1]*, Д. Дечев[1], Р. Бездушний[2], П. Петров[1]

[1] *Институт по Електроника – Българска Академия на Науките, бул. „Цариградско шосе" 72, 1784 София*
[2] *Катедра по Физика на твърдото тяло и микроелектроника, Физически факултет, Софийски Университет „Св. Климент Охридски", бул. „Джеймс Баучер" 5, 1164 София*

(Резюме)

Многослойното покритие от TiN/CrN е твърд и устойчив на износване материал, който се използва широко за изработка на режещи и формоващи инструменти и други компоненти работещи в среда с абразивно износване. Това изследване предлага комбиниран метод за повърхностна модификация на инструментални стомани включващ електронно-лъчева обработка (ЕЛО), плазмено нитриране (ПН) и многослойно покритие от TiN/CrN отложено чрез магнетронно разпрашване.

Фазовият и химичния състав, както и микроструктурата на слоевете са изследване чрез рентгенова дифракция; сканираща електронна микроскопия (СЕМ) и енергийно дисперсионна рентгенова спектроскопия, съответно.

В това изследване е демонстрирана възможност за формиране на многослойно покритие от TiN/CrN върху подложка от инструментални стомани.

Influence of TiO_2 on the thermal stability and crystallization of glasses within $TeO_2 – Bi_2O_3 – Nb_2O_5 – ZnO$ system

Sv. Ganev[1], S. Parvanov[1], S. Slavov[1], A. Bachvarova-Nedelcheva[2]*,
R. Iordanova[2], Y. Dimitriev[1]

[1] University of Chemical Technology and Metallurgy – Sofia, "Kl. Ohridski" blvd. 8, 1756 Sofia, Bulgaria

[2] Institute of General and Inorganic Chemistry, Bulgarian Academy of Sciences, "Acad. G. Bonchev" str., bld. 11, 1113 Sofia, Bulgaria

In this study we selected the $TeO_2 – Bi_2O_3 – Nb_2O_5 – ZnO$ system. The investigation covers TeO_2 – based glasses containing Nb_2O_5 and Bi_2O_3 up to 10 mol%, ZnO from 5 to 10 mol%, while the TiO_2 varies from 5 to 50 mol%. The obtained glasses were transparent and yellow colored (TiO_2 up to 20 mol%). The thermal stability of the samples was determined by DTA using the difference ΔT between exothermic peak of crystallization (T_x) and that for glass transition temperature Tg ($\Delta T = 50–115$ °C). Several crystalline phases were identified by XRD, between them more important are $ZnTeO_3$ and $TiTe_3O_8$ (in compositions above 20 mol% TiO_2) due to their good dielectric properties. The analysis of spectra shows that network of glasses consist mainly of TeO_4 (TBP) units. The preliminary electrical measurements showed that the samples are with low conductivity and there is no significant change of the dielectric losses up to 600 °C. The as-prepared crystalline samples are with low conductivity and good dielectric properties.

Keywords: glass-ceramics, thermal stability, structure, properties.

INTRODUCTION

Currently intensive search is going onto find dielectric materials for Low Temperature Cofired Ceramics (LTCC) technology, that are applicable in wireless communications and broadcasting industry. In the last years as a preferred method for preparation of ferro-electrics materials was used melt quenching and crystallization from glasses (glass-ceramics) [1]. The tellurite glass materials as a matrix are very suitable due to low melting temperature, chemical resistance, good dielectric properties and good solubility of heavy metal ions [2]. Up to now several three-component systems with the participation of Nb_2O_5, TeO_2, Bi_2O_3, ZnO have been studied. Glasses in the $TeO_2 – Nb_2O_5 – Bi_2O_3$ system [3] were characterized with good thermal stability and Tg of glasses are in the range 387–439 °C for compositions containing 85–90 mol% TeO_2. In the last investigation concerning the structure of glasses in the same system [4] was stated the formation of "anti-glass spherolites" and the short range order of glasses was determined by the high energy x-ray diffraction. In the $TeO – Nb_2O_5 – ZnO$ system [5] glasses have been obtained in the range 5–25% ZnO. In a four component glass composition $75TeO_2 – 10Bi_2O_3 – 10Nb_2O_5 – 5ZnO$ was established that introduction of Er^{3+} is suitable for laser materials [6]. In a system with participation of TiO_2 [7] was shown that Bi_2O_3 and TiO_2 influence the glass transition temperature (Tg). Titania (TiO_2) keeps the polymerized structure while Bi_2O_3 destroys the glass network. On the other hand, it was shown that TiO_2 [8] was effective nucleation agent to promote the three dimensional crystallization in $TeO_2 – Bi_2O_3 – Nb_2O_5$ system. Another interesting fact is that heat treatment in oxygen flow (solid state reaction or melting) leads to oxidation and formation of tellurites [9]. It was found that compositions in the $Bi_2O_3 – TiO_2 – TeO_2$ system crystallized as three-component compounds containing Te^{6+} ions. It was also established that these compounds possess good microwave dielectric properties. The above pointed results additionally motivated us to orientate our research toward tellurite glasses.

The purpose of this paper is to study the influence of TiO_2 on the thermal stability and crystallization of selected glasses within the $TeO_2 – Bi_2O_3 – Nb_2O_5 – ZnO$ system.

---
* To whom all correspondence should be sent:
E-mail: albenadb@svr.igic.bas.bg

EXPERIMENTAL

Samples preparation

All specimens are shown in Table 1. The batches were prepared using reagent grade TiO$_2$, TeO$_2$, Bi$_2$O$_3$, Nb$_2$O$_5$ and ZnO. They were homogenized of about 10 grams and were melted in air for 20–30 mins using silica crucibles at temperatures between 800–1100 °C. The melting temperature was selected depending on composition. Compositions containing higher TiO$_2$ (40 mol% – sample 6J and 50 mol% – sample 6K) content were melted at 1100 °C. The glass forming ability of the compositions was determined by pouring of the melts between two copper plates at cooling rate 10^1–10^2 K/s. The obtained glasses were transparent and yellow colored (samples containing up to 20 mol% TiO$_2$).

Samples characterization

The phase formation of the powdered samples was established by X-ray phase analysis with a Bruker D8 Advance diffractometer, using CuKα radiation in the 10 < 2theta < 80 range. The differential thermal analysis (DTA) of selected compositions was carried out on STA PT1600 with Pt/Pt/Rh thermocouples with a heating rate of 10 K/s in air flow, using Al$_2$O$_3$ as a reference material. The thermal stability of the samples was evaluated using the difference ΔT between exothermic effect of crystallization (T$_x$) and that for glass transition temperature Tg (ΔT = Tx – Tg). The IR spectra of the glasses were recorded in the 1400–400 cm^{-1} region using the KBr pellet technique (Nicolet-320 FTIR spectrometer). The optical spectra of selected powder samples at room temperature were recorded with a spectrometer (Evolution 300 UV-Vis Spectrophotometer) employing the integration sphere diffuse reflectance attachment. The samples were measured in the wavelength (λ) range of 200–800 nm with a magnesium oxide reflectance standard used as the baseline. The uncertainty in the observed wavelength is about ±1 nm. The Kubelka – Munk function (F(R∞)) was calculated from the UV–Vis diffuse reflectance spectra. Measurements of the electrical conductivity and dielectric losses of selected samples are performed by LCR Meter MS5308 (Shenzhen Master Industrial) with frequency of 1 kHz using two-terminal method with graphite electrodes.

RESULTS AND DISCUSSION

Phase characterization and thermal stability

The XRD patterns of investigated samples are shown in Fig. 1 (a, b, c, d, e, f) and Table 1 summarized the detected by XRD method main crystalline phases. As it is seen from the figure, both samples containing 5 and 10 mol % TiO$_2$ (samples 6D – 5TiO$_2$.72TeO$_2$.5ZnO.9Bi$_2$O$_3$.9Nb$_2$O$_5$ and 6C – 10TiO$_2$.60TeO$_2$.10ZnO.10Bi$_2$O$_3$.10Nb$_2$O$_5$) are amorphous. The increasing of TiO$_2$ content (20 mol%, sample 6E) led to partial crystallization and appearance of three crystalline phases TiTe$_3$O$_8$ (JCPDS 24-1348), TeO$_2$ (JCPDS 52-0795) and TiO$_2$ (rutile,

Table 1. Detected by XRD crystalline phases and observed by DTA effects in all investigated samples

Sample (abbrev.)	Compositions	Detected crystalline phases by XRD	Observed by DTA effects		
		1100 °C (20 mins)	Tg, °C	Tx, °C	DT = Tx – Tg
6K	50TiO$_2$.20TeO$_2$.10ZnO.10Bi$_2$O$_3$.10Nb$_2$O$_5$	crystals ZnTeO$_3$ + Rutile (TiO$_2$) + TiTe$_3$O$_8$	–	–	–
6J	40TiO$_2$.30TeO$_2$.10ZnO.10Bi$_2$O$_3$.10Nb$_2$O$_5$	glass + crystals TiTe$_3$O$_8$ + TeO$_2$ + (TiO$_2$) Rutile + ZnTeO$_3$	–	–	–
6I	30TiO$_2$.40TeO$_2$.10ZnO.10Bi$_2$O$_3$.10Nb$_2$O$_5$	glass + crystals TiTe$_3$O$_8$ + TeO$_2$ + TiO$_2$ (Rutile)	–	–	–
6E	20TiO$_2$.50TeO$_2$.10ZnO.10Bi$_2$O$_3$.10Nb$_2$O$_5$	glass + crystals TiTe$_3$O$_8$ + TeO$_2$ + TiO$_2$ (Rutile)	420	Tx$_1$ = 470 Tx$_2$ = 500	50
6C	10TiO$_2$.60TeO$_2$.10ZnO.10Bi$_2$O$_3$.10Nb$_2$O$_5$	glass	355	Tx$_1$ = 470 Tx$_2$ = 550	115
6D	5TiO$_2$.72TeO$_2$.5ZnO.9Bi$_2$O$_3$.9Nb$_2$O$_5$	glass	380	Tx$_1$ = 480 Tx$_2$ = 530	100
VI – O	80TeO$_2$.10Bi$_2$O$_3$.10Nb$_2$O$_5$	glass	345	Tx$_1$ = 420 Tx$_2$ = 465	75
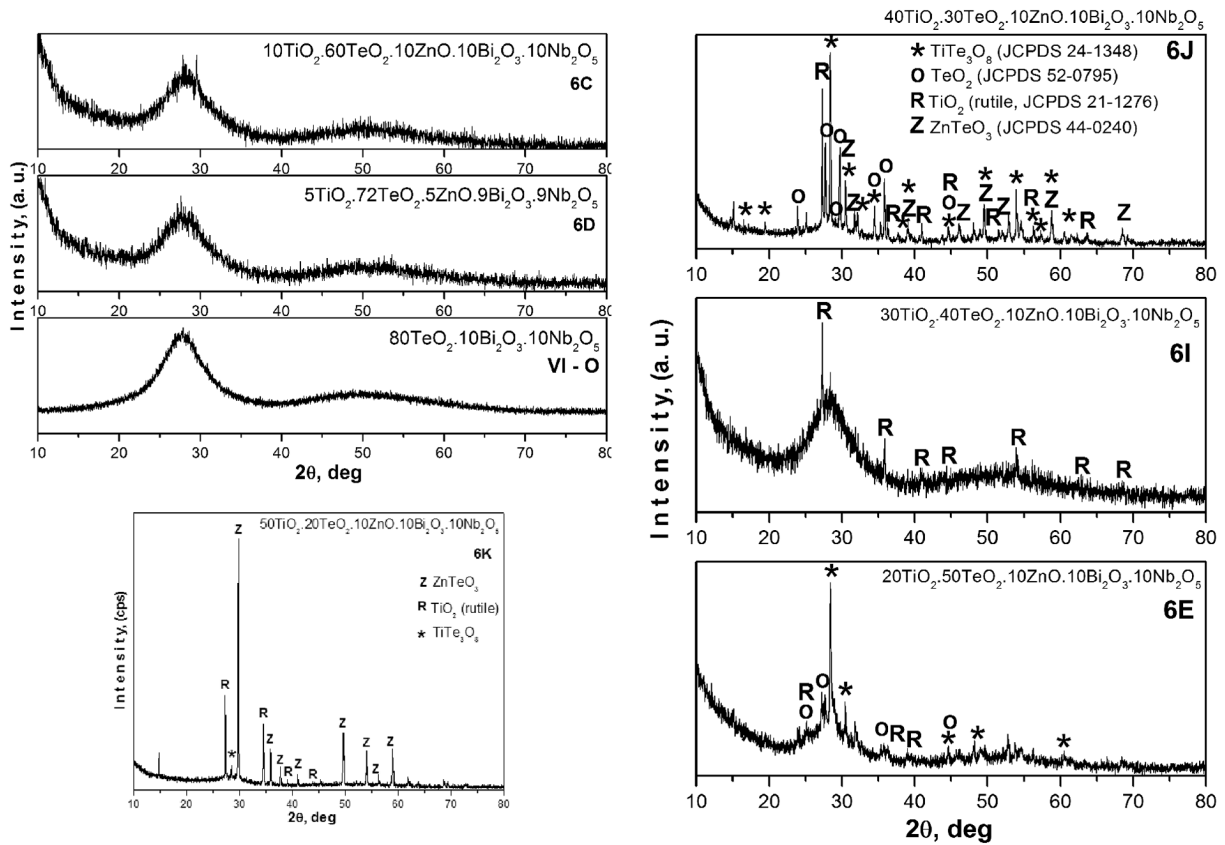
Fig. 1. XRD patterns of the obtained samples: 80TiO₂.10Bi₂O₃.10Nb₂O₅ (VI-0), 5TiO₂.72TeO₂.5ZnO.9Bi₂O₃.9Nb₂O₅ (6D); 10TiO₂.60TeO₂.10ZnO.10Bi₂O₃.10Nb₂O₅ (6C); 20TiO₂.50TeO₂.10ZnO.10Bi₂O₃.10Nb₂O₅ (6E); 30TiO₂.40TeO₂.10ZnO.10Bi₂O₃. 10Nb₂O₅ (6I); 40TiO₂.30TeO₂.10ZnO.10Bi₂O₃.10Nb₂O₅ (6J); 50TiO₂.20TeO₂.10ZnO.10Bi₂O₃.10Nb₂O₅ (6K).

JCPDS 21-1276). At further increasing in TiO₂ content (30 mol%, sample 6I) the XRD pattern exhibited preserving of the amorphous phase along with simultaneous presence of TiO₂ (rutile) and ZnTeO₃ (JCPDS 44-0240). At 40 mol% TiO₂ all above pointed crystalline phases (TiTe₃O₈, TeO₂, rutile and ZnTeO₃) were detected. For sample 6K, containing highest TiO₂ amount (50 mol%) TiTe₃O₈, rutile and ZnTeO₃ were registered without TeO₂. Bearing in mind the obtained results, it could be summarized that addition of above 20 mol% TiO₂ stimulates the crystallization tendency of compositions.

The thermal parameters obtained from DTA curves of quenched samples are summarized in Table 1 and shown in Figure 2. They are characterized with the glass transition temperature (Tg) in the range of 345–378 °C and glass crystallization temperatures (Tx) above 400 °C. In all investigated samples two glass crystallization temperatures were observed related to the separation of two crystalline phases detected by XRD (Fig. 1a, b, c). The calculated ΔT = Tx – Tg was found to be in the range 50–115 °C that determines a good thermal stability
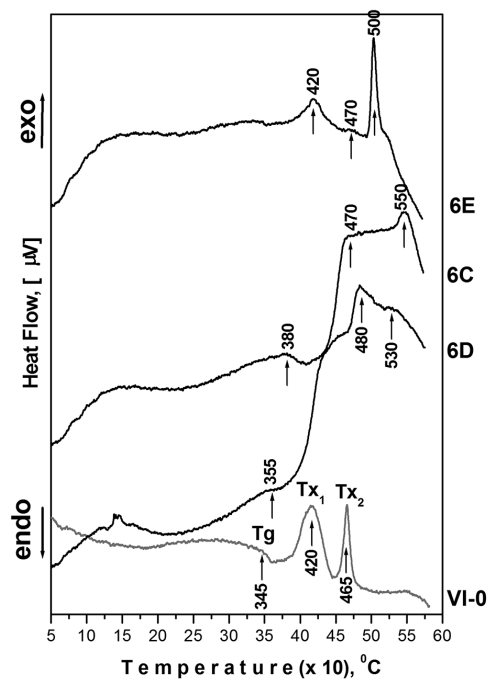
Fig. 2. DTA curves of selected samples VI-O, 6D, 6C and 6E.

of the investigated samples. A selected glass composition (6I) that is X-ray amorphous (Fig. 1b) was subjected to heat treatment at temperature near the glass crystallization temperature (500 °C) in order to identify the products of crystallization. Figure 3 presented the XRD result for sample 6I after 6 h heat treatment at 500 °C. The main crystalline phases TeO_2 and $TiTe_3O_8$ were detected which is different than the XRD result after the free cooling of the melt, where mainly TiO_2 (rutile) crystallized in the amorphous matrix (Fig. 1b).

IR and UV-Vis spectra

The IR spectra of investigated samples are shown in Fig. 4a, b. Two well resolved bands are observed with maxima near 630 and 470 cm⁻¹, as well as very small shoulder near 780 cm⁻¹. The assignment of the bands is made in the framework of the local point symmetry approaches following the methods developed by Nakamoto and Tart [10, 11]. Most of the compositions are with high tellurium dioxide content (50–80 mol%). That is why their spectra will be considered as that for tellurite systems. In amorphous state for tellurite compositions

containing TeO_4 units, according our previous studies on tellurite glasses [12–15], the intensity of v^s_{ax} at 635 cm⁻¹ increases markedly instead of v^{as}_{ax} and becomes a determining one. On one hand, $ZnTeO_3$ which contains distorted TeO_3 units [16, 17] is characterized by bands at 770, 700 and 670 cm⁻¹. As it was suggested in our previous studies, the observed bands are result from removal of the degeneracy of v^d band of TeO_3 vibrations units with C_{3v} point symmetry [12]. On the other hand, $Zn_2Te_3O_8$ which contains two TeO_3^+ units connected with oneTeO_4 units [18] possesses three bands near 750, 685 and 555 cm⁻¹ [10]. For the $TiTe_3O_8$ compound witch has cubic structure [19] the observed bands are at 770, 700 cm⁻¹ and more intensive ones at 670 and 620 cm⁻¹. These bands are cubic for the cubic $TiTe_3O_8$ containing TeO_4 units [12, 20]. That is why the obtained results give us the reason to accept that the structure of the investigated glasses (short range order) is determined by TeO_4 units mainly (bands near 630 cm⁻¹). Probably they participated in the formation of bridging bonds Te–O–Te and Te–O–Ti. The influence of Nb_2O_5, Bi_2O_3 and ZnO is not discussed because their content is near than 10 mol%. Nevertheless, the intensive band around 470 cm⁻¹
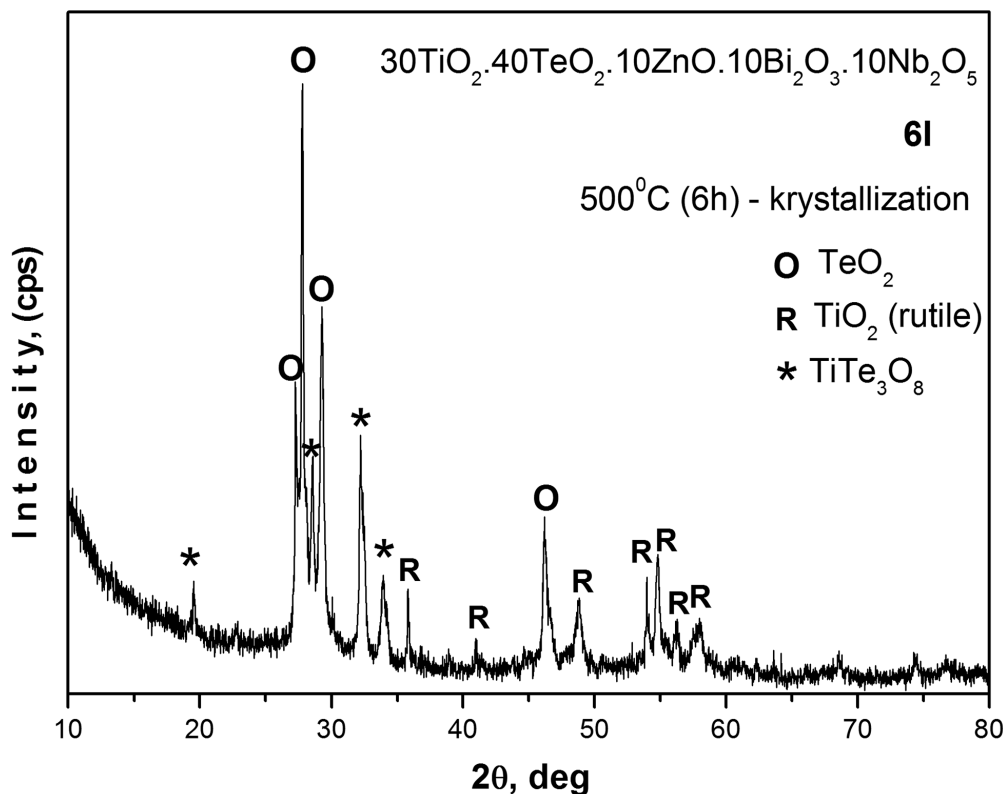
Fig. 3. XRD patterns of (a) $30TiO_2.40TeO_2.10ZnO.10Bi_2O_3.10Nb_2O_5$ (6I) parent sample; (b) sample, heat treated at 600 °C for 5 h.

which obviously is a complex one, is due probably to the vibrations of different building units, such as TiO_6, BiO_n and ZnO_n [20]. In this spectral region are also the symmetric vibrations of the Te–O–Te bridges connecting different tellurite complexes.

The UV-Vis spectrum of a representative composition containing 30 mol% TiO_2 (6I) is shown in Fig. 5. It exhibits two weak absorption maxima at 255 and 260 nm and a stronger one at 330 nm. It is well known that the transitional metal oxides with d° electron configuration give absorption bands in UV-Vis region due to oxygen – metal charge transfer [21]. The position of this electron transfer depends on the ligand field symmetry surrounding the metal (Me) site. For oxygen ligands, the energy transition between 220 and 260 nm is expected for tetrahedral Me compared while for octahedral – between 250 and 360 nm [21, 22]. As it was mentioned above the band at 330 nm is the strongest one which probably suggest the dominate presence of TiO_6 polyhedra. That is why in the IR spectra only one band at 470 cm⁻¹ was observed and the band near 930 cm⁻¹ corresponding to TiO_4 units is absent (Fig. 4).

Dielectric measurements

The preliminary electrical measurements of as prepared sample 6E ($20TiO_2.50TeO_2.10ZnO.10Bi_2O_3.10Nb_2O_5$) containing glass and several crystalline phases (Table 1) is with low conductivity and good dielectric properties (Fig. 6a, b). As it is seen there is no significant change of the dielectric losses with the temperature increasing up to 600 °C.

CONCLUSIONS

Applying the melt quenching method glasses were prepared in the multicomponent $TiO_2 – TeO_2 – Bi_2O_3 – Nb_2O_5 – ZnO$ system and they exhibited

Fig. 4. IR spectra of investigated samples.
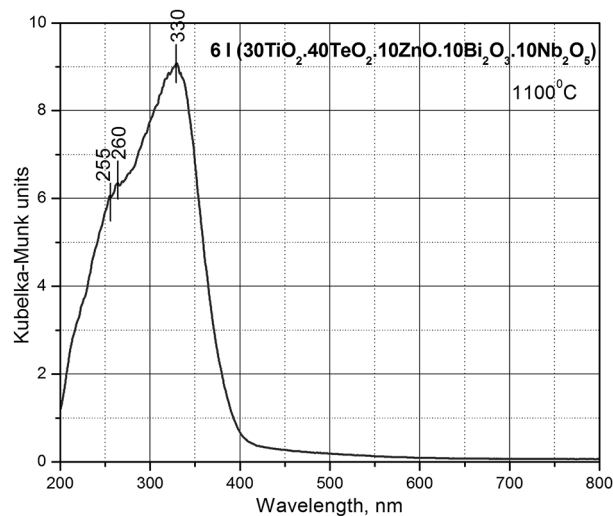
Fig. 5. UV-Vis spectrum of sample 6I ($30TiO_2.40TeO_2.10ZnO.10Bi_2O_3.10Nb_2O_5$).
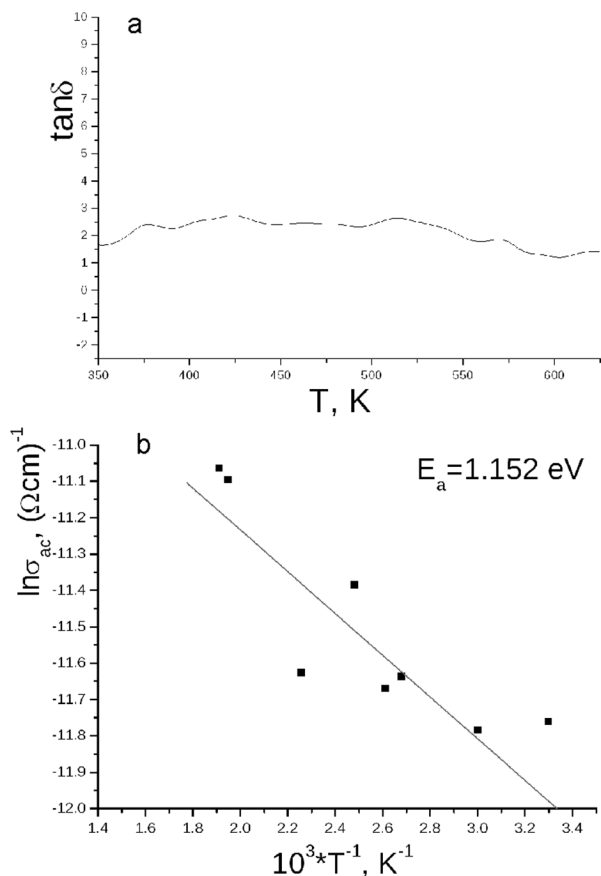
Fig. 6. Electrical measurements of sample 6E (20TiO$_2$.50TeO$_2$.10ZnO.10Bi$_2$O$_3$.10Nb$_2$O$_5$): (a) dielectric losses depending on temperature and (b) Arrhenius plot of activation energy.

good thermal stability up to 400 °C. By IR spectra is proved that the short range order of glasses is determined by TeO$_4$ structural units. It was established that the addition of above 20 mol% TiO$_2$ facilitated the crystallization tendency of investigated compositions. By free cooling of the melts, polycrystalline samples were obtained containing mainly ZnTeO$_3$, TiTe$_3$O$_8$ crystalline phases possessing good dielectric properties.

REFERENCES

1. V. K. Marghussian, Nano-Glass Ceramics, Elsevier Inc. (2015).
2. El-Malawany R, Tellurite glasses, Physical properties and data, CRC Press (2002).
3. Y. Wang, S. Dai, F. Chen, T. Xu & Q. Nie, *Mater. Chem. Phys.*, **113**, 407 (2009).
4. El Sayed Yousef, H. H. Hegazy, S. Almojadah, M. Reben, *Optics & Laser Technol.*, **74**, 138 (2015).
5. M. M. Ahmad, El Sayed Yousef, El Sayed Moustafa, *Physica B*, **371**, 74 (2006).
6. M. C. Wilding, G. Delaizir, Ch. Benmore, Y. Gueguen, M. Dolhen, J.-R. Duclere, S. Chenu, S. Sukenaga, P. F. McMillan, *J. Non-Cryst. Sol.*, (2016) (in press).
7. M. Udovic, P. Thomas, A. Mirgorodsky, O. Durand, M. Soulis, O. Masson, T. Merle – Mejean, J. C. Champarnaud – Mesjard, *J. Sol. State. Chem.*, **179**, 3252 (2006).
8. F. Chen, Q. Yu, B. Qiao, S. Dai, Q. Zhang, *J. Non – Cryst. Sol.*, **404**, 32 (2016).
9. M. Udovic, D. Suvorov, *J. Amer. Ceram. Soc.*, **90** (8), 2404 (2007).
10. K. Nakamoto, Infrared and Raman Spectra of Inorganic and coordination compounds, Wiley, New York, 1978.
11. P. Tarte, *Spectrochim. Acta*, **I8**, 467 (1962).
12. M. Arnaudov, V. Dimitrov, Y. Dimitriev, L. Markova, *Mater. Res. Bull.*, **17** (9) 1121 (1982).
13. Y. Dimitriev, V. Dimitrov, M. Arnaudov, *J. Mater. Sci.*, **18** (5), 1353 (1983)
14. M. Arnaudov, Y. Dimitriev, *Phys. Chem. Glasses*, **42** (2), 99 (2001).
15. R. Gegova, A. Bachvarova-Nedelcheva, R. Iordanova, Y. Dimitriev, *Bulg. Chem. Commun.*, **47** (1), 378 (2015).
16. K. Hanke, *Naturwissen*, **54**, 199 (4967).
17. H. Burger, W. Vogel, V. Kozhkharov & M. Marinov, J. Mater. Sci., **19**, 403 (1984).
18. K. Hanke, *Naturwissen*, **55**, 273 (1966).
19. G. Meunier and J. Galy, *Acta Cryst.*, **B27**, 602 (1971).
20. O. Yamaguchi, M. Morimi, H. Kawabata et al., *J. Amer. Ceram. Soc.*, **70**, c97 (1987).
21. R. S. Singh & S. P. Singh, *J. Mater. Sci.*, **36**, 1555 (2001).
22. R. J. H. Clarck, Chemistry of titanium and vanadium, Elsevier, Amsterdam, 1968.

ВЛИЯНИЕ НА TiO_2 ВЪРХУ ТЕРМИЧНАТА СТАБИЛНОСТ И КРИСТАЛИЗАЦИЯТА НА СТЪКЛА В СИСТЕМАТА $TeO_2 - Bi_2O_3 - Nb_2O_5 - ZnO$

Св. Ганев[1], С. Първанов[1], С. Славов[1], А. Бъчварова-Неделчева[2]*,
Р. Йорданова[2], Я. Димитриев[1]

[1] *Химикотехнологичен и металургичен университет – София, бул. „Кл. Охридски" 8,
1756 София, България*
[2] *Институт по обща и неорганична химия, Българска академия на науките,
ул. „Акад. Г. Бончев", бл. 11, 1113 София, България*

(Резюме)

В настоящото изследване като обект е избрана системата TeO_2–Bi_2O_3–Nb_2O_5–ZnO. Статията разглежда телуритни стъкла, съдържащи Nb_2O_5 и Bi_2O_3 до 10 мол.%, ZnO от 5 до 10 мол.%, докато съдържанието на TiO_2 варира от 5 до 50 мол.%. Получените стъкла са прозрачни и жълти на цвят (състави съдържащи над 20 мол.% TiO_2). Термичната стабилност на образците е определена чрез ДТА, използвайки разликата ΔT между екзотермичния пик на кристализация (T_x) и данните за температурата на застъкляване Tg (ΔT = 60–95 °C). Чрез рентгенофазов анализ са идентифицирани няколко кристални фази, сред които най-важни са $ZnTeO_3$ и $TiTe_3O_8$ (в състави, съдържащи над 20 мол.% TiO_2), притежаващи добри диелектрични свойства. Анализът на спектрите показа, че аморфната мрежа е изградена предимно от TeO_4 (ТВР) структурни единици. Предварителните електрични измервания показаха незначителни изменения на диелектричните загуби с повишаване на температурата до 600 °C. Получените кристални образци са с ниска проводимост и добри диелектрични свойства.

Crystallization of gels in the binary $TiO_2 - M_nO_m$ (M_nO_m = TeO_2, SeO_2, B_2O_3, ZnO) systems

A. Bachvarova-Nedelcheva[1]*, R. Iordanova[1], R. Gegova[1], Y. Dimitriev[2]

*[1] Institute of General and Inorganic Chemistry, Bulgarian Academy of Sciences,
"Acad. G. Bonchev" str., bld. 11, 1113 Sofia, Bulgaria*
*[2] University of Chemical Technology and Metallurgy – Sofia, "Kl. Ohridski" blvd, 8,
1756 Sofia, Bulgaria*

The present investigation deals with the sol-gel synthesis and phase characterization of binary $TiO_2 - M_nO_m$ (M_nO_m = TeO_2, SeO_2, B_2O_3, ZnO) powders with nominal composition $80TiO_2.20M_nO_m$. The competitive influence of different components on the phase formation was verified. According to XRD analysis the heat treated up to 300 °C gels exhibit a predominantly amorphous phase and formation of metallic tellurium or TiO_2 (anatase). The amount of amorphous phase gradually decreases with the temperature increase. Further increase of the temperature (700 °C) results in obtaining of polyphase products containing a mixture of several crystalline phasses (rutile, anatase, $TiTe_3O_8$ and $ZnTiO_3$). The heat treatment of the compositions containing H_2SeO_3 or H_3BO_3 leads to earlier crystallization of TiO_2 (anatase) about 300 °C while in the case of compositions containing Zn acetate or H_6TeO_6, TiO_2 is formed at higher temperatures 400 and 500 °C, respectively.

Keywords: sol-gel, composites, X-ray diffraction.

INTRODUCTION

The sol-gel method is an attractive alternative to the melt quenching route that may be used to extend synthesis and application of new compositions which are usually difficult to be prepared by conventional ceramic routes. Most of the problems that arose during the synthesis of these compositions are related to high melting temperatures, tendencies toward crystallization or liquid phase separation [1]. The sol-gel method also allows to overcome the problems with evaporation of some components such as SeO_2 [2]. It is well known that for the sol-gel synthesis, the titania (TiO_2) is widely used as a main component because its alkoxides are well developed. Up to now low temperature glasses are obtained in the $TiO_2–TeO_2$ binary system rich in TeO_2 (> 70 mol%) by melt quenching [3–5] and sol-gel techniques [6, 7]. First investigations in this system were performed by Weng and Hodgson which in a series of papers reported for the successful synthesis of TeO_2 based thin films and powders [6, 8–10].

Hayakawa et al. [7] prepared the TeO_2/TiO_2 thin films by sol–gel method and studied their optical properties. However, there are scarce data for the sol-gel synthesis of rich in titania (above 70 mol%) TiO_2/TeO_2 compositions [10]. For the binary $TiO_2–SeO_2$ system, several papers have been published concerning mainly the photocatalytic properties of obtained composites [11–16]. In the other binary $TiO_2–B_2O_3$ system, glasses have not been obtained and in the wide concentration range TiO_2 crystallize and phase separation was observed [17]. The photoactivity of $TiO_2–B_2O_3$ catalysts was improved by the boron content [18]. Up to now, many studies have described the sol-gel synthesis of composite materials in the binary TiO_2-ZnO system and their enhanced photocatalytic activity [19, 20]. It was found that the coupled semiconductor TiO_2/ZnO photocatalyst exhibits higher photodegradation efficiency compared to that of the single phase [21–23]. Among all investigations on metal or non – metal ion doping of TiO_2 there are still many unsolved problems concerning the competitive influence of the second component on the phase transformations of TiO_2 upon the heating as well as the thermal stability of the obtained products. This additionally motivates our study, which is a part of our investigations on sol–gel derived composite powders in dif-

ferent binary and ternary systems [24–30]. Several oxides were selected as a second component: a classical network former (B_2O_3), conditional network formers (TeO_2, SeO_2) and an intermediate oxide (ZnO). Bearing in mind our experience on glass formation, structure and properties in different tellurite, selenite, titanate and borate systems as well as the problems that arose during their synthesis [1, 2, 31], we selected several samples with nominal composition $80TiO_2.20M_nO_m$ (M_nO_m = TeO_2, SeO_2, B_2O_3, ZnO) (Table 1).

The present investigation deals with the thermal stability of selected binary gels as well as their phase evolution upon heating up to 700 °C. The competitive influence of different components on the phase formation is verified.

EXPERIMENTAL

Samples preparation

Several samples with nominal compositions $80TiO_2.20M_nO_m$ (M_nO_m = TeO_2, SeO_2, B_2O_3, ZnO) have been selected for detailed investigation. They are situated in the gel formation regions pointed out in our previous investigations [24, 29, 32]. The gelation time for the investigated compositions was from 1 to 5 mins. The aging of gels was performed in air for several days in order to allow further hydrolysis. The compositions, for which precipitates were observed during the synthesis, were not considered as gels and they were not included in the gel formation regions. The investigated compositions are denoted as follow: $80TiO_2.20TeO_2$ (*sample A*), $80TiO_2.20SeO_2$ (*sample B*), $80TiO_2.20B_2O_3$ (*sample C*) and $80TiO_2.20ZnO$ (*sample D*). A different scheme for synthesis with new combination of precursors (organic and inorganic) was applied in this study. Titanium butoxide was used as a main precursor, while the other components were introduced as telluric (VI) acid (H_6TeO_6), selenous acid (H_2SeO_3), boric acid (H_3BO_3) and zinc acetate [$Zn(O_2CCH_3)_2.2H_2O$]. Zinc acetate was used instead of zinc nitrate because during the experiments gels were not obtained using the inorganic precursor. As it was already mentioned in our previous papers, the additional reason to use telluric (VI) acid instead of tellurium alkoxides is its high hydrolysis rate [33, 34]. Ethylene glycol ($C_2H_6O_2$) (99% Aldrich) was chosen as a main solvent. The scheme for synthesis is presented in Figure 1. Solutions (A and B) were prepared via dissolution of the precursors in ethylene glycol by means of vigorous stirring. Thus, transparent gels were obtained and their aging was performed in air for several days in order to allow further hydrolysis. The as-prepared gels were sub-

jected to heating at ~150 °C and subsequently to calcination in the temperature range 200–700 °C. The stepwise heating of the samples from 200 to 700 °C for one hour exposure time in air was performed, until powders were obtained. The calcination temperature was selected on the basis of our previous investigations [24–30].

Samples characterization

The decomposition process of the as prepared and aged in air gels was determined by differential thermal analysis (LABSYS™ EVO apparatus) with Pt-Pt/Rh thermocouple at a heating rate of 10 K/min in air flow, using Al_2O_3 as a reference material. The accuracy of the temperature was ± 5 °C. The heating of the samples was limited up to 600 °C. Bearing in mind that the selenite materials are characterized with high volatilization tendency and the sublimation of SeO_2 occurs above 315 °C at atmospheric pressure the DTA – TG was not performed for sample B ($80TiO_2.20SeO_2$). Gases evolved (EGA) during the thermal treatments were analyzed by mass spectrometry (MS) with a Pfeiffer OmniStar™ mass spectrometer. Mass spectra recorded for samples A, C and D (Fig. 3a, b, c) show the m/z= 15, 18 and 44 signals, being ascribed to CH_3, H_2O and CO_2, respectively. Powder XRD patterns of the heat treated in the temperature range 200–700 °C powdered samples were registered at room temperature with a Bruker D8 Advance diffractometer using Cu-Kα radiation. The average crystallite sizes of the powders at selected temperatures were calculated using Sherrer's equation. The morphology of selected samples was examined by scanning electron microscopy (SEM) using a JEOL JSM 6390 electron microscope (Japan), equipped with an ultrahigh resolution scanning system (ASID-3D). The accelerating voltage was 20 kV, I ~65 µA. Transmission Electron Microscopy (TEM) investigations were performed on a JEOL JEM 2100 instrument at an accelerating voltage of 200 kV. The specimens were prepared by grinding and dispersing them in ethanol by ultrasonic treatment for 6 mins. The suspensions were dripped on standard carbon/Cu grids. The measurements of lattice-fringe spacing recorded in HR-TEM micrographs were made using digital image analysis of reciprocal space parameters. The analysis was carried out by the Digital Micrograph software.

RESULTS AND DISCUSSION

Thermal stability of the gels

The transparent gels were prepared applying the scheme shown in Figure 1 that summarizes all ex-
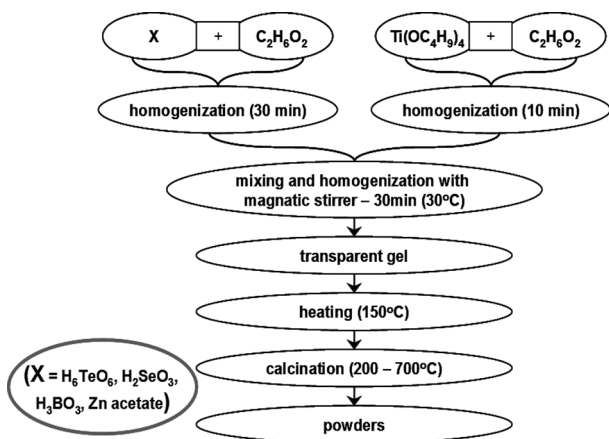
Fig. 1. Scheme for the sol-gel synthesis of TiO$_2$/M$_n$O$_m$ gels.

perimental details already discussed above. The gelation proceeded immediately and the gel formation regions in the binary systems TiO$_2$ – TeO$_2$, TiO$_2$ – SeO$_2$, TiO$_2$ – B$_2$O$_3$ and TiO$_2$ – ZnO were determined (Fig. 2a–d).

DTA/TG curves of as-prepared gels (samples A, C and D) are presented in Fig. 3a–c and their thermal stability was compared to those of pure Ti butoxide [32]. The thermal stability of pure Ti butoxide (TBT) was already discussed in our previous investigations [32]. Generally, several peaks are marked on the DTA/TG curves for all samples (A, C and D) and their thermal behavior is similar to those of the TBT. The common feature of all DTA curves is the appearance of an endothermic effect about 100–110 °C which is attributed to the evaporation of organic solvent and desorption of physically adsorbed water. This peak is accompanied by a weight loss which varies depending on composition (~7% for sample A, ~23% – sample C and ~4% for sample D). The differences in the DTA results concern the exothermic effects that are specific for each composition. The DTA/TG curves for the sample A (80TiO$_2$.20TeO$_2$) showed two broad exothermic peaks registered at about 235 and 285 °C (Fig. 3a). The first one is related to the beginning of the decomposition of the organic groups (weight loss is ~8%) as in the pure TBT. The second exothermic effect appeared at slightly higher temperature (285 °C) with around 15% weight loss which suggests strong combustion of the organic components [34]. The increasing of the curve intensity about 400 °C suggests the presence of an exothermic effect due to the oxidation of Te to TeO$_2$. For comparison, other authors established that the oxidation proceeded at similar temperatures [9, 35, 36]. As it can be seen from the DTA/TG curves of

sample C (80TiO$_2$.20B$_2$O$_3$) two exothermic effects are distinguished (Fig. 3b). The first and sharper one is observed about 310 °C and could be related to the intense combustion of the alkoxide groups bonded to the Ti-atom. According to the TG curve this peak is accompanied by strong weight loss (~ 65%). Contribution to this exothermic effect has also the crystallization of TiO$_2$ (anatase) established by XRD which is further discussed in the paper. The second exothermic peak (about 570°C) is as-
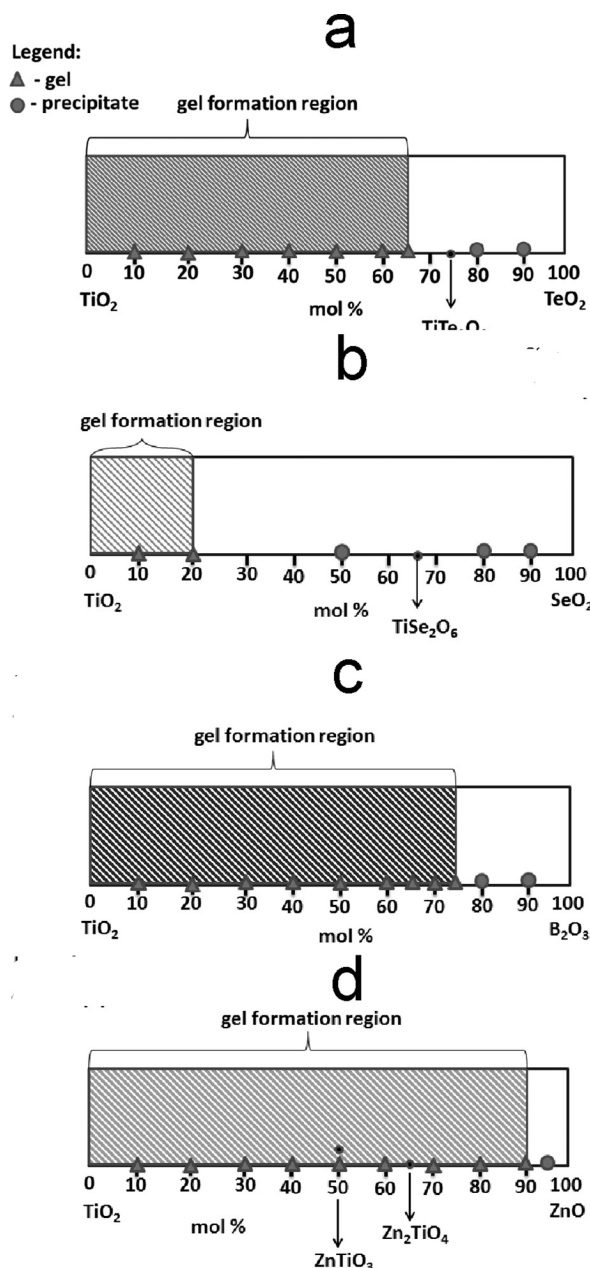
Fig. 2. Gel formation regions in the binary systems: TiO$_2$ – TeO$_2$ (a), TiO$_2$ – SeO$_2$ (b), TiO$_2$ – B$_2$O$_3$ (c) and TiO$_2$ – ZnO (d).
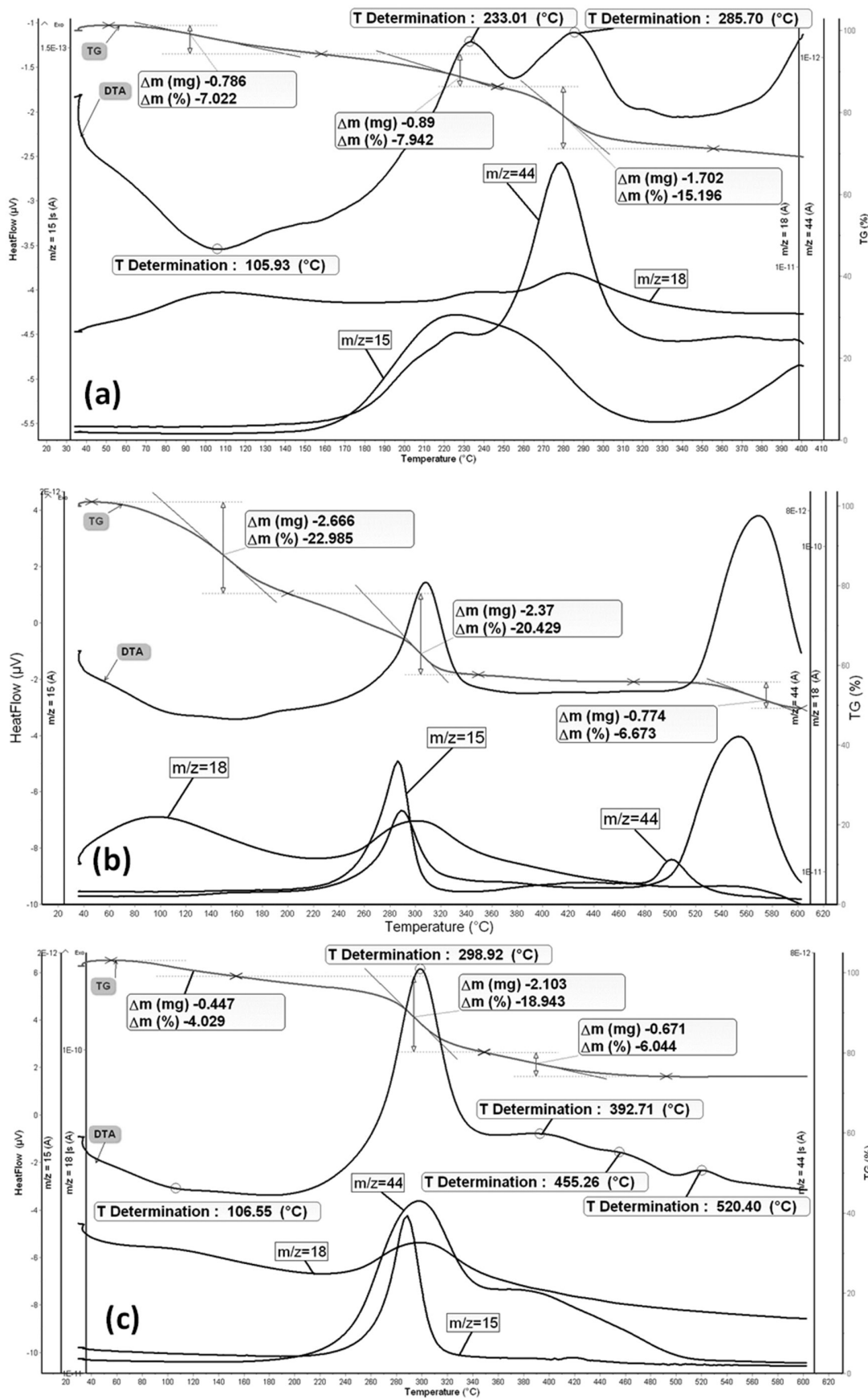
Fig. 3. DTA–TG curves of samples A (80TiO₂.20TeO₂) (a), C (80TiO₂.20B₂O₃) (b), D (80TiO₂.20ZnO) (c).

sociated with the slow oxidation of residual carbon and release of CO_2 accompanied by a little weight loss about 7%. Similar data are obtained by other authors [35–37]. Several exothermic effects at 300, 400, 455 and 520 °C were found in sample D ($80TiO_2.20ZnO$) (Fig. 3c). The first one (~ 300 °C) is the strongest and broadest one and it is related by analogy with the previous samples to the intense combustion of organics (the weight loss is ~ 20%). The next two and small exothermic peaks (at 400 and 455 °C) could be attributed to the crystallization of TiO_2 (anatase) and $ZnTiO_3$ crystalline phases (weight loss about 6%). The last one at 520 °C is associated with the slow oxidation of residual carbon and release of CO_2.

Phase transformations and morphology

The obtained by XRD analysis data are summarized in Table 1. According to the XRD patterns, all samples are amorphous at 200 °C and only in XRD pattern of sample A ($80TiO_2.20TeO_2$) unknown peaks probably due to the organics were detected (Fig. 4). Upon heating, in the temperature range 200–400 °C composite materials consisting of amorphous part and crystalline phases are obtained. For sample A in this temperature range only metallic tellurium (JCPDS 78-2312) was detected, while in the other three samples the first crystals of TiO_2 (anatase) (JCPDS 78-2486) appeared (Fig. 4). It is worth noting that the anatase appeared earlier (300 °C) in samples B ($80TiO_2.20SeO_2$) and C ($80TiO_2.20B_2O_3$) than in sample D ($80TiO_2.20ZnO$), where it was barely registered at 400 °C. For comparison, in pure TBT gel, the anatase crystallization occurs at 400 °C [32]. Irrespective of the fact that

inorganic precursors (H_6TeO_6, H_2SeO_3 and H_3BO_3) were used, we found similar results for phase transformations obtained by other authors [7, 8, 34, 38–40]. The average crystallites size of metallic Te (in sample A) is 27 nm at 250 °C and it increased up to 42 nm at higher temperatures (300 and 400 °C). Tellurium is fully oxidized to TeO_2 (JCPDS 42-1365) above 400 °C in sample A. In addition to TeO_2 the heating at 500 °C of this sample showed presence of $TiTe_3O_8$ (JCPDS 50-0250) and TiO_2 (anatase). At this temperature only TiO_2 (anatase) is registered in the XRD patterns of samples B and C, while in sample D – TiO_2 (anatase) with $ZnTiO_3$ (cubic, JCPDS 39-0190) crystalline phases. At further heating (600 °C), partial transformation of anatase to rutile (JCPDS 21-1276) is detected only in sample B ($80TiO_2.20SeO_2$) while rutile appeared in the other samples at 700°C. The average crystallite size of anatase in all samples (A, B, C and D) heated in the temperature range 400–600 °C was summarized in Table 2. As it is seen from the Table, at 500 °C sample A ($80TiO_2.20TeO_2$) and B ($80TiO_2.20SeO_2$) exhibited more nanosized crystallites (sample A – 10 nm, sample B – 12 nm) in comparison to samples C ($80TiO_2.20B_2O_3$, 75 nm) and D ($80TiO_2.20ZnO$, 90 nm). At higher temperature (600 °C) this tendency is preserved.

Sample B ($80TiO_2.20SeO_2$) heat treated at 200 and 400 °C was subjected for SEM (Fig. 5) and TEM (Fig. 6) investigations in order to verify its morphology as well as the existence of selenium. As one can see, small pieces as a result from the crashing of the monolithic gels during the drying process are observed with average size about 50–150 µm. Small bright spots are distinguished in some areas on the sample surface. The microprobe

Table 1. Detected by XRD crystalline phases in the investigated compositions

Compositions	Detected crystalline phases by XRD					
	200 °C	300 °C	400 °C	500 °C	600 °C	700 °C
$80TiO_2.20TeO_2$	metal-organic compounds	amorphous + Te	amorphous + Te	anatase + α-TeO₂ + $TiTe_3O_8$	anatase + $TiTe_3O_8$	anatase + rutile + $TiTe_3O_8$
$80TiO_2.20SeO_2$	amorphous	amorphous + anatase	anatase	anatase	anatase + rutile	rutile + anatase
$80TiO_2.20B_2O_3$	amorphous	amorphous + anatase	anatase	anatase	anatase	anatase
$80TiO_2.20ZnO$	amorphous	amorphous	anatase	anatase + $ZnTiO_3$	anatase + $ZnTiO_3$	anatase + rutile + $ZnTiO_3$
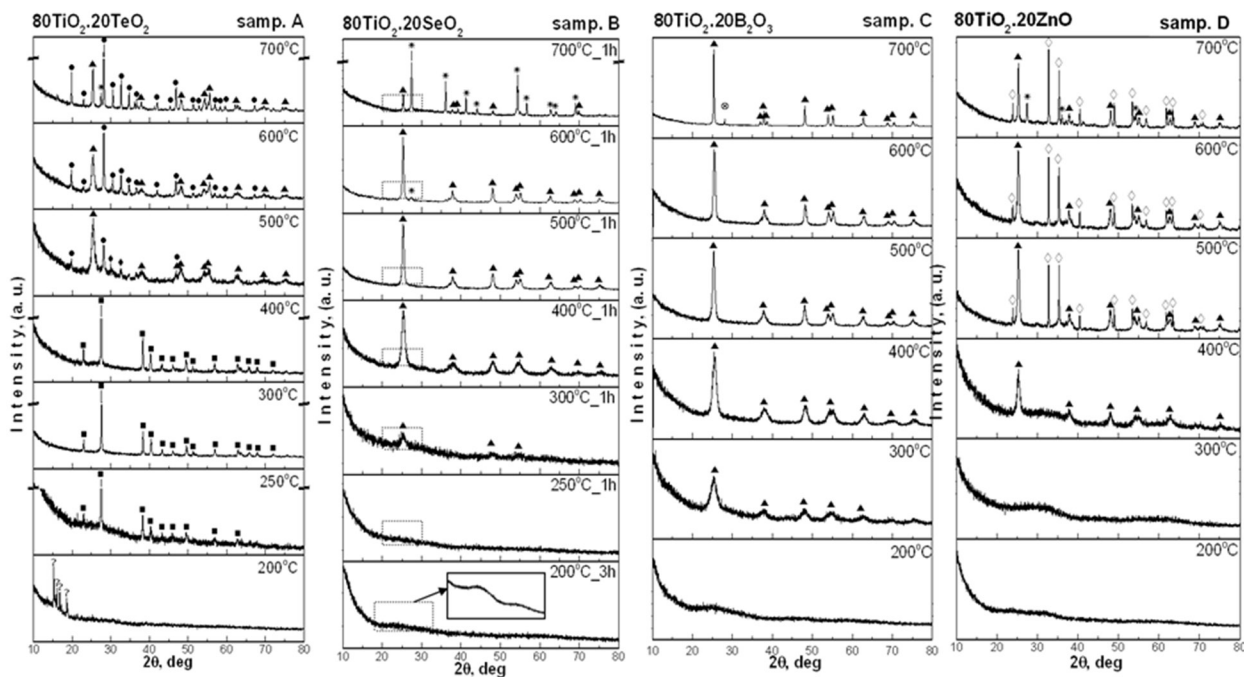
Fig. 4. XRD patterns of the: (a) investigated samples A, B, C and D; (b) pure Ti butoxide (TBT), (■) Te, (♦) α-TeO₂, (▲) TiO₂-anatase, (✳) TiO₂-rutile, (●) TiTe₃O₈, (⊙) H₃BO₃, (◊) ZnTiO₃ (cubic).

Table 2. Average crystallite size of anatase in all samples (A, B, C and D)

TiO₂ (anatase) crystallite size (nm)											
Sample A 80TiO₂.20TeO₂		Sample B 80TiO₂.20SeO₂			Sample C 80TiO₂.20B₂O₃			Sample D 80TiO₂.20ZnO			
500 °C	600 °C	400 °C	500 °C	600 °C	400 °C	500 °C	600 °C	400 °C	500 °C	600 °C	
10	50	10	12	47	45	75	82	45	90	95	
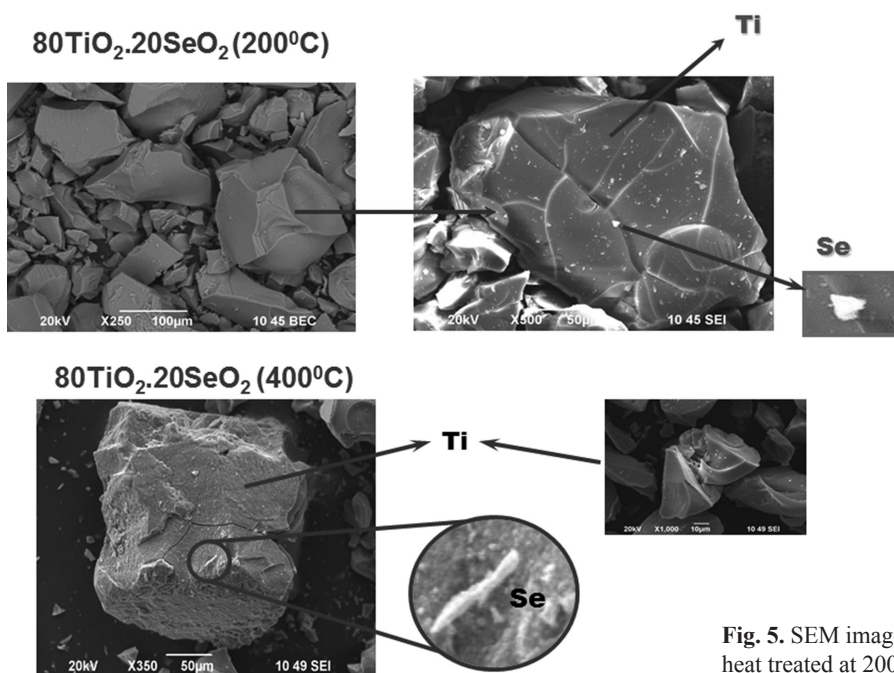
Fig. 5. SEM images of composition B (80TiO₂.20SeO₂) heat treated at 200 °C (a) and 400 °C.

80TiO$_2$.20SeO$_2$ (250^{0}C) 80TiO$_2$.20SeO$_2$ (600^{0}C)
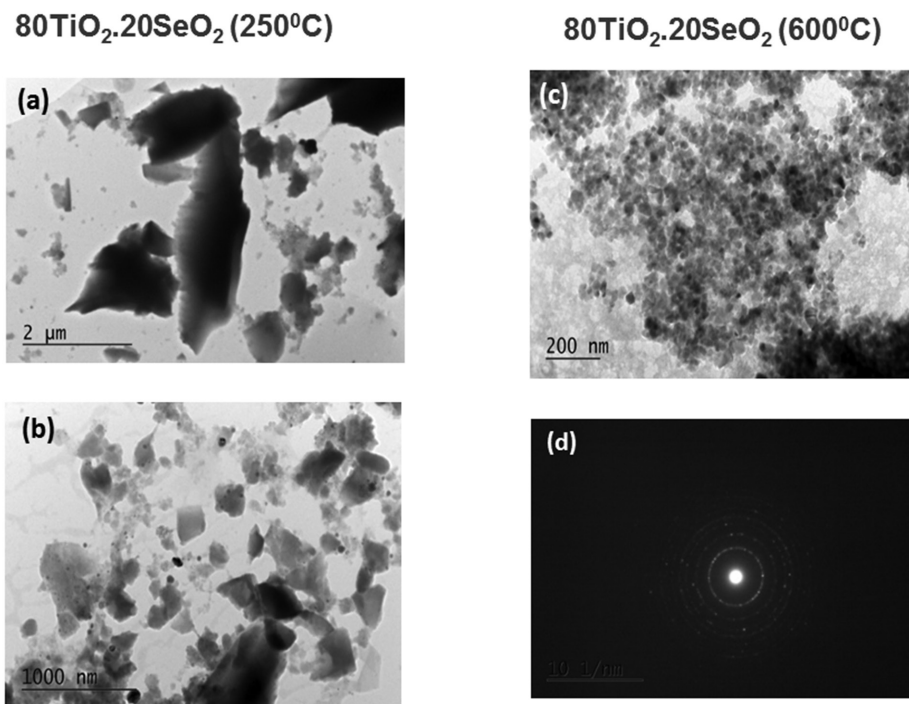
Fig. 6. Bright field TEM images of sample B ($80TiO_2.20SeO_2$) heat treated at 250 °C (a, b) and 600 °C (c); selected area electron diffraction image (SAED) pattern from sample B heat treated at 600 °C (d).

analysis showed that selenium is segregated in these parts which mean that it is not evaporated even at 400 °C (Table 3).

The TEM observations of sample B heat treated at 200 and 600 °C were performed (Fig. 6a–c). At the lower temperature it was confirmed that the sample is amorphous (Fig. 6a, b), while at 600 °C spherical particles were observed with average size of 40 nm (Fig. 6c). The selected area electron diffraction data (SAED) exhibited presence of polycrystalline anatase (Fig. 6d). This result is in good accordance to the XRD data already discussed above.

Analysis of the results

From the above pointed results, it is obvious that two questions 1) related to the amorphous phase in all samples and 2) the stability of anatase crystals at higher temperatures arose. In order to elucidate these problems, a comparison between our results and some published data concerning the stability of the amorphous phase in the investigated $TiO_2 -$ containing systems is made. As it was mentioned above, in our samples the amorphous halo is observed up to 300 °C, and gradually decreases with the increase

Table 3. Microprobe analysis performed in different points of the sample B ($80TiO_2.20SeO_2$) heat treated at 200 and 400 °C

Elements	Microprobe analysis (at%) of sample 80TiO$_2$.20SeO$_2$ (mol%) 27Ti/6Se/67O (at%)	
	200 °C	400 °C
Ti	8.32	27.11
Se	1.76	8.06
O	66.67	64.83
C	23.25	–

of temperature. Applying different method of synthesis and components, many authors [24, 41–48] pointed out different temperatures (from 100 to 400 °C) at which TiO_2 is in amorphous state.

Reznitskij and Filipova [49] found that if the bond energy value of the second component is higher than that of the TiO_2 matrix, this leads to the stabilization of the amorphous matrix and vice versa. Generally, Cr, Al, Zr favor the amorphous state up to ~ 400 °C, while Fe and Cu facilitate the crystallization at about 250 °C. As the Te-O (3.42 eV), Se-O (3.63 eV), B-O (5.55 eV) and Zn-O (2.94 eV) bond energies are higher than that of Ti-O (1.45 eV), the amorphous state in our samples is preserved up to ~300 °C.

The second question is related to the stability of the anatase phase at higher temperature. The type of second and third component and the particle size dimensions may be responsible for the transformation anatase to rutile. According to Hanaor and Sorrell [50] the small cations of low valence (< 4) should promote the anatase to rutile transformation while the large cations of high valence (> 4) should inhibit it. Having in mind these suggestions it is expected B and Zn to be promoters while Te and Se to inhibit, but our results did not confirmed this statement. Generally, the kinetics of the anatase to rutile transformation is affected strongly by many factors and the understanding of this problem is still not exhausted [51, 52].

CONCLUSIONS

The gel formation regions in the binary TiO_2 – M_nO_m (M_nO_m = TeO_2, SeO_2, B_2O_3, ZnO) systems were determined. By the new combination of organic and inorganic precursors a simple route for obtaining of homogeneous gels is offered. It was established that the addition of H_2SeO_3 or H_3BO_3 to Ti butoxide stimulates the earlier TiO_2 (anatase) crystallization (~ 300 °C) while in presence of Zn acetate or H_6TeO_6 the anatase appears at higher temperatures 400 and 500 °C, respectively. No formation of binary crystalline compounds is detected during the heating in the TiO_2–SeO_2 and TiO_2–B_2O_3 systems while in the TiO_2–ZnO and TiO_2–TeO_2 ones, $ZnTiO_3$ and $TiTe_3O_8$ respectively, were found. Nanocomposites consisting of amorphous phase along with metallic Te or TiO_2 (anatase) are derived from gels up to 300 °C while above 400 °C oxide crystalline phases (anatase, α-TeO_2, $TiTe_3O_8$, $ZnTiO_3$ and rutile) only were observed.

REFERENCES

1. S. Sakka, Handbook of sol-gel science and technology: processing, characterization and applications, vols. I, II and III, Kluwer Academic Publishers, The Netherlands, 2004
2. A. Bachvarova-Nedelcheva, R. Iordanova, K. L. Kostov et al., *Opt. Mater.*, **34**, 1781 (2012).
3. M. Udovic, P. Thomas, A. Mirgorodsky, O. Durand, M. Soulis, O. Masson, T. Merle-Méjean, J.C. Champarnaud-Mesjard, *J. Sol. St. Chem.*, **179**, 3252 (2006).
4. E. R. Barney, A. C. Hannon, D. Holland, N. Umesaki, M. Tatsumisago, R. G. Orman & S. Feller, *J. Phys. Chem. Let.*, **4**, 2312 (2013).
5. J.-C. Sabadel, P. Armand, P. E. Lippens, D. C. Herreillat & E. Philippot, *J. Non-Cryst. Sol.*, **244**, 143 (1999).
6. L. Weng, S. Hodgson, *Mater. Sci. Engineer. B*, **87**, 77 (2001).
7. T. Hayakawa, H. Koyama, M. Nogami, et al., *J. Univ. Chem. Technol. Metall.*, **47** (4), 381 (2012).
8. L. Weng, S. Hodgson, X. Bao, K. Sagoe-Crentsil, *Mater. Sci. Engineer. B*, **107**, 89 (2004).
9. L. Weng, S. Hodgson, *J. Mater. Sci.*, **36**, 4955 (2001).
10. S. Hodgson, L. Weng, *J. Mater. Sci.*, **37**, 3059 (2002).
11. T.T.Y. Tan, C. K. Yip, D. Beydoun, R. Amal, *J. Chem. Eng.*, **95**, 179 (2003).
12. P. Zhang, D. L. Sparks, *Environm. Sci. Technol.*, **24**, 1848 (1990).
13. S. Sanuki, T. Kojima, K. Arai, S. Nagaoka, H. Majima, *Metall. Mater. Trans. B*, **30**, 15 (1999).
14. S. – Y. Zhang, X. Chen, Y. Tian, B.K. Jin, J.X. Yang, *J. Crystal Growth*, **304**, 42 (2007).
15. V. Stengl, S. Bakardjieva, J. Bludska, *J. Mater. Sci.*, **46**, 3523 (2011).
16. V. Nguyen, R. Amal, D. Beydoun, *J. Photochem. Photobiol. A: Chemistry*, **179**, 57 (2006).
17. A. Irwin, J. Holmgren & J. Jonas, *J. Non-Cryst. Solids*, **101**, 249 (1988).
18. K. Jung, S. Park & S. Ihm, *Appl. Catal. B: Environmental*, **51**, 239 (2004).
19. A. Fujishima, T. N. Rao, D. A. Tryk, *J. Photochem. Photobiol. C: Photochem. Rev.*, **1**, 1 (2000).
20. C. Hariharan, *Appl. Catal. A: Gen.*, **304**, 55 (2006).
21. G. Marcì, V. Augugliaro, M. J. López-Muñoz, C. Martín, L. Palmisano, V. Rives, M. Schiavello, R. J. D. Tilley, A.-M. Venezia, *J. Phys. Chem. B*, **105**, 1026 (2001).
22. X. Xu, J. Wang, J. Tian, X. Wang, J. Dai, X. Liu, *Ceram. Intern.*, **37**, 2201 (2011).
23. C. Shifu, Z. Wei, L. Wei, Z. Sujuan, *Appl. Surf. Sci.*, **255**, 2478 (2008).

24. R. Iordanova, R. Gegova, A. Bachvarova-Nedelcheva, Y. Dimitriev, *Phys. Chem. Glasses: Eur. J. Glass Sci. Technol. B*, **56** (4), 128 (2015).

25. R. Gegova, A. Bachvarova-Nedelcheva, R. Iordanova, Y. Dimitriev, *Bulg. Chem. Commun.*, **47** (1), 378 (2015).

26. R. Gegova, R. Iordanova, A. Bachvarova-Nedelcheva, Y. Dimitriev, *J. Chem. Technol. Metall.*, **50** (4), 449 (2015).

27. A. Bachvarova-Nedelcheva, R. Gegova, A. Stoyanova, R. Iordanova, V. E. Copcia, N. Ivanova, I. Sandu, *Bulg. Chem. Commun.*, **46** (3), 585 (2014).

28. A. Bachvarova-Nedelcheva, R. Iordanova, A. Stoyanova, R. Gegova, Y. Dimitriev, A. Loukanov, *Centr. Eur. J. Chem.*, **11** (3), 364 (2013).

29. R. Iordanova, A. Bachvarova-Nedelcheva, R. Gegova and Y. Dimitriev, *Bulg. Chem. Commun.*, **45** (4), 485 (2013).

30. A. Bachvarova-Nedelcheva, R. Gegova, R. Iordanova, A. Stoyanova, Y. Dimitriev and N. Ivanova, *Nanoscience and Nanotechnology*, **13,** 56 (2013).

31. S. Doeuff, M. Henry, C. Sanchez, J. Livage, *J. Non-Cryst. Sol.*, **89**, 206 (1987).

32. R. Iordanova, A. Bachvarova-Nedelcheva, R. Gegova, Y. Dimitriev, *J. Sol-Gel Sci. Technol.*, **79** (1), 12 (2016).

33. S. N. B. Hodgson, L. Weng, *J. Non-Cryst. Sol.*, **276**, 195 (2000).

34. A. Lecomte, F. Bamiere, S. Coste et al., J. Europ. Cer. Soc. **27**, 1151 (2007).

35. F. Saylikan, M. Asilturk, H. Saylikan, Y. Onal, M. Akarsu, E. Aprac, *Turk. J. Chem.*, **29**, 697 (2005).

36. J. Madarasz, A. Braileanu, M. Crisan, G. Pokol, *J. Anal. Appl. Pyrol.*, **85**, 549 (2009).

37. C. J. Brinker & G. Scherer, "*Sol-gel science: the physics and chemistry of sol-gel processing*", Academic Press Inc, San Diego, CA, 1990.

38. S. Coste, A. Lecomte, P. Thomas, T. Merle-Mejean, J. C. Champarnaud-Mesjard, *J. Sol-Gel Sci. Techn.*, **41**, 79 (2007).

39. S. Hodgson, L. Weng, *J. Non-Cryst. Sol.*, **297**, 18 (2006).

40. H.-Y. Wei, W.-H. Huang, Z.-B. Feng, D.-W. Li, *Mater. Sci. Engineer. B*, **164**, 51 (2009).

41. Z. Zhang, P. Maggard, *J. Photochem. Photobiol. A:Chem*, **186**, 8 (2007).

42. M. J. Alam, D. C. Cameron, *J. Sol-Gel Sci. Technol.*, **25**, 137 (2002).

43. D. Svadlak, J. Shanelova, J. Malek, L. Perez-Maqueda, J. Criado, T. Mitsuhashi, *Thermochim. Acta*, **414**, 137 (2004).

44. Ch.-W. Hsieh, A.S.T. Chiang, C.C. Lee & Sh.-J. Yang, *J. Non-Cryst. Sol.*, **144**, 53 (1992).

45. M. Khanna, S. Wongnawa, *Mater. Chem. Phys.*, **110**, 166 (2008).

46. H. Li, G. Shao, Z. Chen, B. Song, G. Han, *J. Am. Ceram. Soc.*, **93** (2), 445 (2010).

47. A. Shalaby, Y. Dimitriev, R. Iordanova, A. Bachvarova-Nedelcheva and Tz. Iliev, *J. Univ. Chem. Techn. Metall.*, **46** (2), 137 (2011).

48. A. Shalaby, A. Bachvarova-Nedelcheva, R. Iordanova, Y. Dimitriev, *J. Chem. Techn. Metall.*, **48** (6), 585 (2013).

49. L. A. Reznickij, S. E. Filipova, *Vestnik Moskovskovo Universiteta*, ser. 2, Chemistry, **38** (2), 132, (1997) (in Russian).

50. D. A. H. Hanaor, Ch. C. Sorrell., *J. Mater. Sci.*, **46**, 855 (2011).

51. H. Zhang, J. Banfield, *J. Phys. Chem.* B, **104**, 3481 (2000).

52. H. Zhang, J. Banfield, *J. Mater. Chem.*, **8** (9), 2073 (1998).

КРИСТАЛИЗАЦИЯ НА ГЕЛИ В БИНАРНИТЕ СИСТЕМИ
TiO₂–MₙOₘ (MₙOₘ = TeO₂, SeO₂, B₂O₃, ZnO)

А. Д. Бъчварова-Неделчева¹*, Р. С. Йорданова¹, Р. Д. Гегова¹, Я. Б. Димитриев²

¹ *Институт по Обща и Неорганична Химия, БАН, ул. „Акад. Г. Бончев“, бл. 11, София 1113, България*
² *Химикотехнологичен и Металургичен Университет, бул. „Кл. Охридски“, 1756 София, България*

(Резюме)

Настоящото изследване е посветено на зол-гелния синтез и фазово характеризиране на двукомпонентни прахове TiO₂ – MₙOₘ (MₙOₘ = TeO₂, SeO₂, B₂O₃, ZnO) с номинален изходен състав 80TiO₂.20MₙOₘ. Проверено е влиянието на различни компоненти върху фазообразуването в посочените състави. Според рентгенофазовия анализ, нагретите до 300 °C гели показват преобладаващо аморфна фаза и формиране на метален телур или TiO₂ (анатаз). Количеството на аморфната фаза постепенно намалява с увеличаване на температурата но все още се забелязва при 500 °C. По-нататъшното увеличаване на температурата (700 °C) води до получаването на полифазен продукт, съдържащ едновременно няколко кристални фази (TiO₂ – рутил, анатаз, TiTe₃O₈ и ZnTiO₃). Установено бе, че добавянето на H₂SeO₃ и H₃BO₃ стимулира по-ранната кристализация на TiO₂ (анатаз) около 300 °C, докато в присъствие на цинков ацетат или телурова киселина тази фаза се появява съответно при около 400, 500 °C. За сравнение, при нагряване на чист титанов бутоксид, анатазът кристализира около 400 °C.

Investigation on the crystallization behaviour of sodium-aluminoborosilicate glasses with high concentrations of Ba and Ti

R. Harizanova[1]*, D. Tatchev[2], G. Avdeev[2], C. Bocker[3], D. Karashanova[4],
I. Mihailova[1], I. Gugov[1], C. Rüssel[3]

[1] *University of Chemical Technology and Metallurgy, 8 Kl. Ohridski Blvd., 1756 Sofia, Bulgaria*

[2] *Institute of Physical Chemistry, Bulgarian Academy of Sciences, Acad. G. Bonchev Str, Block 11, 1113 Sofia, Bulgaria*

[3] *Otto Schott Institute for Materials Research, Jena University, Fraunhoferstr. 6, 07743 Jena, Germany*

[4] *Institute of Optical Materials and Technologies Bulgarian Academy of Sciences, Acad. G. Bonchev Str., Block 109, 1113 Sofia, Bulgaria*

The present work reports on the synthesis of $BaTiO_3$ containing glass-ceramics by applying appropriate annealing programs and varying the ratio of Na_2O to Al_2O_3 in a sodium-aluminoborosilicate glass. The phase composition is studied by X-ray diffraction and additionally to the presence of $BaTiO_3$, also some silicate-based phases are detected. The microstructures of the obtained glass-ceramics are investigated by electron microscopy and depending on the ratio between Na_2O and Al_2O_3, the presence of morphologically differing crystalline structures is concluded. Computed tomography is utilized to determine the volume fractions and size distributions of the barium titanate crystals in the glass ceramics. A high volume concentration of crystals is observed.

Keywords: barium titanate; crystallization; microstructure.

INTRODUCTION

The efficient energy storage and energy consumption are some of the most acute and important problems nowadays. Thus, the synthesis and the investigation of the microstructure with respect to the physical properties of materials are of great importance. Barium titanate, $BaTiO_3$ is a phase from the perovskite family – well-known since a long time – and with outstanding dielectric, pyroelectric, piezoelectric and even optical properties, as well as easy to prepare in the form of glass-ceramics. Barium titanate occurs in several crystallographic modifications (tetragonal, cubic, orthorhombic, rhombohedral and hexagonal) but two of them are especially interesting with respect to particular applications: the tetragonal which is ferroelectric and stable at room temperature and the cubic which is stable above the Curie temperature of approximately 120 °C and possesses paraelectric proper-

ties. Both phases have found applications in the preparation of different electronic devices, i.e. as powerful capacitors, as a substitute of the magnetic RAM, e.g. as FRAM [1–5]; multilayered capacitors for energy storage; capacitors for use in high power transmitters and microwave resonant cavities; piezoelectric elements and resistive sensors [1, 3, 4–6]. Depending on its optical properties, $BaTiO_3$ could be a promising candidate for laser preparation for optoelectronic applications [5]. Different experimental techniques are used to obtain barium titanate as bulk material, [1, 2, 4, 5]. The preparation of $BaTiO_3$ in the form of thin films and as separate crystalline beads which are subsequently calcined in larger aggregates is also reported in the literature [3, 6–8]. The stability of each barium titanate modification at room temperature is determined by the size, as well as by the used preparation technique and also by the addition of dopants [1, 2, 4, 6, 10]. Decisive for the controlled crystallization and size-distribution of the obtained crystals is mainly the preparation technique. Actually, there are a large number of methods to prepare barium titanate with or without dopants. Conventionally, barium titanate ceramics are prepared by the chemical reaction of

---

* To whom all correspondence should be sent:
E-mail: ruza_harizanova@yahoo.com

barium carbonate and titanium oxide to barium titanate, accompanied by subsequent milling and sintering. [2]. Furthermore, the preparation of barium titanate nanorods, with potential applications in the construction of UV lasers, by means of a hydrothermal method is reported in Ref. [5]. Gelation and subsequent calcinations is reported in Ref. [7], in order to prepare beads of different perovskite crystals which are first obtained as cubic polymorph and then, after additional thermal treatment, the tetragonal modification is stabilized at room temperature. Also, the addition of appropriate dopants can lead – after applying a suitable time-temperature heat treatment – to composite crystals consisting of one ferroelectric and one ferromagnetic component, exhibiting multiferroic properties [9, 10]. The system $(24-y)Na_2O/yAl_2O_3/14B_2O_3/37SiO_2/25Fe_2O_3$ with y = 8, 12, 14 and 16 and other similar compositions were studied [11–14]. It was shown that in the obtained glasses initially phase separation occurs and droplets with sizes in the range from 100 to 800 nm enriched in B_2O_3 and FeO_x are formed. Within these droplets, magnetite crystals with sizes in the range from 25 to 40 nm with potential application as multicore nanoparticles are precipitated [14].

The present paper reports on the synthesis, as well as on the phase and microstructural characterization of glasses and glass-ceramics with the composition $23.1Na_2O/23.1BaO/23TiO_2/17.4SiO_2/7.6B_2O_3/5.8Al_2O_3$, as well as the composition series $(23.1-x)Na_2O/23.1BaO/23TiO_2/9.8B_2O_3/21SiO_2/xAl_2O_3$, x = 3, 7, 11 mol%. The thermal treatment of the reported glasses results in the precipitation of barium titanate and various crystalline silicate phases. For samples in which only one crystalline phase occurs, morphology and size are investigated by scanning electron microscopy and computed tomography. The crystallization of large volume fractions of barium titanate crystals with crystallite sizes in the submicron and micrometer range is established. The occurrence of phase separation into Ba and Ti rich regions and subsequent crystallization of barium titanate in these regions is suggested.

EXPERIMENTAL

Samples with mol% batch compositions $23.1Na_2O/23.1BaO/23TiO_2/17.4SiO_2/7.6B_2O_3/5.8Al_2O_3$ (further denoted as composition A) and $(23.1-x)Na_2O/23.1BaO/23TiO_2/9.8B_2O_3/21SiO_2/xAl_2O_3$, x = 3, 7, 11 mol% (denoted as compositions B1, B2 and B3, respectively) were melted from the following reagent grade raw materials: Na_2CO_3, $BaCO_3$, TiO_2, $Al(OH)_3$, $B(OH)_3$ and SiO_2. The glasses are melted in 60g batches for 1 h at 1400 °C in air using a Pt crucible in a furnace with $MoSi_2$ heating elements.

The melts are quenched on a copper block without pressing. Then, in order to increase the mechanical stability and to minimize internal stresses, the glass was transferred to a pre-heated graphite-mould and held for 15 min at 480 °C in a muffle furnace. Subsequently, the furnace was switched off and the sample was allowed to cool to room temperature. Crystallization of the samples was, according to the DTA data, carried out at different temperatures and for different times in a muffle furnace as described in Ref. [15].

The phase compositions of the samples from all melted compositions are studied by X-ray diffraction (XRD), *Philips PW1050* using Cu-Kα radiation (λ = 1.5406 Å) and Ni filter. The microstructure and the elemental composition of the prepared glasses and of the crystallized samples is further analysed by scanning electron microscopy (SEM) in combination with energy-dispersive (EDX) analysis, (*JSM-7001F, JEOL Ltd., Japan*) and (*Philips 515 with SEI detector*). Imaging of the crystallized samples is performed on polished samples or on fractured surfaces, or if this did not result in a good contrast, on samples etched for 5 s in 1% HCl solution. The average crystal size and volume fraction of selected samples was investigated by computed tomography (*x-ray microtomograph Brucker SkyScan 1272*).

RESULTS AND DISCUSSION

The samples from the two sets of compositions A and B1-B3 freeze like glasses after pouring the melt, although for the samples A and B1 also some surface crystallization during cooling of the melt occurs – as already shown in [16]. Increasing alumina concentration at the expense of sodium oxide results in better glass formation and hence, surface crystallization does no longer occur in the compositions B2 and B3. This is attributed to the intermediate character of aluminium ions, Al^{3+} in the glass network and has widely been discussed in literature [12, 17–22] as well as in our previous work on similar compositions [14, 15, 23].

The compositions A and B1-B3 are annealed supplying different time-temperature schedules, according to the DTA data as reported in Refs. [15, 16]. Most samples annealed above T_g are visually crystalline even after 15 min annealing time and this is supported by the respective XRD patterns of the bulk specimens as shown in Figures 1a–d. All samples from Figs. 1a–d are annealed at the DTA crystallization peak maximum or near the respective temperature. The samples from composition A show only XRD peaks attributed to $BaTiO_3$ (JCPDS 90-10-801). Applying longer annealing times results in a higher amount of the crystalline phase as expected
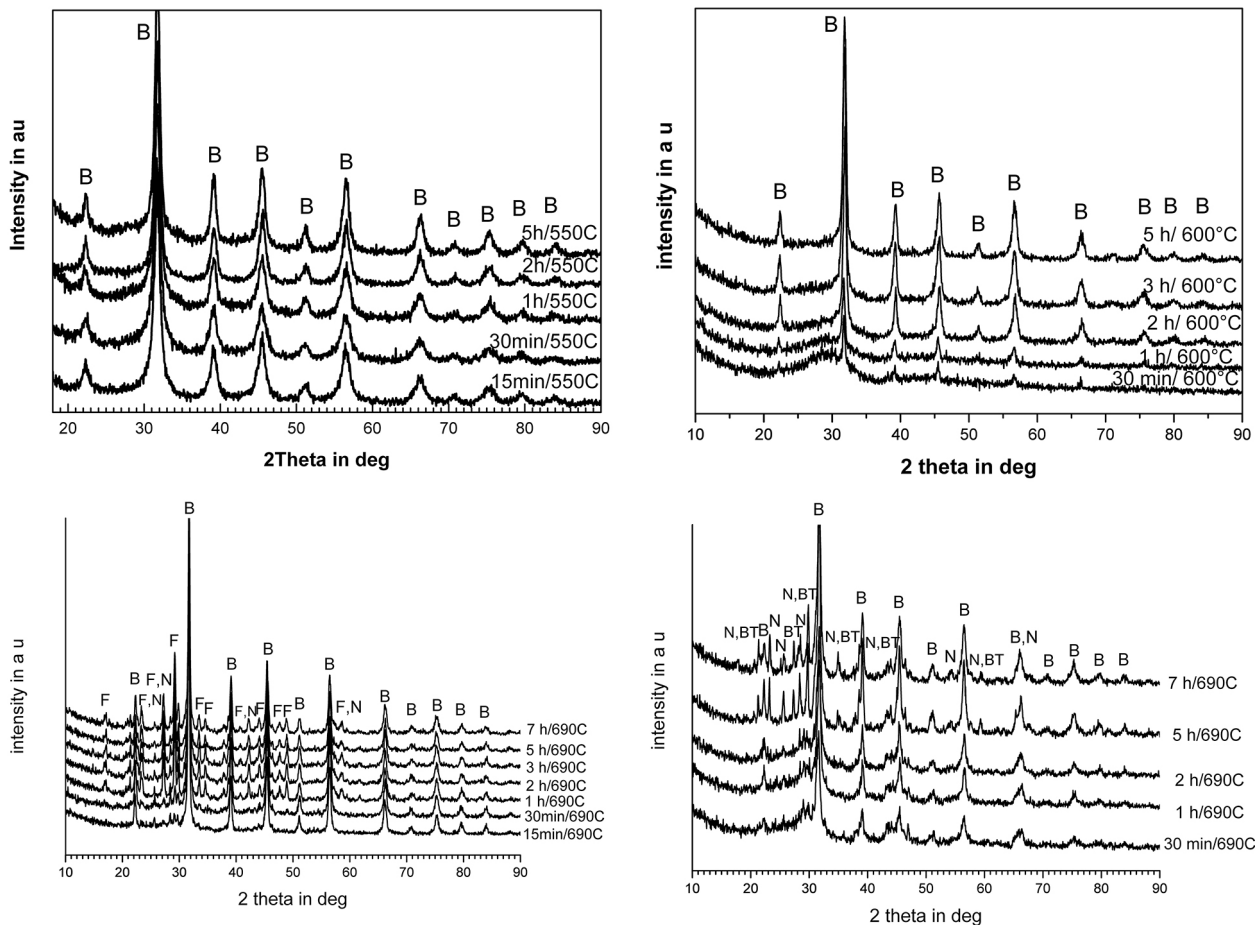
Fig. 1. a) XRD-patterns of samples with the composition A, annealed at the crystallization peak maximum in the DTA profile at 550 °C for different periods of time – cubic $BaTiO_3$ (B) formed; b) XRD-patterns of samples with the composition B1 – crystallization of cubic $BaTiO_3$ (B) after different periods of time at 600 °C; c) XRD-patterns of samples with the composition B2 annealed at 690 °C for different times – growth of cubic $BaTiO_3$(B), $Ba_2TiSi_2O_8$ (F) and $NaAlSiO_4$(N); d) XRD-patterns of samples with the composition B3 annealed at 690 °C for different times – growth of cubic $BaTiO_3$(B), $BaTi_2O_5$ (BT) and $NaAlSiO_4$(N).

in the case of non-constraint isothermal crystallization. If samples B1 are thermally treated near the temperature of the crystallization peak maximum, e.g. the XRD patterns shown in Fig. 1b, the only crystalline phase formed is $BaTiO_3$. However, the variation of the annealing temperature and more precisely, its increase, results for the samples with 3 mol% alumina (composition B1) in the formation of a second crystalline phase – Fresnoite, $Ba_2TiSi_2O_8$ (JCPDS 98-20-1844) as already observed in Ref. [16]. In contrast to the crystallization behaviour of samples with up to 6 mol% Al_2O_3, the XRD patterns of the crystallized specimens with 7 and 11 mol%, (compositions B2 and B3, respectively) are characterized by the occurrence of at least three crystalline phases namely Fresnoite and Nepheline, $NaAlSiO_4$ (JCPDS 35-0424) for B2 and Nepheline, $NaAlSiO_4$ and barium titanium oxide, $BaTi_2O_5$ (JCPDS 70-1188) for B3, cf. Figs. 1c and 1d. Such

crystallization behaviour is supposed to be due to the increasing alumina concentration and the higher annealing temperatures which facilitate the nucleation and growth of Na- and Al-containing silicates [12]. Again, longer annealing times results in a larger crystals for one and the same annealing temperature. Actually, in Figs. 1c and 1d, it is seen that $BaTiO_3$ always occurs as the first crystalline phase precipitated which is attributed to the extremely high concentrations of Ba and Ti. However, for longer annealing times, the amount of the second precipitated phase, Nepheline also increases – especially well seen in Fig. 1d. The easier nucleation and growth of barium titanate, could be attributed to the occurrence of phase separation processes, as observed for similar systems [12, 16, 23, 24], into a Ba, Ti- rich phase and a matrix enriched in all other elements from the composition. Thus, the nucleation of $BaTiO_3$ starts first and after that for

example, nepheline despite the larger ionic radii of Ba^{2+} (1.35 Å) and Ti^{4+} ions (0.56 Å in tetrahedral and 0.75 Å in octahedral coordination) in comparison to those of Na^+ (1.02 Å), Al^{3+} (0.54 Å) and Si^{4+} (0.40 Å). The $BaTiO_3$ phase is recognized as the cubic modification because there is no visible splitting in the characteristic peak at about 45.3° – as it should be in the case for tetragonal $BaTiO_3$ [1, 23–25]. Many authors report different symmetries of the $BaTiO_3$ crystals depending on their size; the larger crystallites are normally tetragonal, while the smaller ones are cubic [1, 25] or a combination of a tetragonal core and a cubic shell is observed during the course of crystal growth [1]. Surprisingly, in the investigation of all the compositions A and B1-B3, despite the different annealing regimes and crystallite sizes, always cubic barium titanate is formed.

The microstructure of the synthesized glasses and the glass-ceramics obtained after thermal treatment was studied by scanning electron microscopy. The micrograph of sample A showed that the crystals formed at the surface are spherically shaped with dendritic needle-like structures as shown in Fig. 2. The shape of the crystallized regions suggests that probably phase separation occurs at some stages during cooling the melt and the spherical particles are enriched in the heavy elements, Ba and Ti which facilitates the formation of $BaTiO_3$ crystals. The same behaviour has been observed for other similar glass systems and compositions as reported in Refs. [12–16, 24]. From Fig. 3, where sample A crystallized for 2 h at 550 °C is shown, the precipitation of
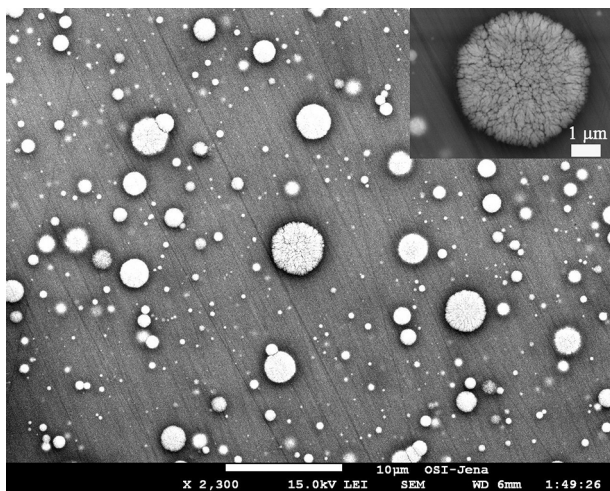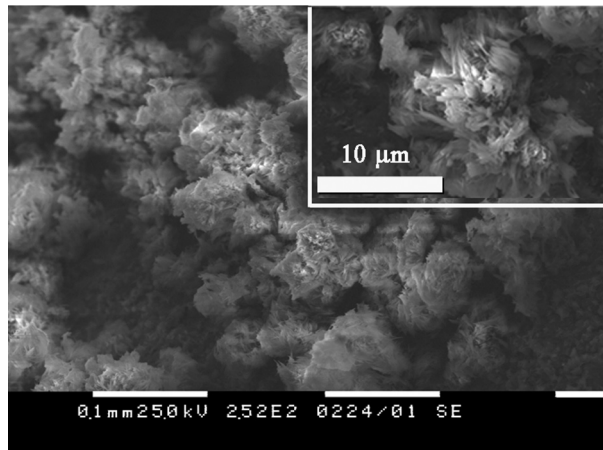
Fig. 3. SEM image of a sample A annealed for 2 h at 550 °C – fractured surface showing growth of globular regions of needle-like crystals of $BaTiO_3$. The inset: magnified image of the same glass-ceramic sample revealing the morphology of the crystals.

a large volume fraction of $BaTiO_3$ crystals gathered in spherically shaped agglomerates is seen. The latter possess sizes of up to hundred micrometers and consist of separate crystals growing together. The inset in Fig. 3 shows that between the spherical particles there are dark regions – the amorphous matrix where separate crystals are found. The morphology of the crystals corresponds to that of the crystals at the surface of sample A (Fig. 2). The SEM investigations of samples B1-B3 reveal that the increasing alumina concentration and the decreasing Na_2O concentration lead to a reduced tendency towards surface crystallization but to the same morphology of the growing crystals. Thermal treatment of sample B1 results in glass-ceramics with $BaTiO_3$ as the only or at least as the dominating crystalline phase, as supported by the XRD patterns shown in Fig. 1b and from previous investigations reported in Ref. [16]. Here, the crystallization temperature of 650 °C and annealing time 3 h lead to barium titanate crystals with similar shape to that in Fig. 3 and large volume fraction, as already reported in Ref. [16]. The results from the SEM imaging in Ref. [16] led to further microstructural investigations of sample B1 with the same thermal history (annealed 3 h at 650 °C) by means of computed tomography (see Fig. 4). The bright phase corresponds to the barium titanate crystals and the dark one – to the amorphous matrix and eventually to some Fresnoite crystals which possess a lower average atomic number, as witnessed by SEM in Ref. [16]. The image from Fig. 4 shows again crystals growing as spherically shaped agglomerates with an average size as determined from the processing of the image of around 17±3 micrometers and a volume fraction of

Fig. 2. SEM-micrograph of a sample with the composition A – glass without heat-treatment with crystals formed on the surface during pouring the melt. Inset: magnified SEM-micrograph of the glass A showing the morphology of the crystals formed at the surface.
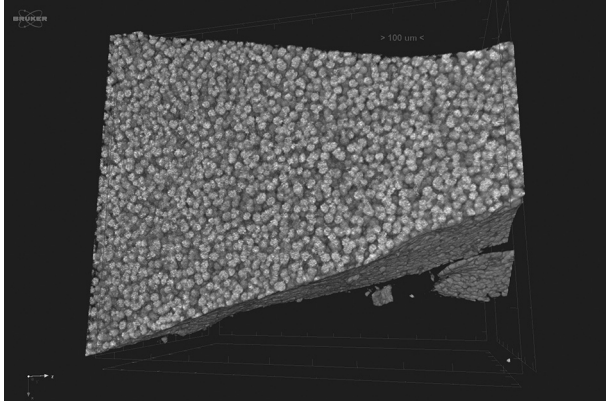
Fig. 4. Glass-ceramic B1 annealed 3h at 650 °C – imaging by means of computed tomography.

Fig. 5. SEM micrograph of a sample B2 crystallized for 7 h at 690 °C – at least two morphologically different types of crystals are present.

approximately 58±1%. The separate particles tend to aggregate and form larger complexes which grow together – as seen in Figures 2 and 3. Similar structures were already observed in other systems where the crystallization is preceded by droplet-like phase separation [14–16, 23, 24]. The microstructural investigation of all annealed samples B1 shows growth of only one morphological type of BaTiO$_3$ crystals. Actually, the SEM investigations of samples with different thermal history and composition suggests that after annealing times t ≥ 3 h, the mean size of the formed globular crystals continues to grow and the separate spherical particles tend to form aggregates. This behaviour differs from the tendency described in [16, 23], where after thermal treatment for more than 3 h, the crystallite size stops increasing. The bright appearance of the formed crystals suggests that they contain the heavier elements of the initial composition, e. g. Ba and Ti. The addition of transition metal oxides other than Ti as dopants, for example Fe was studied in other composition series and is a well-known method for affecting the phase formation and thus, the properties of the resulting crystals [2–4, 8–10, 24, 25]. In Ref. [24], a composition similar to B1 is developed and its crystallization behaviour is reported. There, the presence of Fe leads additionally to the BaTiO$_3$ crystallization also to that of BaTi$_{0.75}$Fe$_{0.25}$O$_{2.888}$ which has a hexagonal symmetry and may possess multiferroic properties, as discussed in [2, 24].

The SEM-micrographs of the annealed samples B2 are characterized by the presence of more than one morphological type of crystals which is shown in Figure 5 for a sample annealed for 7 h at 690 °C. This supports the results from the XRD analyses of this composition shown in Fig. 1c.

Figure 6 shows an SEM micrograph of sample B3 annealed for 7 h at 690 °C where, as also wit-
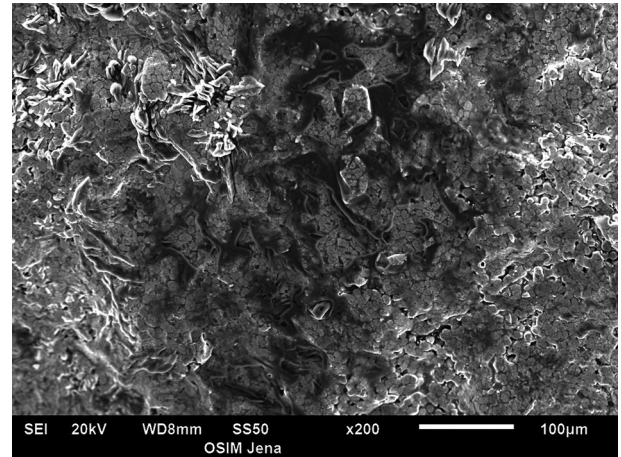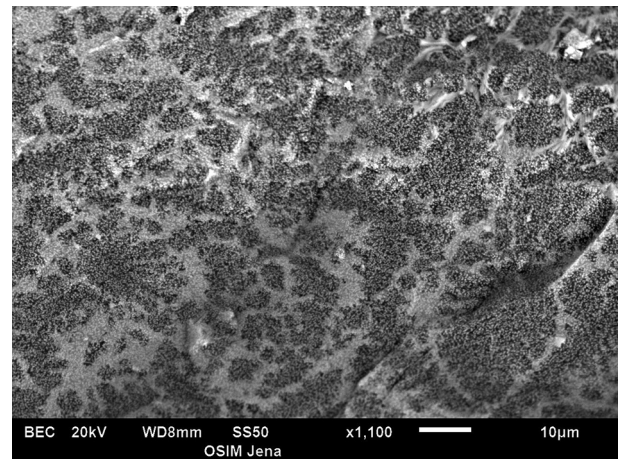
Fig. 6. SEM micrograph of a sample B3 crystallized for 7 h at 690 °C – presence of more than one morphological type of crystals.

nessed from the XRD patterns in Figure 1d, additionally to BaTiO$_3$ other crystalline phases are present. The SEM micrographs shown in Figs. 5 and 6 reveal that the increasing alumina concentration and the decreasing sodium oxide concentration lead to smaller BaTiO$_3$ crystals. This observation could be explained by the higher glass transition temperature and hence, the higher viscosity of the glass with the larger Al$_2$O$_3$ concentration when crystallizing it at the same temperature (690 °C) as described in Ref. [15].

The observed phase composition and morphology of the formed crystals as well as the resulting size variation, depend on the composition of the initial glasses and will affect the dielectric properties

of the obtained glass-ceramic materials which will be a subject of further investigations.

CONCLUSIONS

From melts with compositions $23.1Na_2O/23.1BaO/23TiO_2/7.6B_2O_3/17.4SiO_2/5.8Al_2O_3$ and $(23.1-x)Na_2O/23.1BaO/23TiO_2/9.8B_2O_3/21SiO_2/xAl_2O_3$, $x = 3$, 7 and 11 mol% glasses are obtained during cooling, although the larger sodium oxide concentrations in samples with 5.8 and 3 mol% alumina result in surface crystallization. The increasing alumina concentration leads to decreased crystallization tendency and smaller $BaTiO_3$ crystals for one and the same time-temperature schedule which is attributed to the increased viscosity of the glass. Small Al_2O_3 concentrations and comparatively low crystallization temperatures result in the sole crystallization of $BaTiO_3$, while at higher crystallization temperatures and times, a second crystalline phase, Fresnoite $(Ba_2TiSi_2O_8)$ is formed. The larger alumina concentrations, however, tend to facilitate the crystallization of two or more crystalline phases, at least one of them containing Al, i.e. Nepheline $NaAlSiO_4$. It is observed that $BaTiO_3$ always crystallizes as the first phase and the volume fraction of the crystals, as well as their average size for one and the same composition increases with increasing crystallization time. The method of the computed tomography is successfully utilized to estimate the average size of the barium titanate crystals to be about 17±3 micrometers and their volume fraction – of the order of 58±1% for the glass-ceramics with 3 mol% Al_2O_3.

REFERENCES

1. J. F. Capsal, E. Dantras, L. Laffont, J. Dandurand, C. Lacabanne, *J. Non-Cryst Solids*, **356**, 629 (2010).
2. G. P. Du, Z. J. Hu, Q. F. Han, X. M. Qin, W. J. Shi, *J Alloys Compounds*, **492**, L79 (2010).
3. T. J Jackson, I. Jones, *J Mater Sci*, **44**, 5288 (2009).
4. Z. Libor, S.A. Wilson, Q. Zhang, *J Mater Sci*, **46**, 5385 (2011).
5. R. Vijayalakshmi, V. Rajendran, *Digest J Nanomater Biostruc*, **5**, 511 (2010).
6. C. B. Carter, M. G. Norton, in: Ceramic Materials: Science and Engineering, 1st Ed., Springer, 2007.
7. A. F. Demirörs, A. Imhof, *Chem Mater*, **21**, 3002 (2009).
8. S. F. Mendes, C. M. Costa, C. Caparros, V. Sencadas, S. Lanceros-Mendez, *J Mater Sci*, **47**, 1378 (2012).
9. R. P. Maiti, S. Basu, S. Bhattacharya, D. Chakravorty, *J Non-Cryst Solids*, **355**, 2254 (2012).
10. H. T. Langhammer, T. Müller, T. Walther, R. Böttcher, D. Hesse, E. Pippel, S. G. Ebbinghaus, *J Mater Sci*, **51,** 10429 (2016).
11. R. Harizanova, G. Völksch, C. Rüssel, *J Mater Sci*, **45**, 1350 (2010).
12. W. Vogel, in: Glasschemistry, 3 Ed. Springer-Verlag, Berlin-New York-London-Paris-Tokyo-Hong Kong-Barcelona-Budapest, 1992.
13. R. Harizanova, I. Gugov, C. Rüssel,, D. Tatchev, V. S. Raghuwanshi, A. Hoell, *J Mater Sci: Size Dependent Effects*, **46**, 7169 (2011).
14. C. Worsch, P. Schaaf, R. Harizanova, C. Rüssel, *J Mater Sci*, **47**, 5886 (2012).
15. R. Harizanova, L. Vladislavova, A. Mazhdrakova, C. Bocker, G. Avdeev, G. Tsutsumanova, I. Gugov, C. Rüssel, *Advances in Natural Science: Theory & Applications*, **3**, 21 (2014).
16. R. Harizanova, A. Mazhdrakova, L. Vladislavova, G. Avdeev, C. Bocker, I. Gugov, C. Rüssel, *J Chem Technol Metall*, 50, 375 (2015).
17. K. El-Egili, *Phys B*, **325**, 340 (2003).
18. S. Hornschuh, B. Messerschmidt, T. Possner, U. Possner, C. Rüssel, *J Non-Cryst Solids*, **347**, 121 (2004).
19. L. Hong, P. Hrma, J. D. Vienna, M. Qian, Y. Su, D. E. Smith, *J Non-Cryst Solids*, **331**, 202 (2003).
20. D. Benne, C. Rüssel, M. Menzel, K. Becker, *J Non-Cryst Solids*, **337**, 232 (2004).
21. H. Schirmer, R. Keding, C. Rüssel, *J Non-Cryst Solids*, **336**, 37 (2004).
22. D. Benne, C. Rüssel, D. Niemer, M. Menzel, K. Becker, *J Non-Cryst Solids*, **345–346**, 203 (2004).
23. R. Harizanova, L. Vladislavova, C. Bocker, C. Rüssel, I. Gugov, *Bul Chem Comm*, **46**, 56 (2014).
24. R. Harizanova, M. Abrashev, I. Avramova, L. Vladislavova, C. Bocker, G. Tsutsumanova, G. Avdeev, C. Rüssel, *Solid State Sci*, **52**, 49 (2016).
25. S. D. Vacche, F. Oliveira, Y. Leterrier, V. Michaud, D. Damjanovic, J. E. Manson, *J Mater Sci*, **47**, 4763 (2012), DOI 10.1007/s10853-012-6362-x.

ИЗСЛЕДВАНЕ НА КРИСТАЛИЗАЦИОННОТО ПОВЕДЕНИЕ НА НАТРИЕВО-АЛУМОБОРОСИЛИКАТНИ СТЪКЛА С ВИСОКА КОНЦЕНТРАЦИЯ НА БАРИЙ И ТИТАН

Р. Харизанова[1]*, Д. Тачев[2], Г. Авдеев[2], Хр. Бокър[3], Д. Карашанова[4], И. Михайлова[1], И. Гугов[1], Хр. Рюсел[3]

[1] *Химикотехнологичен и металургичен университет, бул. „Кл. Охридски" № 8, 1756 София, България*
[2] *Институт по физикохимия, БАН, ул. „Акад. Г. Бончев", бл. 11, 1113 София, България*
[3] *Ото Шот институт за изследване на материалите, Университет Йена, ул. „Фраунхофер" № 6, 07743 Йена, Германия*
[4] *Институт за оптични материали и технологии, БАН, ул. „Акад. Г. Бончев", бл. 1091, 1113 София, България*

(Резюме)

В настоящата работа е докладван синтезът на стъклокерамики, съдържащи бариев титанат, $BaTiO_3$ в натриево-алумоборосиликатни стъкла чрез прилагане на подходящи термични програми за отгряване и чрез промяна в съотношението на концентрациите на Na_2O и Al_2O_3. Фазовият състав е изучен с използване метода на рентгеновата дифракция и допълнително на присъствието на $BaTiO_3$, е установена кристализацията на няколко силикатни фази. Микроструктурата на получените стъклокерамики е изследвана по метода на елек- тронната микроскопия и в зависимост от съотношението в концентрациите на Na_2O и Al_2O_3, е установено на- личието на различни като морфология кристални структури. Микрокомпютърната томография е използвана за определяне на обемното съдържание на кристалната фаза и разпределението по размери на бариево-тита- натните кристали в стъклокерамиките. Установено е високо обемно съдържание на кристалната фаза.

Expressing the extinction-free integral breadth

I. Tomov[1]*, S. Vassilev[2], G. Avdeev[3]

[1] *Acad. J. Malinowski Institute for Optical Materials and Technologies, Bulgarian Academy of Sciences, Sofia 1113, Bulgaria*
[2] *Institute of Electrochemistry and Energy Systems, Bulgarian Academy of Sciences, Sofia 1113, Bulgaria*
[3] *Acad. R. Kaischew Institute of Physical Chemistry, Bulgarian Academy of Sciences, Sofia 1113, Bulgaria*

Secondary extinction (SE) is inherently related to the pole density, P. The latter represents a crystalline volume fraction normalised to random distribution that contributes to reflection. In fact, any measured point inside the reflection range $2\Delta\theta$ is affected to a different extent by the SE due to variation of both pole density and energy distribution of the incident beam intensity, I_0. However, to evaluate a SE effect of the reflection as a whole, its integral intensity must account for pole density, $\overline{P}$, being dependent on integral breadth of reflection. Thus, the aim of the present study is to develop a technique for calculating the integral breadth of reflection using extinction free data of both its integral intensity and maximal intensity. The reformed data can be used for sensitive treatment of the SE effect in textures and powders including nanoscale materials as well.

Keywords: secondary extinction, integral breadth, textures, powders, microcrystalline, nanocrystallites.

INTRODUCTION

The effect of extinction is subject to extensive research in characterizing domain size and shape of real crystals in single-crystal diffractometry [1–4], while there is only little interest in conventional X-ray diffractometry, despite that extinction is an intrinsic property of textures. Knowing that secondary extinction effect on reflection profile distortion of textures is not justified, this compromises the correct assessment of the microstructure parameters. As a first step to adequate characterization of the microstructure, one needs a method for eliminating the extinction-induced profile distortion, since this distortion causes a respective reflection enlargement. Thus, the aim of the present study is to convert measured (extinction-affected) profile into a kinematical (extinction-free) one and thus to correctly assess the physical effect due to size-strain broadening controlled by integral breadth [5, 6]. In this context, by treating the SE problem we reconsidered and specified the behaviour of the coefficient k, empirically introduced earlier [7].

WHAT IS COEFFICIENT k?

Based on the relationship $k = (g/PI_0)(2\mu/S)$ between diffraction and extinction, we have found that the coefficient k is an irrational quantity [cm^{-3}] of the scattering space (Fig. 1). In the real space, $1/k$ is a crystalline volume [cm^3] covering those crystallites in the Bragg condition that do not contribute to an increase of the reflectivity and, hence, to the diffraction process. Just the ineffectiveness of this crystalline volume, $1/k$, weakens the level of interaction of the diffraction process by, PI_0, where P represents a crystalline volume fraction normalised to random distribution that contributes to reflection. By its very nature, the relationship between diffraction and extinction specifies the behaviour of the SE coefficients, k and g. We have specially proved that the constancy of k may exist only under *the same structural condition*, i.e. P = const., and proper variation of I_0 alone [8]. Let us analyse this problem.

To distinguish between the behaviour of k and g, we suppose a set of levels of interaction defined in particular. In this context, whereas the pole density P is held to be a constant, the incident beam intensity varies from level $I_{0,i}$ to level $I_{0,i*}$ caused by variation of the generator current from i to $i*$. Then the above relationship is rewritten as

$$k_i = (g_i/PI_{0,i})(2\mu/S), \qquad (1a)$$

_____
* To whom all correspondence should be sent:
E-mail: iv.tomov39@gmail.com
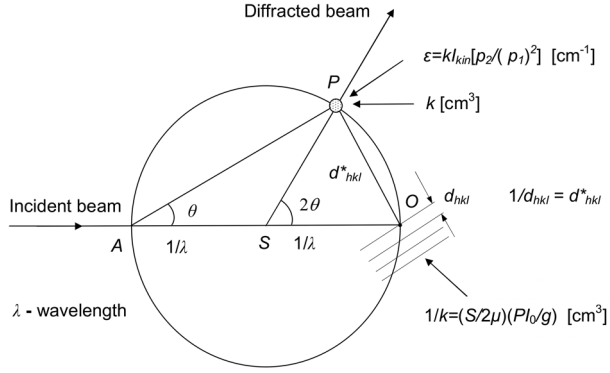
Fig. 1. Diffraction and extinction treated by means of scattering and real spaces. The scattering of X-rays 'operates' at the cross-section of the Evald's and projection spheres (P). The origin, O, of the real space is there, where the sample under study is situated, ε is the SE correction.

Fig. 2. Relationship between four levels of interaction defined by variation of the incident beam intensity from $I_{0,i}$ to $I_{0,i***}$. In the equations A is a constant, V_K is the critical excitation potential of the $K\alpha$ radiation, and n = 1.5 [6].

$$k_{i*} = (g_{i*}/PI_{0,i*})(2\mu/S), \quad (1b)$$

where it is accounted that g_i and g_{i*} are proportional to $I_{0,i}$ and $I_{0,i*}$, respectively, i.e.

$$(g_i/I_{0,i})/(g_{i*}/I_{0,i*}) = 1 \quad (2)$$

Dividing (1a) and (1b) by considering (2) yields

$$k_i = k_{i*}, \quad (3)$$

where k is an invariable independent of the level of interaction of the diffraction process. Therefore, any variation of $I_{0,i}$ does not change the value of k coefficient under P=const. and otherwise equal condition. To reveal the straight proportional dependence of g on (PI_0), one has to rewrite the same relationship between diffraction and extinction as

$$g = (PI_0)(kS/2\mu). \quad (4)$$

Evidently, at lower limiting values of either $(PI_0 \rightarrow 0)$ it is clear that only in the case of absent diffraction ($I_{kin} \rightarrow 0$), there is no extinction ($g \rightarrow 0$) (4). This is in accordance with Matheson's statement that 'extinction is only zero, in absolute sense, when diffracted power is identically zero' [9].

APPARENT EXTINCTION

One may show an apparent SE effect, i.e. a visible effect such as it is. To this end, a data acquisition technique called 'compensative condition' is

elaborated. This condition requires XRD measurements of a reflection to be carried out by using a four-step design presented in Figure 2. To compensate a stepwise decrease of $I_{0,i}$ intensity controlled by the generator current density $i=i,i*,i**,i***$, the time $\tau=\tau,\tau*,\tau**,\tau***$ for data collection is step by step increased to give the same product of τ per a scanned step and current density i:

$$\tau i=\tau*i*=\tau**i**=\tau***i***=const. \quad (5)$$

Profiles were measured by a step scanning mode with conventional X-ray diffractometer using CuKα radiation separated by nickel filter. Figure 3 illustrates the apparent extinction effect. An extinction-free condition means that diffraction would be kinematical and then the profiles should overlap each
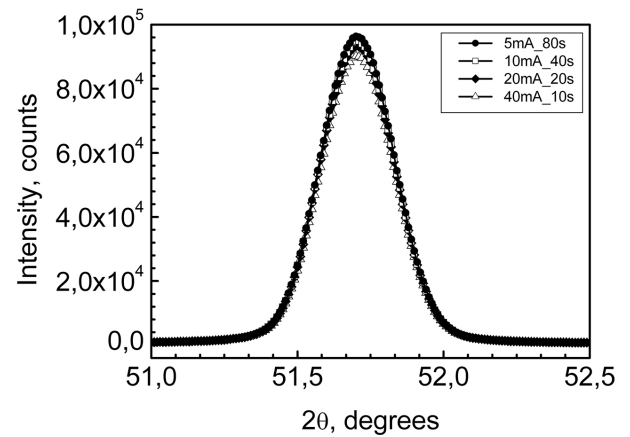
Fig. 3. A four-step measurement procedure applied to 200 reflections of Ni sample illustrates the apparent extinction effects such as they are.

other, i.e. they would be indistinguishable. Thus, for any of the neighbour levels of interaction, $R_{i,i*}$ ratios of the following type are valid:

$$I_{0,i}/I_{0,i*} = I_{kin,i}/I_{kin,i*} = g_i/g_{i*} = i/i* = R_{i,i*} \quad (6a,b,c,d)$$

where,

$$I_{kin,i}/I_{kin,i*} = R_{i,i*} = \left\{\mu I_{m,i}/\left[\mu - k\, I_{m,i}\left(p_2/p_1^2\right)\right]\right\}/ \\ \left\{\mu I_{m,i*}/\left[\mu - k\, I_{m,i*}\left(p_2/p_1^2\right)\right]\right\} \quad (7a,b,c,d).$$

Here, (a, b, c, d) denotes equations corresponding to different combinations. Combining the ratios, $R_{i,i*} = R_{i**,i***}$, $R_{i,i*} = R_{i*,i**}$, $R_{i,i**} = R_{i*,i***}$, $R_{i*,i**} = R_{i**,i***}$ among themselves and then solving them for $k=$const., i.e. $k^s = k_i = k_{i*} = k_{i**} = k_{i***}$ and $k^{max} = k_i = k_{i*} = k_{i**} = k_{i***}$ yield expressions of the type:

$$k^s = \frac{\left[\mu\left(I_{m,i*}^s I_{m,i**}^s - I_{m,i}^s I_{m,i***}^s\right)\right]}{\left[I_{m,i*}^s I_{m,i**}^s\left(I_{m,i}^s + I_{m,i***}^s\right) - I_{m,i}^s I_{m,i***}^s\left(I_{m,i*}^s + I_{m,i**}^s\right)\right]\left(p_2/p_1^2\right)} \quad (8a,b,c,d)$$

$$k^{max} = \frac{\left[\mu\left(I_{m,i*}^{max} I_{m,i**}^{max} - I_{m,i}^{max} I_{m,i***}^{max}\right)\right]}{\left[I_{m,i*}^{max} I_{m,i**}^{max}\left(I_{m,i}^{max} + I_{m,i***}^{max}\right) - I_{m,i}^{max} I_{m,i***}^{max}\left(I_{m,i*}^{max} + I_{m,i**}^{max}\right)\right]\left(p_2/p_1^2\right)} \quad (9a,b,c,d)$$

These coefficients are used for calculation of kinematical intensities and thus to correctly assess the physical effect due to size-strain broadening defined accordingly by integral intensity $I_{kin,i}^s$ [rad] and maximal intensity ($I_{kin,i}^{max}$) of reflection, both affected differently by SE:

$$I_{kin,i}^s = \left\{\mu I_{m,i}^s/\left[\mu - k^s I_{m,i}^s\left(p_2/p_1^2\right)\right]\right\} \quad (10a,b,c,d)$$

$$I_{kin,i}^{max} = \left\{\mu I_{m,i}^{max}/\left[\mu - k^{max} I_{m,i}^{max}\left(p_2/p_1^2\right)\right]\right\} \quad (11a,b,c,d)$$

The latter two equations are used to express extinction free integral breadth:

$$B_i = I_{kin,i}^s/I_{kin,i}^{max} \quad (12a,b,c,d)$$

To illustrate the relationship between k, $1/k$, and P, it may be instructive to use a heuristic device [11]. Heuristic refers to experience-based techniques for problem solving, learning, or discovery that find a solution, which is not guaranteed to be optimal or perfect, but sufficient for immediate goals. In this context, Figures 4a, 4b and 4c represent the behaviour of k^s and k^{max} as well as $1/k^s$ and $1/k^{max}$ of a sharp texture (Ni38) and powders (both microstructured and nanocrystalline CeO_2). We have shown that de-
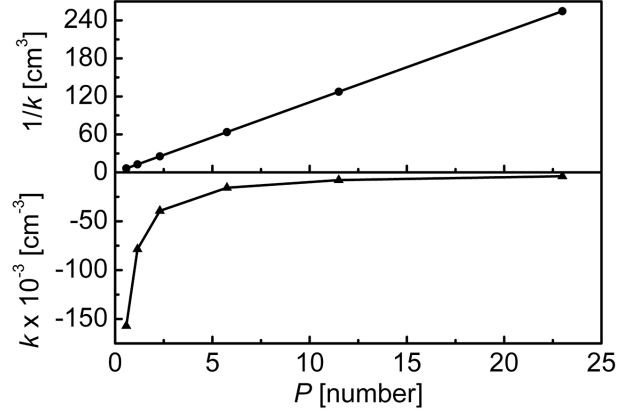
Fig. 4a. A heuristic device used to illustrate the relationship between k, $1/k$, and P. Highly textured Ni: $B = 0.2413$ [rad].
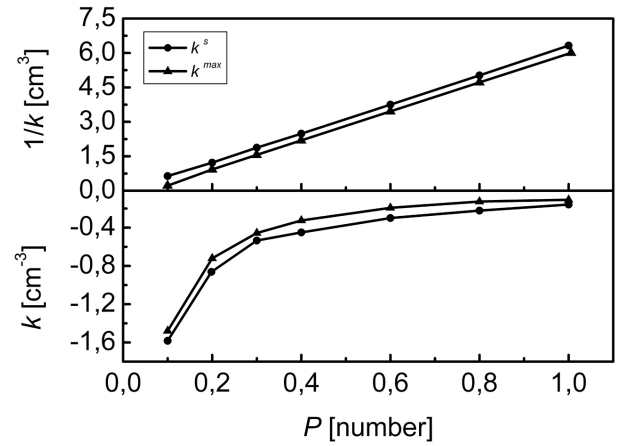
Fig. 4b. A heuristic device used to illustrate the relationship between k, $1/k$, and P. Nanosized CeO_2 : $B = 1.1322$ [rad].
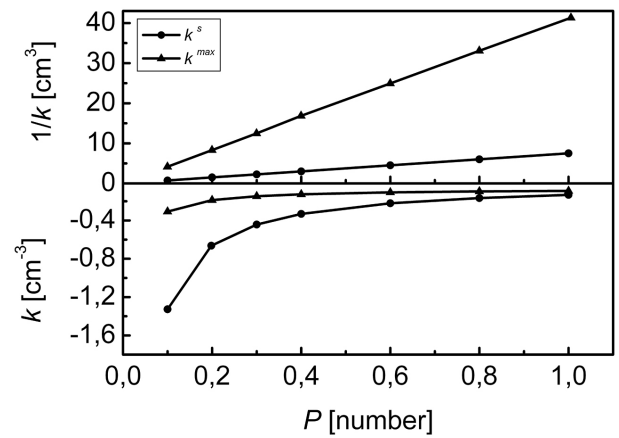
Fig. 4c. A heuristic device used to illustrate the relationship between k, $1/k$, and P. Microstructured CeO_2 sample: $B = 0.1806$ [rad].

pending on P $(0 < P < \infty)$, k and $1/k$ vary in different ways. Whereas the coefficient k reaches to its limits $(-\infty < k < 0)$ asymptotically, its reciprocal $1/k$ is straight proportional to P in the whole interval $(0 < 1/k < \infty)$. These curves demonstrate how the coefficients k and $1/k$ depend on microstructure (crystalline size and strain) in terms of P. In particular, the behaviour of the coefficients k^s and k^{max} proves complete homogeneity of the nanosized sample. However, in case of microstructured sample CeO_2, the behaviour of $1/k^{max}$ exhibits a nearly defect-free structure.

CONCLUDING REMARKS

1. Under pole density $P = $ const., the SE coefficient k is an irrational constant corresponding to the scattering space.

2. In the real space, $1/k$ defines crystallite volume in the Bragg condition that does not contribute to an increase of reflectivity.

3. Based on the constancy of k, a reformed methodology to observe, estimate, and nullify the SE effect is elaborated.

4. The main advantage of this methodology is that it allows for the capability of internal experimental checks revealing simply the real ability of the XRD apparatus to supply precise and accurate data.

5. The accuracy can only be achieved by care in experiment design and experiment realisation.

REFERENCES

1. W. H. Zachariasen, *Acta Cryst.*, **16**, 1139 (1963).
2. P. J. Backer, P. Coppens, *Acta Cryst.*, **A30**, 129 (1974).
3. T. M. Sabine, International Tables for Crystallography, Vol. C. pp. 530–533. Dordrecht: Kluwer Akademik Publishers, 1992.
4. E. Rossmanith, *Acta Cryst.*, **A58**, 12 (2002).
5. M. von Laue, *Z. f. Krist.*, **64(1)**, 115 (1926).
6. M. von Laue, *Ann. Phys.* (*Leipzig*), **26**, 55 (1936).
7. 7 W. L. Bragg, R. W. James, C. H. Bosanque, *Phyl. Mag.*, **42**, 1 (1921).
8. I. V. Tomov, *Bulg. Chem. Com.*, **43**, 325 (2011).
9. A. McL. Mathieson, *Acta Cryst.*, **A35**, (1979).
10. A. Guinier, Theorie et Technique de la Radiocrystallographie. 2nd edition, Paris, Dunod, 1956.
11. https://en.wikipedia.org/wiki/Heuristic.

ОПРЕДЕЛЯНЕ НА СВОБОДНА ОТ ЕКСТИНКЦИЯ ИНТЕГРАЛНА ШИРИНА

И. Томов[1]*, С. Василев[2], Г. Авдеев[3]

[1] *Институт по оптически материали и технологии „Акад. Й. Малиновски“, Българска академия на науките, София 1113, България*
[2] *Институт по електрохимия и енергийни системи, Българска академия на науките, София 1113, България*
[3] *Институт по физикохимия „Акад. R. Каишев“, Българска академия на науките, София 1113, България*

(Резюме)

Вторичната екстинкция (ВЕ) е неотделимо свързана с полюсната плътност, P. Последната представлява нормирана в кратност на хаотично разпределение обемна фракция на кристалити, която дава приноси към рентгеново отражение. В действителност, всяка измерена точка вътре в областта $2\Delta\theta$ на рентгеновото отражение е въздействана в различна степен от ВЕ, дължаща се на двете: полюсната плътност и разпределението на енергията (интензитета) на падащия сноп рентгенови лъчи, I_0. Обаче, за да бъде оценен ефекта на ВЕ върху рентгеновото отражение като цяло, неговия интегрален интензитет трябва да отчита полюсна плътност, $\bar{P}$, която е зависима от интегралната ширина на рентгеновото отражение. Така дефинирана, целта на настоящето изследване е да се развие техника за изчисляване на интегралната ширина, използвайки свободни от екстинкция данни на двата му параметъра: интегрален интензитет и максимален интензитет. Реформираните данни могат да бъдат използвани за чувствително третиране на ефекта на ВЕ в текстури и прахове, включвайки нано-размерни материали също така.

CONTENTS

СЪДЪРЖАНИЕ